HIGH-ORDER METHODS FOR STEADY, UNSTEADY AND TRANSITIONAL FLOW OVER A CYLINDER

By

Maxwell Starr
Supervisor: Dr E Shapiro

A THESIS SUBMITTED TO CRANFIELD UNIVERSITY
FOR THE DEGREE OF DOCTOR OF PHILOSOPHY

Cranfield University
Department of Fluid Mechanics and Computational Science
Cranfield, UK
July 2012

High-order methods for steady, unsteady and transitional flow over a cylinder

Maxwell Starr
Supervisor: Dr E Shapiro

July 31, 2012

Except where acknowledged in the customary manner, the material presented in this thesis is, to the best of my knowledge, original and has not been submitted in whole or part for a degree in any university.

Abstract

In this thesis, the flow around a cylinder is chosen as a test case for higher-order numerical reconstruction techniques. No direct comparison of these higher-order methods has been carried out for this particular test case. Especially for low Mach number, incompressible flows with Implicit Large Eddy Simulation method. The cylinder test case is both a proven test case in literature, as well as a test case that can be scaled up in terms of flow speed with other parameters remaining unchanged. The scaling of flow speed around the cylinder allows ease of flow regime change. Thus the flow was modelled in this thesis from laminar flow to turbulent flow, going through a transitional regime in between.

The simulations were set up such that numerical reconstruction methods could be directly compared to one another at the range of flow speeds, and subsequently in both two-dimensional and three-dimensional flows. The numerical reconstruction methods for the ILES cases ranged from first order reconstruction through to higher-order methods as high as ninth-order (in the weighted essentially non-oscillatory scheme). With the speed of computation for the two-dimensional simulations, it was possible to test all of these schemes directly with one another. However, three-dimensional simulations require a significantly greater CPU run-time. Therefore, based on the results of the two-dimensional simulations, a group of the higher-order methods were chosen for continuing analysis in the three-dimensional simulations.

In the laminar flow regime, all the numerical schemes agreed very well with literature data. As the flow speed increased, discrepancies started to appear in the results, to varying degrees based on the flow speed, the numerical scheme used, and the dimensionality of the flow. An analysis of the results showed that two-dimensional simulations were suitable up to Reynolds 300. From this flow

speed onwards, three-dimensional simulations are deemed necessary. At lower Reynolds number flows the two-dimensional simulations provided good predictions of the flow. At the higher Reynolds numbers, the $3D$ simulations outperformed the $2D$ simulations.

Specific numerical reconstruction schemes were found to perform better at certain aspects of the flow. For example, the coefficients around the cylinder or the velocities in the wake varied based solely on the numerical scheme used.

Finally, during the course of the post-processing of the simulations, a spectral analysis was carried out. The flow field was analysed at specific points in the wake (ranging from near, medium and far wake). The spectral analysis proved suitable for examining the fluctuations in the wake of the cylinder, showing the redistribution of energy in the wake towards higher frequencies. In addition, the wake showed increased power densities for the fluctuations as the flow moved away from the cylinder, before then decreasing again as dissipation into the surrounding flow occurred.

Acknowledgements

Lord Melchett: "Lord Blackadder. Our foremost cartographers have given us a map of the area you'll be traversing."
Edmund Blackadder: "But it's blank!"
Melchett: "Yes, they'd like you to fill it in as you go."

Richard Curtis and Ben Elton

* * * * *

There is no denying that at times this PhD (apparently like most others) has been a real struggle over the last few years. I have a long list of people who I wish to thank for helping me stay the course and see it through, though first and foremost I want thanks to go to my supervisor: Dr Evgeniy Shapiro. With Professor Dimitris Drikakis in the earlier years, I was given invaluable advice, kept challenged and received a kick when I needed it! Special thanks have to go to Dr Shapiro, though, for believing I could do this and for the subsequent many hours that he invested in helping me achieve it. This work would have undoubtedly been impossible without his input.

There really are too many friends to thank, due in part to my involvement with running the Ultimate Frisbee club and involvement with the MR2 clubs. However, special thanks must go to some friends who have often felt like family. This is especially true of Marc Spiller, Massimo Lai and Sarah Thiollet all of whom helped keep me on track, keep laughing and think optimistically - all while putting up with my particular foibles. Additionally, Shiroshana Tissera, Matyas Benke, Philip Barton, Felipe Inok, Ioannis Kokkinakis and Ben Thornber; my friends from the FMACS group. Thanks for all the fruitful technical discussions, techniques, tips and suggestions. They may not have all worked, but my word did they help! Guido Monterzino, Megan Barnett, Sven Peets, Kat Low, Steve Fowler, Manuela Donetti, Marco Nunez, Tim Cartledge and Guy Thallon; you were always there with encouragement just when I needed you and helped keep me on the road in more than a literal sense! Thanks to my saviours who offered a roof over my head when I needed one! Dr Christophe Della Vedova, Duncan Brewer and Toby Capel; I blame you guys for giving me the initial push to do a PhD. Thank you. Dave Ellis and Mukesh Joshi - as well as

Toby - who ensured my snowboard got some action at least once during the PhD course and for the endless silly emails. Thanks also to Teresa Townsend, without whom the last couple of years would have probably been impossible to handle, and Sue Richardson who works tirelessly for the CSA and helped me with my clubs as well as listening to my complaints! Although we're no longer in touch, an old challenge from my Maths teacher from School, Hassan Lakiss, has also been a very strange motivational tool over the years!

My family have been a loving source of guidance and inspiration. No words can express how thankful I have been just to have you all on the end of the phone to talk when I needed it, your patience when I've not been in touch for weeks or come home in months; just always being there and being understanding. No matter how many family occasions marked a target for submission of this thesis, I managed to completely miss them all!

My most vivid memories with my Grandfather are being sat on the floor with him watching Formula One races in the late 1980s, and him teaching me maths; both of which combined most likely led to my subsequent interests in aerodynamics and computational mathematics and inspired me to take this on in a research degree.

Finally, thanks to Rezvan Darbarbar, my Uncle. He became extremely ill in my second year (shortly after my own serious car accident), and passed away 14th May 2010. In a way, he reminded me what it meant to put things in perspective, and acknowledge that in spite of everything else, I still had my health and could manage. His strength for his fight for life inspired me to push on with my own personal fight. Rezvan, I may not have known you as well as I'd have liked, but you're greatly missed, and I dedicate this thesis to you.

Max Starr

* * * * *

Addendum: Two days prior to submission of this thesis, my Grandmother, Olwen, had a serious stroke, putting paid to the plans we had for after I submitted. She had touched many lives, and inspired all those around her. She continues to inspire me now.

Olwen Louisa Brace Starr, 1919 – 2011

Contents

List of Figures

List of Tables

Abbreviations and Symbols

Acronyms

CFD	Computational Fluid Dynamics
CPU	Computer Processor Unit
CV	Control Volume
DNS	Direct Numerical Simulation
ENO	Essentially Non-Oscillatory
FVM	Finite Volume Method
ILES	Implicit Large Eddy Simulation
LES	Large Eddy Simulation
LMNT	Low Mach Number Treatment
MUSCL	Monotone Upstream-centred Schemes for Conservation Laws
NSE	Navier Stokes Equations
PDE	Partial Differential Equations
PIV	Particle Image Velocimetry
RANS	Reynolds Averaged Navier Stokes
RK	Runge-Kutta
SGS	Sub Grid Scale
TVD	Total Variation Diminishing
VL	Van Leer
WENO	Weighted Essentially Non-Oscillatory

Terms

D	Diameter of cylinder (non-dimensionalised as 1)
x/D	x position non-dimensionalised based on cylinder diameter
Re	Reynolds number
M	Mach number
A	area
dA	elemental surface area
V	Volume
dV	elemental volume
$\overrightarrow{u}$	velocity vector
t	Real time
n	timestep number
p	pressure
ρ	density
$\overline{\overline{\tau}}$	shear stress tensor
x, y, z	Displacement in Cartesian form
i, j, k	Directional indices
u, v, w	Velocity Components (Momentum) in the X, Y and Z (Cartesian) directions
$\overline{u}, \overline{v}, \overline{w}$	Averaged velocity components in the X, Y and Z (Cartesian) directions
u', v', w'	Fluctuating velocity components in the X, Y and Z directions
u_0	centreline velocity
St	Strouhal Number, $St = f\frac{D}{V}$
C_d	Coefficient of Drag
C_l	Coefficient of Lift
C_f	Coefficient of Friction
C_p	Coefficient of Pressure
C_{p_b}	Base Pressure Coefficient
θ_{sep}	Separation Angle
L_{RZ}	Length of Recirculation Zone
$\frac{L_{RZ}}{D}$	Length of Recirculation Zone relative to cylinder diameter
U_{min}	Minimum Streamwise velocity
KE	kinetic energy
T	absolute static temperature
R	specific gas constant

Greek Symbols

τ_{ij}	Specific Reynolds Stress Tensor, $-\overline{u_i' u_j'}$
τ_{xy}	Specific Reynolds Shear Stress, $-\overline{u'v'}$
$\tau_{xx}, \tau_{yy}, \tau_{zz}$	Specific normal Reynolds stresses, $-\overline{u'^2}$, $-\overline{v'^2}$,$-\overline{w'^2}$

1

Introduction and Literature Review

Perfect as the wing of a bird may be, it will never enable the bird to fly if unsupported by the air. Facts are the air of science. Without them a man of science can never rise.

Ivan Pavlov (1849 - 1936)

* * * * *

Fluid flow surrounds us. It is everywhere, only we cannot always see it. When we walk, air (referred to as a fluid in engineering terms) passes around us. When an aircraft is in flight, this same air allows it to achieve a force of lift to keep it airborne. Then, there are the fluids we can see such as water flowing down a mountain. However for scientists and engineers, just knowing that it's there is not enough. We need to know how we can embrace it - how we can use it. Knowledge of fluid properties started from the definition of the Navier-Stokes equations (fundamental fluid equations derived by Claude-Louis Navier and George Stokes, with papers published in 1822 and 1845 respectively) and has allowed the explanation of many everyday 'problems' in nature, such as why ripples are formed in a steady pool of water, and how water flows through rivers.

Recently a robot was developed by PhD research students at the University of California that was able to fold towels [1]. This robot is capable of carrying out this task only; requiring further intervention and programming from a human researcher to do anything else. In order to carry

out its task, it has to analyse this towel, find the corners and determine how best to fold it. A large number of numerical steps and computational calculations are required in order to carry out what is - to humans - a routine and very simple task. Human intuition helps us carry out a number of assumptions and simplifications for many things. So it is for fluid flow. When we pass our hand under a tap that has water flowing out, we know that the water will hit our hand and flow around it. A computer cannot know this, and so a computational model is required to tell it that this is the behaviour it should expect the flow of water to do.

This is a simplified representation of Computational Fluid Dynamics (CFD). In reality, CFD is made up of a great number of numerical models and formulae, all of which are based on scientific fact and centuries of research following the initial findings by Navier and Stokes. It allows us a glimpse into the world of fluid flow in different states of being - states that cannot otherwise be replicated easily at all. With the use of computers to perform the millions of calculations that allow us to simulate fluid flows and interactions, we can begin to get a more detailed picture of the world around us as it relates to fluids. However, this detailed picture is still only an approximation; even with high-speed supercomputers a great deal of computational time is required to balance the equations to a satisfactory level. Constant advances are being made in computational power as well as research in fluid dynamics to develop software that allows quicker, more accurate, determination of fluid flows in all kinds of situations. The range of scenarios being researched is vast; from micro-fluids through to transonic flows, from blood flow in vessels in the body (with even specific computational techniques devised to aid in determining such blood flows [2]) to cloud formation for numerical weather prediction [3]. All of these are being researched to some degree.

The computing power that has been available has been a large determining factor in the progress of development of CFD. Determining the best possible solution to the equations through manual calculations is near-impossible unless a great deal of time is spent on a single (simple) problem. The advent of computing technologies meant that such mathematical problems could be dealt with with greater speed and accuracy. Historically computational facilities have been made available primarily for cutting-edge research projects, as even the oldest computers can resolve mathematical models much faster than a human could. As transistor technology for computers has developed, so too has the speed with which the mathematical problems could be solved; consequently the models being computed became more and more complex (themselves requiring greater amounts of storage space for the computations and the ensuing results). With resources now available such as cluster computing (including supercomputers), we can now examine a wider range of numerical problems than was possible even twenty years ago. Computational resources have developed at an astounding rate, as quantified by Gordon Moore in a seminal paper in 1965 [4]. Recently, though, Moore stated that in spite of continuing developments in computational technology, the rate of development of computing cannot continue at its previous rate [5].

A significant amount of time is still - even today - required to compute more complex simulations, and thus multiple techniques have been developed for CFD that allow for efficiencies to be developed in different ways, through adapting for particular situations or models. The three

main techniques in use are Direct Numerical Simulation (DNS), Reynolds-Averaged Numerical Simulation (RANS) and Large Eddy Simulation (LES). Each of these techiques differs in how they compute the Navier-Stokes equations and account for different effects in the flow.

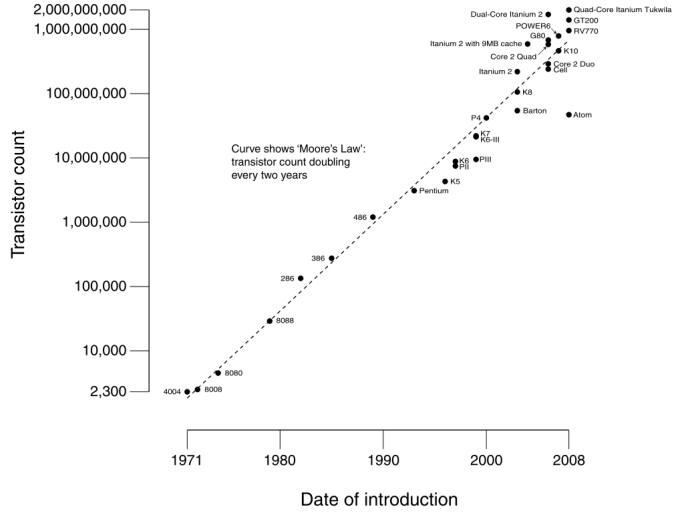

FIGURE 1.1: Increase in computational processing power as compared with Moore's Law (Up to 2008). Plot produced by Oleg Alexandrov and placed in public domain [4]

1.1 Turbulent Flow

Flow separation has been a highly studied area during the history of fluid mechanics (a history that is almost some five centuries in length, since the first studies by Leonardo) as it is a major contributor to flow loss and so is an undesirable factor in many applications concerning flow. It is a process that is unsteady leading to turbulent zones with vortices. Thus, many attempts have been made to accurately simulate the process of turbulent flow and the subsequent vortical shedding; a topic that this thesis aims to examine. The subject of turbulent flow has received attention for centuries. It is visually evident in everyday life, whether in water flow, smoke formations or the mixing of different fluids. It is present in both natural and man-made situations. Turbulence exists in flows of all manners of environment and scale. We can see turbulent mixing taking place when we add milk to tea, and yet this turbulent mixing shares important characteristics with turbulence visible in meteorological storm systems.

Even half a century since the pioneering attempts by Kolmogorov to predict the properties of flow at very high Reynolds numbers, it is almost impossible to accurately predict how turbulent mixing takes place, particularly at the higher Reynolds numbers. It is notoriously difficult to measure turbulence in either a natural environment or in laboratory conditions, and thus no unifying theory has been inferred. However, as numerical procedures have developed, the possibility of using computing power to model turbulent flow has become more realistic. Despite

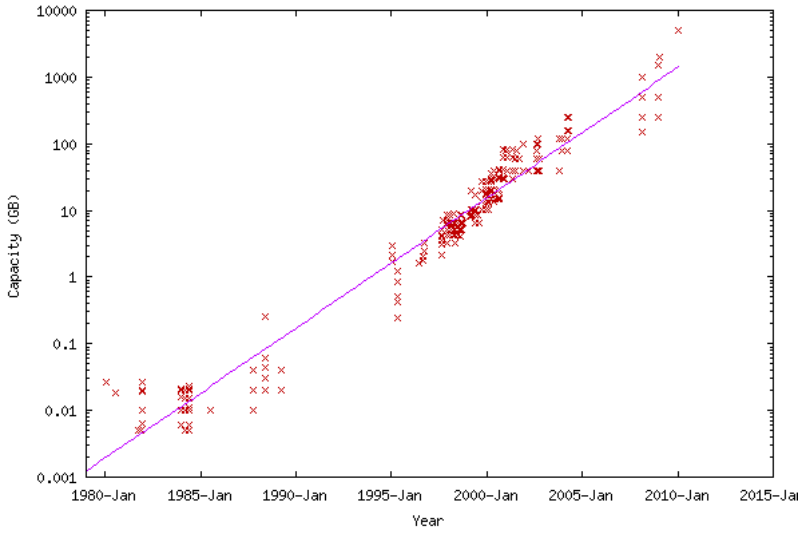

FIGURE 1.2: Increase in Hard drive capacity. Plot based on data available in the public domain [4]

improvements in simulation techniques and increases in computing power, however, it will remain almost impossible to accurately predict turbulence of higher Reynolds number flows for many years - particularly without the use of models to replicate effects taking place within the flow.

Some of the earliest applied forms of fluid mechanics involved the use of simplified mathematical models to solve numerical problems. One such use aided in weather prediction. Although initially proposed in 1904 by V. Bjerknes, it wasn't until 1950 - when computing power would be sufficient enough to allow rapid calculations - that the first successful use of fluid mechanics (by determining a simple form of atmospheric dynamics) for numerical weather prediction took place. Since then, further improvements in weather prediction techniques allow good prediction of such weather phenomena as typhoons and hurricanes, as our understanding of these weather anomalies has improved. On a large, overall-scale, these phenomena can now be forecast with a fair degree of accuracy. However, it is still almost impossible to determine the smaller turbulent effects within these phenomena. This is still a subject of great importance to the scientific community for practical purposes. One such area where this prediction would be important was previously investigated by this student, where errors are introduced into GPS satellite data due to cloud formations [6] - particularly in more severe weather. This is due to differing air moisture levels that cause a diffraction in transmission signal angle from particular satellites - resulting in errors introduced into location positioning 1.3(b). The Gulf Stream itself, which is one of these potential error sources for transmissions, is a turbulent wall-jet type of flow.

That is not the greatest scale of natural occurrence of turbulent effects. In fact, turbulent effects have been observed on the surface of the Sun, when solar flares are emitted. Interstellar gas clouds (gaseous nebulae) are turbulent. Equally, turbulent effects have been observed at the microscopic level with specialists examining plasma turbulence, while an examination has been carried out

on microscopic organisms to determine whether they are affected by turbulent flows [7] (interestingly, it was found that the small-scale turbulence these micro-organisms are exposed to seem to help modulate algal and bacterial nutrient uptake and growth, when compared with still-water micro-organisms, demonstrating a natural use of turbulence). Chemical engineers make use of turbulence to fully mix and homogenise fluid mixtures, and accelerate chemical reaction rates in liquids or gases. The flowing motions of water in rivers and canals is turbulent. Of more relevant interest to aerospace engineers, the wakes of ships, cars and aircraft are turbulent in nature. Thus, it can be seen that turbulence affects almost everything around us, in some scale or another. Consequently it can be seen that turbulence is very relevant in many subject areas, and so the study of it is an interdisplinary activity. For the focus of this study, however, the work in this thesis aims to focus purely on turbulence with regards to air flow, in engineering applications.

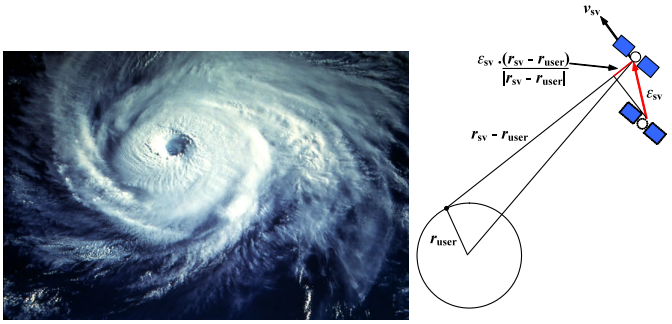

(a) (b)

FIGURE 1.3: (a) Typhoon Odessa as observed in September 1986 from the Shuttle Discovery during mission STS 51-I [8]
(b) Determination of errors introduced into GPS satellite readings due to signal diffraction [6]

Giving a definition of turbulence is somewhat difficult. Numerous texts on turbulence have been written, (for example [9–11]) but none have successfully given a straightforward definition of turbulence without discussing some of the key characteristics that define a turbulent flow; some of these characteristics will be discussed between sections 1.1.1 and 1.1.6.

1.1.1 Irregularity of flow

The first characteristic, that is perhaps most obvious when observing a turbulent flow, is the irregularity of the flow. This makes the ability to attain a definitive map of a turbulent flow impossible. Instead, the best that can be achieved is a map of flow based on statistical determination methods. That is, one can obtain an average of flow or a statistically good approximation of a flow rather than an exact flow derivation.

1.1.2 Diffusivity and mixing of Turbulence

A second key characteristic of turbulence - and perhaps the single most important characteristic as far as engineering applications are concerned - is the diffusivity of the turbulent flow. The diffusion of turbulence results in rapid mixing and an increase in rates of momentum, mass and heat transfer [9]. Mixing through turbulence can allow for transport of contaminants such as heat, particles and moisture. Diffusivity is a key characteristic as it can be used to influence the behaviour of boundary layer separation. An example of this is on an airfoil that is at a high angle of attack, or flow in a pipeline (a channel flow) where turbulence is the chief source of flow resistance.

The irregularity of flow discussed in the previous section cannot be taken to be the sole indicator of turbulent flows. The flow should also spread velocity fluctuations into the surrounding flow. If this doesn't happen the flow cannot be turbulent.

1.1.3 Dissipation of Turbulence

Viscous shear stresses within the flow result in deformation work, increasing the internal energy of the fluid. This results in an imbalance in energy within the system. Thus, a continuous source of additional energy is required to account for the viscous losses. Without additional energy, the turbulence will decay rapidly. This leads to turbulent flows being dissipative, as generally the additional energy source does not exist. This is a differentiating characteristic between turbulence and random wavelike motion (such as random sound waves which have insignificant viscous losses).

The dissipation of energy in turbulent flow is considered as one of the basic empirical laws of fully developed turbulence [12]. That is, if all the parameters in an experiment on turbulent flow are kept the same, except for the viscosity which is lowered as much as possible, the energy dissipation per unit mass (dE/dt) behaves in a way that is consistent with a finite positive limit. This holds (at least approximately) for almost any turbulent flow.

1.1.4 Turbulence in High Reynolds Number Flows

The Reynolds number is a dimensionless number that gives a measure of the ratio of inertial forces to viscous forces. The value for Reynolds numbers quantifies the importance of each of these forces in a particular flow scenario. As it is a ratio, use of the Reynolds number in setting up test cases allows for maintenance of dynamic similitude between different numerical and experimental cases, particularly as the Reynolds number is specified scaled to the size of the test object. The Reynolds number is determined as:

$$Re = \frac{UL}{\nu}$$

where U is the mean flow velocity, L is a chosen characteristic length scale, and ν is the fluid kinematic viscosity (defined as equal to dynamic viscosity divided by density, or $\nu = \mu/\rho$).

Turbulent flows always occur at high Reynolds numbers [9]. Flows which are initially laminar develop if the Reynolds number is increased too far. This is due to interactions between viscous terms and nonlinear inertia terms in the equations of motion. The mathematics of the interaction is very complex involving nonlinear partial differential equations. Due to the combination of the randomness and nonlinearity of the terms, the equations of turbulence are almost impossible to solve. Mathematical tools and models have been developed to help with approximating the turbulent flow (some of which will be discussed later in this work), but no single method to solve the problems through the equations is possible.

1.1.5 Three-dimensional Vortical Fluctuations

Turbulence is a rotational and three dimensional flow, with high levels of fluctuating vorticity. Thus the dynamics of vorticity are essential for the proper definition of turbulent flows. This leads to the realisation that turbulent flows are three-dimensional as an important mechanism for vorticity, called vortex stretching, does not exist in two-dimensional flow. Without vortex stretching, the random vortical fluctuations characterising turbulence could not maintain themselves. The vortex stretching becomes more rapid and considerable as Reynolds numbers reach high values, as demonstrated by the mean energy dissipation that occurs [12]. Therefore, turbulent flows always show high levels of fluctuating vorticity. An analogy of this is random waves on ocean surfaces; these do not have turbulent motion as they are irrotational.

1.1.6 Turbulent Flows are Flows

> "Turbulence is not a feature of fluids but of fluid flows."[9]

This is an important definition for turbulence; The dynamics of turbulence do not change, regardless of the state of the fluid (whether it is a liquid or gas) if the Reynolds number is high enough. The main characteristics of the turbulent flow are not affected by the molecular properties of the fluid that is in flow.

For fluid flow, no single general solution to the governing equations, the Navier-Stokes equations, exists. It follows that the same condition applies to turbulent flows; no general solution exists. Additionally, as every flow is different, every turbulent flow is also different – even though all turbulent flows share a number of characteristics. This sharing of characteristics allows those who study turbulent flows to easier formulate models to describe the flows. As fluid flows have characteristics related to their initial and boundary conditions, turbulent flows also depend on their environment. This means models are designed to operate within a specified range of boundary and environment conditions.

1.1.7 The different Length Scales of Turbulence

Kolmogorov theorised about the transfer of energy from large to smaller eddies, how much energy is contained within eddies of a particular size, and how much energy is dissipated by eddies

at each size. There are, essentially, three main turbulent length scales: the integral scale, the Taylor scale and the Kolmogorov scale.

If we consider fully turbulent flow at a high Reynolds number (as discussed earlier, Reynolds number is given by $Re = \frac{UL}{\nu}$), we note that the turbulent flow consists of eddies of differing sizes. An eddy cannot be precisely defined, but is conceived as a turbulent motion, localised over a region of size l, that is at least moderately coherent over this region. However, within this region can also be smaller sized eddies. Defining the eddies to have size l, we consider that the characteristic velocity is $u(l)$ and characteristic time scale $\tau(l) \equiv l/u(l)$. Eddies within the largest size range are characterised by the lengthscale l_0, which is comparable to the flow length scale L [9]. The characteristic velocity of these largest eddies is given by $u_0 \equiv u(l_0)$ and is of the order of the r.m.s. turbulence intensity $u\prime \equiv (2k/3)^{\frac{1}{2}}$, which is comparable to U. The turbulent kinetic energy is defined as:

$$k = \frac{1}{2} < u_i u_i >= \frac{1}{2}(\overline{u'^2} + \overline{v'^2} + \overline{w'^2}) \tag{1.1}$$

The Reynolds number of these eddies ($Re_0 = u_0 l_0/\nu$) is large (when compared to Re) and so the direct effects of viscosity on these eddies are negligibly small.

The Integral Length Scale and the Energy Cascade

For the largest length scale, the Integral length scale, we can determine an estimate of the length scale (l_0) of the larger eddies. Eddies of this size l_0 have a timescale $\tau_0 \equiv l_0/u_0$ and a characteristic velocity $u_0 \equiv u(l_0)$. This velocity is on the order of the r.m.s. turbulence intensity $u\prime \equiv (2k/3)^{1/2}$. We can therefore assume that the energy of the eddy with velocity scale u_0 is dissipated over time τ_0. This allows us to then derive the equation for the length scale:

$$l_0 \propto \frac{k^{3/2}}{\epsilon} \tag{1.2}$$

where ϵ is the energy dissipation rate (in m^2/s^3). This proportionality is of the order of one, and is usually referred to as the integral length scale of turbulence. The Reynolds number that is associated with these largest eddies is referred to as the turbulence Reynolds number Re_L, and is defined as:

$$Re_L = \frac{k^{1/2} l_0}{\nu} = \frac{k^2}{\epsilon\nu} \tag{1.3}$$

The large eddies within this largest length scale are somewhat unstable, and so break up and transfer their energy to smaller eddies. These smaller eddies also break-up, transferring their energy to smaller still eddies. This process is termed 'The Energy Cascade' whereby energy is transferred to successively smaller and smaller eddies until such a point that the Reynolds number of the eddies is small enough with eddy motion being stable and molecular viscosity being effective in dissipating the kinetic energy. At these smaller scales, the kinetic energy of turbulence is converted to heat energy. At the end of the process of the energy cascade, we have dissipation, ϵ. The rate of this is determined by the first processes - the transfer of energy from the largest eddies to the next size down. The eddies have energy of the order of u_0^2 and timescale

$\tau_0 = l_0/u_0$ and so we can derive the rate of transfer of energy as scaling according to $u_0^2/\tau_0 = u_0^3/l_0$. Thus we can say the energy cascade has dissipation rate, ϵ, proportional to u_0^3/l_0 and independent of ν (at high Reynolds numbers).

Kolmogorov's hypotheses and length scale

Kolmogorov derived many details on the scales of turbulence, as well as a range of other characteristics, in his seminal paper in 1941. This is detailed by Pope [10] where Kolmogorov's theories are explained. These theories were based on three important hypotheses along with dimensional arguments and experimental observations. These are not discussed in detail here - instead some pertinent points are included for discussion.

Kolmogorov hypothesised that in the case of homogenous turbulence, the turbulent kinetic energy (k) is the same everywhere. If the turbulence is isotropic, the eddies will also behave the same in each direction. That is: $\overline{u'^2} = \overline{v'^2} = \overline{w'^2}$. The directional biases of the larger scales appear to be lost in the chaotic scale-reduction process as energy is transferred to smaller and smaller scale eddies. Thus Kolmogorov stated that in the case of isotropy at small scales:

> *At sufficiently high Reynolds numbers, the small-scale turbulent motions ($l \ll l_0$) are statistically isotropic [10].*

Turbulence at larger scales can still be anisotropic. The characteristic length separating the smaller isotropic scales from the larger anisotropic scales is termed l_{EI}, with $l_{EI} \approx l_0/6$ for many higher Reynolds number flows. This does, however, mean that under a certain lengthscale (l_{EI}), all the information about the geometry of the larger eddies is lost and the statistics of the smaller scale motions are considered substantially universal and similar in every high Reynolds number flow. This consideration led to Kolmogorov's first similarity hypothesis:

> *In every turbulent flow at sufficiently high Reynolds number, the statistics of the small scale motions ($l < l_{EI}$) have a universal form that is uniquely determined by the dissipation rate ϵ and the viscosity ν. [10].*

This now leads to the concept of the universal equilibrium range for eddies of scale $l < l_{EI}$. Using the viscosity and dissipation rate, we can form unique velocity (v), length (η) and time (τ) scales to characterise these eddies:

$$v \equiv (\nu\epsilon)^{1/4}, \qquad \eta \equiv \left(\nu^3/\epsilon\right)^{1/4}, \qquad \tau \equiv (\nu/\epsilon)^{1/2} \tag{1.4}$$

These scales are known as the Kolmogorov length scales, and are indicative of the smallest eddies present in the flow field; the scale at which energy is dissipated. That is, consistent with the energy cascade concept, the kinetic energy is transmitted from the largest scales to Kolmogorov scales, at which point the energy is dissipated by the viscous forces. It is at this point that the Reynolds number is equal to unity. That is, the Kolmogorov Reynolds number Re_η of the small eddies is equal to 1.

A size range (where $l < l_{EI}$) is referred to as the universal equilibrium range, where Komogorov noted that a distinction can be made. The timescales in this range are small compared

to l_0/u_0 and so the eddies can adapt quickly to maintain dynamic equilibrium with the energy transfer rate imposed by the large eddies. For this, Kolmogorov stated in his second similarity hypothesis:

> *In every turbulent flow at sufficiently high Reynolds number, the statistics of the motion scale l in the range of $l_\eta \ll l \ll I_0$ have a universal form that is uniquely determined by ϵ, independent of ν. [10].*

This allows the definition of a new length scale, l_{DI}, with $l_{DI} \approx 60\eta$ for many turbulent high Reynolds number flows. This range can therefore be written as $l_{EI} > l > l_{DI}$. This itself can be split into two subranges:

- The inertial subrange ($l_{EI} < l < l_{DI}$) where motions are determined by the inertial effects and viscous effects are negligible
- The dissipation range ($l < l_{DI}$) where motions experience viscous effects.

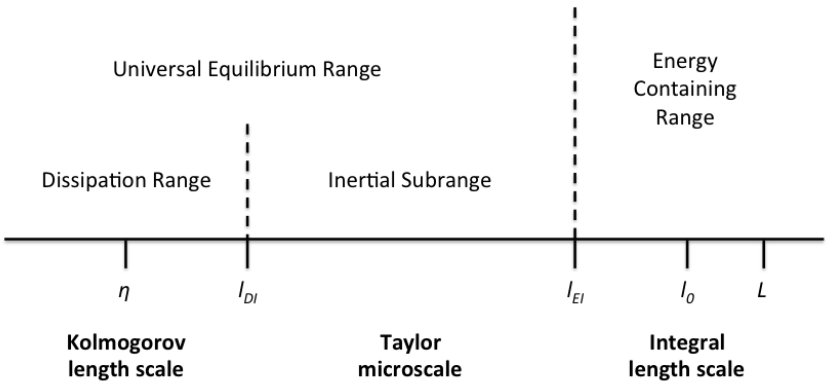

(a)

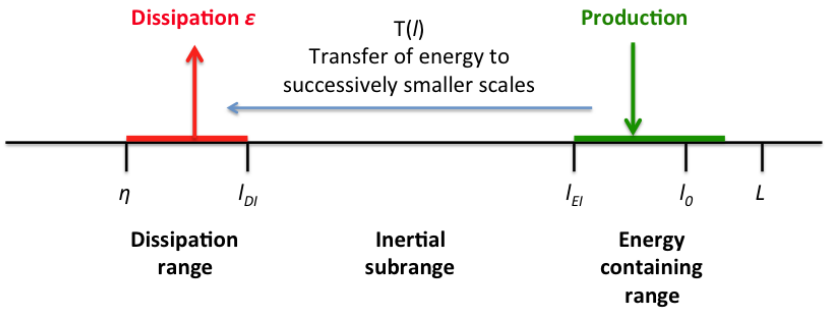

(b)

FIGURE 1.4: (a) Sizes and ranges of turbulent structures according to Kolmogorov for flows at high Reynolds numbers. The bulk of the energy is contained in the larger eddies within the size range $l_{EI} = l_0/6 < l < 6l_0$ – called the energy containing range.
(b) Energy transfer rate from large scales to the smaller scales, represented by $T(l)$.

The Kolmogorov Spectrum

Leading on from Kolmogorov's second similarity hypothesis, an energy spectrum can be derived, $E(\kappa)$, which is non-dimensionalised and solely dependent on ϵ and κ. The length scales related by Kolmogorov's work are those that are included in the universal equilibrium range. In the Fourier space, the wavenumber κ is defined as $\kappa = 2\pi/l$ (where $E(\kappa)$ is the energy contained in eddies of size l and wavenumber κ). The turbulence kinetic energy, k is, by definition, the integral of $E(\kappa)$ over all wavenumbers:

$$k = \int_0^\infty E(\kappa)d\kappa \tag{1.5}$$

The energy in eddies with wavenumbers between κ_A and κ_B is therefore:

$$k_{(\kappa_A,\kappa_B)} = \int_{\kappa_A}^{\kappa_B} E(\kappa)d\kappa \tag{1.6}$$

By non-dimensionalising $E(\kappa)$ using ϵ and κ, we obtain the energy spectrum function:

$$E(\kappa) = C_\kappa \epsilon^{2/3}\kappa^{-5/3} \tag{1.7}$$

Equation 1.7 describes the famous Kolmogorov $-\frac{5}{3}$ spectrum function. C_κ is the universal Kolmogorov constant which has been found through experiment to be $C_\kappa = 1.5$. This spectrum equation states that the turbulent kinetic energy in the subinertial range decays as $\kappa^{-5/3}$, as shown in the plot in figure 1.5.

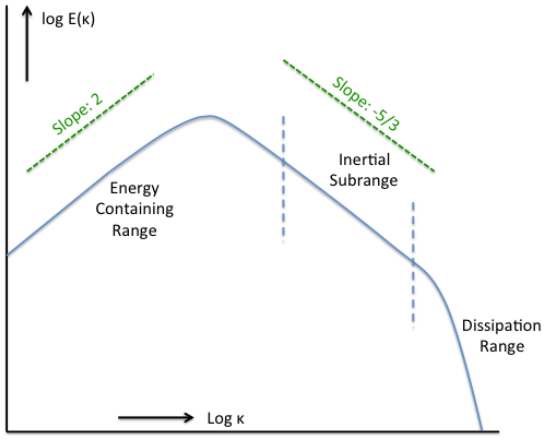

FIGURE 1.5: Kolmogorov Energy Spectrum

In the process of carrying out LES and RANS simulations with fauvre averaged data, the fourier transform of the instantaneous data (wavenumbers against real-time) can be determined. If turbulent characteristics are evident in the flow, the decomposition of the energy will scale according to Kolmogorov's determined length scale of $\kappa^{-5/3}$.

1.1.8 Relevance of turbulence to engineering applications

Interest in fluid dynamics for engineering applications began with the increase in interest in airfoils. From the mid-1700s, hopeful aeroplane designers realised more needed to be known about how air flows over surfaces. Examination of bird flight had not given sufficient information to begin the design of a useable airfoil. As such, the realisation was made that scientific experiments would have to be carried out to determine the best shapes for flight; these experiments could either involve a test shape moving through the air, or air moving over a stationary model.

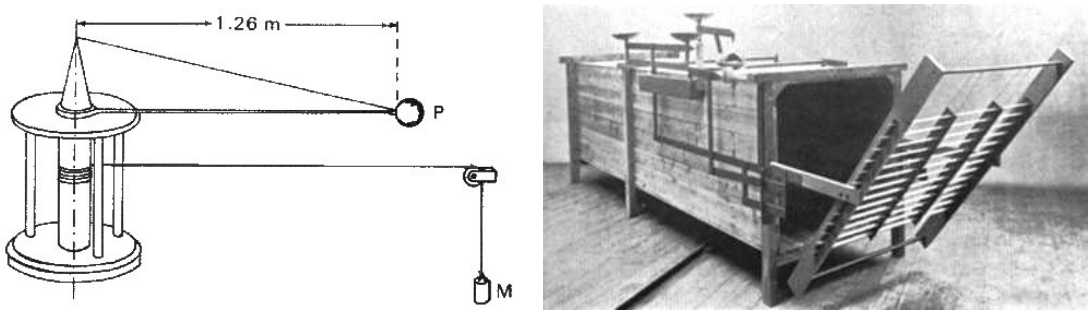

(a) (b)

FIGURE 1.6: (a) Benjamin Robins experiment proving air resistance was a critical factor in the flight of projectiles. The weight of falling object M caused the arm holding object P to whirl resulting in known velocity of air flow over the object. [13]
(b) Hiram Maxim's wind tunnel to measure the lift and drift of aeroplanes and airfoils. [13]

One of the earliest known relevant experimental apparatus was devised by the English mathematician Benjamin Robins [14] in 1746, where a whirling arm device allowed him to prove that air resistance is a critical factor in projectile flight. This was followed with similarly designed whirling arm apparatus through the following decades, with test models increasing in complexity to include such models as airfoils. Then, in 1871, Frank H. Wenham designed the first wind tunnel. This tunnel was 12 feet long and 18 inches square in size, with air powered by a steam-powered fan that could produce a maximum flow velocity of 40 miles per hour. This was, being the first, a very unsophisticated wind tunnel (particularly when compared with its modern-day equivalents), however this was clearly the future of airflow testing. Figure 1.6(b) shows one of the earliest photographs of a wind tunnel; a wind tunnel built by Hiram Maxim. Drawing a comparison to todays wind tunnels, this seems no more than a closed box.

As more was learnt about the mechanisms of flight, the importance of such factors as lift and drag became greater, and so knowledge of these factors equally increased. Experimental procedures were further and further developed that allowed for accurate simulation of these physical phenomena, while taking measurements.

Obviously, since the earliest forms of wind tunnels, the quality of measurements we can take

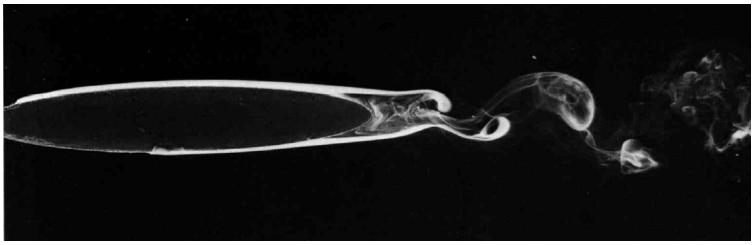

(a)

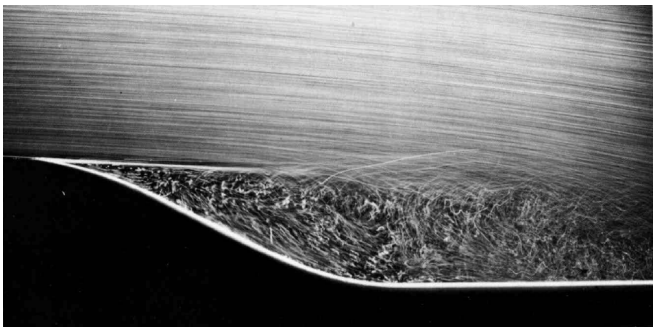

(b)

FIGURE 1.7: (a) Laminar separation on a thin 6:1 elliptic cylinder at Reynolds number 4,000. The laminar boundary layer can be seen separating at the rear. [15, plate 32]
(b) Laminar separation from a curved wall at Reynolds number 20,000. [15, plate 38]

from experiments carried out have become much more diverse, the models we can carry out the experiments on have become more complex while airflow speeds have drastically increased. Such examples of work carried out in wind tunnels is shown in figure 1.7, taken from the glorious Album of Fluid Motion by Milton van Dyke [15] which contains many more such experimental images from wind tunnels.

The use of wind tunnels allowed further understanding of the fundamentals of aerodynamics, and subsequently how fluids behave under specific circumstances. Through examining how changes in an airfoil design change particular characteristics of that airfoil, theories defining such factors as the coefficients of lift and drag (including how this leads to induced and interference drag). Thus, mathematical models defining physical occurrences such as lift and drag could be defined. These have now become key factors in engineering designs, having a significant impact on the final characteristics of the object in question.

The frontal profile of an object (the surface that faces the oncoming flow, which is dependent on model geometry and flow direction) determines the coefficient of drag (some examples of which are illustrated in figure 1.8). A friction force is applied due to the flow hitting the front surface of the object. In order for the object to continue movement through the flow, the thrust applied by the object (pushing it forwards) must be greater than the coefficient of drag. There are other resisting forces that reduce the velocity of an object, or increase the amount of thrust (work) needed by the object to move, however the definition of these additional forces is beyond

this scope of this thesis. With regards to road-going vehicles, the coefficient of drag generally becomes an important factor once the object has already gained momentum (i.e. once the object is already moving in airflow). Reducing the coefficient of drag of a vehicle is a key component in the external design of a vehicle. Even with very powerful engines, there are a number of sports cars that have a limited top speed solely due to their aerodynamic profiles, with the drag increasing so drastically at higher speeds that the thrust provided by their engines can no longer overcome the increase in rearward forces.

Initial experimentation on coefficient of drag, and how it was affected by the shape of an object in flow, was carried out on simple objects such as circular and square cylinders. From here, investigation moved to airfoils as a decrease in drag helps with increasing lift (and thus makes an airfoil profile much more useful in practical applications). As can be seen on figure 1.8, the more curved profiles provide a lower coefficient of drag.

At the rear of the object in the airflow, we have interesting flow characteristics. Directly behind the object in flow is the wake. This is the flow region directly influenced by the presence of an object in flow. Above and below this wake region (position and size varies according to the flow direction and the object geometry) exist turbulent regions where turbulent eddies are formed due to a small region between the high-speed free-stream flow and the lower speed wake flow. A third important region for consideration is the boundary layer. This is a small layer that surrounds the object, following the contours of the object geometry until a point of flow separation. The boundary layer increases in thickness as the flow speed increases, and is a significant cause of drag in the flow of an object as flow speed increases. In a laminar flow, the thickness of the boundary layer increases as shown by equation 1.8a. In a turbulent flow, the boundary layer will have unsteady flow effects, and as such has a differently sized boundary layer, which can be defined as equation 1.8b [9]. For equation 1.8, l is the diffusion distance, L is the scale distance of the flow field, the characteristic velocity fluctuations are of order u', and reference free-stream

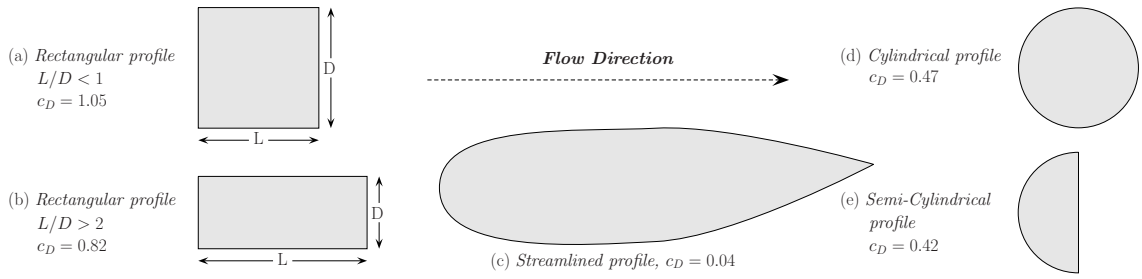

FIGURE 1.8: Comparison of Coefficients of Drag for a variety of shapes [16]. The streamlined shape has the same height as the cylindrical profile, yet has a much lower C_D due to the airfoil type shape.

velocity is U.

$$\frac{l}{L} \sim \left(\frac{v}{UL}\right)^{\frac{1}{2}} = Re^{-\frac{1}{2}} \tag{1.8a}$$

$$\frac{l}{L} \sim \frac{u'}{U} \tag{1.8b}$$

These flow factors are all, as discussed, important considerations in the design of an object within engineering. Immediately visible applications such as vehicles (cars and trucks) are obvious, though the same flow principles apply for aircraft, spacecraft, cables raised high (and thus susceptible to high wind-speeds), buildings, bridges, and a great many more man-made objects which interact with air.

Understanding of the physical phenomena that take place, and how these can be accurately modelled has been carried out over the centuries. Primarily these were carried out as experimental methods in windtunnels. The advance in windtunnels previously discussed has allowed more fine measurements to be carried out. Subsequently, we have had improvements in the modelling of each factor in the flow. As a result of all this, as well as the core equations of fluid mechanics, computational solvers of the flow have become more advanced. Thus, a variety of different solving techniques have been borne out of models of flow in different scenarios.

1.2 Modelling Turbulent Flows

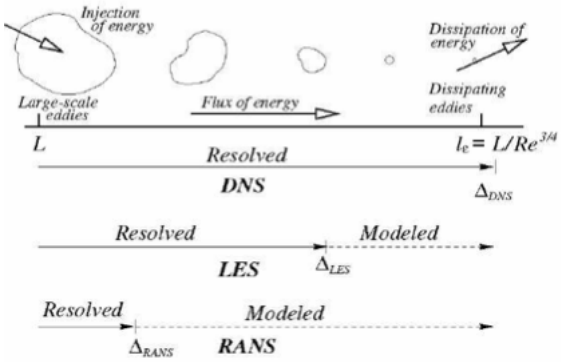

FIGURE 1.9: An illustration of the length scales of flow resolved by the numerical methods

As has been briefly mentioned, there are three classical (and most commonly applied) numerical techniques that are applicable to solving the mathematical models derived. However, these simulations are still restricted in their accurate determination of the effects of turbulent flow. This is due to the absence of a closed theory for the classical fluid equations which is unlikely to be

determined in the near future. Thus the three classical techniques for Computational Fluid Dynamics have evolved as computational use of solving the mathematical models have concurrently evolved. These three techniques are Direct Numerical Simulation (DNS), Reynolds Averaged Numerical Simulation (RANS) and Large Eddy Simulation (LES). These are discussed briefly in the following sections. The Implicit Large Eddy Simulation (ILES) technique that has been utilised in this thesis will be discussed in more detail in a later section. The scales resolved explicitly by each scheme are illustrated in figure 1.9.

1.2.1 Direct Numerical Simulation

The Direct Numerical Simulation (DNS) method of CFD resolves fluid motion at all temporal and spatial (time and motion) scales, making it one of the most accurate of the techniques, but also the most computationally expensive. All of the spatial scales of turbulence are resolved within the computational domain.

Due to the fact that even the smallest dissipative turbulent effects have to be resolved by the method, the grid size is dependent on the scale of turbulent eddies that will be present in the simulation. The grid resolution is derivative of the scale of turbulent effects and, ultimately, the Reynolds number. Thus, a high Reynolds number will require a very fine grid for the domain to resolve all the artefacts sufficiently. Equally, a greater number of timesteps (with a smaller Δt determined by the Kolmogorov scale) will be required for proper convergence of values to a satisfactory solution. The number of calculations required to satisfactorily complete the solution has been found to be proportional to the number of grid points and the number of time-steps to a scale of Re^3. This estimate of the scaling shows one of the key limitations of the DNS technique; that as Reynolds number gradually increases, the relative increase in computational cost is very high. Though in actuality, the computational cost of DNS even at Low Reynolds numbers still is high.

This is a fundamental problem as common engineering applications of CFD occur at relatively high Reynolds numbers or very small scale (resulting in a high number of grid points). Thus the computational resources required to satisfactorily reach a solution for most common engineering applications of CFD would exceed the capability of even the most powerful computers available today. It was demonstrated by Moin and Kim [17] that the computational requirements of using DNS for a 50 meter long aircraft fuselage and wings, with the aircraft at cruising altitude and speed (250 m/s and 10,000 meters altitude), were massive. Ten quadrillion (10^{16}) grid points would be required in this case to appropriately simulate the turbulence near the aircraft surface with a reasonable level of detail. At the time of writing, a computer capable of teraflop computing - that is, carrying out ten trillion (10^{12}) floating-point operations per second (as compared to a standard desktop carrying out around 2×10^9) - was just around the corner, but even this computer would require several thousand years of computational time to compute the flow for one second of flight time! Thirteen years later, in June 2010, the top 500 list of computers was released showing that the fastest computer (the Cray Jaguar at Oak Ridge National Laboratory [18]) is capable of 1759 teraflops. Even with these speeds, the same calculation will still take decades to

complete!

Thus it can be seen that the computational cost of DNS is very high, limiting its application to many common CFD simulations. However, DNS does still have some use as a tool for CFD, particularly for turbulent flow. DNS can be used to carry out numerical simulations of flows that, in a laboratory experiment, would be very difficult (or impossible) to obtain precise information from. This allows improvements in the turbulence models used for practical applications by the alternative CFD methods. An example of this is the development of the sub-grid scale models that are used in Large Eddy Simulations (LES). Therefore, the DNS method has proved invaluable in implementing the alternative methods for practical engineering applications, but generally remains confined for use in low Reynolds number applications.

Direct Numerical Simulation is a numerical technique that models the flow while allowing for different turbulent resolutions to either be ignored if they are of sufficiently small scale, or modelled appropriately according to the turbulent eddy size. The scale that determines modelling has been investigated by Komlogorov and is thus called the Komlogorov scale, as discussed in section 1.1.7.

1.2.2 Reynolds Averaged Navier-Stokes Simulation

The Reynolds Averaged Navier-Stokes (RANS) technique is a form of Computational Fluid Dynamics derived from the techniques developed through DNS by Osborne Reynolds. The equations used in this technique are a time-averaged set of equations defining fluid flow. With the use of mathematical models (approximations for particular features of the flow) gained through DNS techniques, this is a versatile method for dealing with turbulent flows. This method averages out the unsteadiness, that is regarded as part of the turbulence.

The exact solution for the flow is formed through decomposition of the flow into a statistical average and a fluctuating turbulent regime. The decomposition used is based on the Reynolds decomposition technique. This method essentially splits a given flow variable (such as instantaneous velocity u) into a mean component (ensemble-averaged, $\bar{u}$) and a fluctuating component (u'). These split variables are summed such that:

$$\mathbf{U}(\phi, t) = \overline{\mathbf{U}}(\phi) + \mathbf{u}'(\phi, t)$$

Note that $\phi = (x, y, z)$ represents the position vector in each of the three cartesian directions; a variable that varies in time.

The decomposed parts can be defined as:

$$\overline{\mathbf{U}} \equiv \frac{1}{T} \int_{t}^{i+T} u(t) dt$$

$$u' \equiv u - \overline{u}$$

T has to be a long enough time to allow the fluctuations in u to be fully averaged. By definition, the mean of the fluctuating quantity (u') must be zero ($\bar{u}' = 0$).

	Number of additional transport equations
Mixing length model	0
Spalart-Allmaras	1
$k-\epsilon$	2
$k-\omega$	2
v^2-f	4
Reynolds Stress Model	7

TABLE 1.1: Common RANS turbulence models. Note: The additional number of transport equations to be solved denotes the number of additional partial differential equations that are being solved

The averaging method used is normally dependent on the type of problem encountered. That is, a spatial-averaging method would be used for a flow that is two-dimensional in nature, while a time-average method would be used for a flow that is steady in nature. This is quite a useful technique as most flows reach a statistically steady state when averaged over a period of time. Therefore, for flows where there are very few changes in external flow for free-stream flows, or changes in inlet conditions for internal flows, the time-averaged method tends to be preferred. However, the method is still quite limiting in that the simulated time duration has to be significantly longer than the largest time scale in the flow for averaging to be effective.

It can be seen that the RANS technique describes the change in mean quantities of the flow. While giving an overall view of the flow, it does not allow for the effects of turbulent fluctuations and is therefore generally regarded as a statistical approach to the solution of the Navier-Stokes equations. When the decomposition is carried out on the governing equations, a new set of equations for the mean-flow field (compared to the original Navier-Stokes equations) include a term correlating the fluctuating velocities: $-\overline{\rho u_i' u_j'}$. This is known as the Reynolds Stress Tensor, and represents the influence of the turbulence on the mean flow field from the fluctuating components. This term is estimated by a turbulence model to close the system of equations [11]. The estimation of the Reynolds stresses is not unique, and thus a range of empirical, or semi-empirical, turbulence models useful for particular flows are available in the literature, and in a range of CFD codes. Examples of these (there are around 200 models in existence in the literature) are given in table 1.1.

Within each model group is generally a range of sub-models that allow the models to be suited to different applications, with each subject to different limitations and weaknesses. For example, the RNG (Renormalization Group Method) and Realisable $k-\epsilon$ models are both subject to a range of limitations due to the isotropic eddy viscosity assumption, while the Reynolds Stress model approach is computationally more expensive while also tightly coupling the momentum and turbulence equations. This assumption of isotropic nature of the eddy (or turbulent) viscosity (μ_t) is an important point to consider - turbulent viscosity is not homogeneous in nature. That is, it varies in space. This turbulent viscosity term, however, appears within the derivation of the

Reynolds Stress Tensor as:

$$\tau_{ij} = -\overline{\rho u_i' u_j'} = \mu_t \left(\frac{\partial U_i}{\partial x_j} + \frac{\partial U_j}{\partial x_i} \right) \tag{1.9}$$

The assumption that the eddy viscosity is isotropic is suitable for a range of flows, but not those where separation is strong, or where a swirl in the flow is present. Furthermore, each model has coefficients, the values for each of which have to be determined from results from experimental and DNS data.

With these weaknesses of some of the models, the inherent problems with RANS become evident. The models do not fully or accurately represent the complex physical structures of turbulent flows at different scales. Small scale turbulence generally is influenced greatly by viscosity and exists in many regions within the flow, while larger scale turbulence has its greatest influence from inertia and the boundary conditions used. No one model is useable for all these scales and kinds of turbulent flows. There are a number of different reviews regarding the performance of different turbulence models for RANS, with appropriate models required for specific cases. However, in spite of a great deal of ongoing research in the area of turbulence, current models available still require careful problem-specific calibration and specification prior to use in a simulation.

Yet RANS has become one of the most commonly used methods of CFD [19]. This is in part due to the characteristic of RANS to provide a time-averaged solution; a solution that is often sufficient for use in engineering applications. Additionally, it is a numerically simple technique that is capable of reaching convergence more rapidly than the competing techniques. However, the inability of RANS to produce consistent, reliable results for turbulent flows led to exploration of other methods. An approach that has become more feasible for study as computational power has increase is the Large Eddy Simulation technique, a technique that is generally considered as a half-way house between DNS and RANS.

1.2.3 Large Eddy Simulation

As mentioned at the end of the last section, the Large Eddy Simulation (LES) technique is often considered as a method that is between DNS and RANS, particularly with regards to computational cost and accuracy of the results. LES does not require as much computational effort as DNS (which is computationally very expensive, as discussed in section 1.2.1) but equally, more resources are required than the RANS technique that solves the Reynolds-Averaged Navier-Stokes equations. However, LES provides a greater amount of detail in solution than RANS; RANS is capable of providing only an averaged set of results (as implied by the name), while LES is capable of predicting instantaneous flow characteristics and resolving turbulent flow structures. This infers that LES can provide significantly better results than RANS for such flows that involve flow separation. However, LES becomes computationally significantly expensive when complex scenarios such as presence of walls in flow are simulated. When encountering such solid boundaries, errors are introduced in the spatial derivatives [20]. Although methods have been devised to resolve the small scale turbulence present, these methods themselves introduce new errors

which are then removed by correction terms [21]. Accurately simulating such flows using only LES could potentially be so demanding computationally that to do so would stretch even todays supercomputers. Thus, a zonal approach to simulations is often adopted, with the simpler RANS method (or other simplifying models) being applied in the regions near to the wall.

LES solves the partial differential equations governing turbulent fluid flow in a three-dimensional, time-dependent form. Whilst DNS requires a grid that can account for the smallest scales in the flow, (even though much of the turbulent kinetic energy that is present is contained in the larger eddies present in the flow) LES computes the larger scale eddies and models the less energetic (but still computationally demanding) smaller eddies. In 1941, A. N. Kolmogorov theorised on the characteristics of turbulence. One of the theories defining turbulence was the theory of self similarity, [12] essentially stating that while smaller eddies are self similar and have universal characteristics, larger eddies are much more dependent on the flow geometry and set up. Thus a solution is obtained explicitly for the larger eddies, while the effects the smaller eddies have on the large ones are modelled appropriately. The smaller scale eddies are modelled using a sub-grid scale model (SGS) technique.

In order to produce a solution for the Navier-Stokes equations, an additional sub-grid scale stress term is added to the equations. The sub-grid scale models primarily aim to reflect the dissipation of energy that cascades from the larger scales of turbulence. This is done in such a way that an eddy viscosity term is added to the governing equations, thus resolving the presence of the turbulence. As an initial step, filtering takes place such that the flow scales from the domain size, L, to a filter size, Δ, are explicitly resolved (details on suitable grid resolution and filter size are given in [10]). The filtered variables are used within the continuity and momentum equations:

$$\frac{\partial \rho}{\partial t} + \frac{\partial \rho \tilde{u}_j}{\partial x_j} = 0 \tag{1.10}$$

$$\frac{\partial \rho \tilde{u}_i}{\partial t} + \frac{\partial \rho \tilde{u}_i \tilde{u}_j}{\partial x_j} = -\frac{\partial \tilde{p}}{\partial x_i} + \frac{\partial \tau_{ij}}{\partial x_j} + \frac{\partial \sigma_{ij}}{\partial x_j} \tag{1.11}$$

where τ_{ij} is the filtered Reynolds stress tensor, while σ_{ij} represents the subgrid-scale Reynolds stresses. The higher the width of the variable filter, the more scales there are removed from the velocity field and modelled. Thus we can see the addition of the term that - as with the RANS formulation - needs to be estimated to close the system, the subgrid-scale stress term. These are generally modelled as:

$$\sigma_{ij}^s - \frac{1}{3}\partial_{ij}\sigma_{kk}^s = -2\mu_t S_{ij} \tag{1.12}$$

Again, as was the case with RANS, the eddy viscosity term is represented by μ_t while S_{ij} represents the rate of the strain tensor.

LES was initially postulated in the 1960s, increasing in popularity as the models used have matured. The earliest models were developed by Joseph Smagorinsky for Numerical Weather Prediction in simulating atmospheric air currents. In the decades since then, the use of LES has been extended to many more engineering applications. However, it was the pioneering work of

Smagorinsky [22] that made the Large Eddy Simulation technique so applicable for computing flows; a consequence of this work is that the most commonly used SGS models are the Smagorinsky model (that would model μ_t above) and variants of this model. The modelling of eddy viscosity within the Smagorinsky model is:

$$\mu_t = (C_s\Delta)^2 \sqrt{2\overline{S}_{ij}\overline{S}_{ij}} = (C_s\Delta)^2 |S| \tag{1.13}$$

where C_s is the Smagorinsky constant, usually having a value between 0.1 and 0.2.

It is immediately clear from the potential values of the Smagorinsky constant alone that – as with all numerical approaches – there are inherent errors in using classical LES for simulations. This is also due, in large part, to the approximation of the variables and the numerical discretisation. Furthermore, the use of the sub-grid scale modelling can also lead to truncation errors, while sub-grid scale models are proving difficult to determine for complex high Reynolds number flows.

1.2.4 Implicit Large Eddy Simulation

As described in the previous section, LES solves the fluid governing equations for turbulent flow through the use of direct calculations on the larger scales of motion, and models for the effects of the smaller, unresolved, scaled turbulent motions of flow. This allows for good representation of the entire range of scales of turbulent flow – a range that is very large. The models used for the smaller turbulent eddies are called sub-grid scale (SGS) models. The implicit large eddy simulation does away with these sub-grid models, instead resolving the smallest scale eddies implicitly using a class of non-oscillatory finite-volume numerical solvers. These non-oscillatory schemes have been used in CFD for decades, though implicit large eddy simulation as a technique is much younger, with much development in recent years. Although more detail on the ILES technique is given in chapter 3, a brief overview of the method is introduced here.

ILES has been shown to be comparable to LES, particularly in the case of three-dimensional flow where the larger turbulent effects that are directly modelled are the dominant force with SGS models appropriately applied to the case [20, 23, 24]. In particular, the flows where the best relationships exist between LES and ILES are when the flows are far from boundaries.

The implicit part of ILES ensures that the dissipation that is necessary in order to maintain a stable solution is produced by the numerical schemes. In order to do this, Riemann-solvers are used [25] as well as high-resolution methods [20, 26]. The equations solved in ILES do not require the filtering that the equations in LES are exposed to, and so it is the original Euler equations that are solved. The numerical schemes used are then designed such that physical aspects of the flow are accounted for. Furthermore, the high-resolution methods that are used are intrinsically non-linear and thus not strictly dissipative. Therefore, any energy backscatter (where smaller scale structures feed energy into larger scale structures) is taken into account during the computation of the solution. This provides results that – unlike LES where the solution is driven to be consistent with Kolmogorov's spectrum – are in line with Kolmogorov's turbulence spectrum due to the design of the numerics.

Designing the physics of the flow into the numerics again provides both strengths and weaknesses. Filters are not required and so it is possible to obtain good solutions even on coarse grids. However, it is not possible to know exactly how the numerics will behave in terms of turbulence computation and so the user has little direct control on the solution. In spite of this, the implicit modelling of turbulence has been widely proven in a range of applications (as shown in [27–30].

One of the earlier forms of ILES that has been proven to be usable for CFD was the Monotonically Integrated Large Eddy Simulation (MILES) technique. This is an ILES method that makes use of high-resolution monotone algorithms that are non-linear (due to the use of the higher-resolution schemes). A developed version of this technique has been used for the CFD code used in this thesis. As the numerical dissipation on the grid is assumed to separate large scale eddies from the smaller scale eddies, no subgrid scale stress tensor is needed for ILES (as is needed in the case of LES). Thus, adaptive non-linear methods are used to aid in solving the governing laws. Attention in this thesis will be chiefly aimed at the ILES properties of MUSCL and WENO family of numerical schemes.

1.3 Cylinder Flow

Flow around a circular cylinder, which is the focus of the present work is a fascinating problem, combining extreme geometric simplicity with substantial complexity of the flow phenomena observed. As such, it provides an ideal benchmark for the investigation of turbulence modelling approaches. In this section, the key properties of this flow will be discussed.

Vortical instabilities in wakes have been a key investigative subject for engineers and scientists for many years providing many challenges in understanding the flow characteristics behind a bluff body. Advancements in the understanding of this vortical flow has allowed significant engineering advancements such as reduction of drag on wing tips due to changes to the vortical flow from alterations in component design. Further understanding of the flow in the near wake has allowed insight into why the shedding of these vortices in the near wake cause a variety of fluctuating pressure forces that can be inflicted on a body causing structural vibrations or resonance, which could lead to early structural failure. The engineering implications of being able to accurately simulate this flow are significant. However, complexities arise due to the interactions of several shear layers within a small area around the body; namely the boundary layer, a separating free shear layer and the wake. The boundary layer (a thin viscous layer on the surface of the body) can now be appropriately modelled with the use of equations that allow an estimation of its growth.

The flow around a bluff body results in a separated region; this is a region where the flow separates from the body resulting in a recirculating region immediately downstream of the body. This is illustrated in figure 1.10. A wake is also formed downstream of the body. This is a consequence of fluid viscosity and is a diffusive region that grows such that further downstream the fluid velocity is lower than the free-stream velocity. The free-stream velocity is exhibited forward of the body, with the inviscid flow being free stream flow. This flow is also present outside the regions effected by the boundary layer, the separated region and the wake. The boundary layer

is laminar near the front of the body, becoming turbulent further around the body. The point along the surface of the body at which the boundary layer becomes turbulent, and at which the separated region begins, is highly unsteady and changes according to flow characteristics (such as Reynolds number).

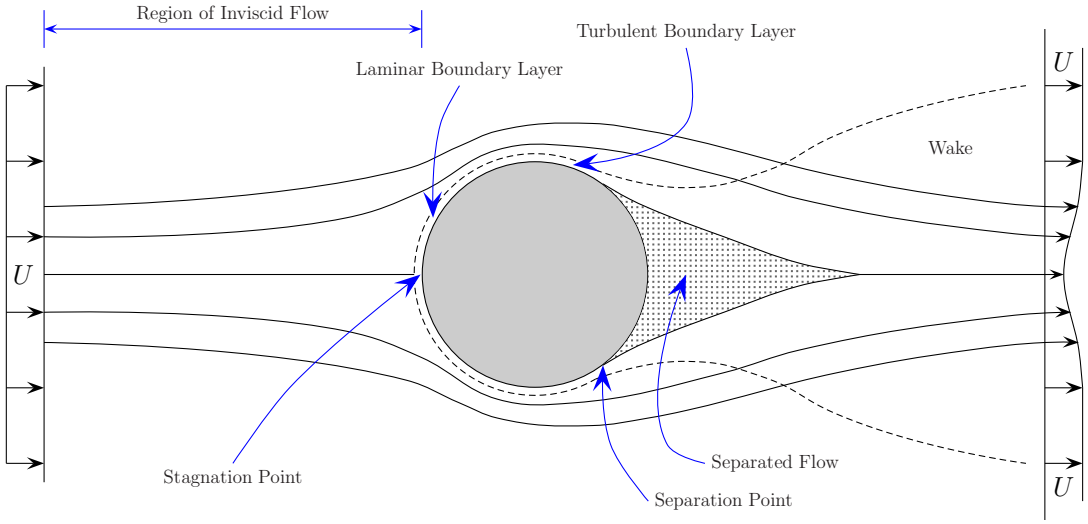

FIGURE 1.10: An illustration of flow around a blunt body

Interest in the flow often centres on the drag; the force the body exerts on the flow around it. This is of interest in engineering terms as an understanding of drag factors has allowed for design improvements in many areas. In order to help understand drag and correctly model it, many experiments and computational analyses have been carried out on the flow around a cylinder, each focusing on their own aspect of the flow (some reviews on the different flow aspects are given in [31–36] and references therein). However, many of the analyses historically performed with bluff body flows - including flows around a cylinder - give results in emperical, descriptive terms [33]. Flow around a cylinder is generally seen as being a very good (and geometrically simple to describe) representation of the bluff body problem. A simulation of flow around a cylinder is well suited for validation purposes as there exists a great deal of quantitative data from both experimentation as well as a wide range of numerical simulations.

The position of separation of the flow changes for different reasons; be it the cylinder parameters such as length and cross-sectional profile, the roughness of the cylinder surface, or the flow speed. However, assuming identical cylinders, a review of the different drag coefficients can be determined, allowing one to understand the significance of the separation region. The primary flow parameter influencing the drag around a blunt body is the Reynolds number [37]. Separation occurs at a sufficiently high Reynolds number in the flow around a blunt body. At low Reynolds numbers, there is no separation (and in these cases, the drag coefficient is simple to determine and is solely based on the Reynolds number). At Reynolds numbers where $Re \geqslant 10$ separation begins at a small area to the rear of the sphere, reaching a maximum region size at $Re \cong 1000$. The

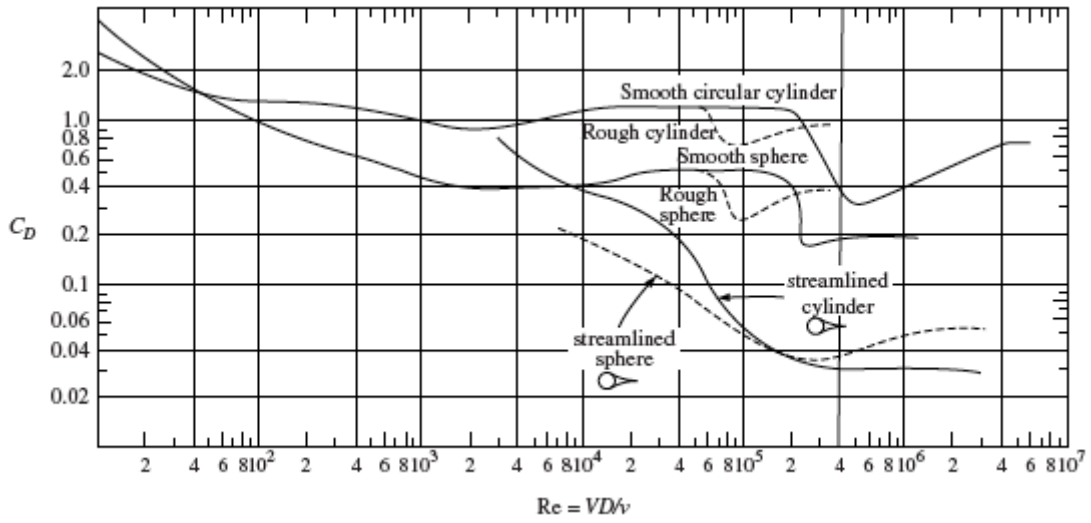

FIGURE 1.11: Drag coefficients for flow around spheres and long cylinders [37]

drag coefficient then remains relatively constant until around $Re = 2 \times 10^5$ where a sudden drop occurs. After this drop, the drag coefficient once again rises as Reynolds number increases. This is shown in figure 1.11.

The sudden drop in drag coefficient occurs due to a change in the boundary layer; the boundary layer transitions at this point from being a laminar flow to a turbulent flow. A turbulent boundary layer has an advantage in carrying more momentum and thus being able to move the separation region further backwards. This is a significant difference, allowing a decrease in drag by as much as 80 percent. In order to exploit this, the body's surface could be roughened causing the boundary layer to transition to turbulent flow earlier. This is achieved on golf balls through the use of the dimples on the golf ball; an identical ball that is smooth only manages half the flight time.

1.3.1 Vortex Shedding

Long cylindrical bodies in a flow exhibit vortex shedding. This is emission of small vortices that are initiated on the surface of the body and, once a certain size is reached, are shed from the surface of the body and become part of the wake.

Some of the earliest, most important, work in vortical shedding within cylinder flow was carried out by Theodore von Kármán who determined - amongst his many other significant aerodynamic contributions - theories of the unsteady wakes in cylinder flow. From this work we gain the term "Kármán Vortex Street". This is a repeating pattern of vortices that is formed by the separation of flow around a bluff body. Examples of this occurring at differing flow velocities are shown in figure 1.12. Von Kármán's work inspired many further analyses of vortex arrays, the many results of which fill books and are beyond the scope of this work. For a more detailed review of vortical dynamics in the wake of a cylinder, the reader is referred to the review paper

by Williamson [35]. However, some discussion of the vortical dynamics that take place in the flow at different Reynolds numbers is necessary, in order to correctly predict the flow that will be observed in simulations.

Vortex shedding from a circular cylinder is most frequently characterised by the Strouhal number representing dimensionless frequency of the process.

$$St = \frac{fD}{V} \tag{1.14}$$

Strouhal number can only be determined from simulations or experiments; no definite method exists to determine numerical data for different cases through equations, though models and approximations have been derived from previous works. This is, however, an important figure to determine for real-world designs. Vortices such as those illustrated are shed from many things exposed to fluid flow: electrical wires, tall towers and bridges being just a few examples. If the shedding frequency matches (or is approximate to) a structure's harmonic frequency (or if it is a multiple of the structure's harmonic frequency), then there is a high chance that damage would occur to the structure due to resonance.

Differing Reynolds numbers for the flow result in differing flow behaviour downstream of the cylinder in the flow. Generally, higher Reynolds numbers will result in significantly more turbulence directly downstream of the cylinder, as well as larger vortices in the wake of the cylinder. Initial experimental observations of cylinder flow indicate that that $St = 0.185$ for cases where $400 < Re < 1k$ and $St = 0.195$ for $1.8k < Re < 5.4k$. These observations have been repeated and refined over the intervening years, such that more detailed values have been determined for a wide range of Reynolds numbers, and relationships between Strouhal number and Reynolds numbers established. The range of Reynolds number encompassing different flows can be split into different groups as follows.

Laminar shedding, $Re \leqslant 190$

At low Reynolds numbers, above $Re \approx 5$, a pair of symmetric counter-rotating vortices form behind the cylinder, remaining fully laminar up to approximately $Re \approx 40$ and not shedding. The process of vortex shedding (also known as the Karman vortex street) is reported to begin at $Re_o = 47$ [34, 38]; an onset characterised as a supercritical Hopf bifurcation. This is joined, at this Reynolds number, by the onset of fluctuating lift. Flow at the Reynolds numbers close to onset, Re_o, has been found to be truly two-dimensional, regardless of the cylinder end conditions used [34, 39, 40]. As Reynolds number increases, the parallel shedding conditions lose their two-dimensionality, and if standard fixed cylinder end plates are used, the shedding forms a slanted shape at $Re \approx 70$ [34]. Williamson discovered that with some end plate manipulation, the flow could be modified to maintain the two-dimensional form of shedding to higher Reynolds numbers until $Re \approx 190$ [35]. This was further evidenced in numerical simulations [41], where it was also shown that the lift fluctuations at these Reynolds numbers have an almost perfectly sinusoidal form.

Based on published numerical data available at the time, Norberg [38] formed an approximate

relationship for the lift coefficients against the Reynolds number, for flows that have modified cylinder end plates up to Reynolds number 200; that is, for flows that are two-dimensional in form of shedding. This relationship first has a supercritical parameter defined, based on the Reynolds number for onset of vortex shedding, $Re_o = 47$. This supercritical parameter is given as:

$$\epsilon = \frac{Re - Re_o}{Re_o} \tag{1.15}$$

Without the end manipulation, slanted shedding begins to occur at $Re \approx 70$, as mentioned. This gives $\epsilon \approx 0.5$. With the end manipulation forcing longer two-dimensional shedding, the r.m.s. lift coefficient can be approximated by the following relationship:

$$C_{L'} = \sqrt{\epsilon/30 + \epsilon^2/90} \tag{1.16}$$

This relationship was shown to give a mean standard deviation with tested data of only 0.004, or around 1.7%, for data of $47.5 \leqslant Re \leqslant 200$. At this Reynolds number range, we are now starting to see the beginnings of the slanted (and oscillating in direction) shedding to the rear of the cylinder. Although this will not produce any overall lift, we can determine the r.m.s values of the lift produced at each extreme of oscillation direction. For the list of two-dimensional, low Reynolds number, numerical simulations used to help determine this relationship, the reader is referred to the paper by Norberg [38]. Equally, a representation of the Strouhal to Reynolds number relationship using only two constants was given as:

$$St = A + B/\sqrt{Re} \tag{1.17}$$

Using a least-square fit method to the available data gave $A = 0.2663$ and $B = 1.019$ with a mean absolute relative error of only 0.3% for the resulting calculated Strouhal number [38]. Both Strouhal number and the r.m.s. lift coefficient were thus determined to rapidly increase within the laminar shedding regime. The Strouhal number is found to increase from $St = 0.12$ at shedding onset ($Re \approx 47$) to $St = 0.19$ at $Re \approx 190$. Equally, the r.m.s. lift coefficient raises from zero, at shedding onset, to $C_{L'} = 0.45$ at $Re \approx 190$.

Mode A Instability, $190 \leqslant Re \leqslant 260$

The next differentiated regime of vortex shedding in the cylinder wake occurs at Reynolds numbers greater than approximately 190, up to 260. This regime has been termed the *Mode A Instability* by Williamson [35]. Using a three-dimensional Floquet stability analysis of the cylinder wake, it has subsequently been suggested that the critical value of Reynolds number for onset of this regime is $Re = 188.5 \pm 1.0$ [42], however this value is dependent on the cylinder end conditions, and has been found to range from $Re = 160$ to $Re = 190$ [38]. This regime is characterised by a critical spanwise wavelength of instability of around four cylinder diameters at its onset, and is the first regime to display this intrinsic three-dimensional instability. The three-dimensional instabilities induce a highly disturbed shedding flow with higher Reynolds numbers producing

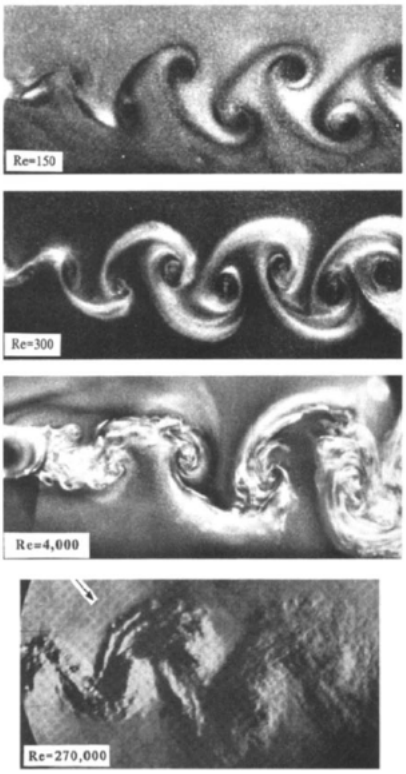

FIGURE 1.12: An illustration of laminar and turbulent vortex streets. The formation of Karman Vortex Streets over a wide range of *Re* is shown. [35]

a mix between mode A instability structures and large-scale, spot-like "vortex dislocations", now commonly referred to as mode $A^{\bullet}$ [38, 43].

The change from two-dimensional vortex dynamics to the three-dimensional dynamics produced in the $A^{\bullet}$ mode involve a dramatic drop in the spanwise correlation of velocity fluctuations in the wake, as well as a significant drop in shedding frequency [35] (determined experimentally with an observation of fluctuation frequencies using PIV). Equally, the r.m.s. lift coefficient drops in this process. Thus two-dimensional simulations of this flow regime will result in large discrepancies in results with real-life experiments, and it is now recognised that for Reynolds numbers higher than 250, two-dimensional calculations will yield incorrect values for flow parameters such as Strouhal number, drag and lift coefficients [44, 45]. When in mode $A^{\bullet}$, the spanwise correlation length associated with the near-wake velocity fluctuations is of the same order of the wavelength of the most unstable mode A instability. It has been found that a spanwise correlation length of around 7 diameters is present at $Re = 230$. Within flow mode $A^{\bullet}$ both Strouhal number and r.m.s. lift coefficient increase as *Re* is increased [35, 46].

At the higher end of the Reynolds numbers of Mode A and $A^{\bullet}$ instability, the characteristics of the mode A flow fade with the near-wake vortex shedding stabilising. The following mode of instability, *Mode B Instability*, gradually becomes the more dominant form of wake feature. Flow

begins to transition to Mode B at $Re \approx 230$, eventually showing fully the characteristics of Mode B instability at $Re \approx 260$. Thus, for the Mode A and $A^{\bullet}$ flow, Norberg [38] determined an approximate linear relationship to estimate the r.m.s. lift coefficient, based upon three-dimensional simulations available at the time:

$$C_{L'} = \begin{cases} 0.43 \times (Re/230) & (165 < Re \leqslant 230) \\ 0.78 \times (Re/260) - 0.26 & (230 < Re \leqslant 260) \end{cases} \tag{1.18}$$

However, this relationship has some ambiguity when $165 \leqslant Re \leqslant 190$, due to the effects of the cylinder end conditions as referenced in the laminar shedding section. It is also worth noting that there appears to be little, or no, mention regarding the presence of lift and drag pulsations in the transitions between different wake regimes for circular cylinders. Such effects have been observed in simulations of transitional flows around sharp-edged (e.g. square) cylinder. One explanation given is that the lift pulsations observed are due to a mismatch in phase between the lift and the shedding frequency variations; this is a mismatch that is not seen in the case of the circular cylinder [38].

Mode B Instability, $Re > 260$

As the Reynolds number increases above approximately 260, the flow exhibits a transition to a finer scale of three-dimensionality. The initial development takes place up to Reynolds number of approximately 300, during which phase the wake has turbulence forming within it. Above Reynolds number 300, it is assumed that turbulent shedding conditions will be a prevalent characteristic [38].

In this regime, the spanwise characteristic length is around one cylinder diameter, with the three-dimensional cylinder wake becoming more chaotic as Reynolds number increases. This leads to a reduction in base pressure coefficient (the negative of the base suction coefficient). Shear layers separate from the cylinder and become unstable at a Reynolds number between 300 and 3000. The value of this critical Reynolds number varies widely due to the separating shear layers being very sensitive to the various experimental factors such as free-stream turbulence level, acoustic noise, cylinder vibrations, end boundary conditions and aspect ratio [34, 45, 47].

In this regime, Zdravkovich [48] stated that the Strouhal number could be estimated through the empirical relation given by:

$$St = 0.212(1 - 12.7/Re) \quad Re > 300 \tag{1.19}$$

1.3.2 Wall Effects and Blockage

As the Reynolds number increases, the flow characteristics change accordingly. However, the presence of a wall can also affect the overall flow characteristics, changing the dynamics of the vortex shedding. Due to the influence of the flow over a rigid wall, the flow over the body is subject to a non-symmetric influence. There are, additionally, influences from vorticity of the

wake-induced boundary layer from the wall upon the vortices shed from the cylinder. With a small gap between wall and cylinder, the interaction between boundary layers and vortices is large, such that the entire wake is drastically changed to the rear of the cylinder. Due in part to the engineering implications of these changes to flow (for example, in marine engineering, where structures such as oil rigs have large cylinders inserted into the seabed), a variety of investigations into these effects have been demonstrated in a number of experiments and simulations [49–55] with Reynolds numbers ranging from $Re = 2 \times 10^4$ to 10^5. These experiments showed that as the distance between wall and cylinder changed, the flow exhibited a variation of aerodynamic forces on the cylinder as well as a change in vortex shedding frequency downstream of the cylinder. The presence of a wall results in movement of the frontal stagnation point towards the wall resulting in upward lift of the cylinder and change of wake direction away from the wall (as illustrated in figure 1.13).

Furthermore, blockage effects can be evident in experimental work. The blockage is influenced in wind tunnel experiments by the distance of the tunnel walls from the cylinder in the flow. This is generally given as a ratio of blockage, D/B, where the breadth of the tunnel, B, is varied in relation to the cylinder diameter, D. It has been shown that, even at low Reynolds numbers [56] (as low as $Re = 20$), as the ratio D/B is increased (that is, as the walls are brought closer to the cylinder), the vortices shed behind the cylinder reduce in length, effecting the overall wake structure downstream of the cylinder. Furthermore, instabilities within the near-wake are introduced, forming spikes along the free shear layers, resulting in a wavy trail downstream.

Due to the effects that blockages and walls in flow can produce, the intention of this numerical experiment was to avoid such features, thus setting reasonably far-field boundaries for the domain.

1.3.3 The Three-Dimensionality of flow

A significant proportion of computational investigations into flow around a cylinder have been carried out in 2D, particularly at higher Reynolds numbers. This was in part due to the belief that flow around a long and nominally two-dimensional cylinder submerged in a uniform free-stream had to be two dimensional [57]. It was also assumed that cylinder ends were the root cause of three-dimensional flow. As a result of these beliefs and assumptions, research into aspect ratio effects was considerably delayed. Furthermore, these led to assumptions that different real-life cylinder-in-flow situations could be assumed to have two-dimensional effects.

Most wind tunnels have a closed test area, with the cylinder fixed such that it stretches from one wall to the opposing wall. The wall boundary layers separate from the wall, rolling depthwise between the cylinder ends. These in turn form horseshoe-shaped swirl systems. Already, we see the three-dimensional effects of having a cylinder within a walled test section in a wind tunnel. An alternative method of experimental test involves the use of a wind tunnel with an open test section and the cylinder protruding into the free jet. However, this results in end effects due to the jet shear layers. A method devised to minimise these end effects is to use end plates (similar in use to winglets on the tips of aircraft wings). These are designed such that they prevent

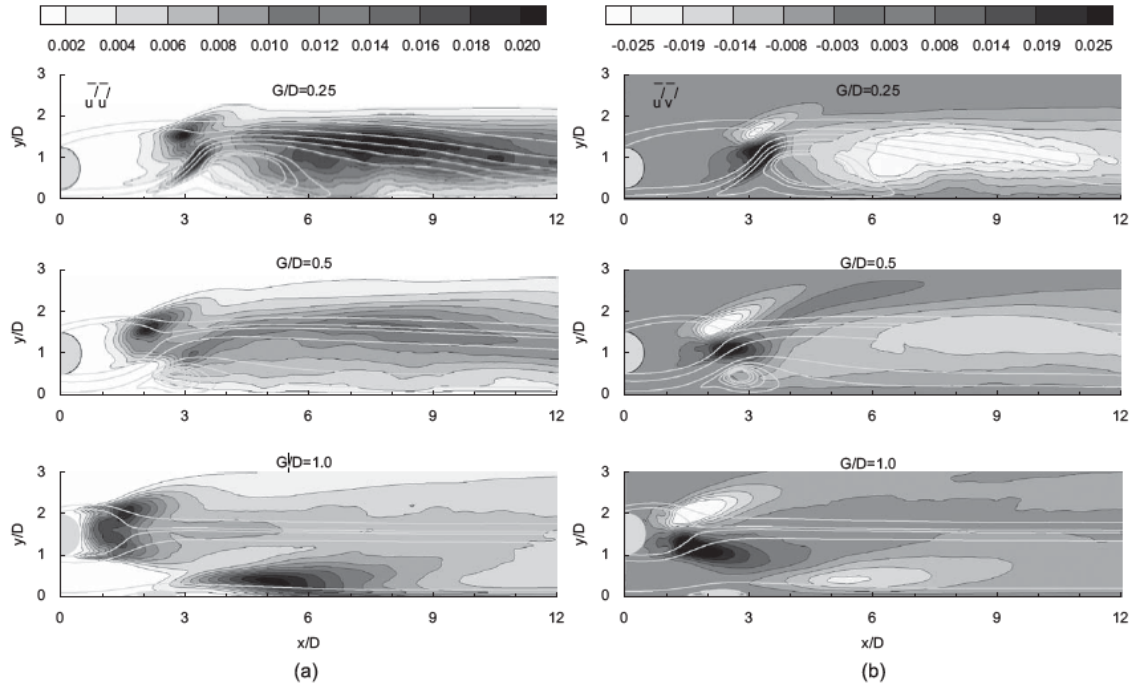

FIGURE 1.13: Iso-contours of(a)Reynolds normal stress and (b) Reynolds shear stress for Ground to Diameter ratios of 0.25, 0.5 and1.0 [54]

transverse flow along the span of the cylinder. However, these end plates can affect the flow such that an entirely different near-wake in size and shape is formed.

Thus it can be seen that obtaining a fair experimental representation of cylinders in flow in engineering applications such as tall chimney stacks, TV Towers, wheels and frisbees is difficult without influencing the flow from such wind tunnel features as end plates. However, techniques in wind tunnel experimentation have been evolved greatly (see [34]) - particularly since the realisation of the effects of differing aspect ratio - such that in recent decades, results can be taken to be more reliable.

There is a fairly similar story with regards to computational simulation. Due to the beliefs that the cylinder in flow was essentially a two-dimensional flow without any three-dimensional effects, simulations have traditionally been run solely in two-dimensions. This was compounded with limited computing power restricting the size of computational simulations. However, improvement in computational power has led to more investigations of 3D flows; particularly with the use of Large Eddy Simulation (LES) techniques. Further questions have been raised regarding the effect of three-dimensionality on the resulting flow within computational simulations (see [58] and [44]) with Mittal and Balachandar concluding that even at low Reynolds numbers, the lift and drag forces on cylinders computed from 2D simulations differ from those computed with 3D simulations, with the 3D simulations providing results better matched to experimental results. It was inferred that this showed that it is three-dimensional effects that lead to the discrepancy

between experimentally measured values and those computed (and recorded) in 2D simulations. Furthermore, the differences between the 2D and 3D simulation results are themselves dependent on the cylinder geometry (with differences more significant for bluffer bodies when elliptical cylinders are used). It was found that higher in-plane Reynolds stresses were the main root of over-prediction of drag in the 2D simulations.

This was further demonstrated in a paper by Labbé [59], where it was concluded that a finite spanwise cylinder depth is sufficient to predict the flows past an infinitely long circular cylinder within low Reynolds numbers (demonstrated up to $Re = 1000$). However, in the region of flows below $Re = 300$, a spanwise depth of up to 4 cylinder diameters is required. As Reynolds number increases, a shorter spanwise depth can be used, ranging between $\pi D/2$ and πD to sufficiently predict force components, Strouhal number and also the $3D$ instabilities.

In a very recent paper by Cao et al [60], an investigation was carried out into the effect on shear flow around a circular cylinder at different Reynolds numbers. They discovered that for their simulations of Reynolds numbers of $Re = 200$ and $Re = 220$, the spanwise depth had to be set at $8D$ (as opposed to their choice of $4D$ for other Reynolds number simulations) due to a transient phase at this Reynolds number resulting in an instability with wavelength approximately $4D$ in the spanwise direction. Increasing the simulated model depth allowed better illustration of this unstable wake dynamic. Without examining shear flow effects, the same depth in the spanwise direction may not be required, however it is worth noting that transitional flow features at these Reynolds numbers may affect the resulting flow.

Investigations were carried out by Prasad [47] to determine the effect of spanwise end conditions on the cylinder wake at a range of Reynolds numbers (from $Re = 200$ to $Re = 10,000$). They found that through manipulation of the end conditions, oblique and parallel vortex shedding patterns could be induced such that the total spanwise-integrated unsteady fluid forces on the body are dramatically reduced to a value almost of zero.

1.3.4 Surface Roughness

The roughness of the surface of the cylinder has an effect on the overall flow. According to Prandtl (translated and requoted in [48]):

> Slightly rough surfaces may be regarded as effectively smooth when the irregularities are completely embedded in the laminar boundary layer. At high Re, when the laminar boundary layer becomes thinner, such roughness may become effective causing an increase in drag.

Zdravkovich [48, 57] describes the chief effect as being upon the boundary layer. In particular, when the flow is transitioning between different flow regimes, the influence on the boundary layer can be fairly significant. These then go on to effect such parameters as the drag coefficient, separation angle and Strouhal number. This was shown experimentally by Ribeiro [61] for a two-dimensional case (although these were at higher Reynolds numbers, being in the range $50,000 \leqslant Re \leqslant 400,000$), where changing the roughness of the experimental cylinder (by sanding it down) resulted in greater differences between the parameters as the relative roughness

increased. Furthermore, the increase in roughness showed an earlier transition to a higher flow regime, resulting in different flow characteristics - particularly downstream of the cylinder where such factors as the presence of vortices could be affected solely through differing roughness.

In experimental work, some accounting should usually be made of the surface roughness of the cylinder in the flow. An example of this is in the work by Cantwell and Coles [62] where experimental data was collected for a cylinder within a flow with Reynolds numbers varying from $70,000$ to $340,000$. In this paper an aim was laid out to avoid, as much as possible, detrimental effects from such factors as aspect ratio, blockage, and surface roughness. As such, a brief overview of the surface roughness of the cylinder, and how this was achieved, is given in the paper. Achenbach [63, 64] also investigated the influences of surface roughness on the cylinders he tested (albeit at high Reynolds numbers, intially up to $Re = 5 \times 10^6$ [63] and then $40k < Re < 3M$ [64]). Through his work, Achenbach was able to measure skin friction and static pressure distributions around the cylinders, and define an equivalent sand roughness for the emery paper used to wrap the cylinder. Achenbach showed that at these high Reynolds numbers, the variation of surface roughness had a significant affect on the flow around the cylinder (i.e. direct effects on the boundary layer) such that the separation point would be initially pushed backwards around the cylinder before then moving forwards again as the roughness increased.

Due to the resulting effects on flow due to surface disturbances, any experimental results may differ from the numerical results of the same flow if surface roughness is not considered within the numerical simulation. This is worth noting, and where possible a paper with negligible surface effects should be sought. However, from the results given by Achenbach and Heinecke [65], it would seem that for Reynolds numbers below 10^4, Drag differences due to surface roughness are negligible (and differences remain small for low surface roughness up to $Re = 10^5$) while Strouhal number is relatively unaffected up to Reynolds numbers just above $Re = 10^5$.

1.4 Aims and Objectives

This work aims to evaluate the application of the Implicit Large Eddy Simulation technique in CFD for predicting low-speed flows - at laminar, transitional and turbulent regimes. This is carried out by examining different test cases of a circular cylinder in fluid flow flow, using a broad range of numerical methods within the Implicit Large Eddy Simulation approach. The results of the simulations are compared between Reynolds numbers and numerical schemes for a range of statistical outputs. Further, the effects of three-dimensionality is shown for the higher Reynolds number flows. The cylinder in flow is chosen as it is a classic validation case, being geometrically simple, but computationally challenging.

The objectives of this PhD work can be summarised as:

- Simulation of two-dimensional cylinder flow from steady state laminar regime to fully turbulent regime and comparative analysis of the accuracy of various reconstruction methods for the convective flux.

- Simulation of three-dimensional cylinder flow at Reynolds numbers corresponding to three-dimensional transitional and turbulent regimes and comparative analysis of the accuracy of various reconstruction methods for the convective flux.
- Evaluation of spectral properties of the cylinder wake from steady flow to turbulence.

1.5 Thesis Structure

1. Chapter 2: The initial theory is introduced, with an overview of the Governing equations.
2. Chapter 3: The numerical approach and implementation of the schemes is introduced and described, with further Numerical Methods relevant to the CFD procedures carried out discussed, including the concept of the higher order methods. Computational methods are also reviewed, with such areas as boundary conditions and multi-block processing also discussed.
3. Chapter 4: In this chapter, the simulation methodology and processes used are discussed, as well as a discussion of the cases to be run.
4. Chapters 5 and 6: The results from cylinder in Flow in two-dimensional and three-dimensional simulations respectively are presented and discussed.
5. Chapter 7: In this chapter, a final summary of the results obtained during the course of work are reviewed, with conclusions drawn up on the work as appropriate.
6. Appendix A: In this appendix chapter, the non-dimensionalisation of the Navier-Stokes equations is discussed, as well as the implementation of these within the CFD code.
7. Appendix B: Due to the large number of two-dimensional simulations carried out, a number of the plots were moved to the appendix, and are contained in this chapter.
8. Appendix C: As a part of the work carried out for this thesis, some work was done on a frigate ship geometry, leading to a contribution to a published paper. A brief overview of the work is presented in this chapter.

1.6 Paper Published

As a supplementary piece of work to this thesis, a contribution was made to a published paper. Details of the work are given in Appendix C. The paper published was: B. Thornber, M. Starr and D. Drikakis, “Implicit Large Eddy Simulation of Ship Airwakes”, The Aeronautical Journal, December 2010, Volume 114, No 1162, pp715-736. [30]

2

The Governing Equations

Science is facts; just as houses are made of stones, so is science made of facts; but a pile of stones is not a house and a collection of facts is not necessarily science. ***Henri Poincare (1854 - 1912)***

* * * * *

In this chapter, the basic philosophy and governing equations are discussed - and where appropriate, derived - as these equations are the initial building blocks from which all of Computational Fluid Dynamics is based. The Navier-Stokes equations, which describe the fundamental fluid flow, can be derived by examining a controlled volume of fluid in a fluid flow, and separating that from the fluid. By examining this flow, we can derive the governing equations of fluid dynamics: the Continuity, the Momentum and the Energy equations. These governing equations apply three fundamental physical principles upon which fluid dynamics - and in fact most dynamic systems - is built upon:

1. Mass is conserved.
2. Momentum is conserved.
3. Energy is conserved.

The governing equations can be obtained in different forms, and appear in these different forms in different texts. These different forms of equations are relevant and of great interest in CFD (moreso than in aerodynamic theory) as different governing equations can result in different numerical results, incorrect results, or instability of the model. However, deriving all the different forms of the governing equations is beyond the scope of this thesis. In this chapter, the governing equations will be derived in integral form rather than differential. This integral form is of most interest for use in the Finite Volume Method that is applied to this groups code. There is a subtle (yet important) difference between the integral and the differential forms of the governing equations. The integral form allows for discontinuities within the fixed volume being examined (i.e. each cell). The differential form of the governing equations, however, assumes that the flow properties across the cell are differentiable and thus continuous with mathematical continuity. Thus the integral form of the equations is often considered to be of more applicability for calculating a flow with real discontinuities.

For a more detailed account of the derivation of these equations in any of their forms, other texts can be sought out such as [66], [67], [25] and [26]. In studying the fundamentals of CFD, it was these texts that were studied by this student, and so all information gleaned for this chapter can be said to be from these sources.

2.1 The integral form of the governing equations

The governing equations can potentially be solved by different numerical means. The method chosen by many for CFD, and indeed chosen by the FMCS group at Cranfield, is the Finite Volume Method (FVM). This is a very flexible method for discretisation of the equations for CFD.

In this method, the geometry we wish to simulate is placed into a domain. The domain represents the entire simulated area where fluid flow is to exist. The domain is then split into a number of different elements - referred to as cells or control volumes (CVs). Each cell has at its centre a nodal point - an infinitesimally small point at the centre. The Finite Volume in "Finite Volume Method" is a reference to the small volume that surrounds each of these nodal points - the cell. The three principles identified at the beginning of this chapter are then applied to the cell mathematically as fluxes at each surface. The flux is defined as the movement of a flow attribute through the cell surface per unit time. This could, for example, be the momentum flux (the rate of transfer of momentum across the cell surface), heat flux (the rate of heat flow across the cell surface), volumetric flux (rate of volume flow across the cell surface) or mass flux (the rate of mass flow across the cell surface). The flux that enters a particular cell is identical to the flux that left the adjacent cell in order to satisfy the three principles given at the beginning of this chapter. That is, the flow from cell to cell, or over the whole domain, is conservative. What one cell loses, another gains.

With this in mind, we can now say that when the differential form of the governing equations are integrated, the conservation laws stated must be satisfied. If we are calculating values at the nodal points at the centre of each cell, the flux values are still required. These are determined through the use of interpolation profiles between nodal points. Different interpolation techniques

are applied to describe behaviours of the variable in question as it is passed from one cell to the next. This leaves us with a discretised equation; an expression of the conservation principles inside the cell. Thus the conservation of individual quantities is satisfied from cell to cell. With each cell physically satisfied in this way, the overall computational domain (regardless of the number of cells or definition of the domain) is satisfied. The integral form of the governing equations applies for a volume with finite size.

Conservation of Mass

Mass is conserved; it is not created or destroyed

To start with, we examine the law that mass is conserved. As is often done, this is easiest explained with a diagram.

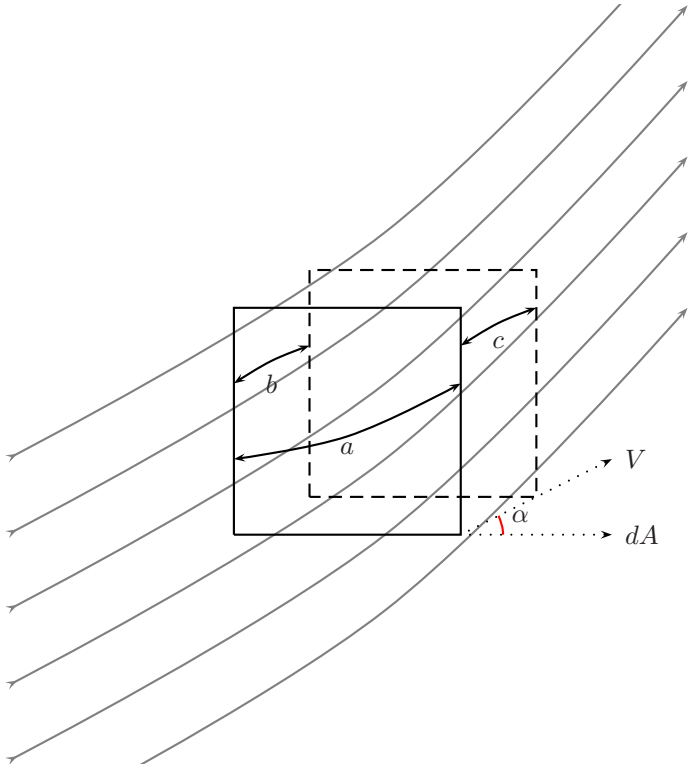

FIGURE 2.1: Control Volume illustrated

Figure 2.1 represents a quantity of matter in a flow at a time t - represented by the solid outline. At a time later ($t + \Delta t$) the boundary of the system is in a different location in the flow - as represented by the dotted line. Three regions are presented: a, b and c. At time t, the volume occupies region a. However, at time $t + \Delta t$, the volume occupies region $c + (a - b)$. Thus, by examining the mass (m) of the volume of the different regions at the different timesteps, we obtain:

$$m_a(t) = m_a(t + \Delta t) - m_b(t + \Delta t) + m_c(t + \Delta t) \tag{2.1}$$

If we rearrange this for the mass of the region, a and divide for the difference in time, Δt, we get:

$$\frac{m_a(t + \Delta t) - m_a(t)}{\Delta t} = \frac{m_b(t + \Delta t) - m_c(t + \Delta t)}{\Delta t} \tag{2.2}$$

As the time difference, Δt, approaches the limit of zero (that is, $\Delta t \to 0$), the left side of this equation becomes:

$$\lim_{(\Delta t \to 0)} \frac{m_a(t + \Delta t) - m_a(t)}{\Delta t} = \frac{\partial}{\partial t}(m)_{cv} = \frac{\partial}{\partial t}\int_{cv} \rho dV \tag{2.3}$$

We've now introduced new variables where ρ is the density, V is the volume of the sample in the flow and cv denotes which of the functions represent the control volume that is a known size fixed in the flow.

Equally, as Δt approaches zero, the right hand side of equation 2.2 becomes:

$$\lim_{(\Delta t \to 0)} \left\{ \frac{m_b(t + \Delta t) - m_c(t + \Delta t)}{\Delta t} \right\} = \dot{m}_{in} - \dot{m}_{out} \tag{2.4}$$

We now have the mass flow rate into and out of the control volume, given by $\dot{m}_{in}$ and $\dot{m}_{out}$. We now take this equation and reform it to determine the mass flow rate across the control surface (cs). That is, we find the rate of change of flow through the outer perimeter of the control volume.

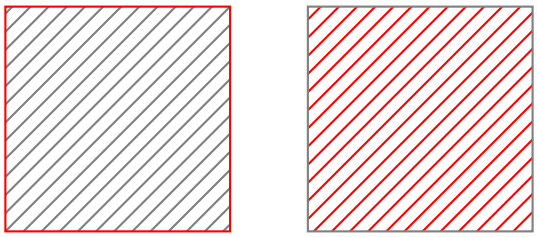

FIGURE 2.2: On the left, the Control Surface of a shape, cs, is shown highlighted in red. The Control Volume, cv, is highlighted on the right.

$$\dot{m}_{in} - \dot{m}_{out} = -\int_A \rho u \cos\alpha dA = -\int_{cs} \rho U \cdot dA \tag{2.5}$$

Now the rate of mass flow in and out of the Control Volume is presented in terms of the density and velocity vector (U) across the area bounded by the control surface. The velocity vector U is derived from the magnitude of the velocity, u and the angle of motion between the velocity vector and the normal - as shown by α in figure 2.1. Combining equations 2.3 and 2.5 gives the continuity equation for the control volume:

$$\int_{cs} \rho U \cdot dA = -\frac{\partial}{\partial t} \int_{cv} \rho dV \tag{2.6}$$

Equation 2.6 gives the continuity equation in integral form, stating that the net rate of mass flow from the control surface is equal to the rate of decrease of mass inside the control volume. However, as the control volume is fixed, the right-hand side of equation 2.6 is zero for steady flow.

Momentum

Newton's second law; $F = ma$

Newton's second law affects fluid mechanics by imposing the law that a force that is exerted on a body is equal to the rate of change of momentum over a known period of time, Δt. Thus the force F acting on a fixed mass area is given as:

$$F = \frac{dM}{dt} \tag{2.7}$$

Assuming a constant force over time Δt we get:

$$F\Delta t = \Delta M \tag{2.8}$$

M represents the total linear momentum of the area. Treating momentum as mass was treated in equation 2.1, and referring to figure 2.1, this becomes:

$$\Delta M = M_a(t + \Delta t) - M_b(t + \Delta t) + M_c(t + \Delta t) - M_a(t) \tag{2.9}$$

Once again, rearranging and dividing by Δt we get:

$$\frac{\Delta M}{\Delta t} = \frac{M_a(t + \Delta t) - M_a(t)}{\Delta t} + \frac{M_c(t + \Delta t) - M_b(t + \Delta t)}{\Delta t} \tag{2.10}$$

By taking this equation to the limit of $\Delta t \to 0$ the equation changes such that the first half of the right hand side of the equation becomes:

$$\lim_{\Delta t \to 0} \frac{M_a(t + \Delta t) - M_a(t)}{\Delta t} = \frac{\partial}{\partial t}(M)_{cv} = \frac{\partial}{\partial t} \int_{cv} \rho U dV \tag{2.11}$$

The second half becomes:

$$\lim_{\Delta t \to 0} \frac{M_c(t + \Delta t) - M_b(t + \Delta t)}{\Delta t} = \lim_{\Delta t \to 0} \left\{ \frac{(\sum \Delta M_c(t + \Delta t))_c}{\Delta t} - \frac{(\sum \Delta M_b(t + \Delta t))_b}{\Delta t} \right\} \tag{2.12}$$

This can be expressed as:

$$\sum_c \Delta \dot{M} - \sum_b \Delta \dot{M} = \{ \sum \Delta \dot{m} U \}_{out} - \{ \sum \Delta \dot{m} U \}_{in} = \int_{cs} U \rho U \cdot dA \tag{2.13}$$

This is based on the mass continuity equation expressed in equation 2.5 as $M_c(t+\Delta t) - M_b(t+\Delta t)$ is the momentum expressed as the mass that has crossed through the boundary into the area c during time change Δt. Thus, putting equation 2.10 into equation 2.8, and substituting, for the right hand side of equation 2.10, the derived values from equations 2.11 and 2.13 we end with:

$$F = \frac{\partial}{\partial t}\int_{cv} \rho U dV + \int_{cs} U\rho U \cdot dA \tag{2.14}$$

The force, F, is a total force that is made up of both surface forces (shear, F_s, and pressure, F_p, forces) and a body force (F_b). The surface forces, F_s, occurring due to pressure acting on the surface of the body, dA, are:

$$F_p = -pdA$$

This is a negative force as the direction of the force is opposite to the direction of travel U. So the integrand giving the total magnitude of this force across the surface area is:

$$F_p = -\int_{cs} pdA$$

However, viscous flow adds additional parameters due to shear and normal viscous stresses that add a force. The effect for the viscous forces is treated similarly to the pressure such that:

$$F_s = \int_{cs} \tau dA$$

The body forces (B) give the net force exerted per unit volume on the fluid inside the Control Volume. Thus the body force is effected by fluid density and is stated as:

$$F_b = \rho B dV$$

This is valid across the whole of the Control Volume, V, such that it is:

$$F_b = \int_{cv} \rho B dV$$

Adding F_p, F_s and F_b to give F, and substituting this back into equation 2.14, we get the momentum equation in integral form:

$$-\int_{cs} pdA + \int_{cs} \tau dA + \int_{cv} \rho B dV = \frac{\partial}{\partial t}\int_{cv} \rho U dV + \int_{cs} U\rho U \cdot dA \tag{2.15}$$

Energy

The first law of thermodynamics: $Q - W = \Delta E$

Based on the first law of thermodynamics, we can derive an equation for the energy change in the system (ΔE). The heat added to the system is represented by Q while W represents the work

done by the system. The change in energy can be expressed as the difference between the final energy, E_f and the initial energy, E_i, over a time, Δt:

$$\frac{Q}{\Delta t} - \frac{W}{\Delta t} = \frac{E_f - E_i}{\Delta t} \tag{2.16}$$

Examining this equation using figure 2.1 for reference, we get:

$$\frac{E_f - E_i}{\Delta t} = \frac{E_a(t+\Delta t) - E_b(t+\Delta t) + E_c(t+\Delta t) - E_a(t)}{\Delta t} \tag{2.17}$$

Rearranging we get:

$$\frac{E_f - E_i}{\Delta t} = \frac{E_a(t+\Delta t) - E_a(t)}{\Delta t} + \frac{E_c(t+\Delta t) - E_b(t+\Delta t)}{\Delta t} \tag{2.18}$$

By taking this equation to the limit of $\Delta t \to 0$ the first-half of the right hand side of the equation becomes:

$$\lim_{\Delta t \to 0} \frac{E_a(t+\Delta t) - E_a(t)}{\Delta t} = \frac{\partial}{\partial t}(E)_{cv} = \frac{\partial}{\partial t}\int_{cv} e\rho dV \tag{2.19}$$

The second-half of the right hand side of equation 2.18 can be defined as:

$$\frac{E_c(t+\Delta t) - E_b(t+\Delta t)}{\Delta t} = \frac{(\sum E_s)_{c|t+\Delta t}}{\Delta t} - \frac{(\sum E_s)_{b|t+\Delta t}}{\Delta t} \tag{2.20}$$

Where E_s is a representation for the stored energy: $\Delta m.e$. The summation of this term allows for the mass crossing the surface with Δm being the typical mass and e the stored energy by this mass. By allowing this equation to approach the limit of $\Delta t \to 0$ this becomes:

$$\lim_{\Delta t \to 0} \frac{E_c(t+\Delta t) - E_b(t+\Delta t)}{\Delta t} = \int_{out} e d\dot{m} - \int_{in} e d\dot{m} = \int_{cs} e\rho U \cdot dA \tag{2.21}$$

Thus, substituting equations 2.19 and 2.21 into equation 2.18 we have a suitable equation for the energy difference, being:

$$\lim_{\Delta t \to 0} \frac{E_f - E_i}{\Delta t} = \frac{\partial}{\partial t}\int_{cv} e\rho dV + \int_{cs} e\rho U \cdot dA \tag{2.22}$$

The convective derivative represented above is equal to the change of the energy due to the heat flux through the boundary and the work of the shear stress as will be described in the following sections.

Closing the Navier-Stokes Equations

The full Navier-Stokes equations as presented above (with full continuity, momentum and energy equations) do not have a sufficient number of equations to the number of variables in order to sufficiently close the system of equations. Therefore, further equations are required. By considering the thermodynamic properties of the flow, we can draw upon further equations to define the flow. The Navier-Stokes equations describe the motion of the flow, however, there are other

characteristics that we can consider. One such characteristic is the equation of state. Due to the electrical charge of some of the particles, a 'force field' pervades the space around them – this is known as the intermolecular force. If the particles of a gas are far enough from one another, the influence of the intermolecular force is negligible. In this case, the gas is defined as a perfect gas, and so the following relationships are defined:

Equation of State

$$p = \rho RT \tag{2.23}$$

where R is the specific gas constant, 287.05 Nm/(kg·K). However, as can be seen, the Equation of State (equation 2.23) introduces a seventh unknown: temperature T. Thus an additional equation is required in order to close the set of equations. This is generally achieved using a thermodynamic relationship between the variables of state. With the moderate temperatures to be examined in this work, it can be assumed that the specific heats remain constant.

Diffusive Coefficients

The diffusive coefficients are made up of the thermal conductivity k, and viscous coefficients λ and μ. These are related to the thermodynamic variables by means of kinetic gas theory. Their derivation is detailed in [68].

It is possible to compute the Prandtl Number Pr, which is defined as

$$Pr = \frac{\mu c_p}{k} \tag{2.24}$$

where c_p is the specific heat at constant pressure.

Sutherland's Law

A relationship for the variation of temperature of μ for air is given by Sutherland's law,

$$\frac{\mu}{\mu_0} = \left(\frac{T}{T_0}\right)^{3/2} \frac{T_0 + S_u}{T + S_u} \tag{2.25}$$

where T and S_u are in kelvin and μ_0 is a reference viscosity at a reference temperature T_0.

The reference values for viscosity and temperature are taken at standard atmospheric conditions at sea level. This gives $\mu_0 = 1.7894 \times 10^{-5} kg/\left(m \cdot s\right)$ and $T_0 = 288.16K$. The Sutherland temperature is taken as being $S_u = 110.4K$.

2.2 Differential Form of the Navier-Stokes Equations

The derivation of the integral form of the equations governing fluid flow has been demonstrated. We can now examine the governing equations in differential form; a form that allows for a fixed,

infinitesimally small volume. These lead to the Navier-Stokes Equations. In conservative form these are written as

Continuity

Referring back to equation (2.6) - the integral form of the continuity equation – which was:

$$\int_{cs} \rho U \cdot dA = -\frac{\partial}{\partial t} \int_{cv} \rho dV \tag{2.6}$$

To this equation we apply the divergence theorem (also known as the Gauss theorem). This is applicable in vector calculus as a procedure relating the flow (in this case, the flux) through a cell surface to the behavior of the flow within the defined cell volume. Essentially the outward flux through a cell surface is equal to the volume integral of the change of flux within the region bounded by the surface. Alternatively the sum of all flow sources, with the the sum of all flow sinks (the negative of sources) subtracted, gives the net flow (flux change) out of the region bounded by the surface. As the divergence theorem relates the integral and differential forms of the continuity equation, it can be applied to the left side of the above equation giving a volume integral for that side as well:

$$\int_{cv} \nabla \cdot (\rho U) dV + \frac{\partial}{\partial t} \int_{cv} \rho dV = \int_{cv} \left(\nabla \cdot (\rho V) + \frac{\partial \rho}{\partial t} \right) dV = 0$$

The control volume is a known arbitrary size; thus the integrand is zero. This gives the differential form of the continuity equation as:

$$\frac{\partial \rho}{\partial t} + \nabla \cdot (\rho u) = 0 \tag{2.26}$$

Where ρ is the density, t is time, and u is the velocity components.

The ∇ is a vector representing the components in the three principle directions of a Cartesian co-ordinate system. These are partial differentiations with respect to the three directions. That is, with u, v and w representing the basis vectors in the x, y and z directions respectively, we have:

$$\nabla = u\frac{\partial}{\partial x} + v\frac{\partial}{\partial y} + w\frac{\partial}{\partial z}$$

Thus the continuity equation in Cartesian form is:

$$\frac{\partial \rho}{\partial t} + \frac{\partial}{\partial x_i}(\rho u_i) + \frac{\partial}{\partial y_i}(\rho v_i) + \frac{\partial}{\partial z_i}(\rho w_i) = 0 \tag{2.27}$$

Momentum

$$\frac{\partial \rho u}{\partial t} + \nabla \cdot (\rho u \otimes u) = -\nabla \cdot S \tag{2.28}$$

The stress tensor, S, is a representation of the effects of viscous stresses and the thermodynamic pressure.

Energy

$$\frac{\partial e}{\partial t} + \nabla \cdot (eu) = -\nabla \cdot (S \cdot u) - \nabla \cdot q \tag{2.29}$$

Where e is the energy per unit volume, and q is the heat flux.

2.3 Governing Equations in Non-Dimensionalised Form

Usually, for computational use, as in Computational Fluid Dynamics, the Governing Navier-Stokes Equations are given in a dimensionless form. This reduces the risk of poorly conditioned flow states and ensures that, numerically, the solution is properly balanced. What's more, by grouping together a range of geometrical and physical quantities, the number of input variables can be reduced, allowing for better comparison with experimental data, while also showing some similarities between flows that - on first appearances - seem very different. To non-dimensionalise the variables, each one is related to a characteristic reference value, which is chosen individually. That is, in the case of length, one length of the problem set up (commonly the length or height of a shape being modelled, or of the channel the flow passes through) is chosen for the characteristic length, l_c. Equally for the characteristic variables for velocity (u_c), density (ρ_c) and viscosity (μ_c), a fair representation for the flow (usually the bulk, or freestream, values) will be chosen. Thus the dimensionless variables are obtained as:

$$\begin{aligned} t^* &= \frac{t}{l_c/u_c}, \quad x^* = \frac{x}{l_c}, \quad y^* = \frac{y}{l_c}, \quad z^* = \frac{z}{l_c} \\ \rho^* &= \frac{\rho}{\rho_c}, \quad u^* = \frac{u}{u_c}, \quad v^* = \frac{v}{u_c}, \quad w^* = \frac{w}{u_c} \\ e^* &= \frac{e}{\rho_c u_c^2}, \quad p^* = \frac{p}{\rho_c u_c^2}, \quad \mu^* = \frac{\mu}{\mu_c} \end{aligned} \tag{2.30}$$

For each of the terms in equation 2.31, the variables with an asterix represent the non-dimensionalised term. We can now introduce the units for each of these equations and show that each one cancels out, and thus satisfies the requirement of a non-dimensionalised equation. For the variables x, y and z, we take the unit of measure to be metres. Thus, substituting this unit in for l_c as well, it is clear that the x^*, y^* and z^* will be dimensionless. Equally, when velocity is given in ms^{-1} for u_c, as well as for the component velocity values, the variables u^*, v^* and w^* will be dimensionless. Density (with units kgm^{-3}) will cancel to give a dimensionless value. Treating time and viscosity similarily obtains the dimensionless values for those variables.

A note about Nabla, and how it simplifies Notation

As stated just below equation 2.26, the ∇ is a vector representing the components in the three principle directions of a Cartesian co-ordinate system. These are partial differentiations with respect to the three directions. That is:

$$\nabla = \frac{\partial}{\partial x} + \frac{\partial}{\partial y} + \frac{\partial}{\partial z}$$

Thus, we can take the non-dimensional equations given and use these to determine a non-dimensional form for ∇ as follows:

$$\nabla = \frac{\partial}{\partial (x^* l_c)} + \frac{\partial}{\partial (y^* l_c)} + \frac{\partial}{\partial (z^* l_c)} = \frac{1}{l_c} \cdot \left(\frac{\partial}{\partial x^*} + \frac{\partial}{\partial y^*} + \frac{\partial}{\partial z^*} \right) = \frac{\nabla^*}{l_c}$$

2.4 Governing Equations in Matrix Form

The Governing Equations, as given in equations 2.26 to 2.29, can be rewritten in a simplified form such that inputting them as a computational procedure is made easier. That is, writing them in conservative Cartesian matrix form gives a single equation for the whole system of governing equations:

$$\frac{\partial \mathbf{U}}{\partial t} + \frac{\partial \mathbf{E}_i}{\partial x} + \frac{\partial \mathbf{F}_i}{\partial y} + \frac{\partial \mathbf{G}_i}{\partial z} = \frac{\partial \mathbf{E}_v}{\partial x} + \frac{\partial \mathbf{F}_v}{\partial y} + \frac{\partial \mathbf{G}_v}{\partial z} \tag{2.31}$$

Where

- $\mathbf{U}$ is the array of the conservative variables
- $\mathbf{E}_i$,$\mathbf{F}_i$ and $\mathbf{G}_i$ are the the Cartesian inviscid flux vectors
- $\mathbf{E}_v$, $\mathbf{F}_v$ and $\mathbf{G}_v$ are the Cartesian viscous flux vectors

These arrays such that:

$$\begin{aligned}
\mathbf{U} &= \begin{pmatrix} \rho \\ \rho u \\ \rho v \\ \rho w \\ e \end{pmatrix}, \quad \mathbf{E}_i = \begin{pmatrix} \rho u \\ \rho u^2 + p \\ \rho v u \\ \rho w u \\ (e+p)\, u \end{pmatrix}, \quad \mathbf{F}_i = \begin{pmatrix} \rho v \\ \rho u v \\ \rho v^2 + p \\ \rho w v \\ (e+p)\, v \end{pmatrix}, \quad \mathbf{G}_i = \begin{pmatrix} \rho w \\ \rho u w \\ \rho v w \\ \rho w^2 + p \\ (e+p)\, w \end{pmatrix} \\
\mathbf{E}_v &= \frac{1}{Re} \begin{pmatrix} 0 \\ \tau_{xx} \\ \tau_{xy} \\ \tau_{xz} \\ u\tau_{xx} + v\tau_{xy} + w\tau_{xz} - \frac{\gamma}{Pr} q_x \end{pmatrix}, \quad \mathbf{F}_v = \frac{1}{Re} \begin{pmatrix} 0 \\ \tau_{yx} \\ \tau_{yy} \\ \tau_{yz} \\ u\tau_{yx} + v\tau_{yy} + w\tau_{yz} - \frac{\gamma}{Pr} q_y \end{pmatrix} \\
\mathbf{G}_v &= \begin{pmatrix} 0 \\ \tau_{zx} \\ \tau_{zy} \\ \tau_{zz} \\ u\tau_{zx} + v\tau_{zy} + w\tau_{zz} - \frac{\gamma}{Pr} q_z \end{pmatrix}
\end{aligned} \tag{2.32}$$

The heat flux, q, is split into its three differing components, x, y and z. γ represents the ratio of specific heats, and is generally 1.4 for air. The ratio of specific heats (c_p and c_v) are joined by the relationships:

$$\gamma = \frac{c_p}{c_v}, \quad c_p - c_v = R, \quad c_v = \frac{R}{\gamma - 1}, \quad c_p = \frac{\gamma R}{\gamma - 1}$$

Where the gas constant of air is given by R and is 287.05 Nm/(kg·K). Pr is the Prandtl number, a dimensionless parameter that varies between 0.680 and 0.744 for temperatures between 175K and 1900K [69]. The Prandtl number can be computed using equation 2.33, where μ represents the air density, c_p is the specific heat value at a constant pressure and k is the thermal conductivity. For an experiment or simulation with a single reference temperature, the relevant values (including a pre-computed Prandtl number) can be found directly from literature [69].

$$Pr = \frac{\mu c_p}{k} \tag{2.33}$$

In equation 2.32, viscous stresses are represented by the values given by τ. Each of these has a subscript which denotes which direction the stress is exerted on, and onto which plane. That is, for τ_{xy}, the viscous stress in the y direction is being exerted on a plane that is normal to the x axis.

2.5 Transforming to Curvilinear Coordinates

The equations of flow have been presented in the Cartesian Coordinate system. That is, in a system represented by coordinates of x, y and z as used in many mathematical models. However, these assume an orthogonal relationship between cells with equal spacing. This would be adequate for a fully uniform structured, rectangular grid. However, most grids can not be this simple, as such a grid system would only work for the most geometrically simple of cases. Thus, in order to allow for curved lines or other complex geometries, a more complex coordinate system has to be applied. The coordinate system usually applied is the curvilinear coordinate system. This requires a transformation of the governing equations from the x, y and z Cartesian Coordinate system into the ξ, η, and ζ curvilinear coordinate system. Conversion of the Cartesian (x, y and z) forms to the generalised curvilinear system fixed in time is given by:

$$\xi = \xi(x,y,z) \quad \eta = \eta(x,y,z) \quad \zeta = \zeta(x,y,z). \tag{2.34}$$

For a structured (or block-structured grid, the above transformation is implicitly introduced by the numbering of the grid nodes, i.e.:

$$i = \xi(x,y,z) \quad j = \eta(x,y,z) \quad k = \zeta(x,y,z). \tag{2.35}$$

The complete description of the transformation and its metrics can be found in [26].

The inviscid flux vectors in curvilinear form are then given by:

$$\tilde{\mathbf{E}}_\mathbf{i} = J(\mathbf{E}_\mathbf{i}\frac{\partial \xi}{\partial x} + \mathbf{F}_\mathbf{i}\frac{\partial \xi}{\partial y} + \mathbf{G}_\mathbf{i}\frac{\partial \xi}{\partial z}) \tag{2.36}$$

$$\tilde{\mathbf{F}}_\mathbf{i} = J(\mathbf{E}_\mathbf{i}\frac{\partial \eta}{\partial x} + \mathbf{F}_\mathbf{i}\frac{\partial \eta}{\partial y} + \mathbf{G}_\mathbf{i}\frac{\partial \eta}{\partial z}) \tag{2.37}$$

$$\tilde{\mathbf{G}}_\mathbf{i} = J(\mathbf{E}_\mathbf{i}\frac{\partial \zeta}{\partial x} + \mathbf{F}_\mathbf{i}\frac{\partial \zeta}{\partial y} + \mathbf{G}_\mathbf{i}\frac{\partial \zeta}{\partial z}) \tag{2.38}$$

where J is the Jacobian of the transformation. Similarly, viscous fluxes are trsansformed as:

$$\tilde{\mathbf{E}}_\mathbf{v} = J(\mathbf{E}_\mathbf{v}\frac{\partial \xi}{\partial x} + \mathbf{F}_\mathbf{v}\frac{\partial \xi}{\partial y} + \mathbf{G}_\mathbf{v}\frac{\partial \xi}{\partial z}) \tag{2.39}$$

$$\tilde{\mathbf{F}}_\mathbf{v} = J(\mathbf{E}_\mathbf{v}\frac{\partial \eta}{\partial x} + \mathbf{F}_\mathbf{v}\frac{\partial \eta}{\partial y} + \mathbf{G}_\mathbf{v}\frac{\partial \eta}{\partial z}) \tag{2.40}$$

$$\tilde{\mathbf{G}}_\mathbf{v} = J(\mathbf{E}_\mathbf{v}\frac{\partial \zeta}{\partial x} + \mathbf{F}_\mathbf{v}\frac{\partial \zeta}{\partial y} + \mathbf{G}_\mathbf{v}\frac{\partial \zeta}{\partial z}) \tag{2.41}$$

The final system of equations to be solved in the curvilinear coordinate system is then given by:

$$\frac{\partial \tilde{\mathbf{U}}}{\partial t} + \frac{\partial \tilde{\mathbf{E}}_\mathbf{i}}{\partial \xi} + \frac{\partial \tilde{\mathbf{F}}_\mathbf{i}}{\partial \eta} + \frac{\partial \tilde{\mathbf{G}}_\mathbf{i}}{\partial \zeta} = \frac{\partial \tilde{\mathbf{E}}_\mathbf{v}}{\partial \xi} + \frac{\partial \tilde{\mathbf{F}}_\mathbf{v}}{\partial \eta} + \frac{\partial \tilde{\mathbf{G}}_\mathbf{v}}{\partial \zeta}\ , \tag{2.42}$$

where $\tilde{\mathbf{U}}$ is the transformed vector of conserved variables

$$\tilde{\mathbf{U}} = J\mathbf{U} \tag{2.43}$$

The numerical methods employed for the discretisation of the above system will be discussed in the following chapter.

3

Numerical Approach and Implementation

In science one tries to tell people, in such a way as to be understood by everyone, something that no one ever knew before. But in poetry, it's the exact opposite. ***Paul Dirac (1902 - 1984)***

* * * * *

In this chapter, the numerics and implementation details will be discussed. The analysis presented in this thesis was performed using the CNS3D computational code developed by FMCS Group. While the development of the code itself was not a key part of this thesis, relevant details of numerical methods and treatment of boundary and initial conditions implemented in CNS3D will be discussed in the following sections to provide background for the analysis of results in the following chapters.

3.1 Temporal Discretisation

CNS3D is an explicit finite volume compressible code operating on a block-structured discretisation of the computational domain. This allows for separate time and spatial discretisation,

allowing a wide range of freedom for differing levels of approximation for the derivatives. With the grid in use as static in nature, the volume of each cell is assumed to be unchanged between time-steps and so the volume can be kept separate from the time derivative. Therefore, the time derivative can be approximated using the non-linear scheme in [70]

$$\frac{V}{\Delta t}\Delta\overrightarrow{W}^n = -\frac{\zeta}{1+\omega}\overrightarrow{R}^{n+1} - \frac{1-\zeta}{1+\omega}\overrightarrow{R}^n + \frac{V}{\Delta t}\frac{\omega}{1+\omega}\Delta\overrightarrow{W}^{n-1} \tag{3.1}$$

where

$$\Delta\overrightarrow{W}^n = \overrightarrow{W}^{n+1} - \overrightarrow{W}^n$$

is the solution correction step. The superscript n gives the current time-point, while Δt represents the time step. The parameters ζ and ω determine the nature of the time-stepping method; that is whether it will be an implicit or explicit ($(\zeta = 0)$) scheme.

Explicit Runge-Kutta Time Integration

Following initial tests, the explicit time stepping in this thesis was implemented through second order Runge-Kutta scheme (e.g. [26]) with global time-stepping having a Courant-Friedrichs-Lewy (CFL) number of 0.06 for all simulations. The latter was adjusted based on the tests of the effect of time step on the solution in order to ensure that main source of the numerical error is associated with spatial rather than temporal discretisation.

Methods characterised with a new value of the solution at time $n+1$ can be explicitly expressed in terms of values obtained from previous timesteps (i.e. $n < n+1$) for each cell in the domain. This allows the solution to be propagated in time with the use of an algebraic expression based on previously known solutions, and evaluating these expressions. The most basic time-stepping scheme can be obtained by setting both ζ and ω as 0 in equation Equation (3.1). This gives an approximation of the time-derivative based on a forward difference method, which is generally referred to as the first-order in time forward Euler stepping method [26]. The residual (R) is evaluated at each successive time-step as:

$$\overrightarrow{W}^{n+1} = \overrightarrow{W}^n - \frac{\Delta t}{V}\overrightarrow{R}^n \tag{3.2}$$

This is a single-step scheme as the next solution - W^{n+1} - is obtained from a single evaluation of the residual. There exist multi-stage (e.g. 2^{nd} or higher order accuracy) time-stepping schemes such as the Runge-Kutta (RK) methods. These evaluate the solution at each new time-step by advancing through intermediate steps where the residual is calculated at each step. Weighting coefficients are used to weigh the residual value at each stage.

A general form for the Runge-Kutta method to advance a solution from time n to $n+1$ with

timestep Δt through m stage(s) is given in [71] as

$$\begin{aligned} \overrightarrow{W}^{0}_{I,J,K} &= \overrightarrow{W}^{n}_{I,J,K} \\ \overrightarrow{W}^{k}_{I,J,K} &= \overrightarrow{W}^{0}_{I,J,K} - \Delta t \sum_{j=0}^{m} \zeta_{kj} R^{j}_{I,J,K} \\ \overrightarrow{W}^{n+1}_{I,J,K} &= \sum_{k=1}^{m} \xi_k R^{k}_{I,J,K} \end{aligned} \tag{3.3}$$

where k identifies the Runge-Kutta stage $(k = 1, \ldots, m)$, while ζ_{jk} and ξ_k are real numbers with $(j = 0, \ldots, m)$. This gives a truly explicit method as long as $\zeta_{jk} = 0$ for values of $j \geq k$. The Runge-Kutta time integration method is widely used, as it has a low cost requirement per time-step while providing a high stability region. Furthermore, the order of accuracy of the Runge-Kutta method is fairly straightforward to increase by increasing the number of stages of m.

Timestep Calculation

When a time-step (Δt) is defined or computed, there is a limitation to the maximum time-step that should be used. This maximum value is governed by the cell sizes such that any wave propagating through a cell should pass a distance no greater than the cell being passed. That is, a stable solution is obtained if no wave travels beyond one cell-size distance in the domain. With the well-known link between distance, time and speed, we can deduce that in order to decrease the distance covered by a wave of fixed speed, we can reduce the time-step. This avoids instabilities introduced with a wave passing right through a cell within a single time-step (and ultimately not being sufficiently captured). It can thus be seen that as cell size is decreased, the maximum allowable time-step decreases. This can result in a requirement to decrease the time-step to very small values - particularly in the presence of solid surfaces.

The stated link between distance, speed and time can be extended to a relationship between time-steps and distances moved with fixed speeds. This would be written as:

$$\Delta t = \frac{\Delta x}{\max speed} \tag{3.4}$$

When an implicit time-step is used, the physical time-step between simulation times can be set to a specific value - and it is up to the user to ensure this value is suitable to sufficiently capture the flow and remain stable (while also ensuring it is large enough to avoid the simulation from needing too long to run). However, when an explicit time-stepping method is used, the Courant-Freidrichs-Lewy (CFL) condition has to be satisfied, such that if a wave is crossing a discrete grid, the time-step must be less than the time taken for the wave to travel between adjacent grid points. This CFL condition is used as a coefficient in time-step, within the explicit scheme, for the time-step defined in equation 3.4 such that the time-step is given the definition of:

$$\Delta t = \min \left(C \frac{\Delta x_{I,J,K}}{\max speed} \right) \tag{3.5}$$

where C represents the CFL coefficient, which is given a positive value between 0 and 1, and whose purpose is to allow further control of the value of δt to provide optimal stability. This one dimensional formulation can be swept in each of the three dimensions in the three-dimensional domain - this is the process of directional splitting. This formulation incorporating the CFL number allows for the non-linear nature of the governing equations (which can in turn lead to waves behaving in non-linear manners). As stated at the beginning of this section, the value for CFL was set to be 0.06 following a range of initial tests, with the use ofa second-order Runge-Kutta scheme.

3.2 Flux Discretisation and Reconstruction Methods

The viscous fluxes were discretised using second order central difference approach (e.g. [26]). For example, for the ξ-sweep of the domain, the ξ derivative of ξ viscous flux at the cell face is approximated as follows:

$$\left(\frac{\partial \tilde{\mathbf{E}}_{\mathbf{v}}}{\partial \xi}\right)_{i+\frac{1}{2}} = \tilde{\mathbf{E}}_{\mathbf{v,i+1}} - \tilde{\mathbf{E}}_{\mathbf{v,i}} \tag{3.6}$$

where the properties of the transformation employed have been taken into account. Namely, since ξ coordinate of the curvilinear space corresponds to the i-index of the grid, $\Delta\xi = 1$. The above equation is written at the centroid of the face $i + \frac{1}{2}, j, k$ and the grid metrics required at the face centroid are evaluated using averages over the nodes belonging to the face.

The computation of the inviscid flux is based on the approximate HLLC Riemann solver [25]. The HLLC solver utilises a three wave approximation of the Riemann problem to evaluate the linearised flux at the cell face directly. To illustrate the concept, we consider the Riemann problem evaluated during ξ sweeps at the interface between cells i and $i+1$ for a Cartesian grid. The vector of the conserved variables at the left side of the cell face $i + 1/2$ are denoted as $\mathbf{U_L}$ and that on the right side of the face as $\mathbf{U_R}$. The intermediate region between the left and right wave is referred to as the "star region" and corresponding values are denoted by "*" subscript. As shown in Toro [25], the flux is calculated as follows:

- Firstly, pressure in the star region is estimated as

$$p_* = \frac{1}{2}(p_L + p_R) - \frac{1}{2}(u_R - u_L)(\bar{\rho}\bar{a}) \,, \tag{3.7}$$

  where $\bar{\rho}$ and $\bar{a}$ are the density and speed of sound averaged between the left and right states and u is the x velocity component

- The wave speeds of the left and right wave, S_L and S_R, are then calculated as

$$S_L = u_L - a_L q_L \,, \quad S_R = u_R - a_R q_R \,, \tag{3.8}$$

  where

$$q_L = \begin{cases} 1 & \text{if} \quad p_* \leq p_L \\ [1 + \frac{\gamma+1}{2\gamma}(p_*/p_L - 1)]^{\frac{1}{2}} & \text{if} \quad p_* > p_L \end{cases} \,, \tag{3.9}$$

and q_R is obtained in the same manner by replacing pressure of the left state with that of the right state.

- The speed of the contact wave is then determined as

$$S_* = \frac{p_R - p_L + \rho_L u_L(S_L - u_L) - \rho_R u_R(S_R - u_R)}{\rho_L(S_L - u_L) - \rho_R(S_R - u_R)} \,. \tag{3.10}$$

- The state to the left of the contact wave $\mathbf{U}_{*\mathbf{L}}$ is calculated as

$$\mathbf{U}_{*L} = \rho_L \left(\frac{S_L - u_L}{S_L - S_*}\right) \begin{pmatrix} 1 \\ S_* \\ v_L \\ w_L \\ \frac{E_L}{\rho_L} + (S_* - u_L)\left[S_* + \frac{p_L}{\rho_L(S_L - u_L)}\right] \end{pmatrix} . \tag{3.11}$$

with the right state $\mathbf{U}_{*R}$ computed in the same manner by replacing left state values with the right state values in the above expression.

- Finally the intercell inviscid flux is then given by:

$$\mathbf{E}^{HLLC}_{i+1/2} = \begin{cases} \mathbf{E}_L & if \quad 0 \leq S_L \\ \mathbf{E}_L + S_L(\mathbf{U}_{*L} - \mathbf{U}_L) & if \quad S_L \leq 0 \leq S_* \\ \mathbf{E}_R + S_R(\mathbf{U}_{*R} - \mathbf{U}_R) & if \quad S_* \leq 0 \leq S_R \\ \mathbf{E}_R & if \quad 0 \geq S_R \end{cases} . \tag{3.12}$$

The accuracy of the above expression is limited by the accuracy of the determination of the left and right states $\mathbf{U}_L$ and $\mathbf{U}_R$. The selection of the cell-averaged value in cells i and $i+1$ yields a first order scheme. The accuracy can be further improved by the reconstruction of the left and right state from the cell averaged values of neighbouring cells using a suitable interpolation technique. The choice of the reconstruction method affects the dissipative properties of the resulting discretisation scheme. In the context of the ILES approach, this effectively changes the properties of the implicit subgrid dissipation. The different reconstruction methods, that allow for higher-order reconstruction, used in this thesis will be discussed according to the family of schemes they belong.

3.2.1 Reconstruction schemes

When in the process of solving the partial differential equations (PDE's) for the numerical analysis of the flow, we need to ensure that any calculations that are carried out are as conservative as possible. This is to ensure the satisfaction of conservation of momentum and mass. Sergei Godunov devised a conservative numerical scheme in which variables are considered as piecewise constant between cells from one time-step to the next. The time evolution would be dependant on the exact solution of the Riemann problem (a one dimensional sod shock tube) at the cell faces.

However, the nature of a piecewise constant as suggested by Godunov is first-order. Godunov himself stated in his theorem that the monotone methods (the linear numerical schemes) to solve partial differential equations can be - at most - first-order accurate. Since this theorem, a broad range of further (higher-resolution) numerical methods have been developed, to achieve a higher-order of accuracy and avoid spurious oscillations. This leads to the definition of these higher-order methods as being non-oscillatory methods [26]. These methods have a self-adaptive nature whereby the stencil used changes as a function of the solution itself. This is the key difference between high-resolution methods and high-order (linear) finite differencing schemes. These higher-resolution methods are particularly useful in such flows with discontinuous characteristics, such as interfaces and steep shear layers.

Monotonic Upwind Scheme for Scalar Conservation Laws Schemes

The first group of reconstruction methods detailed is the Monotonic Upwind Scheme for Scalar Conservation Laws (MUSCL) introduced by van Leer [72, 73]. This was an extension to Godunov's method whereby, instead of assuming piece-wise constant data, van Leer assumed piecewise linear giving a second-order accurate solution. The values used on either side of the Reimann problem are a better approximation of the real interface values. The non-linearity used is given with the use of 'slope limiters' - functions restricting the slope imposed on each cell around the discontinuity to help maintain the monotonicity. These restrictions reduce the maxima and increase the minima, bringing them closer together and thus avoiding the creation of spurious oscillations. The disadvantage of this was that in the region of a shock-wave, the scheme would default to first-order accuracy. Thus a variety of limiters have been devised to improve resolution of discontinuities. It has been found that there is a correlation between this improved resolution and dissipation [74], however, even the most dissipative schemes are an improvement over the first-order methods.

For MUSCL reconstruction, the left and right states of the conservative variables at the cell interfaces are computed for each conserved variable $f \in \mathbf{U}$ (see also [25]) as:

$$\begin{aligned} f^L_{i+1/2} = &\quad f_i + \quad \frac{1}{4}\left[(1-k)\,\phi\left(r^L\right)(f_i - f_{i-1}) + (1+k)\,\phi\left(\frac{1}{r^L}\right)(f_{i+1} - f_i)\right] \\ f^R_{i+1/2} = &\quad f_{i+1} + \quad \frac{1}{4}\left[(1-k)\,\phi\left(r^R\right)(f_{i+2} - f_{i+1}) + (1+k)\,\phi\left(\frac{1}{r^R}\right)(f_{i+1} - f_i)\right] \end{aligned} \tag{3.13}$$

Where k is a free parameter which is in the interval $[-1, 1]$ and is $1/3$ for the third-order limiter, ϕ is a limiter function that is based on the variables within and is different for the different subschemes, r is the ratio of slopes and i is a label for the cell in question.

All of the second-order and third-order limiter functions use the following slope ratios

$$r^L_i = \frac{(f_{i+1} - f_i)}{(f_i - f_{i-1})} \quad , \quad r^R_i = \frac{(f_{i+1} - f_i)}{(f_{i+2} - f_{i+1})} \tag{3.14}$$

The $\phi(r)$ term is the limiting function. A negative value for this would imply an extremum, at which point the limiting function would revert to first-order. The most popular second-order limiters are available in a variety of CFD textbooks including Laney [67], and Toro [25]. These are fairly widespread in use in CFD including in the CFD code used at Cranfield. The relevant limiters for this thesis include:

MinMod limiter

$$\phi_{MM} = \min(1, r)$$

Van Leer limiter

$$\phi_{VL} = \frac{2r}{1+r}$$

Third-order Limiter

$$\phi_{M3} = 1 - \left(1 + \frac{2Nr}{1+r^2}\right)\left(1 - \frac{2r}{1+r^2}\right)^N$$

The third-order MUSCL limiter (from [75]), ϕ_{M3} has a 'steepening' parameter N which gives better resolution of discontinuities. In this thesis the value of $N = 2$ was used. The MinMod limiter is generally considered as the most dissipative of these limiters (and therefore the most robust traditional limiter) while the Van Leer limiter provides best accuracy reliably.

Kim and Kim suggested a fifth-order limiter [76] which is a little more complex due to the use of a six-point stencil rather than the four-point stencil used by lower order methods. Thus the slope ratios are defined as:

$$r_i^L = \frac{(f_{i+1} - f_i)}{(f_i - f_{i-1})} \quad , \quad r_i^R = \frac{(f_i - f_{i-1})}{(f_{i+1} - f_i)} \tag{3.15}$$

where ϕ is given by:

$$\phi_{M5,L} = \frac{-2/r_{i-1}^L + 11 + 24r_i^L - 3r_i^L r_{i+1}^L}{30} \tag{3.16}$$

$$\phi_{M5,R} = \frac{-2/r_{i+2}^R + 11 + 24r_{i+1}^R - 3r_{i+1}^R r_i^R}{30} \tag{3.17}$$

The limiters used for the fifth-order scheme in order to maintain monotonicity are:

$$\phi_{M5,L} = \max\left(0, \min\left(2, 2r_i^L, \phi_{M5,L}\right)\right)$$
$$\phi_{M5,R} = \max\left(0, \min\left(2, 2r_{i+1}^R, \phi_{M5,R}\right)\right)$$

This approach maintains the monotonicity though in smooth regions of the flow, the accuracy could still be further improved. Once again, this scheme reverts to first-order when extrema are present. The notional order of accuracy of this scheme could be increased further still, but doing so would likely return little improvement for significant cost.

3.2.2 Weighted Essentially Non-Oscillatory Schemes

Another class of reconstruction methods used in the present thesis is the Weighted Essentially Non-Oscillatory (WENO) reconstruction [77, 78]. In WENO reconstruction several possible reconstruction stencils are combined in order to achieve a high order essentially non-oscillatory solution. In general, a WENO reconstruction for $f \in \mathbf{U}$ at the cell face $i + 1/2$ can be defined as:

$$f_{i+1/2} = \sum_{k=1}^{s} \omega_k f^k_{i+1/2}, \tag{3.18}$$

where $f^k_{i+1/2}$ is the interpolated value for kth stencil at the interface $i + 1/2$ and ω_k is the weight for kth stencil. The combination of the stencils is adaptive as the weight of each stencil is based on the local flow properties. The rationale for the selection of the weights is that the smooth region of the flow should have a higher contribution to the reconstruction, thus limiting the utilisation of stencils across discontinuities in the flow. The weights ω_k can then be expressed as [79]:

$$\omega_k = \frac{\alpha_k}{\sum_{i=1}^{s} \alpha_i}\,, \tag{3.19}$$

$$\alpha_k = \frac{\bar{\omega_k}}{(\epsilon + \beta_k)^p}\,, \tag{3.20}$$

where $\bar{\omega_k}$ is the optimal weight and β_k is the so-called smoothness indicator for kth stencil. p is a free parameter (taken to be equal to 2 in this thesis based on literature [74]) and ϵ is a small positive number used to prevent division by zero in case of a uniform flow.

For a stencil of length s, WENO schemes can reach accuracy of $2s - 1$. In this thesis 5^{th} and 9^{th} order WENO schemes are employed as implemented in CNS3D by Mosedale and Titarev. The 5th order WENO scheme will be described here to provide an example and the reader is referred to [74, 79] for details of the implementation of 9th order schemes. 5th order reconstruction employs three stencils as follows

$$f_{j+1/2} = \sum_{k=1}^{3} \omega_k f^k_{j+1/2} \tag{3.21}$$

where the stencils are given by

$$\begin{aligned} S_1 =& (j, j+1, j+2)\,, \\ S_2 =& (j-1, j, j+1)\,, \\ S_3 =& (j-2, j-1, j)\,. \end{aligned} \tag{3.22}$$

The smoothness indicators are given by

$$\begin{aligned} \beta_1 =& \frac{13}{12}(f_j - 2f_{j+1} + f_{j+2})^2 + \frac{1}{4}(3f_j - 4f_{j+1} + f_{j+2})^2\,, \\ \beta_2 =& \frac{13}{12}(f_{j-1} - 2f_j + f_{j+1})^2 + \frac{1}{4}(f_{j-1} - f_{j+1})^2\,, \\ \beta_3 =& \frac{13}{12}(f_{j-2} - 2f_{j-1} + f_j)^2 + \frac{1}{4}(f_{j-2} - 4f_{j-1} + 3f_j)^2 \end{aligned} \tag{3.23}$$

with the optimal weights for the left reconstructed variable $f^L_{j+1/2}$

$$\bar{\omega_0} = \frac{3}{10}\,, \bar{\omega_1} = \frac{3}{5}\,, \bar{\omega_2} = \frac{1}{10}. \tag{3.24}$$

A further correction is employed as in [80] to improve the accuracy around critical points (see also [74]), with the modified weights given by

$$\omega_k^M = \frac{\alpha_k^*}{\sum_{i=1}^3 \alpha_i^*}\,, \tag{3.25}$$

$$\alpha_k^* = g_k(\omega_k)\,, \tag{3.26}$$

$$g_k(\omega_k) = \frac{\omega_k(\bar{\omega}_k + \bar{\omega}_k^2 - 3\bar{\omega}_k\omega_k + \omega_k^2)}{\bar{\omega}_k^2 + \omega_k(1 - 2\bar{\omega}_k)}\,. \tag{3.27}$$

where ω_k are the unmodified weights.

Generally WENO schemes don't dissipate undesirable oscillations, instead keeping the same level of accuracy in all areas of the flow by using an adaptive stencil. A convex combination of all available stencils (with discontinuous stencils being given zero weight) are used, resulting in a smoother flux whilst holding the optimal accuracy (as stated, equivalent to $2s - 1$ where s is the stencil length). They are able to calculate relatively stable results at fifth, ninth, or higher, orders of accuracy. The additional cost imposed of evaluating the larger stencils could be made up for in a reduction of grid resolution (however, in this thesis, this investigation wasn't carried out as a direct comparison on equivalent mesh sizes was desired). A more in-depth discussion and comparison of the different WENO schemes can be found in [78, 81].

3.2.3 Low Mach Number Treatment

The standard MUSCL scheme results in a uniform dissipation of kinetic energy as Mach number reaches zero. This was demonstrated analytically in [82]. It was shown that dissipation in a Godunov scheme is proportional to the speed of sound and the velocity jump squared, resulting in heavy dampening of any low Mach features. Initially demonstrated on a compressible flow, there should be no reason why this modification cannot be extended to any compressible method with a reconstruction phase. A modification has been made that extends the validity of the method to low Mach numbers with a lower limit of at least $M \approx 10^{-4}$. This procedure was proposed in [83] and examined in more detail in [82].

A simple solution to stop excessive numerical dissipation was suggested as carrying out a modification to the velocity jump across the cell interface through introduction of a function z. That is, the treatment works by correcting the left and right values given by reconstruction such that a decrease in local Mach number does not result in any additional dissipation. The formula with which this is achieved was proposed in [83] and is:

$$u_L = \frac{u_L + u_R}{2} + z\frac{u_L - u_R}{2}$$
$$u_R = \frac{u_L + u_R}{2} + z\frac{u_R - u_L}{2} \tag{3.28}$$

z has limits of

$$z = \min\left(M_{total}, 1\right) \quad , \quad M_{total} = \max\left(M_L, M_R\right) \tag{3.29}$$

where M_L is the Mach number to the left of the cell face and M_R is the Mach number to the right of the cell face.

An interesting point of comparison can thus be explored for schemes of the same nominal order of accuracy but different dissipative properties (e.g. 2nd-order Van Leer vs MinMod and 5th-order MUSCL vs WENO), as will be discussed in the Results chapters. In order to maintain this direct comparison, the low Mach number treatment was used for all numerical schemes to reduce dissipation where possible.

3.3 Boundary Conditions

At each edge of the overall computational domain, a definition is required for what happens to the flow when that edge is reached. Boundary conditions (BCs) are generally either transmissive or reflective boundary conditions. The former BCs are those that allow flow through them (whether the flow is affected in some way or not), with reflective BCs being those that prevent the flow from passing through (this includes such boundaries as solid walls and symmetrical conditions that reflect the flow directly). All of the simulations carried out were run at a low Mach number of 0.2. With a Mach number lower than 1, these simulations should be run with specific boundary conditions for inflow and outflow walls of the domain. However, initially these were run with supersonic inflow and outflow boundary conditions as these were readily available within the code. It was subsequently found that, although satisfactory results were given for cylinder flow at low-orders of run, the boundary conditions chosen were clearly adversely affecting the flow even in the freestream regions upstream of the cylinder. The higher order runs (particularly 5^{th} and 9^{th} order runs) exhibited higher flow velocities than expected, upstream of the cylinder. Thus, subsonic boundary conditions were implemented in order to determine whether this was the cause of the unexpected velocities. Note that the higher order reconstruction methods are more sensitive to incorrect boundary conditions.

In order to simplify this section, a couple of short cuts to notation are taken. The first is that, in most cases within this section where flow velocity is referenced, the velocity parameter u will be given (with subscripts where appropriate). However, flow simulations can be two- or three-dimensional, and so the actual velocity parameters involved are u, v and w. Therefore, where

u is referenced, v and w should also be determined where the simulation is of a two- or three-dimensional nature. That is, where extrapolation is discussed the following is written:

$$u_0 = 2u_1 - u_2 \tag{3.30}$$

The above corresponds to the second order centered discretisation of the linear extrapolation in ijk space:

$$\frac{\partial^2 u}{\partial \xi^2} = 0 \tag{3.31}$$

and it is assumed that the other velocity components are treated in the same manner.

The second notation simplification within this section is that all reference to the boundary conditions are made around a "left" boundary. This is normally a boundary to the left-most side of the co-ordinate in question (i, j or k) within the block or domain in question.

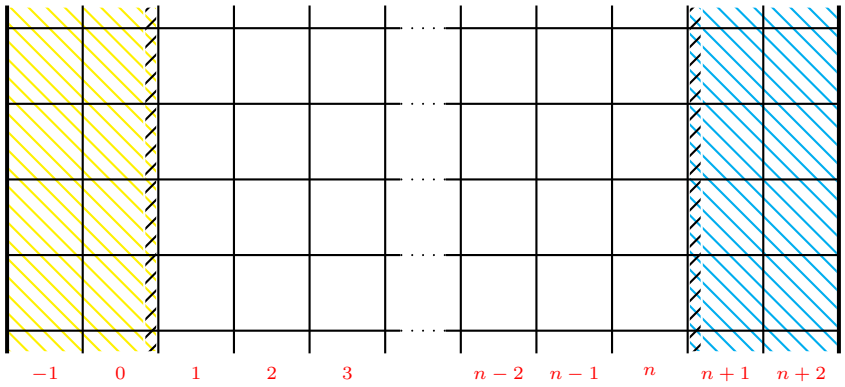

FIGURE 3.1: A 'sketch' of grid boundary cell demarkation

With the left side of the boundary used, all notation presented will be given with respect to the current cell, $n = 0$. Thus, Eq. 3.30 refers to the u velocity on the left boundary, whereby the values for cell 0 are extrapolated from the neighbouring cells, 1 and 2. Cell -1 is then extrapolated in the same way. The matching equation for the right hand side is omitted from this section, but used where the boundary is a right hand boundary. In these cases, the cells referenced change such that the values for cell $n + 1$ are extrapolated from cells i and $n - 1$. That is, for a right hand boundary, values are extrapolated from the left, and vice-versa for a left hand boundary.

3.3.1 Inflow

In the case of the subsonic inflow, one variable must be set to float as one of the characteristics is pointing into the boundary from the computational domain ([84], Fig. 3.3.1). The velocity is chosen, partly for simplicity of calculation, but from a physical point of view, we know that the mass flow into the domain has to be able to adjust to the proper steady state of the domain. Allowing the velocity to float over time makes sense from a physical point of view to this regard. However,

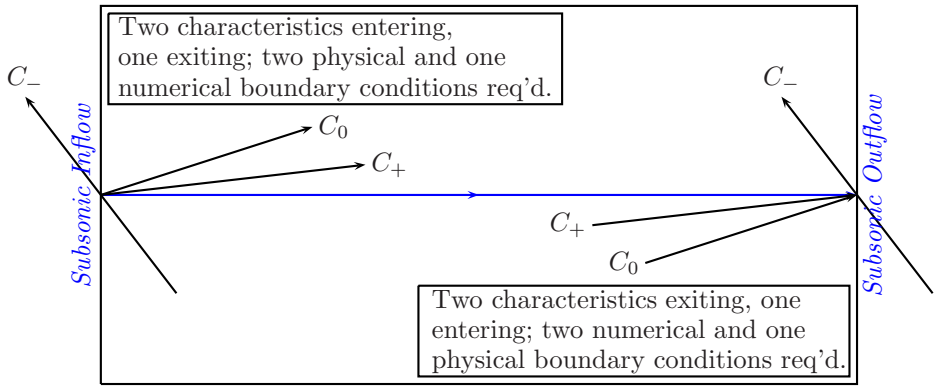

FIGURE 3.2: Boundary conditions for subsonic flow summarised

the magnitude of the velocity changes over time, and thus has to be calculated from information available within the flow-field solution in the internal flow points. This is done through the linear interpolation for the 0th ghost cell on the left boundary as follows

$$u_0 = 2u_1 - u_2 \tag{3.32}$$

Further ghost cells are computed according to the above formula recursively. The right boundary is treated in the same manner. Note that in the first simulation time step, these values must be set to be equal to the initialisation velocity values.

ρ and ρE must be specified such that they are equal to the initialisation values. That is:

$$\rho_1 = \rho_{init} \tag{3.33}$$
$$E_1 = E_{init} = E_\infty \tag{3.34}$$

3.3.2 Outflow

For subsonic outflow, two variables must now be allowed to float at the boundary point. The wave slope for characteristic value C_- is now in a direction moving into the domain. This means that one flow variable has to be specified as a physical boundary condition at this boundary. For the purposes of the simulations run for this thesis, either the outlet Temperature or outlet Pressure could be specified. As the simulations involve solid bodies within 'open domains' that are not of design analogous to a nozzle, the outlet pressure can be set as p_∞.

Thus, for the subsonic outlet, we end with the boundary condition of:

$$u_i = 2u_{i-1} - u_{i-2} \tag{3.35}$$
$$\rho_i = 2\rho_{i-1} - \rho_{i-2} \tag{3.36}$$
$$E_1 = \text{Calculated value based on fixed } P \tag{3.37}$$

3.3.3 Planes of Symmetry

Edges with a boundary condition set as symmetry act in a way that flow properties in only a single direction are reflected across the specified edge of the cell. This essentially mirrors the flow in one direction, resulting in an effect similar to the flow bouncing off of the edge in the single direction (while retaining other flow characteristics) as illustrated in figure 3.3. The direction of flow reversal is in the normal to the boundary edge. Computationally, this is expressed as $\phi = -\phi$ (where ϕ represents the relevant normal velocity, or transport property).

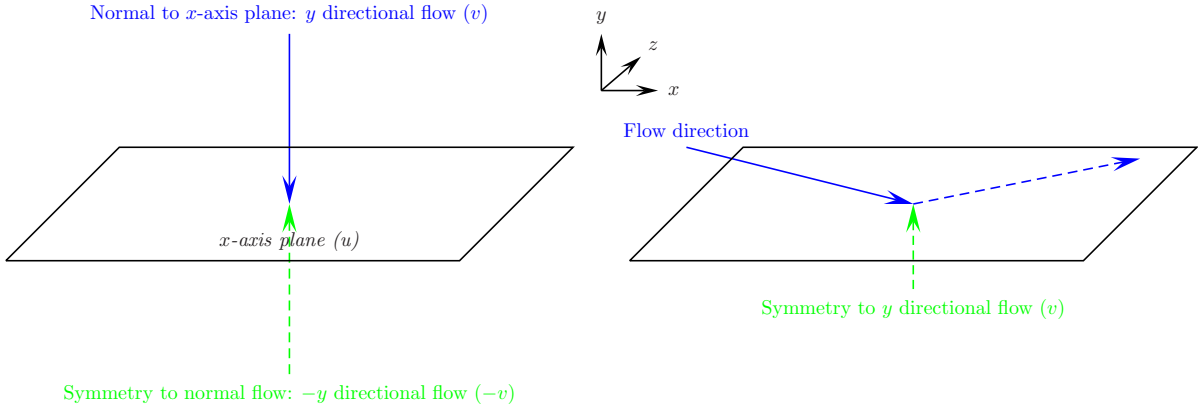

FIGURE 3.3: Illustration of plane symmetry

3.3.4 Inter-block communication and Periodicity

Inter-block communication is used to transfer cell data from one block to the neighbouring block. Neighbouring blocks have to share one face, and thus each cell at the edge of the block has the same co-ordinates on the neighbouring face. These co-ordinates are used to match each cell to one another. This allows the splitting of the CFD problem into a number of smaller blocks that can each be dealt with individually.

Periodicity within the domain takes this inter-block communication a step further (though it is equally applicable to a single block problem). Rather than communicating directly with a cell that shares identical co-ordinates on one face, communication is carried out with a cell that shares only two identical co-ordinates. This is perhaps easiest explained with the use of an illustration, as in figure 3.4.

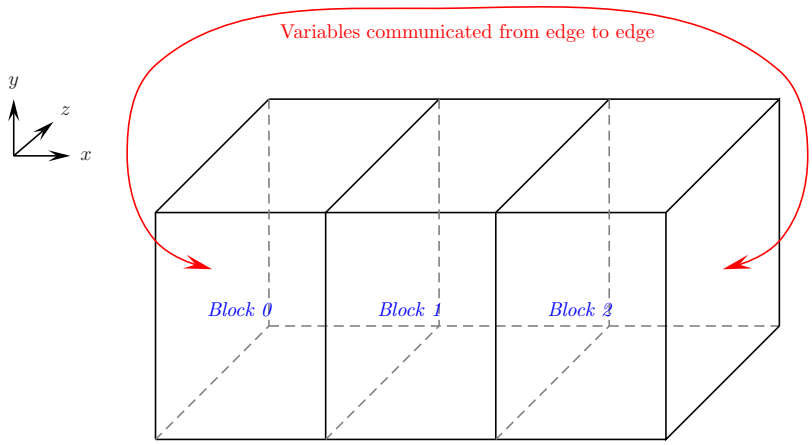

FIGURE 3.4: Illustration of plane periodicity

In figure 3.4, we have periodicity on the two end edges, in the x-direction. Thus, the code will take each individual cell on these edges and examine the other periodic edge to find the cell that has only the same y and z co-ordinates. The code knows which edge to examine for the matching cells as, in the initial set-up, the appropriate edges are pre-defined.

With each corresponding cell identified, the flow data is copied from one periodic edge to the other. In the example shown in figure 3.4, if flow was going out of the domain (in the positive x direction) from the right-most edge, it would 'appear' coming back into the domain on the left-most edge, having the same velocities as well as the same energy and density.

3.3.5 Solid Surface

Edges that are defined as solid surfaces are set up within the CFD code such that the relative fluid velocities are effectively zero at the interface between the surface and the fluid immediately at the surface. This can be done by reversing all of the flow properties on the opposite side of the solid surface (within the ghost cells). In order to do this, the neighbouring ghost cell (essentially a cell within the solid) has these opposing flow properties. This is illustrated in figure 3.5. Density and energy are copied directly to the solid cell from the neighbouring fluid cell.

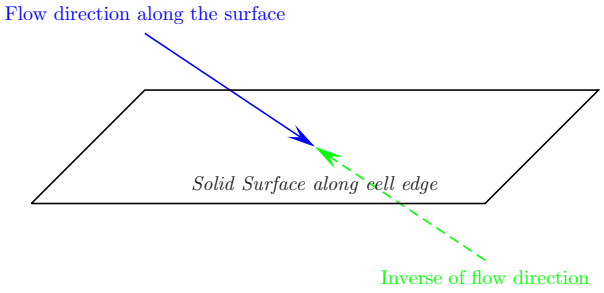

FIGURE 3.5: Illustration of boundary conditions at a solid boundary

This approach corresponds to the discretisation of the no-slip condition

$$u = v = w = 0 \tag{3.38}$$

and pressure derivative condition

$$\frac{\partial P}{\partial n} = 0 \tag{3.39}$$

to at least second order of accuracy.

3.4 Initial Conditions

At the beginning of a computational fluid dynamics simulation, values must be applied to the flow in the overall domain for the calculation to begin. All values input to the simulation are defined relative to a chosen reference system. In the case of this simulation, the reference is the Diameter of the cylinder, which is essentially taken to be $D = 1$. The simulation then works from these initialisation values towards a final computed solution.

The initial conditions replicated dry air at standard atmospheric conditions, at a temperature of $293K$. This gave a free-stream pressure of $100,000 Nm^{-2}$ and an air density of $1.204 kg.m^{-3}$ [69]. As the flows are all subsonic, low speed flows, a Mach number of 0.2 was chosen. This value was chosen such that it not only represents a low speed, subsonic, flow, but sets the simulations as being within the incompressible regime (for which Mach number, M must be less than 0.3). This subsequently allows the air density to be non-dimensionalised as a value of 1 for the free-stream flow.

Based on the initialisation values, the energy for each cell is computed individually during the initialisation process as:

$$E\left(t=0\right) = \frac{P_\infty}{\left(R_\infty \times Q_\infty\right)^2 \times \left(G_\infty - 1\right)} + 0.5 \times \left(u*^2 + v*^2 + w*^2\right)$$

More details on the non-dimensionalisation of the initial values is given in the appendix chapter A.

Variable	Dimensional	Non-Dimensional
Reference Length	Cylinder Diameter, D	1
Mach Number, M	0.2	0.2
Reference Velocity Q_∞	$68ms^{-1}$	1
$u\,(t=0)$	Q_{ref}	1
$v\,(t=0)$	0	0
$w\,(t=0)$	0	0
Density, $\rho_{free}\,(t=0)$	$1.204kg.m^{-3}$	1
Gamma, γ_∞	1.4	1.4
Reynolds number	*n/a*	Case Dependent

TABLE 3.1: Cylinder Flow Initialisation Parameters

4

Simulation Methodology

First you guess. Don't laugh, this is the most important step. Then you compute the consequences. Compare the consequences to experience. If it disagrees with experience, the guess is wrong. In that simple statement is the key to science. It doesn't matter how beautiful your guess is or how smart you are or what your name is. If it disagrees with experience, it's wrong. That's all there is to it. ***Richard Feynman (1918 - 1988)***

* * * * *

The examination of literature led to a plan to examine flow around a circular cylinder within a set domain. The chosen flow configuration consists of a three-dimensional cylinder with Diameter D within a rectangular domain (thus giving a H-type mesh). All domain dimensions are non-dimensionalised based on the cylinder diameter. Thus the width of the domain (x axis) is $45D$ with extents from $-15D$ to $30D$. The height of the domain (y axis) is $30D$ with the cylinder at the centre height. The spanwise depth (in $3D$) of the domain (z axis) is $4D$ - a depth shown by Breuer [85] to be sufficient and not affect the end result due to aspect ratio effects (for more information on the differences between a two-dimensional and three-dimensional simulation, refer also to section 1.3.3). However, at Reynolds number 200, spikes in the shear stresses around the cylinder affected flow. Due to the wavelength of these spikes being greater than $4D$ in the spanwise direction, for Reynolds number 200 the depth was increased.

The simulation is illustrated in figure 4.1. Experimentation with Boundary Conditions had to be carried out, due to some initial uncertainty that affected results, though ultimately in the upstream, streamwise direction a subsonic inflow BC was used, while downstream had a subsonic outflow BC. In the spanwise directions, periodic boundary conditions were used and for the vertical directions symmetric boundary conditions were used.

4.1 Meshing

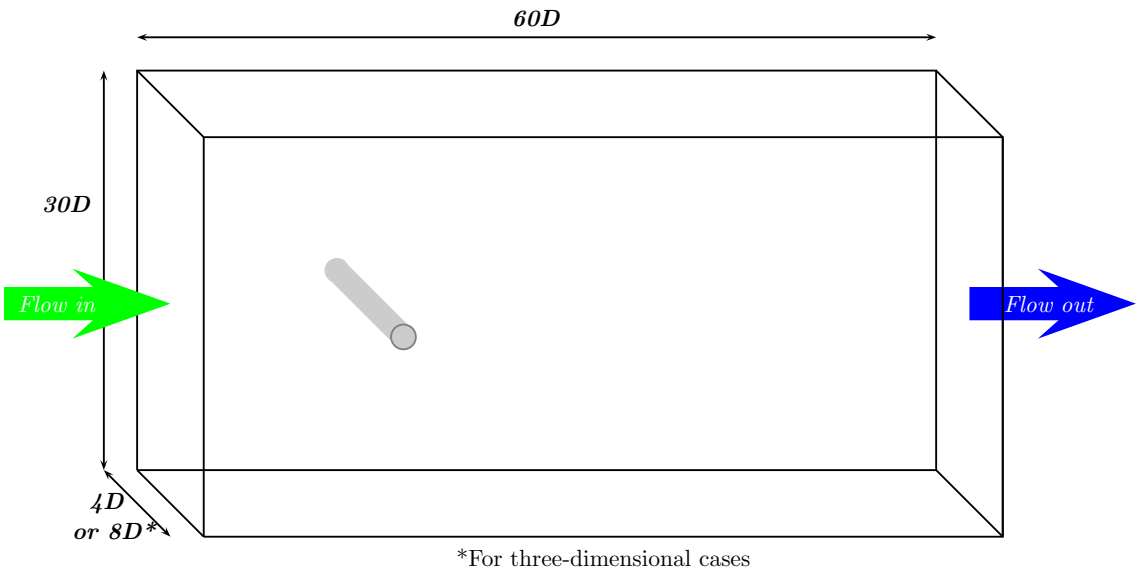

FIGURE 4.1: A sketch of the design for the simulation

The first stage in setting up a computational fluid dynamics simulation involves the definition of the computational domain within which calculations are to be carried out. This domain is the grid that is used for the simulation encompassing both the region of flow of interest, as well as any objects and unusual wall layouts within that flow. As this is an external flow type of problem, with interest primarily in the wake region of the cylinder (particularly with the vortical flow expected to form behind the cylinder), attention must be paid to the distance of the domain boundaries from the location of the cylinder within the domain. By not prescribing a large enough distance between cylinder and the upper and lower boundaries, we could find the boundary effects of the top and bottom influence the flow passing around the cylinder. Equally, the width of the domain has to be limited to a reasonable size in order to maintain computational accuracy and cost.

Meshes were created in Gridgen, a commercial package created by Pointwise, the use of which was learnt through the course of this PhD. As this is a commercial program with its own user manual, going into specific details about its usage would be superfluous to this thesis. However, at the later stage of this project, it could be used for output to the group code thanks to

the work of two other members of the group who had developed a translator program from the standard Flow3D output of gridgen to a series of grid files usable by the CNS3D code ([86] and [87]).

CFD is a computationally intensive task, with simulations (particularly of 3-dimensional flows) requiring a huge amount of processing power, and a significant amount of processing time. As with everything, there is a cost to this computing use - access to the computing facility and power usage for example. Thus, where possible, methods are developed to either make computations more efficient (produce results as good as other methods while having a lower computing requirement) or to reduce the time spent using the computational resources.

One such technique used to reduce the time used on computing facilities is to reduce a large problem into a number of smaller blocks - decomposing the overall domain. It should be noted that this does not necessarily reduce the actual time the computers are used for. An analogue would be a labour-intensive building job requiring 20 man hours. Rather than one man spending 20 hours on that job, 10 men could each spend two hours completing the same job. The same principle applies to the use of multi-block domains in CFD. Your job may still require 20 hours of processor time, but split across 10 processors the time taken for the job is actually only two hours.

In order to do this, when at the grid generation (pre-processing) stage, the domain (overall computational grid) is split into a pre-chosen number of smaller sub-grids. Each of these sub-grids is then assigned to its own separate processor. The governing equations and the problem within each sub-grid can be applied in a parallel process across the specified number of computing processors as a number of smaller problems. The sub-grids are referred to commonly (and from here on in this thesis) as blocks. This represents the computational blocks that are computed separately on each processor.

The sizing of each block is chosen based on the number of blocks as well as an attempt to evenly match the expected work-load across the blocks. The choice of the number of blocks is usually based on a compromise between the available number of processors and the complexity of the problem being simulated. This also allows problems that would be computationally (i.e. in terms of memory requirements) too large for a single processor to still be possible.

As discussed in the examination of the derivation of the governing equations, each cell requires data from its neighbour at each iteration in order to balance its own variables. Likewise, each block requires data from its neighbouring blocks at each iteration in order to calculated its own values. In order to do this, a method of MPI (Message Passing Interface) is implemented in the CFD code allowing data exchange between blocks [88]. Data from one block is overlapped into the adjoining block as ghost cells in the adjoining block. These ghost cells are then treated as a separate form of boundary condition on the block, allowing cell-to-cell data swap between blocks (see also section 3.3.4 for a brief discussion of the boundary condition). However, the MPI process allows more than just data swap between processors. There is also a modicum of control from one processor to the next. Returning briefly to the analogy of the builders used earlier: one person overlooks the project to ensure work is carried out in the correct order, so it is with MPI, that one processor generally carries out some of the more mundane, single-run, processes and each processor waits for all the others to reach programmed points in the code before continuing.

These techniques all allow a very versatile use of a domain split into multiple blocks.

Grid Resolution	$x \times y$ cells	z cells
Low	64×64	16
Medium	165×165	32
High	325×325	64

TABLE 4.1: Grid resolutions

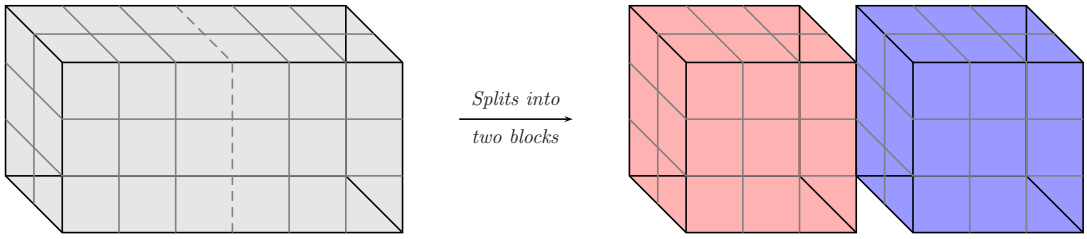

FIGURE 4.2: Illustration of the splitting of a domain into multiple blocks

Initially, an O-mesh style domain was set up to carry out the simulation. This domain style was chosen as it was an identical set up to that given in literature, such as Breuer [89] for a high-Reynolds number case. However, some computational problems (in particular with boundary conditions) arose with this setup, leading to a change to a H-type grid. Additionally, it was felt the H-type mesh would test the implicit CFD code harder than the O-type grid, as the cells would have greater skewing close to the cylinder surface. Thus, the domain shown in figure 4.1 was defined as a suitable final set up for this problem. A schematic of the decomposition of H-mesh into blocks is shown in figure 4.3. The same pattern was repeated in slices in z-direction to generate additional blocks. An illustration of the mesh in x-y plane is presented in figure 4.1. An eight block grid was used for the two-dimensional runs in order to exploit the computing cluster cores which are allocated in groups of four cores. For the three-dimensional cases, this was extended to 40 blocks - having five blocks each in the spanwise direction to exploit the computing facilities as much as possible.

A range of grid resolutions were considered based on grids used in literature. Table 4.1 states the different grid resolutions used for the $2D$ cases, where a single cell in z was specified. The number of cells tested in the z direction for the $3D$ cases is also shown in table 4.1. The tests of optimum grid resolution were carried out at Reynolds number 40 and 300, for both first-order runs and the second-order Van Leer high-order scheme. The low order schemes were selected for the convergence tests as these should exhibit slowest grid convergence. Figure 4.1 shows the comparison of the values of Coefficient of Drag and Strouhal number for the different grid resolutions for Reynolds number 300 with the second-order scheme.

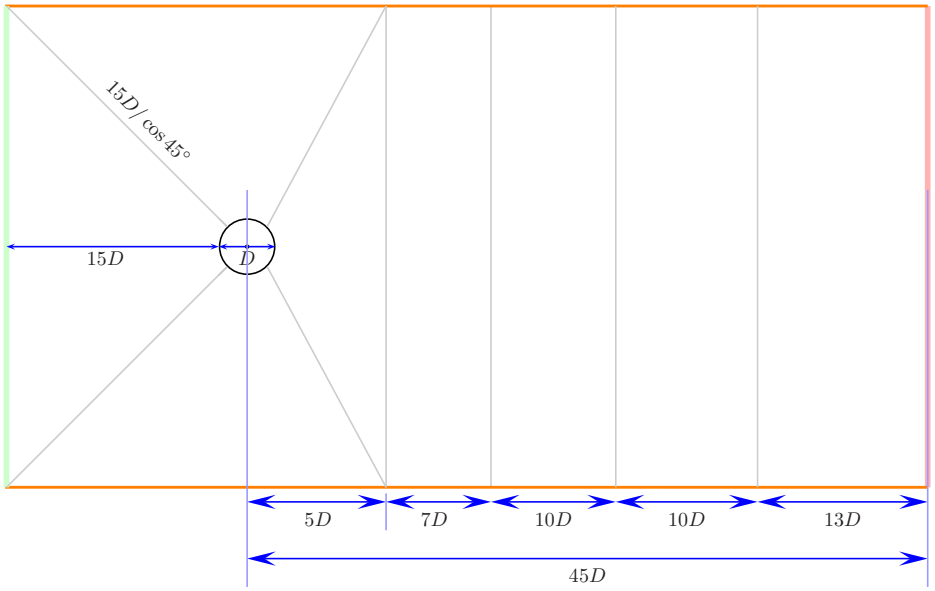

FIGURE 4.3: Schematic of the H-Mesh layout

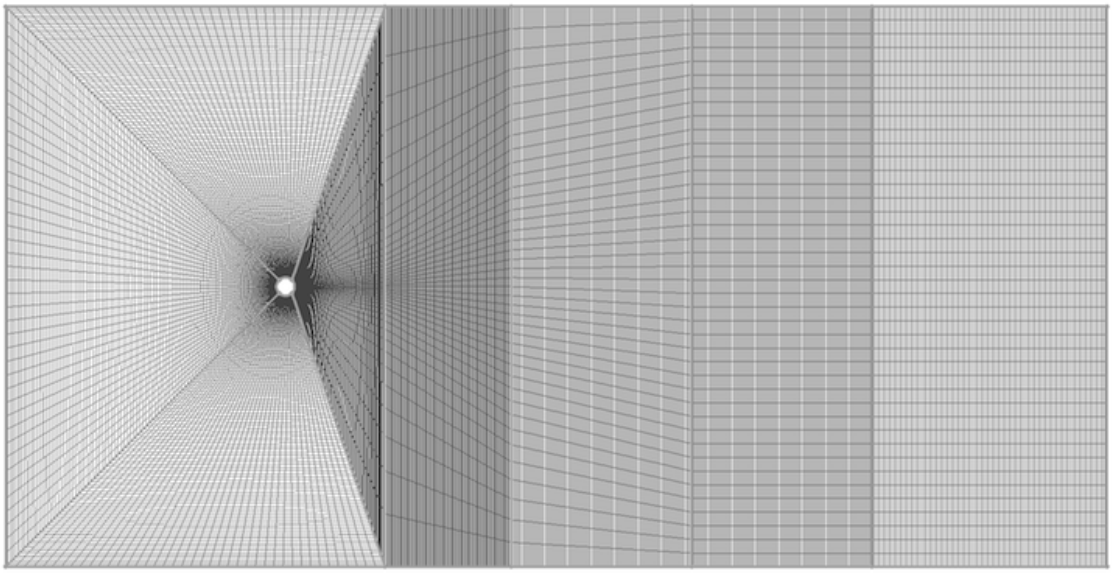

FIGURE 4.4: Grid details showing an overview of the H-Mesh Grid

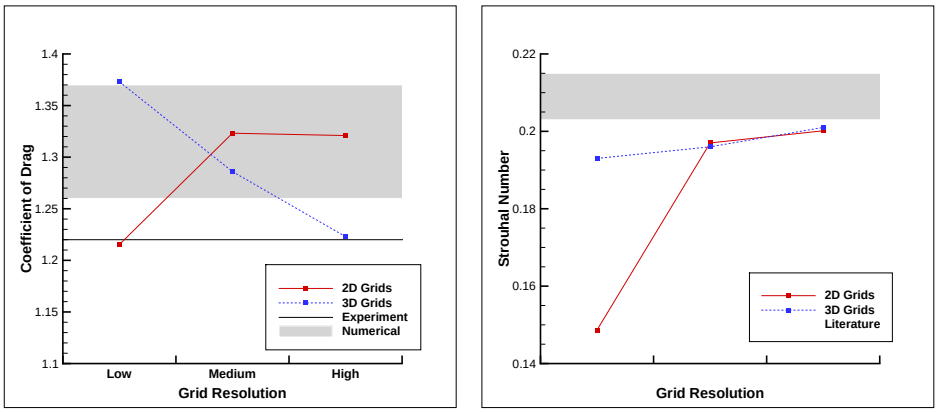

(a) Coefficient of drag (b) Strouhal Number

FIGURE 4.5: A comparison of averaged values for different grid resolutions in $2D$ and $3D$, for the second-order Van Leer simulation at $Re = 300$. The range of values given in literature is represented by the shaded regions.

On each grid used, the boundary layer was resolved by the use of fine grids in the near-wall region (near to the cylinder surface), with the first cell being smaller in size than the expected size of the established boundary layer. The boundary layer is generally fairly thin for laminar flow, with an estimate for the laminar boundary layer thickness being $\delta \approx 1/\sqrt{Re}$ (as stated in equation 1.8), as appropriate for the low Reynolds number flows considered. The assumed boundary layer thicknesses for the different Reynolds numbers is given in table 4.2. A minimum of 10 cells were desired within the boundary layer, and thus the smallest cell sized used was an order of magnitude lower than the assumed boundary layer thickness. Furthermore, the smallest cell sizes were fixed for the 10 cells closest to the cylinder surface, with cell sizes increasing beyond that. Grid clustering was applied, with the cells closest to the cylinder surface having the specified δy. The initial ten cells from the cylinder surface also had a size constrained by the minimum cell size, δy. Beyond that, the cell size was increased as the distance from the cylinder increased, with a function based on the hyperbolic tangent function. The hyperbolic tangent function is the main distribution function available within the grid software Gridgen [90], which is based on one-dimensional stretching functions [91].

The distribution scheme functions such that between two unconstrained points on an edge, grid points are distributed uniformly using a simple uniform interpolation scheme. With spacing unconstrained at only one end, an alternative one-sided hyperbolic tangent distribution function is used, which skews distribution of cell edges towards a chosen block edge.

Furthermore, the grid clustering was designed in all three dimensions such that, where possible, any points where data was to be output (i.e. the marker points in the flow) would be taken at a cell centre, rather than on a cell edge. As the values are calculated at the centre of each cell, this would provide data extraction points as close to required co-ordinates as possible.

As with the grid independence and dimensionality studies, test simulations were run at

Reynolds number 40 and 300 for three different smallest cell sizes ($0.010D$, $0.001D$ and $0.0001D$) to determine the optimal choice of smallest cell sizing for the different flow regimes. A smallest cell size of $0.010D$ was found to provide a good balance between simulation time and results compared to literature, while the size $0.001D$ was found to be suitable for the remaining Reynolds number simulations.

The lower Reynolds numbers runs were shown in the literature to be two-dimensional in nature, as described in section 1.3.3. However, for Reynolds number 200 and above, a three-dimensional numerical simulation should give improved results due to $3D$ instabilities, and spanwise shear stresses [60]. In addition, due to the transient phase of the flow at $Re = 200$, that flow requires a longer spanwise depth. Therefore, for flows of $Re = 200$ and above, three-dimensional simulations were run in addition to the two-dimensional simulations, with spanwise depth at $Re = 200$ being $8D$ and spanwise depth at the remaining reynolds number runs being $4D$; a depth greater than πD, which is large enough to sufficiently predict force components and $3D$ instabilities.

4.2 Post-processing

A variety of techniques were devised and programmed into the code in order to output a number of data from the simulations that were run. An overview of the techniques used to accurately carry out a comparison of simulation data with literature data is given in this section.

4.2.1 Flow Field Output

Implementation of the CFD General Notation System (CGNS, [92]) was done in the CNS3D code to facilitate postprocessing. It is an output file format devised for the general and portable storage of CFD analysis data. It is an open-source format that is self-descriptive, well documented, and administered by an international steering committee that was conceived in 1994. Updates to the standard have constantly been made as required, with the most recent version being released in August 2009.

One of the principle motivations of the CGNS file format was to help stabilise the archiving of any aerodynamic data available, and thus the ability to share this data as required. The system is compact, stored in binary format, platform independent and relatively easy to implement in a number of different languages. To aid in this procedure, guides exist in multiple forms, such

Reynolds Number	$\delta \approx 1/\sqrt{Re}$	Smallest Cell Size used
40	0.1581	$0.010D$
200	0.0707	$0.001D$
300	0.0577	$0.001D$
3900	0.0160	$0.001D$

TABLE 4.2: Smallest cell sizes on cylinder wall at the various Reynolds numbers

as Fortran examples in the Open Source community that demonstrate the usage of all CGNS functionality.

The CGNS data files can store a great number of flow data, for either structured, unstructured or hybrid grids. The data files as used in the simulations carried out for this thesis were formatted to hold flow Momentum data, pressure, energy, and coefficient of pressure - amongst other flow data added or removed as required.

The CGNS data files could then be loaded with the Commercial Software package Tecplot in order for closer analysis of either individual points in the flow, or the overall flow domain, to determine final results, or just to determine whether a simulation was behaving as expected. Developing macro files for Tecplot allowed further manipulation of the data, such as extracting data at specific points - or along polylines - over a specified time period of the simulation run. However, due to the size of CGNS files compared to the point marker files, (i.e. significantly larger due to containing entire flow field data) the time interval of CGNS output was set to be much less than the marker file data.

4.2.2 Wake Data Acquisition

As marker points could be placed very precisely in the flow, it is this method that is chosen as preferable to output data for graphing purposes. The specified marker points in the flow were supplemented with data output for grid points around the cylinder surface for the cylinder cases. Importantly, all data output was output as the cell centre data, as opposed to nodal data. Points were chosen in the flow at which the flow data could be output. Some of the data was obtained from the cylinder surface, while other data came from marker points in the domain, away from the cylinder. Marker positioning was generally chosen based on values used in the literature, (i.e. [45, 62, 89, 93, 94]) however two extra points were added further down-stream for the y-plane marker points to allow for additional wake data. The marker points chosen along the $x - axis$ were:
$x/D = [0.58, 1.00, 1.06, 1.20, 1.50, 1.54, 2.00, 2.02, 2.50, 3.00, 4.00, 5.00, 6.00, 7.00, 10.00]$

These marker points were output for heights ranging as $-10 \leqslant y/D \leqslant 10$. In addition, data was output along the symmetry line ($y/D = 0$) along the length of the domain, though the chief area of interest was the region directly aft of the cylinder. An illustration of the marker positioning in the grid is shown in figure 4.6.

Some papers examining flow over a cylinder using numerical techniques averaged their marker data across the entire spanwise (z) direction. This was carried out for the simulations for this thesis as well as extracting the data from points with specific co-ordinates in all three dimensions. However, it was found that the difference in the time averaged data in the symmetry plane time/span averaged data is negligible.

Velocities and Reynolds stresses were acquired at the marker points distributed along lines as shown in figure 4.6.

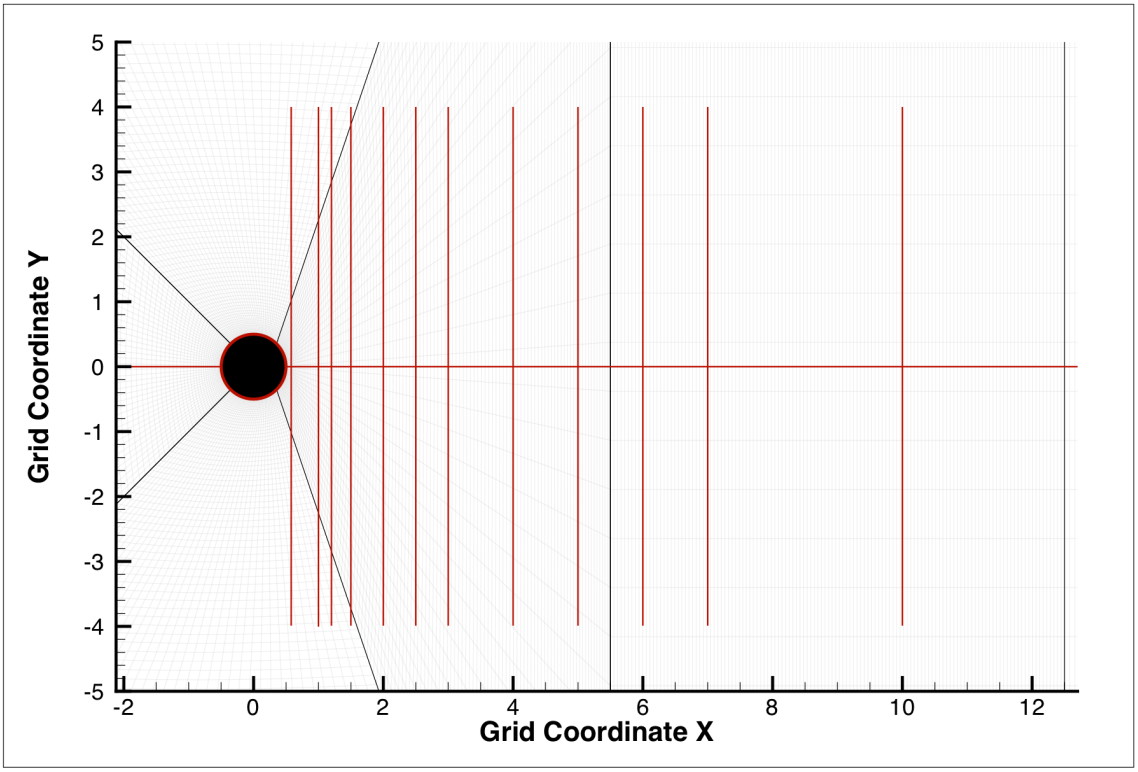

FIGURE 4.6: Marker positioning in the grid, with red lines indicating the positioning of Marker points. Some lines omitted (where they would be very close to others) to aid clarity. In addition, vertical output lines (i.e. those along the x/D region) extend as $-10 \leqslant y \leqslant +10$, though they are shown only as $-4 \leqslant y \leqslant +4$.

4.2.3 Cylinder Surface Data Aquisition

Along with the marker data, further data was extracted around the surface of the cylinder. This was set up such that every cell on the cylinder surface reported the required values. A range of pressure, shear stress and velocity values were output. All of these were combined externally using a separately written post-processing application (designed to carry out appropriate time-averaging of data) such that the following overall data could be determined:

- Coefficient of Pressure, C_p
- Coefficient of Lift, C_l
- Coefficient of Drag, C_d
- Coefficient of Friction, C_f
- Flow Separation Angle, θ_{sep}
- Strouhal Number, St

Computation of each measurement is briefly discussed below. Analytical testing of C_p, C_l and C_d was carried out to validate the implementation of postprocessing. By using known arbitrary input values for each cell around the cylinder surface, and integrating these values numerically outside the main code, the values output by the code could be compared to confirm calculation of the coefficient values. Asymmetric values were input around the cylinder surface such that any agreement between input and output values were not due to the symmetry of the geometry. It was found that the differences between coefficient values were so low they could be attributed to machine numerical error.

Further, forces acting on the cylinder curface were computed. The lift force component is normal to the airflow, while the drag force component is parallel to the direction of airflow. From these force components, we can determine the non-dimensional coefficients required. A simplified form of determining a non-dimensional force coefficient can be expressed as:

$$C_F = \frac{F}{\left(\frac{1}{2}\rho V^2\right)_\infty A_{ref}} \tag{4.1}$$

F is the force we are seeking the non-dimensional form of; being either the lift or drag component. V is the net velocity experienced by the object, ρ is the density of the fluid and A_{ref} refers to the specified reference area.

Coefficient of drag is split into two components: a pressure component and a viscous component. These are added as [48, 93]:

$$C_d = C_{d_p} + C_{d_v} \tag{4.2}$$

The pressure drag is defined as:

$$C_{d_p} = \frac{1}{\frac{1}{2}\rho V_\infty^2 D} \int_0^{2\pi} P_\theta \cos(\theta) d\theta \tag{4.3}$$

and the viscous drag is defined as:

$$C_{d_v} = \frac{1}{\frac{1}{2} Re_D V_\infty} \int_0^{2\pi} \tau_{wall} \sin(\theta) d\theta \tag{4.4}$$

where θ is the local angle in the polar coordinate system. The total drag is computed around the cylinder and output per time-step. These values are then averaged against time for the period of interest.

As with the coefficient of drag, the coefficient of lift can be calculated around the boundary of the cylinder using the following calculation:

$$C_l = C_{l_p} + C_{l_v} \tag{4.5}$$

The pressure lift is defined as:

$$C_{l_p} = \frac{1}{\frac{1}{2}\rho V_\infty^2 D} \int_0^{2\pi} P_\theta \sin(\theta) d\theta \tag{4.6}$$

The viscous lift is defined as:

$$C_{l_v} = \frac{1}{\frac{1}{2}Re_D V_\infty} \int_0^{2\pi} \tau_{wall} \cos(\theta) d\theta \tag{4.7}$$

Again, the total lift is computed around the cylinder and output per time-step. These values are then averaged against time for the period of interest.

From the experimental cylinder tests run by Achenbach, [63] the dimensionless term for the experimental skin friction was given as:

$$C_f = \frac{\tau_\omega}{\rho U_\infty^2} \sqrt{Re}$$

where τ_ω is the wall-shear stress.

The angle at which flow separates from the circular cylinder was determined in the post-processing phase. By examining the skin friction around the circumference of the cylinder, the separation point could be determined. The point is defined as being the point around the cylinder at which the skin friction is equal to zero leading to

$$\left(\frac{\partial u_{||}}{\partial n}\right)_w = 0 \tag{4.8}$$

where $u_{||}$ is the component of velocity tangential to the wall, n is the normal and w indicates that the derivative is evaluated at the wall. The above was discretised using 1st order difference formula.

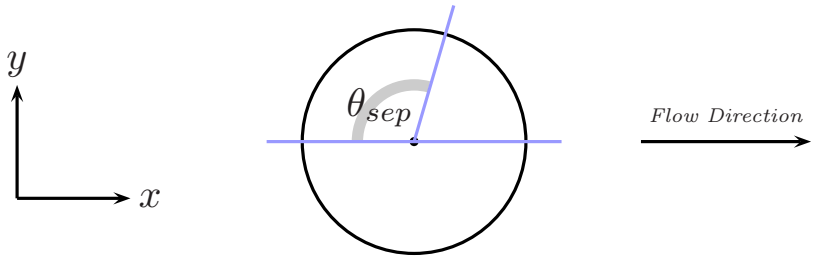

FIGURE 4.7: Defining the direction of the separation angle

Further, the coefficient of pressure was recorded:

$$C_p = \frac{p - p_\infty}{\left(\frac{1}{2}\rho V^2\right)_\infty} \tag{4.9}$$

as well as the base pressure coefficient, reported in some studies used for comparison of the results

$$C_{p_b} = \frac{p_b - p_\infty}{\left(\frac{1}{2}\rho V^2\right)_\infty} \tag{4.10}$$

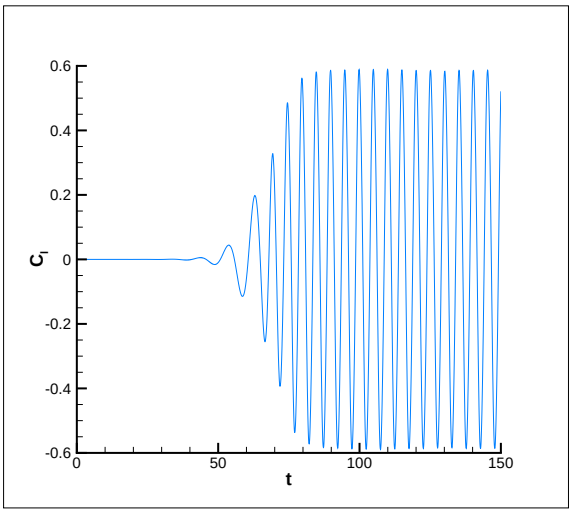

FIGURE 4.8: Reynolds Number 300, 2^{nd} order Van Leer run, showing development of Coefficient of lift over time, giving $St = 0.197$

4.2.4 Strouhal Number

In order to measure the Strouhal number, additional markers were to be placed in the flow, replicating the effect of probes in a windtunnel. It was found that, for most cases of Reynolds numbers to be used in this thesis, (as demonstrated in [95]) positioning a marker at 8 and 23 diameters downstream of the cylinder would be sufficient to determine and confirm the Strouhal number of the flow. These marker points would be placed slightly offset from the line of symmetry to allow influence mostly from the vortices on one side of the Karman Street. Through experimentation, it was found the Strouhal number could more easily be measured numerically using actual flow time output from the simulations, against the overall coefficient of lift. Thus the development of C_l was plotted against time, giving the frequency of vortices formation illustrated in figure 4.8. The actual value was recovered with an additional postprocessing subroutine measuring the distance between peaks in the lift coefficient.

4.2.5 Time Averaging

All the parameters output from the flow were time-averaged against the period of interest. For a flow variable, ϕ, this is defined as:

$$\overline{\phi_t} = \frac{\sum_{i+1}^{n} \phi_i \Delta t}{\sum_{i}^{n} \Delta t} \tag{4.11}$$

Initially the solution was computed and the lift coefficient was monitored for periodicity in order to exclude transient behaviour from the averaging process. It should be noted that whereas

for 2D cases, all simulations were run from cold start initialisation, the 3D simulations were initialised from 2D developed flow runs to speed up the process.

Once past the initial transients as confirmed by visual monitoring of the lift coefficient, the computations were restarted to assemble time-averaged data. The time averaging was performed until the mean value of the lift coefficient has settled to within 10%, which corresponded to at least 30 cycles of the lift coefficient. The same time window was used to average the data acquired on the surface of the cylinder (pressure coefficient, friction coefficient and separation angle) and in the wake (velocity distributions, fluctuations and Reynolds stresses).

4.3 Overview of Simulated Cases

Given all the information about how the computational method was developed, a series of simulation runs were planned. An overview of the simulations run is given in table 4.3.

Reynolds Number	2D / 3D	Order[1]							Grid Resolution[2]			Smallest Cell Size[3]		
		1	2-MM	2-VL	3-KK	5-KK	W5	W9	Low	Med	High	10^{-2}	10^{-3}	10^{-4}
47	$2D^4$	◇		◇					◇	◇		◇	◇	
	$2D$	●	●	●	●	●	●	●	●			●		
200	$2D$	●	●	●	●	●	●	●		●			●	
	$3D$			●		●	●			●			●	
300	$2D^4$	◇		◇			◇		◇	◇	◇	◇	◇	
	$2D$	●	●	●	●	●	●	●		●			●	
	$3D^4$			◇			◇		◇	◇		◇	◇	
	$3D$			●		●	●			●			●	
3,900	$2D$	●	●	●	●	●	●	●		●			●	
	$3D$			●		●	●			●			●	

TABLE 4.3: An overview of the simulations of the cylinder case that were run. The simulations marked with ◇ indicate the test simulations[4].

[1] 1: First Order, 2-MM: 2nd Order Min-Mod, 2-VL: 2nd Order Van Leer, 3-KK: 3rd Order Kim-Kim, 5-KK: 5th Order Kim-Kim, W5: WENO 5th Order, W9: WENO 9th Order

[2] Grid resolutions as well as clustering information is given in section 4.1.

[3] The smallest cell was the cell lying on the cylinder surface. The size denotes the height of the cell, δy, compared to the cylinder diameter. The sizing of the smallest cell is discussed in section 4.1.

[4] Reynolds numbers 47 and 300 were used as a test for all the computational procedures, as well as grid independence, and are detailed in the marked rows.

4.4 Computer Information

The simulations were chiefly carried out on one of three grid cluster computers available to the students at Cranfield University. This grid computer is named "Astral". It is a grid computer made up of over 800 processor cores from 200 compute nodes available. The compute nodes are HP DL140 G3 servers, each with two Intel "Woodcrest" 5160 Xeon, dual-core processors running at 3GHz. In addition, each node has 8GB of shared memory between the 4-cores. Each dual-core processor has a shared 4MB L2 cache, and runs at $1333MHz$ at the front-side bus. This processor family supports Intel 64 (using Intel's x86-64 implementation) allowing the use of 64-bit option switches when compiling applications to be run on it.

For the use of the Fortran software compilation, the Intel Fortran compiler is installed on Astral. This has evolved through the different versions from Intel 9.1 Fortran compiler through to Intel 11.1 Fortran compiler during the course of this project.

5

2D Simulation Results

Results! Why, man, I have gotten a lot of results. I know several thousand things that won't work. ***Thomas Edison (1847 - 1931)***

* * * * *

5.1 Chapter description

This results chapter contains the results from the cylinder in the two-dimensional flow runs. The results are broken up according to Reynolds numbers due to the differences in flow characteristics present in the flow as the flow speed increases. These characteristics change significantly as the Reynolds number changes; at the higher Reynolds numbers, the effects of two-dimensionality and the accompanying inability to correct simulate turbulence become evident. The simulations were run in two-dimensions in order to allow a determination of the capability of higher-order methods without the third-dimension present prior to moving on to three-dimensional simulations (the two-dimensional simulations can be run significantly quicker, allowing a greater number of simulations). Furthermore, the laminar flow of $Re = 40$ can be resolved sufficiently in a two-dimensional simulation, while the runs at $Re = 200$ are expected to provide results satisfactorily close to experimentation due to this flow speed being just above the critical Reynolds number where three-dimensional effects begin to influence the flow.

The Reynolds numbers whose results are presented in this section are as follows (with section numbers given in brackets):

- Reynolds Number = 40 (5.2)
- Reynolds Number = 200 (5.3)
- Reynolds Number = 300 (5.4)
- Reynolds Number = 3900 (5.5)

The range of Reynolds numbers chosen for the $2D$ simulations allows an examination of flow features from laminar, steady flow ($Re = 40$), through a critical transitional flow phase ($Re = 200$), on to fully turbulent unsteady flow ($Re = 3900$).

5.2 Reynolds Number = 40

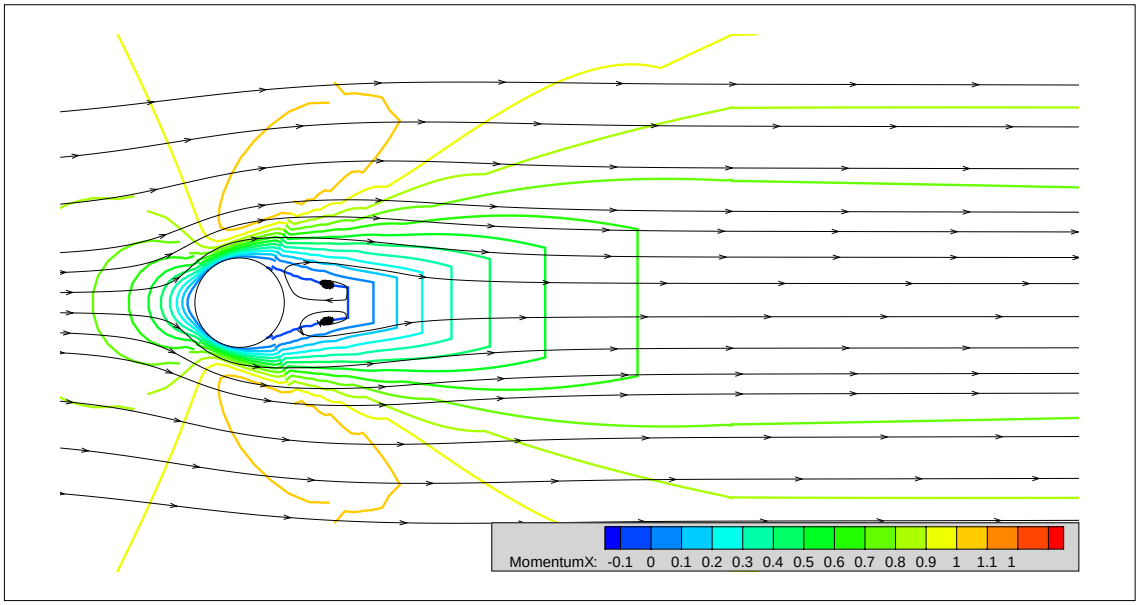

FIGURE 5.1: Time averaged plot of Reynolds number 40 $2D$ flow, 5^{th} Order WENO scheme

The flow around the circular cylinder at $Re = 40$ is the first flow to be computed, as it allows a study of several parameters that are present in laminar flow. Due to the laminar nature of this flow, comparison with experiments and simulations should be consistent and reliable. At this low flow speed, no wake oscillations are present, and vortical flow in the wake is low in size. Figure 5.2 shows a time-averaged overview of the flow at Reynolds 40, as computed with the 5^{th} Order WENO scheme (similar plots for all the numerical schemes are presented in Appendix B). The

time-averaged flow field is almost identical across the different numerical schemes, only with a differing wake length. The first-order scheme shows the weak vortical flow, but with the smallest wake of all the schemes.

The flow at this flow speed has characteristics whereby the flow remains attached to the cylinder for a large portion of the circumference of the cylinder. Separation of flow to the wake occurs quite far to the rear of the cylinder. There is only a single separation point, with acceleration of the flow not being strong enough for a reattachment of the flow to occur around the circumference of the cylinder. At the fore of the cylinder is a stagnation point.

Figure 5.2 shows the plots of Coefficient of pressure and Coefficient of drag around the cylinder at Reynolds number 40, for the different numerical schemes. Subfigure 5.2(a) shows good agreement of the coefficient of pressure of the higher-order simulations with literature data available, however, the simulations do appear to under-predict the values slightly, with results closer to the experimental values of $Re = 30$ than the literature values at $Re = 40$. The first-order run, however, does not fully resemble the flow, giving high differences from all of the higher order plots. This corresponds with the coefficient of friction plot in figure 5.2(b), where it is clear the first-order simulation gives markedly different levels of friction to the higher order plots, as well as a later angle of separation. The wake in the first-order run is the weakest (shortest) of all the simulations, and the velocity just upstream of the stagnation point on the cylinder is the lowest in the first-order run. This results in the highest C_p value for the first-order run at the front of the cylinder.

With the exception of the first-order scheme, in a comparison of the different numerical schemes against each other, for both C_p and C_f, it can be seen that results between each are very similar. The second-order Min Mod, under-predicts values around the cylinder slightly more than the other higher-order numerical schemes, but not by a large degree.

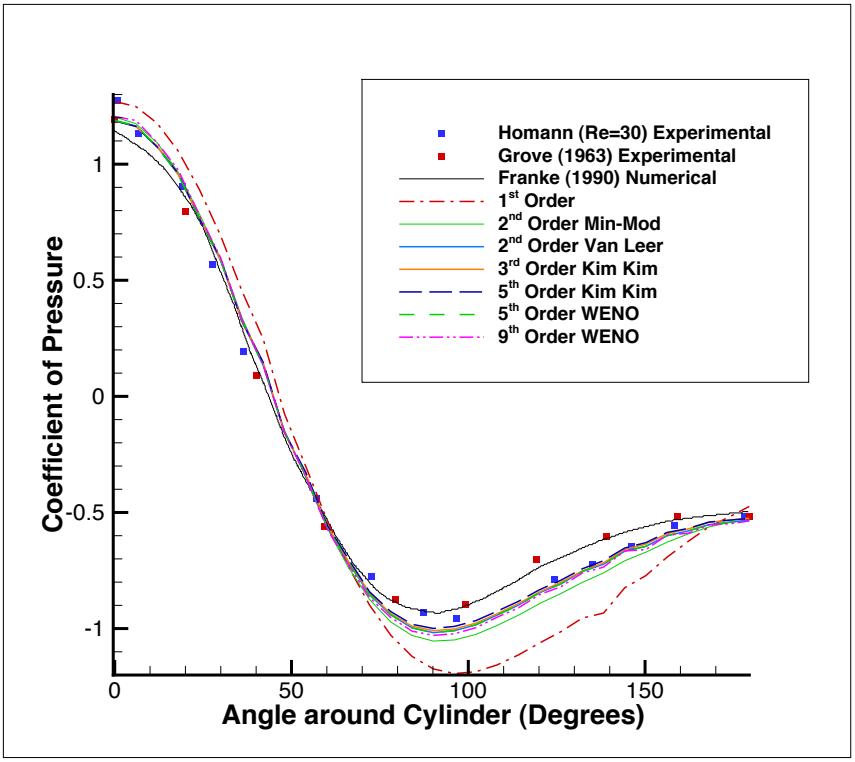

(a)

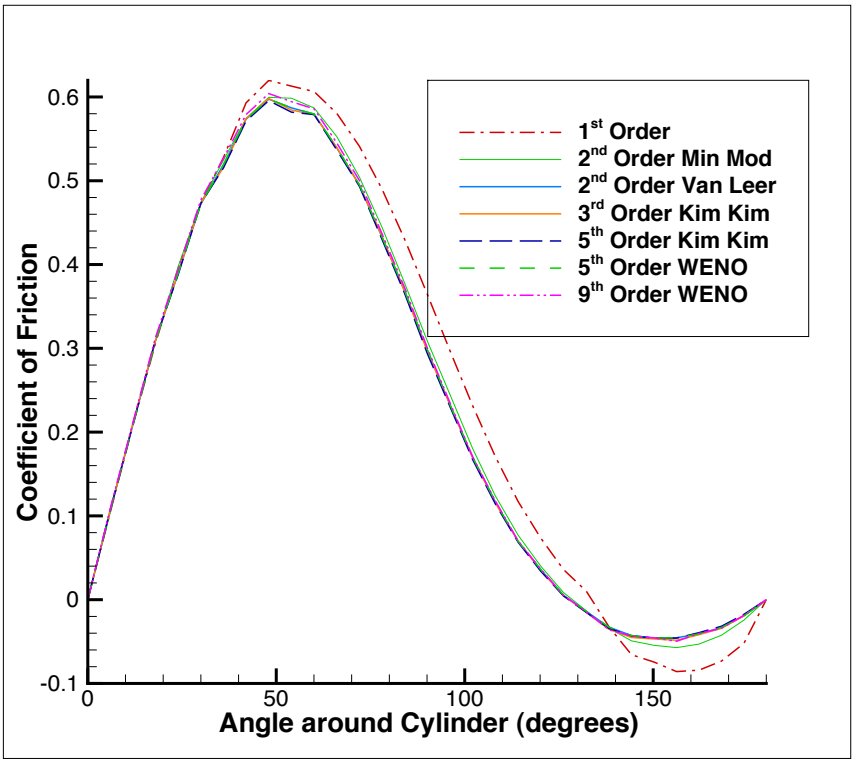

(b)

FIGURE 5.2: Reynolds Number 40, 2*D* flows giving coefficient of pressure 5.2(a) and coefficient of friction 5.2(b) around the cylinder for differing orders of run.

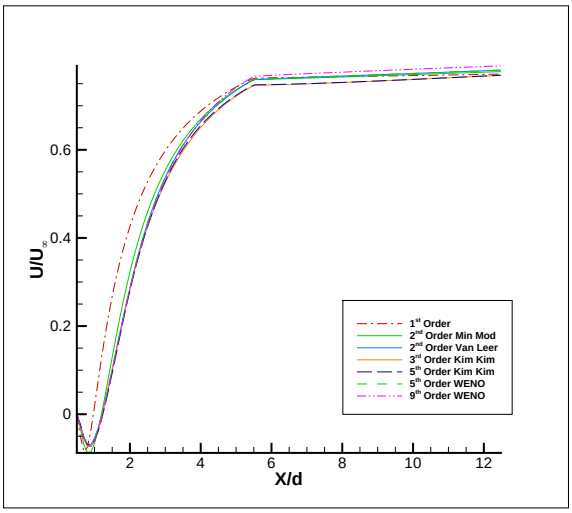

FIGURE 5.3: Time averaged streamwise momentum in the wake at Reynolds number 40

Figures 5.4 and 5.5 show the time-averaged flow values for the different simulations, in the wake of the cylinder. Figure 5.4 shows the flow in the stream-wise direction, while figure 5.5 shows the cross-stream flow - that is, momentum in X and momentum in Y respectively. Each of these figures is split into two, to differentiate between the different numerical schemes. It is quite clear from looking at figure 5.4 that the flow in the x-direction (stream-wise) continues to be affected to the rear of the cylinder quite far down-stream of the cylinder (the figures go as far downstream as $x/D = 6$). The momentum at each point is shown graphically as momentum $(U/U_\infty - 1)$ added to the x/D position in the domain, thereby showing the difference in momentum from freestream flow at each x/D position.

Figure 5.5 shows that the effects of the cylinder on the y-direction of flow dissipate rapidly. By the point $x/D = 6.0$, the variations in cross-stream flow have almost completely disappeared. This is evident in all of the numerical schemes.

The time-averaged flow values along the line of symmetry ($y/D = 0$) to the rear of the cylinder are shown in figure 5.3. The streamwise momentum show clear agreement across the different numerical schemes, once again with the exception of the first-order scheme directly to the rear of the cylinder that has streamwise velocity reduced at the aft of the cylinder in comparison to the higher order schemes.

Due to the laminar nature of the flow, no velocity fluctuations were expected in the wake in either flow direction, regardless of the numerical scheme used. Thus the spectral plot investigation carried out at higher Reynolds number wasn't considered an important contributory factor at this Reynolds number and isn't considered.

Table 5.1 shows a comparison of numerical values from the Reynolds number 40 simulations compared to literature values. Values for Coefficient of lift were determined to be zero for the simulations, agreeing with values found in the literature, as well as the expected lift for this Reynolds number. A similar situation exists for the Strouhal number; in [105], no Strouhal number was

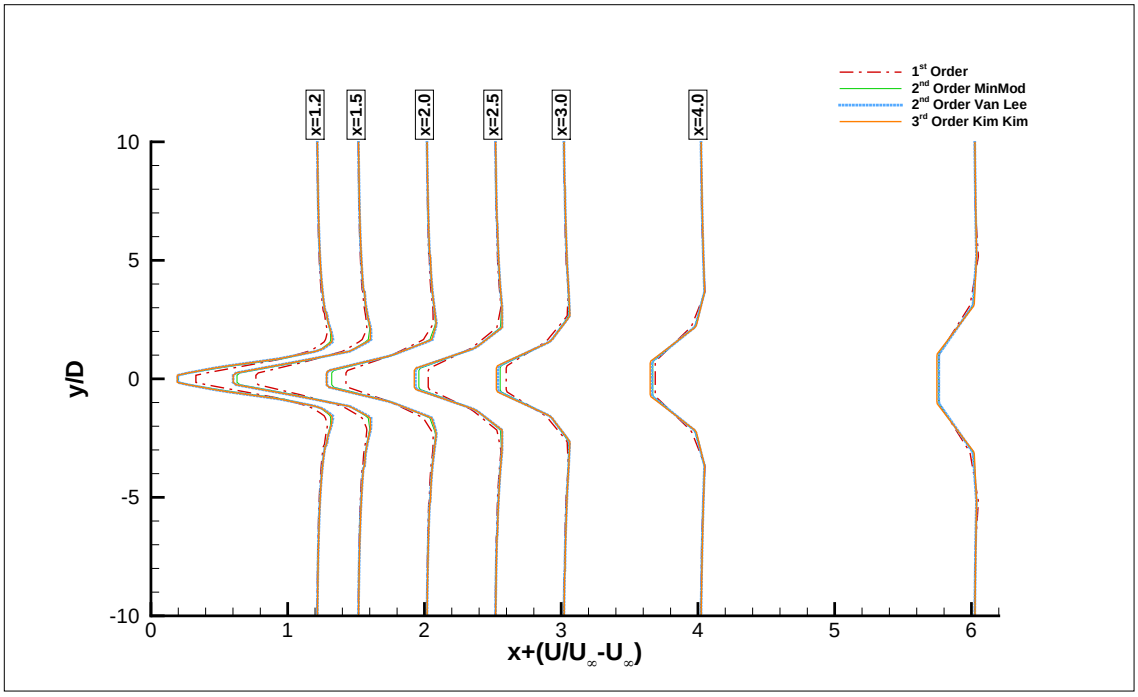

(a) Streamwise momentum along vertical lines in the wake

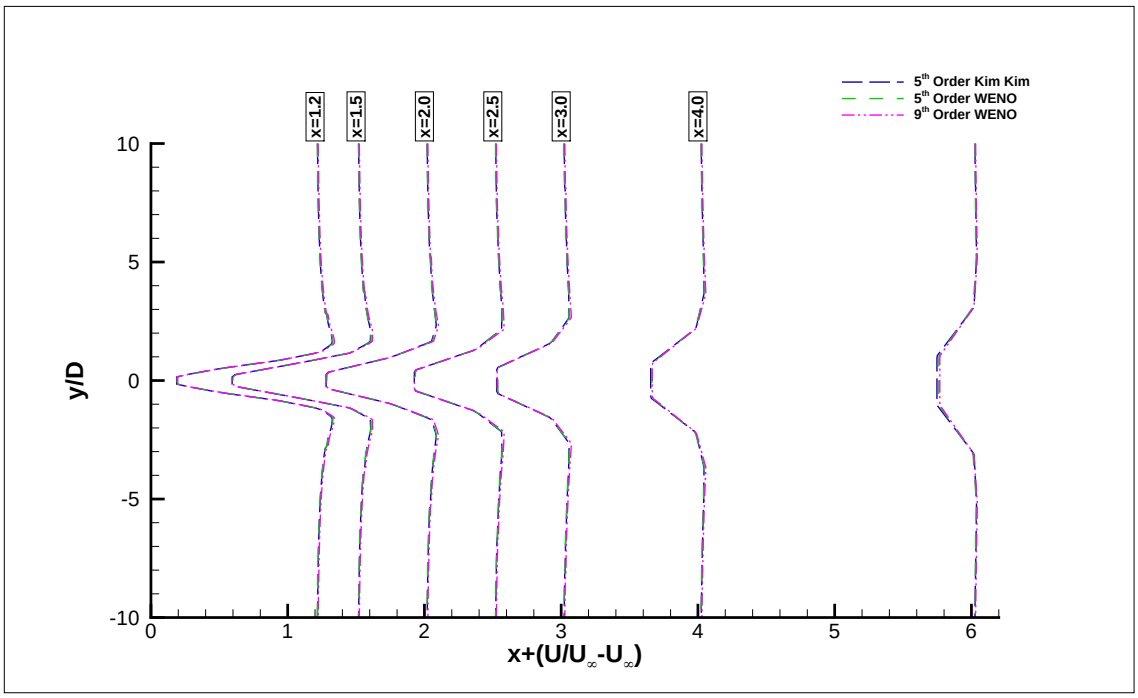

(b) Streamwise momentum along vertical lines in the wake

FIGURE 5.4: Reynolds Number 40, 2*D* flows (a) showing lower-order stream-wise flow momentum, and (b) showing the higher order stream-wise flow momentum.

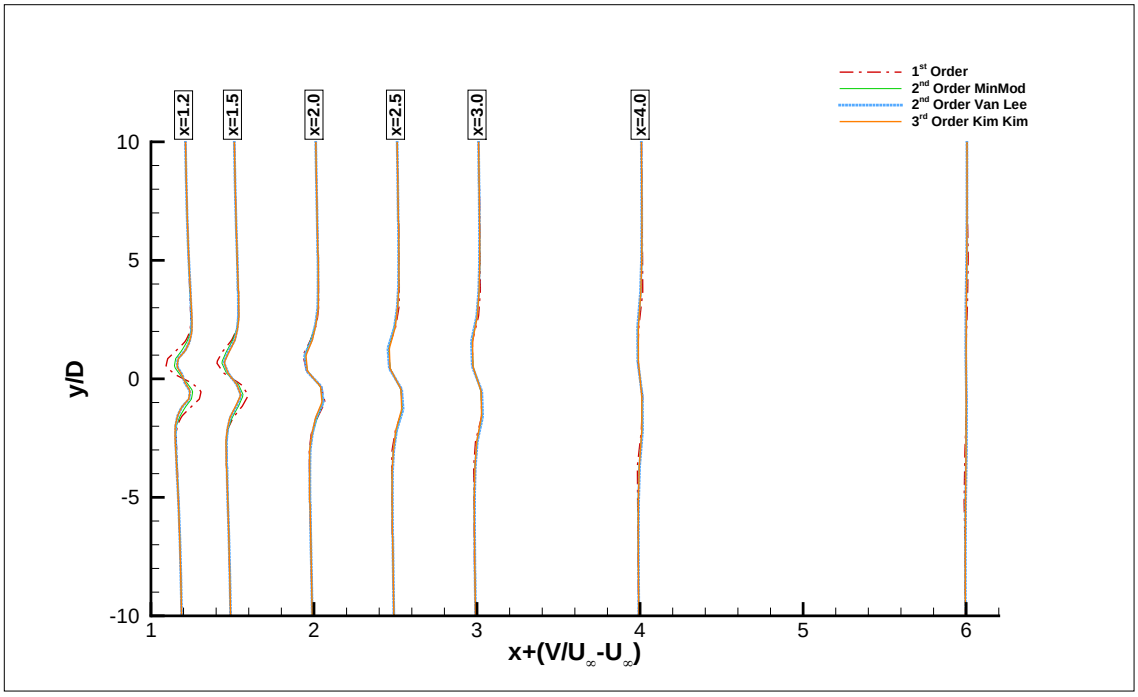

(a) Crossflow momentum along vertical lines in the wake

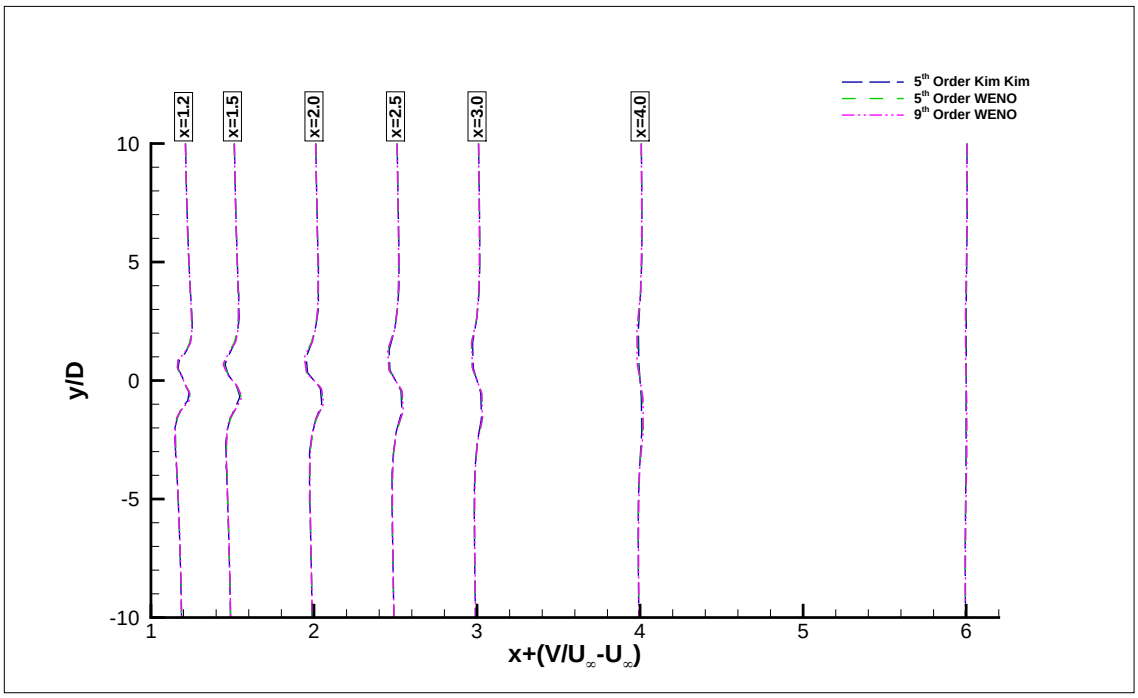

(b) Crossflow momentum along vertical lines in the wake

FIGURE 5.5: Reynolds Number 40, 2*D* flows (a) showing lower-order Cross-flow momentum, and (b) showing the higher order Cross-flow momentum.

Dataset Info		C_d	θ_{sep}[1]
Exp.	Tritton [96]	1.59	-
	Grove [97]	-	137.2°
	Coutanceau [56]	-	126.5°
Numerical	Son [98]	1.56	126.1°
	Dennis [99]	1.52	126.2°
	Fornberg [100]	1.498	125.0°
	Borthwick [101]	1.507	126.3°
	Franke [102]	1.39	123.0°
	Henderson [103]	1.54	-
	Kravchenko [93]	1.52	-
	Kirkpatrick [104]	1.535	126.45°
This Work	First-Order	1.56	133.7°
	Second Order MinMod	1.56	128.6°
	Second Order Van Leer	1.49	127.9°
	Third Order Kim-Kim	1.48	126.7°
	Fifth Order Kim-Kim	1.47	127.5°
	Fifth Order WENO	1.48	127.9°
	Ninth Order WENO	1.51	127.8°

TABLE 5.1: $Re = 40$ Numerical Results

determined at $Re = 43$, while a Strouhal number of 0.14 was found at $Re = 49$. Franke's paper [102], shown in the table, found the Strouhal number at 0.116, though this was determined for a Reynolds number of 50. However, the flow regime at $Re = 40$ is on the limit of being either a steady separated region, or having periodic laminar wake [106]. This confirms the laminar flow and lack of oscillating vortices to the rear of the cylinder at $Re = 40$ and shows that at only a marginally higher Reynolds number (generally considered to be around $Re = 47$, as discussed in section 1.3.1) the oscillations are present.

5.3 Reynolds Number = 200

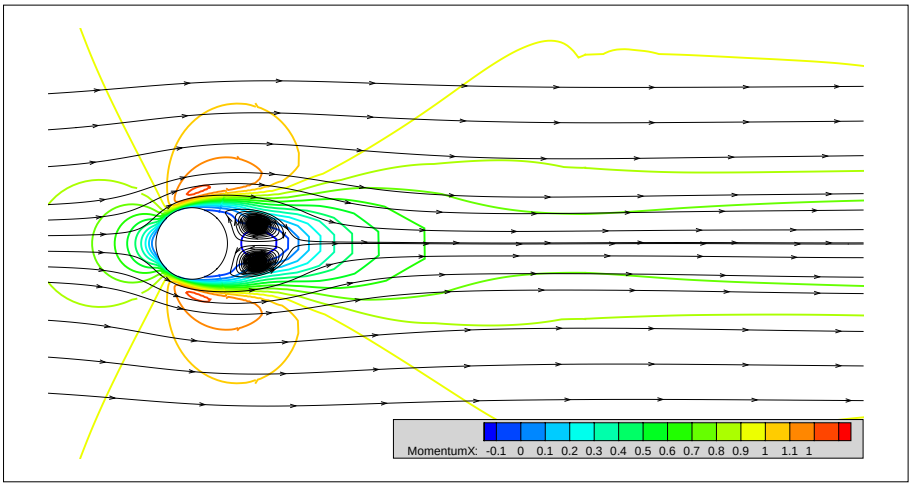

(a) Time averaged plot of Reynolds number 200 2D flow

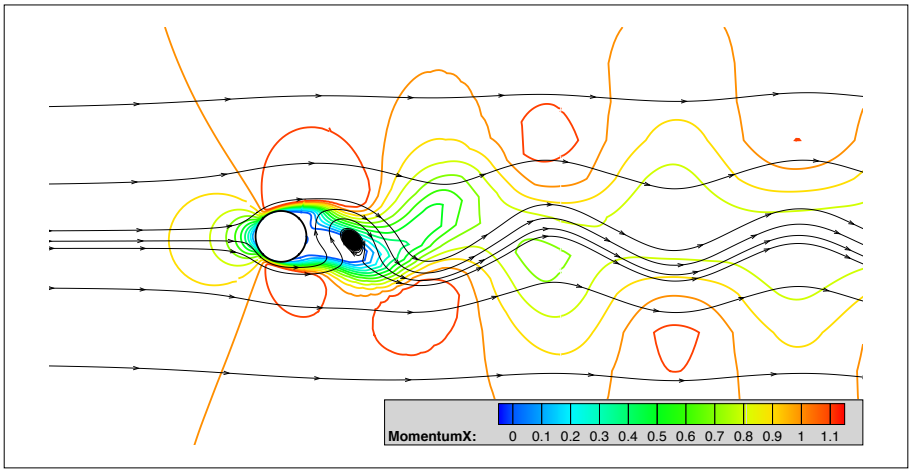

(b) Instantaneous plot of Reynolds number 200 2D flow

FIGURE 5.6: Time averaged (subfigure 5.6(a)) and instantaneous (subfigure 5.6(b)) plots of Reynolds number 200 2D flow, 5^{th} Order WENO scheme.

As the flow speed increases to Reynolds number 200, the von Karman instability and vortex streets are generated naturally within the flow, and equally in most of the simulations. To the rear of the cylinder, vortex shedding is observed, whereby the vortices generated just above and below the near wake of the cylinder 'break away' from the surrounding flow. This is most clearly observed in an instantaneous plot of the flow, as in figure 5.6(b). However, the oscillations in the wake are periodic, as is the shedding of the vortices, and so a plot of the time-averaged flow (as in figure 5.6(a)) reveals a more steady overview of what's taking place with fixed vortices to the rear of the cylinder.

At this Reynolds number, the flow regime changes due to the presence of three-dimensional shear stresses. The flow has now entered a phase of transition in the wake for the formation of Karman Vortex Streets that separate from the cylinder in the wake [106]. In normal flow, where the third direction of momentum is present (i.e. not in a restricted two-dimensional flow such as this flow), three-dimensional instabilities should lead to the formation of stream-wise vortices. In [107], it was reported that above a value of $Re = 170$, the periodic solution becomes unstable, with any two-dimensional perturbations more rapidly damped than three-dimensional perturbations. At this Reynolds number, fluctuations of finite-amplitude play a decisive role in the determination of the 'branch' that the system will follow, influencing the state of the wake significantly [108].

Figure 5.7 shows the plots of Coefficient of pressure and coefficient of lift around the cylinder at Reynolds number 200, for the different numerical schemes. Subfigure 5.7(a) shows good agreement of the higher-order simulations with literature data available, however, the simulations do appear to under-predict the values slightly compared to the experimental literature results as the flow reaches and passes the separation point. At the suction peak, the simulated data performs better than those presented by Rajani [109]. In contrast to this, there is good agreement between the measured data and the numerical data simulated for this investigation at the accelerating flow zone on the fore of the cylinder. The discrepancies could be attributed to an inaccurate prediction of the point of unsteady flow separation on the cylinder surface, or due to the three-dimensional instabilities in the wake that have been observed experimentally.

The first-order run dramatically over-predicts the coefficient of pressure - particularly behind the separation point. As is evident by the first order run data in the coefficient of lift plot (figure 5.7(b)), the first order simulation remains steady at this Reynolds number; in fact oscillations in the value of C_l did occur very late in the simulation run (by a time at which all the other simulations had developed). However, whereas C_l for the higher-order schemes was of the magnitude 10^{-1}, the coefficient of lift for the first order simulation was of the magnitude 10^{-5}, essentially showing a continual steady-state.

The pattern shown in the coefficient of pressure plot continues to the coefficient of friction plot 5.8(a), such that the different numerical schemes are closer in value to the numerical literature data than the experimental data. However, both the numerical literature data, as well as the simulation data are closer to the results from a higher Reynolds number run of $Re = 287$. The experimental data shows a relatively large difference in coefficient of friction between these two Reynolds numbers, suggesting that there is a greater consistency in the form of the flow between Reynolds numbers 200 and 287 in experimental form.

As seen earlier, the first-order run is again the outlier in the data, under-predicting the friction values around the circumference of the cylinder. The separation point is at an earlier point around the cylinder than the higher-order methods, but the wake itself exhibits steady flow formation. The steady flow formation is clearly obvious even examining a late (in terms of simulation time) instantaneous plot, as in figure 5.9. External perturbations could have been introduced to the flow in order to induce periodicity of the wake and flow around the cylinder, however the remaining simulations that were run at the higher-order were able to naturally exhibit the periodic behaviour. Thus, it was decided to maintain similarity with the other simulations and avoid the

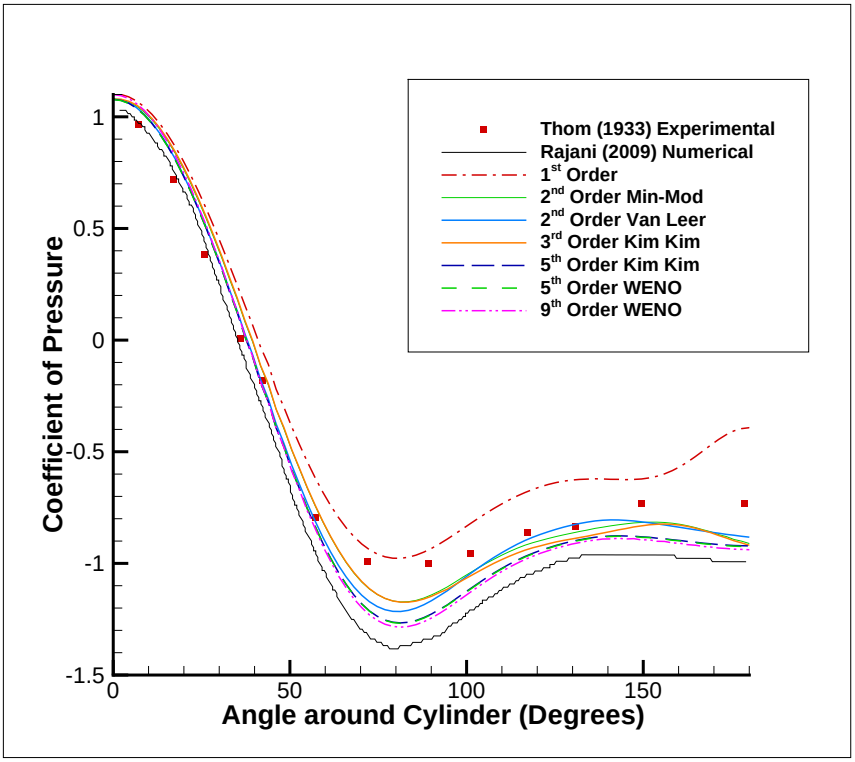

(a) C_p around the cylinder. Note: Experimental data from [105] ($Re = 229$), numerical data from [109]

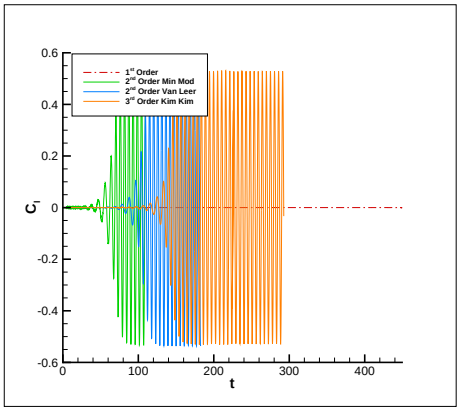

(b) Development of coefficient of lift over time, Lower-order schemes

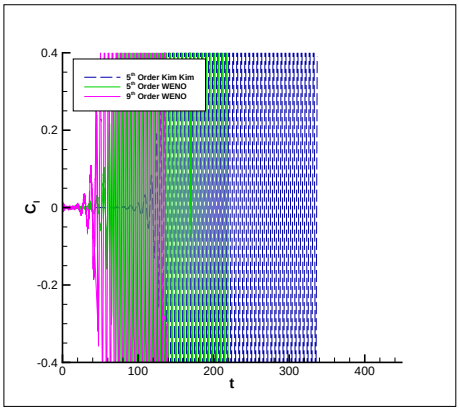

(c) Development of coefficient of lift over time, Higher-order schemes

FIGURE 5.7: Reynolds Number 200, 2D flows giving coefficient of pressure 5.7(a) and coefficient of lift over time, around the cylinder for differing orders of run.

imposition of external perturbations.

The figures in 5.10 show the stream-wise momentum along the line $y = 0$ behind the cylinder.

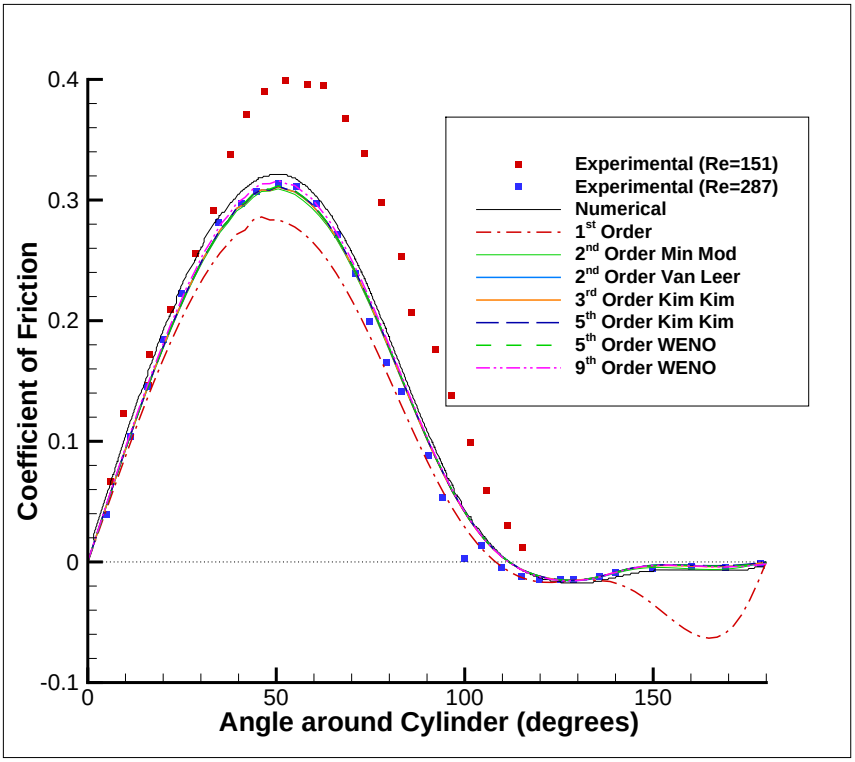

(a) C_f around the cylinder. Note: Experimental data from [110], numerical data from [109]

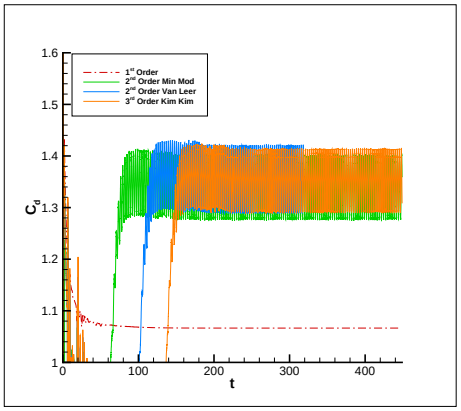

(b) Development of coefficient of drag over time, Lower-order schemes

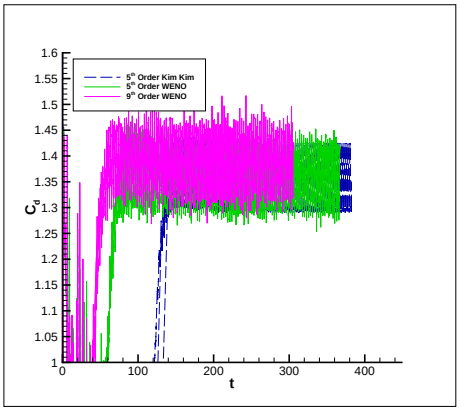

(c) Development of coefficient of drag over time, Higher-order schemes

FIGURE 5.8: Reynolds Number 200, 2D flows showing coefficient of friction 5.8(a) and coefficient of drag around the cylinder for differing orders of run.

The Kim Kim simulations show lower average velocities along the wake than the other simulations, and with almost identical values downstream as one another. The WENO schemes also exhibit almost identical values downstream from the cylinder.

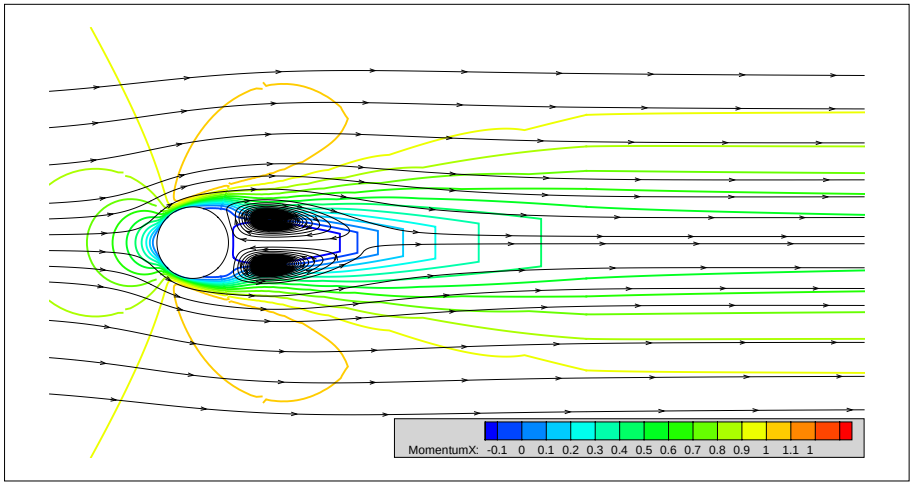

FIGURE 5.9: Instantaneous plot of Reynolds number 200 2D flow, first order scheme.

Figures 5.11 and 5.12 show the time-averaged flow values for the different simulations, in the wake of the cylinder. Figure 5.11 shows the flow in the stream-wise direction, while figure 5.12 shows the cross-stream flow - that is, momentum in X and momentum in Y respectively. Each of these figures is split into two, to differentiate between the different numerical schemes. Examining figure 5.11, it can be seen that the first-order plot continues to be the exception to the other simulations with regards to uniformality of results; the flow speed is greatly reduced compared to the other higher-order runs, due to the laminar flow in the wake of the cylinder.

Figure 5.12 shows that the effects of the cylinder on the y-direction of flow dissipate rapidly. By the point $x/D = 6$, the variations in cross-stream flow have almost completely disappeared. This is evident in all of the numerical schemes.

Figure 5.13 shows the fluctuations in the momentum, in time-averaged form, in the near wake of the cylinder. The behaviour previously observed in the first order scheme is visible in the fluctuating momentum, which are zero in both the stream-wise and cross-flow directions. Appendix B shows more results of the fluctuations in the flow in the wake, showing the continuing reduction of fluctuations in the wake, downstream of the cylinder. The fluctuations of the velocity increase slightly downstream as the flow dissipates into the surrounding flowfield, before steadily dropping again.

The plots of Reynolds stresses in the wake show the same patterns as the fluctuations (which is to be expected, due to the relationship between fluctuating velocity and Reynolds stress), and so plots for Reynolds stresses are included for completion in Appendix B. The Reynolds stresses $u'v'$ show a definite symmetry across the line $y = 0$ in the wake of the cylinder.

Figures 5.14 and 5.15 show the spectral plots of frequency of fluctuations, which are now much more defined. It seems that although there is a clear harmonic frequency for most of the simulations, the 2^{nd} order Van Leer and 9^{th} order WENO schemes both show a wide number of sub-harmonic fluctuations close in energy to the main harmonic frequency. The spectral plots, as with the fluctuation values, show a strengthening of flow in the wake before dissipation continues

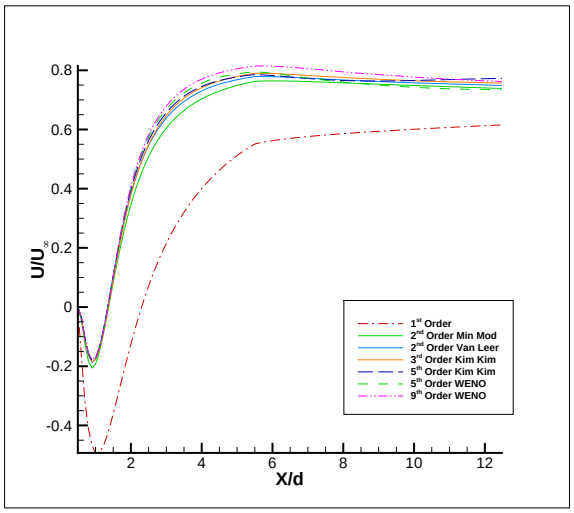

FIGURE 5.10: Reynolds Number 200, 2D flow. Time-averaged streamwise momentum in the wake of the cylinder, along the line $y/D = 0$.

again; that is, the flow directly to the rear of the cylinder does not begin to dissipate, until a point of around $x/D = 1.50$. Examination of the first major peaks in the spectral plots reveal that the 9^{th} order WENO and 2^{nd} order Van Leer schemes have the greatest amount of low frequency fluctuations. However, at higher frequencies these also show an increase in spectrum density; this isn't a particularly physical phenomenon raising the question of the validity of these results and suggesting a strong requirement for the presence of a third-dimension to capture the 3D vortices. The first order simulation once again shows a lack of energy fluctuations, corresponding to the laminar nature of the flow field.

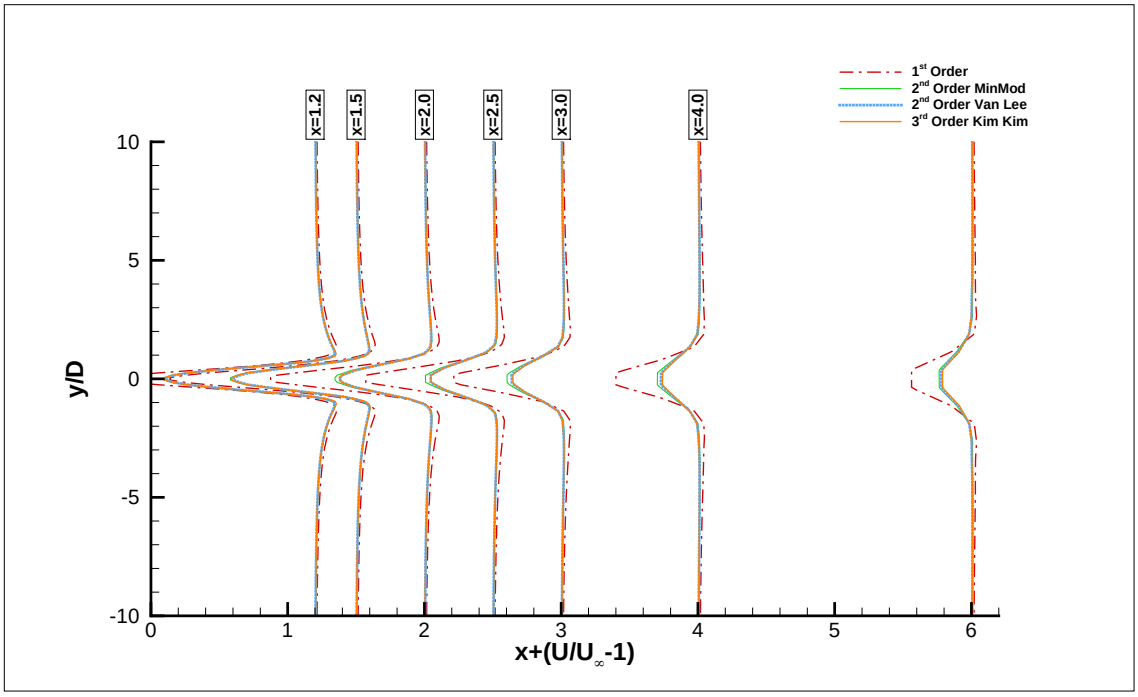

(a) Streamwise momentum along vertical lines in the wake

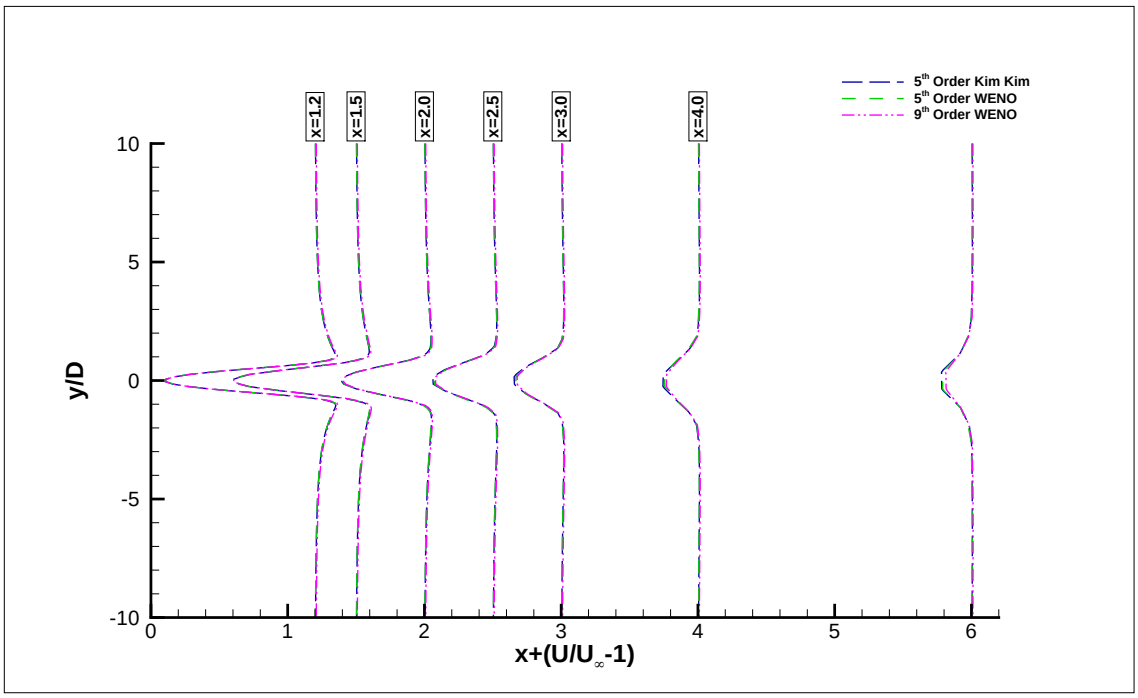

(b) Streamwise momentum along vertical lines in the wake

FIGURE 5.11: Reynolds Number 200, 2*D* flows (a) showing lower-order stream-wise flow momentum, and (b) showing the higher order stream-wise flow momentum.

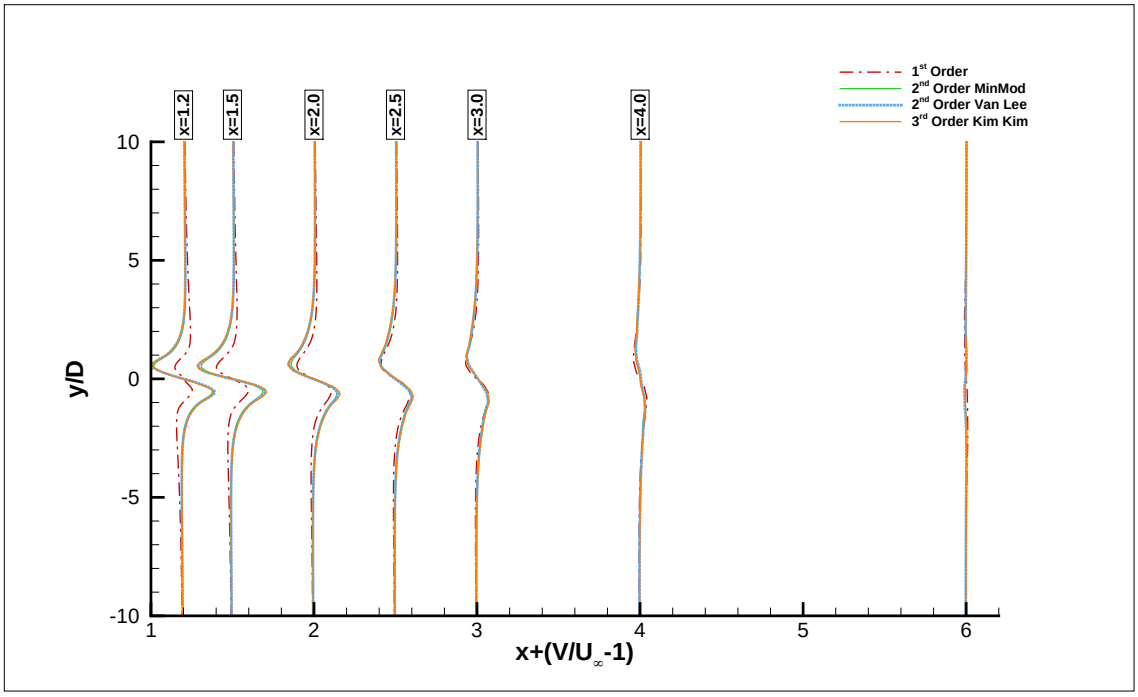

(a) Crossflow momentum along vertical lines in the wake

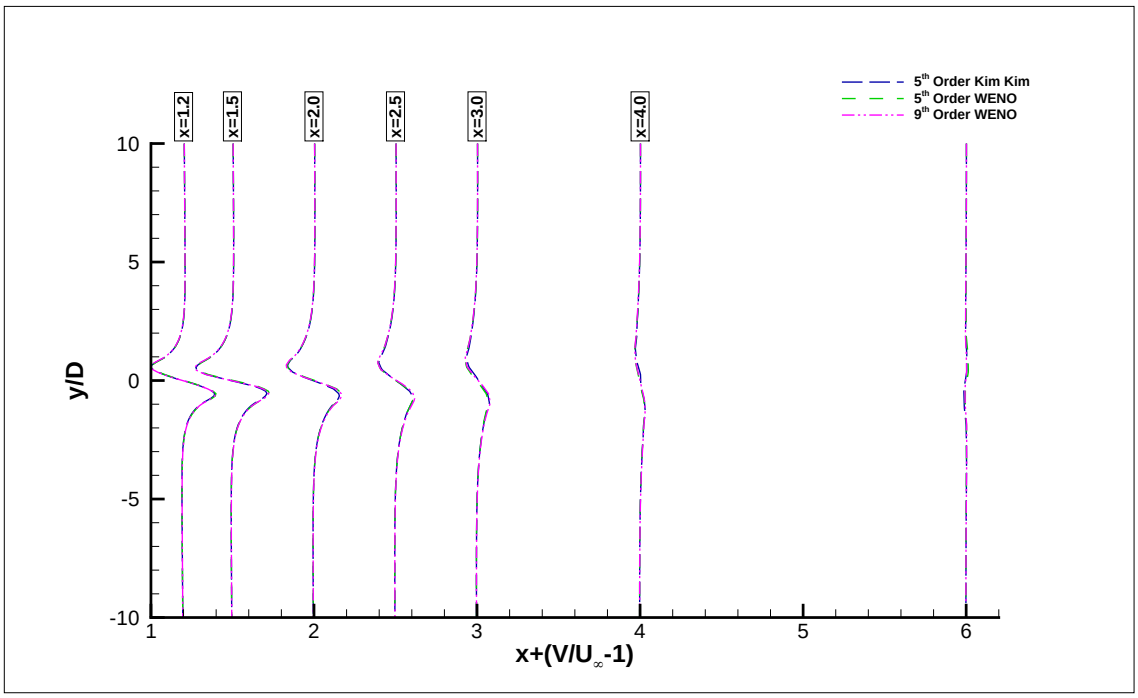

(b) Crossflow momentum along vertical lines in the wake

FIGURE 5.12: Reynolds Number 200, 2*D* flows (a) showing lower-order Cross-flow momentum, and (b) showing the higher order Cross-flow momentum.

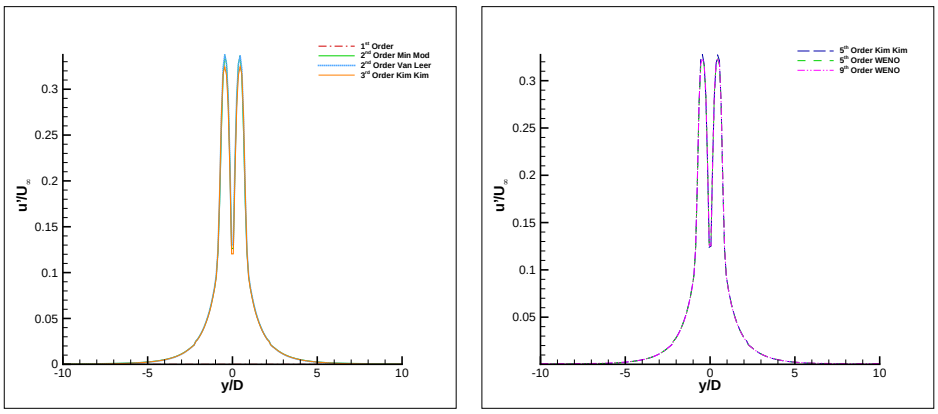

(a) Streamwise fluctuations at $x/D = 1.00$

(b) Streamwise fluctuations at $x/D = 1.00$

(c) Crossflow fluctuations at $x/D = 1.00$

(d) Crossflow fluctuations at $x/D = 1.00$

FIGURE 5.13: Reynolds Number 200, $2D$ flow. Fluctuations in the near wake, at $x/D = 1.00$.

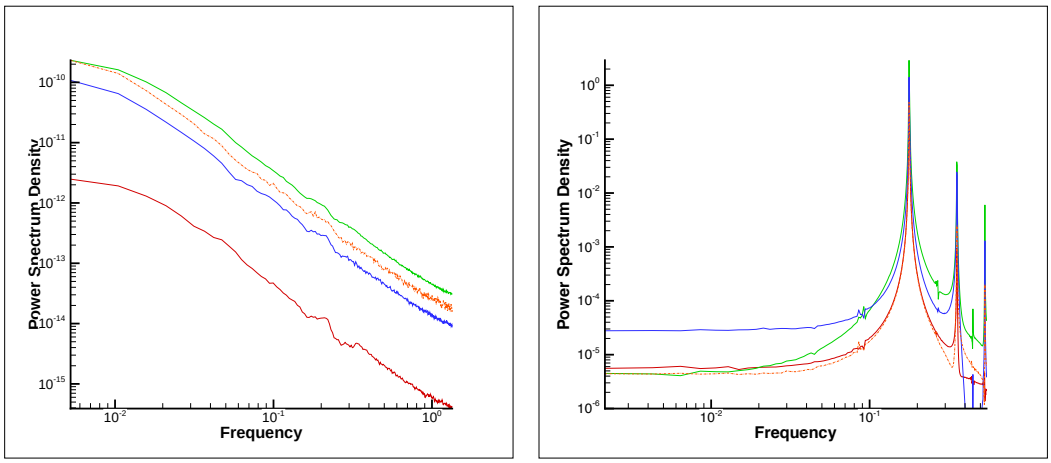

(a) First-Order

(b) Second-Order Min Mod

(c) Second-Order Van Leer

FIGURE 5.14: Reynolds Number 200, 2D flows. Plots showing spectral plots for points at $y/D = 0$, with Red Line: $x/D = 0.58$, Green Line: $x/D = 1.50$, Blue Line: $x/D = 4.00$ and Orange Line: $x/D = 7.00$. Plots shown for each numerical scheme.

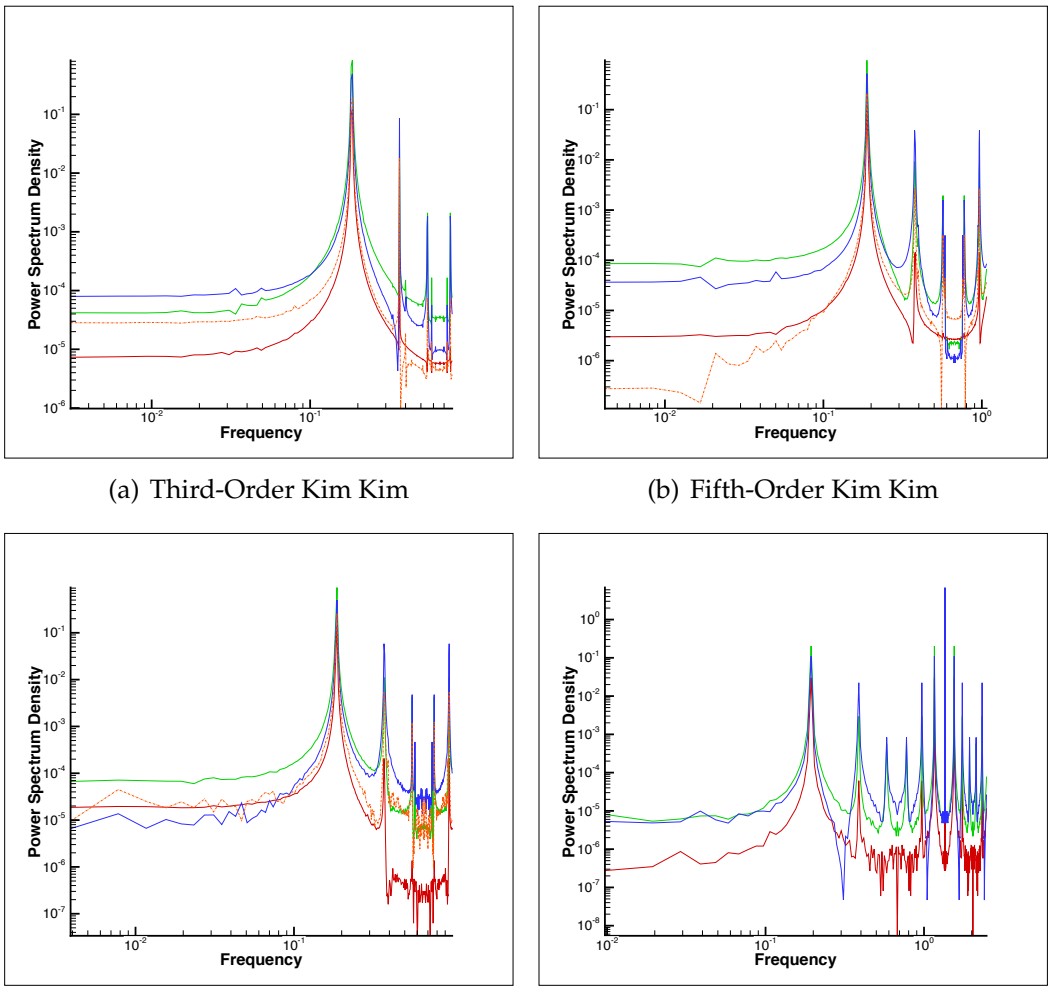

(a) Third-Order Kim Kim

(b) Fifth-Order Kim Kim

(c) Fifth-Order WENO

(d) Ninth-Order WENO

FIGURE 5.15: Reynolds Number 200, 2D flows. Plots showing spectral plots for points at $y/D = 0$, with Red Line: $x/D = 0.58$, Green Line: $x/D = 1.50$, Blue Line: $x/D = 4.00$ and Orange Line: $x/D = 7.00$. Plots shown for each numerical scheme.

Dataset Info		C_d	C_l	U_{min}	θ_{sep}[1]	St
Exp.	Wieselsberger [111] (from [46])	1.28	-	-	-	-
	Williamson [35]	-	-	-	-	0.184
Num.	Franke [102]	1.31	0.65	-	111.5°	0.194
	Zhang [46]	1.42	0.531	-	-	0.202
	Persillon [108][2]	1.321	-	-	109.5	0.198
	Rajani [109]	1.337	-	-	111.904°	0.196
	Cao [60]	1.300	-	-	-	0.186
This Work	First-Order	1.07	-	-0.543	108.2°	-
	Second Order MinMod	1.35	0.53	-0.218	111.7°	0.178
	Second Order Van Leer	1.36	0.54	-0.199	111.8°	0.185
	Third Order Kim-Kim	1.35	0.53	-0.197	111.7°	0.185
	Fifth Order Kim-Kim	1.36	0.53	-0.193	111.8°	0.188
	Fifth Order WENO	1.36	0.53	-0.186	111.8°	0.187
	Ninth Order WENO	1.40	0.55	-0.188	111.6°	0.190

TABLE 5.2: $Re = 200$ 2-dimensional Results

Table 5.2 shows numerical data extracted from the simulations, compared to literature values. The first-order scheme shows the resulting numerical effects of the laminar flow; no lift, and no Strouhal number. The remainder of the simulations show generally good agreement with the literature values. At this Reynolds number, it would seem that the 9^{th} order WENO scheme over-predicts the coefficients of lift and drag slightly compared to literature values as well as the other simulations. However, it is still in relatively good agreement with literature data overall, and as is evident from the plots of C_l and C_d over time, flow develops into the appropriate state more rapidly than most of the other schemes.

[1]For simulations carried out for this work, θ_{sep} has potential errors of $\pm 1.08°$, due to the resolution of cells (and their subsequent arc sizes) around the circumference of the cylinder

[2]From $2D$ case

5.4 Reynolds Number = 300

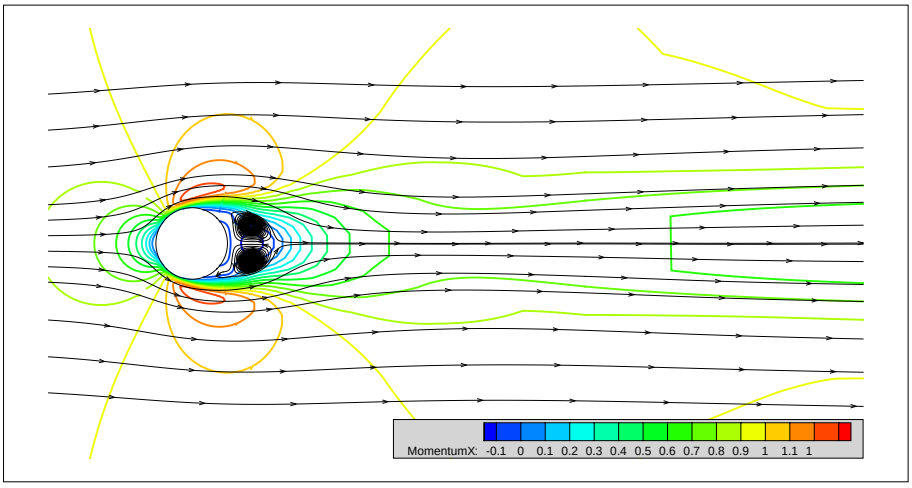

(a) Time averaged plot of Reynolds number 300 2D flow

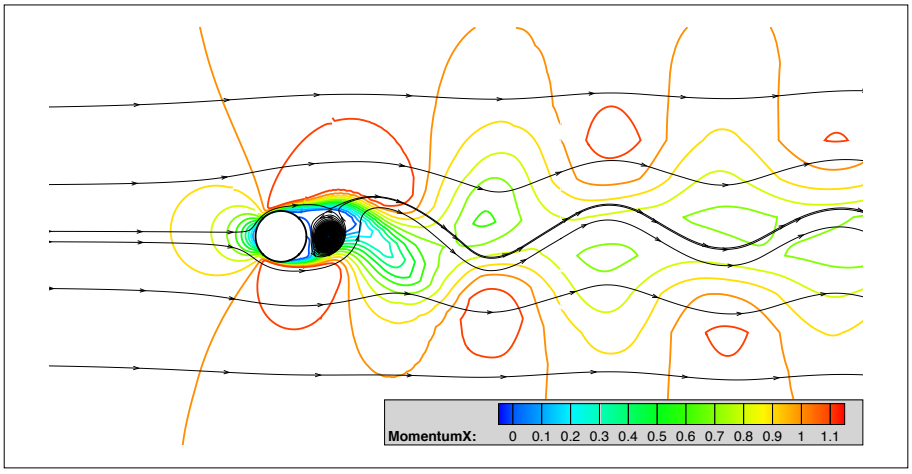

(b) Instantaneous plot of Reynolds number 300 2D flow

FIGURE 5.16: Time averaged (subfigure 5.16(a)) and instantaneous (subfigure 5.16(b)) plots of Reynolds number 300 2D flow, 5^{th} Order WENO scheme.

With the flow now at the higher Reynolds number of 300, the flow is now well within the region of vortex formation and shedding to the rear of the cylinder [106]. In this regime, the flow around the cylinder oscillates in the upwards and downwards directions resulting in an oscillating wake directly to the rear of the cylinder. The frequency with which this happens, combined with the viscosity of the fluid (which together define the Reynolds number) is such that the vortical formations to the rear of the cylinder are broken away from the wake as the wake oscillates in direction. It is these broken-away formations that make up the vortex street flow in the wake. This is most evident in the instantaneous time plot given in figure 5.16(b). Averaged

over a long period of time, these oscillations appear as a steady flow, due to the symmetry of the oscillations along the line $y = 0$ to the rear of the cylinder. This time-averaged flow is visible in figure 5.16(a), which illustrates the same flow as the instantaneous plot, merely time-averaged over a time-period spanning a number of oscillations.

As this is a two-dimensional flow, any three-dimensional perturbations are not computed, and thus the periodic solution remains stable in this flow, with two-dimensional perturbations being damped more rapidly than three-dimensional perturbations would be (as also reported in [107]).

Figure 5.17 shows the plots of Coefficient of pressure and coefficient of lift around the cylinder at Reynolds number 300, for the different numerical schemes. Subfigure 5.17(a) shows good agreement of the higher-order simulations with literature data available, however, the simulations do appear to under-predict the values slightly compared to the experimental literature results as the flow reaches and passes the separation point. At the suction peak, the simulated data performs better than that shown by Rajani [109]. In contrast to this, there is good agreement between the measured data and the numerical data simulated for this investigation at the accelerating flow zone on the fore of the cylinder. The discrepancies could be attributed to an inaccurate prediction of the point of unsteady flow separation on the cylinder surface, or due to the three-dimensional instabilities in the wake that have been observed experimentally. However, similar effects have been previously observed in two-dimensional simulations [112], whereby it was concluded that at this Reynolds number, two-dimensional simulations do an unsatisfactory job of predicting key cylinder surface coefficient quantities, yet Strouhal number is predicted accurately.

Examining the figures for coefficient of lift (figures 5.17(b) and 5.17(c)), it is clear that while the higher-order simulations reached a point with satisfactory fluctuations in the cylinder lift relatively quickly, the fluctuations did not develop in the first-order run until quite a number of iterations had been completed. Furthermore, the first-order run under-predicted the coefficient of lift compared to the remainder of the simulations. This is a pattern that recurs with the coefficient of drag plots (shown in figures 5.18(b) and 5.18(c)). Another interesting feature of both the C_l and C_d plots is that of the 5^{th} order WENO scheme; this does not have fluctuations that are constant in values. This was a feature repeated with the 9^{th} order WENO scheme - which is omitted from the plots for reasons of legibility of the plots.

The first-order simulation shows further anomalies compared to literature data as well as the higher-order plots. In the plot of coefficient of pressure (figure 5.17(a)), the pressure around the cylinder is clearly too high - particularly to the rear of the cylinder. This behaviour is mirrored in the coefficient of friction plot (figure 5.18(a)) where the friction is underpredicted, with a large drop in friction to the rear of the cylinder. Thus it seems that although the first-order plot now shows the relevant fluctuations in coefficients over time, it can not fully resolve the flow around the cylinder to a satisfactory degree. Equally, the separation point in the first-order scheme occurs quite early around the circumference of the cylinder - earlier than any of the remaining numerical data

Figures 5.19 shows the stream-wise momentum along the line $y = 0$ behind the cylinder. The resultant effect in the wake of the first-order simulation's difference in friction and pressure

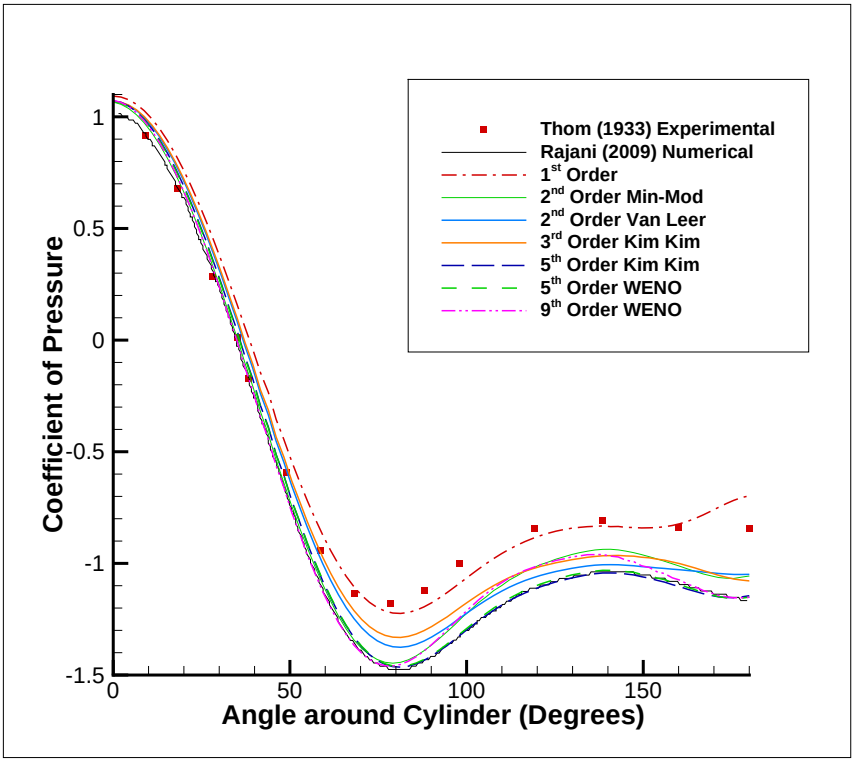

(a) C_p around the cylinder. Note: Experimental data from [105] ($Re = 229$), numerical data from [109]

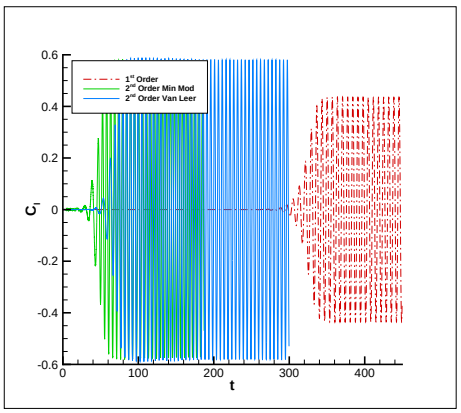

(b) Development of coefficient of lift over time, Lower-order schemes

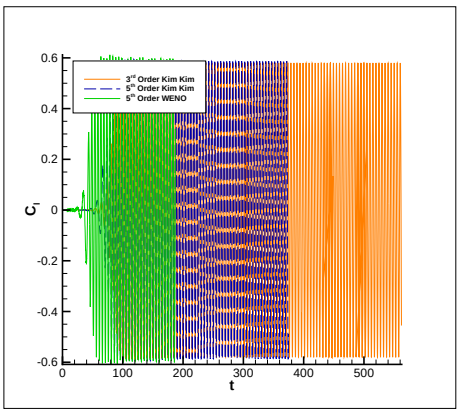

(c) Development of coefficient of lift over time, Higher-order schemes

FIGURE 5.17: Reynolds Number 300, 2D flows giving coefficient of pressure 5.17(a) and coefficient of lift over time, around the cylinder for differing orders of run.

around the cylinder are clearly evident on the flow velocity. In the stream-wise direction, there exists a stronger suction towards the rear of the cylinder, with the wake following being consequently slowed.

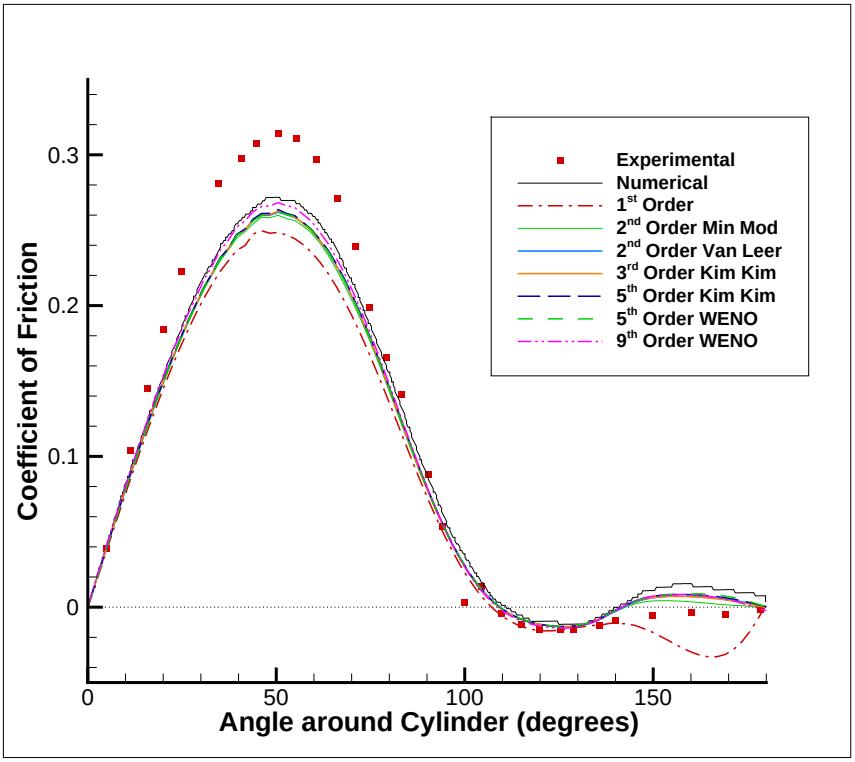

(a) C_f around the cylinder. Note: Experimental data from [110] at $Re = 287$, numerical data from [109]

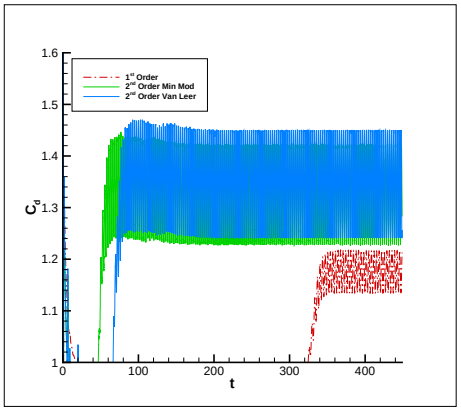

(b) Development of coefficient of drag over time, Lower-order schemes

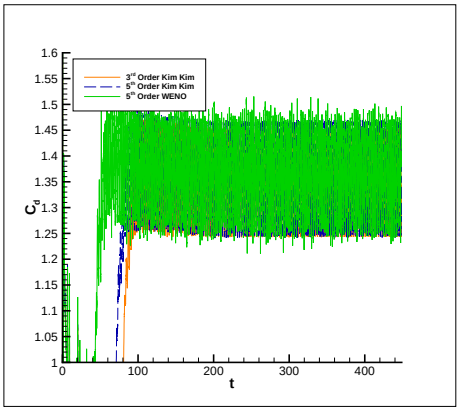

(c) Development of coefficient of drag over time, Higher-order schemes

FIGURE 5.18: Reynolds Number 300, 2D flows showing coefficient of friction 5.18(a) and coefficient of drag around the cylinder for differing orders of run.

This behaviour is demonstrated well in figures 5.20 and 5.21 that show the time-averaged flow values for the different simulations, in the wake of the cylinder. Figure 5.20 shows the flow in the stream-wise direction, while figure 5.21 shows the cross-stream flow - that is, momentum

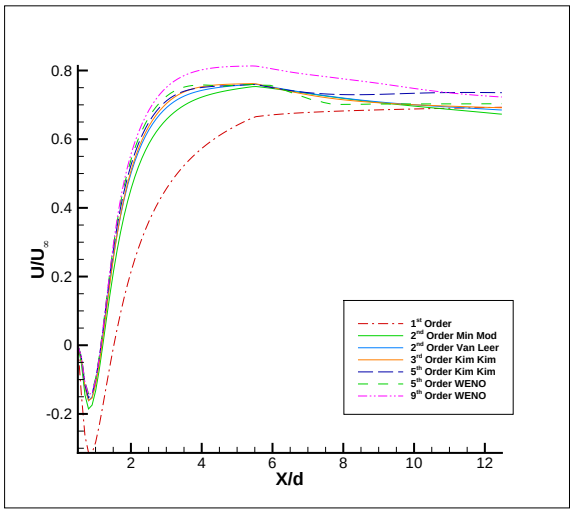

FIGURE 5.19: Reynolds Number 300, 2D flow. Time-averaged streamwise momentum in the wake of the cylinder, along the line $y/D = 0$.

in X and momentum in Y respectively. Each of these figures is split into two, to differentiate between the different numerical schemes. The first-order velocity data in the stream-wise direction is the slowest of all the numerical schemes, whilst the remainder of the numerical schemes have flow dissipating at almost equal amounts. Another exception is the 9^{th} order WENO scheme; downstream in the wake, in the region of $x/D = 3$ onwards, this scheme has flow dissipating to freestream flow velocity faster than any of the other schemes.

Figure 5.22 shows the fluctuations in the momentum, in time-averaged form, in the near wake of the cylinder. The behaviour previously observed in the first order scheme is visible in the fluctuating momentum, which are reduced in both the stream-wise and cross-flow directions compared to the remaining numerical schemes. Appendix B shows more results of the fluctuations in the flow further in the wake, showing the continuing reduction of fluctuations in the wake, downstream of the cylinder. The fluctuations of the velocity increase slightly at $x/D = 1.20$ as the flow dissipates into the surrounding flowfield, before steadily dropping again.

The plots of Reynolds stresses in the wake show the same patterns as the fluctuations (which is to be expected, due to the relationship between fluctuating velocity and Reynolds stress), and so plots for Reynolds stresses are included for completion in Appendix B. The Reynolds stresses $u'v'$ show a definite symmetry across the line $y = 0$ in the wake of the cylinder.

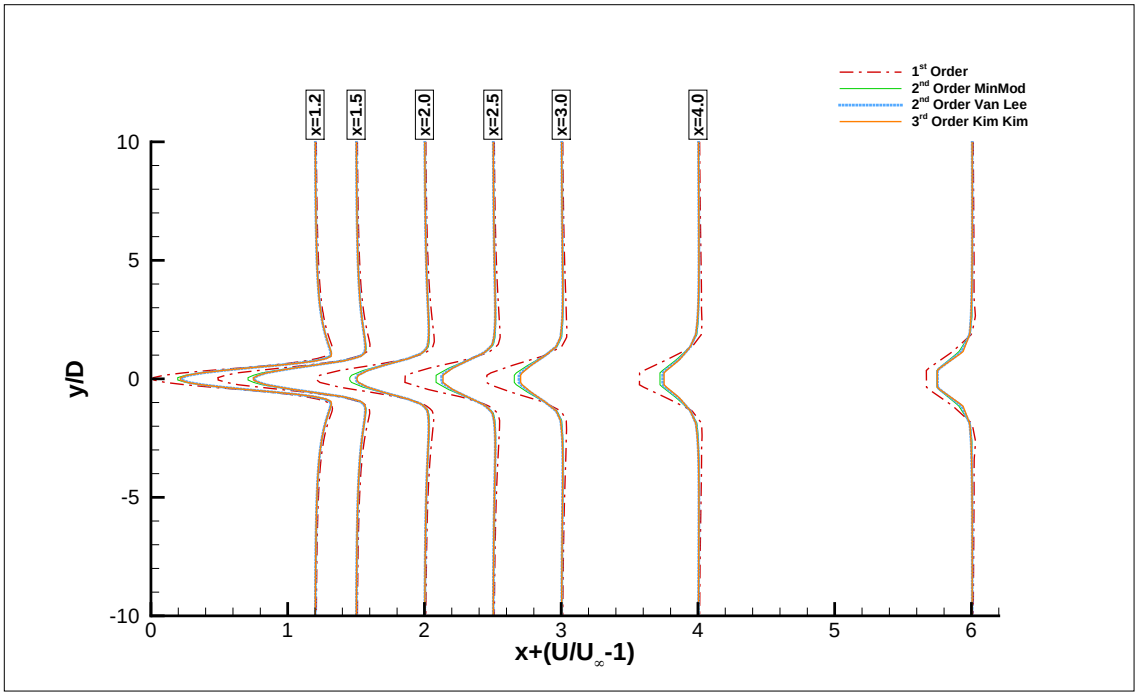

(a) Streamwise momentum along vertical lines in the wake

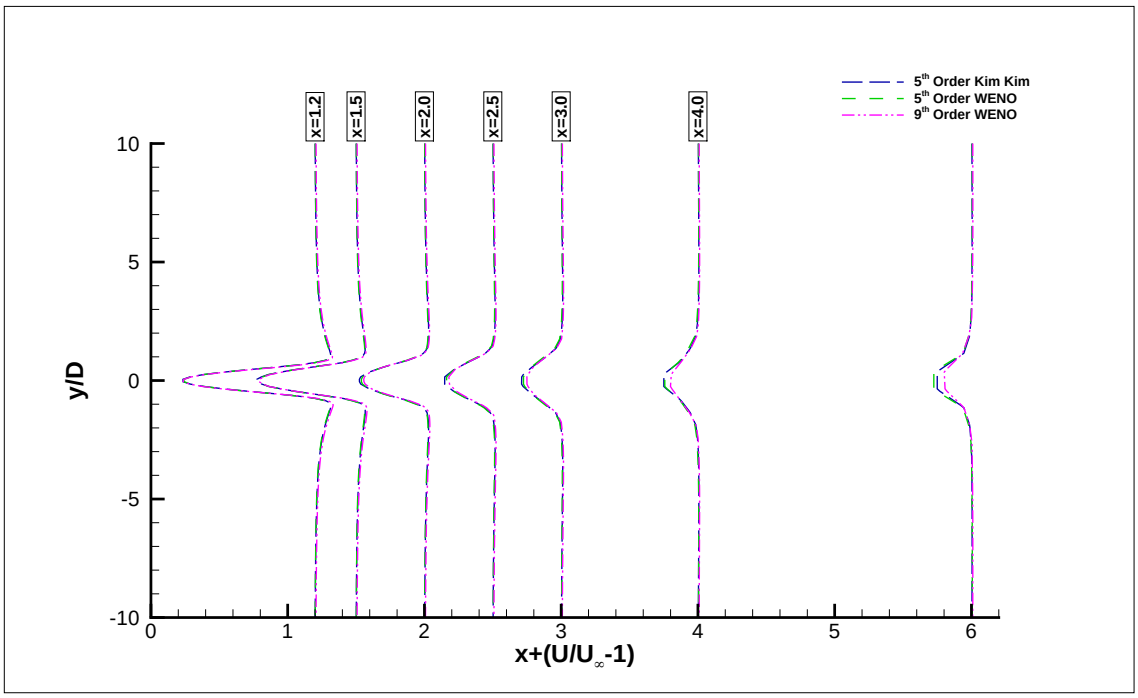

(b) Streamwise momentum along vertical lines in the wake

FIGURE 5.20: Reynolds Number 300, 2*D* flows (a) showing lower-order stream-wise flow momentum, and (b) showing the higher order stream-wise flow momentum.

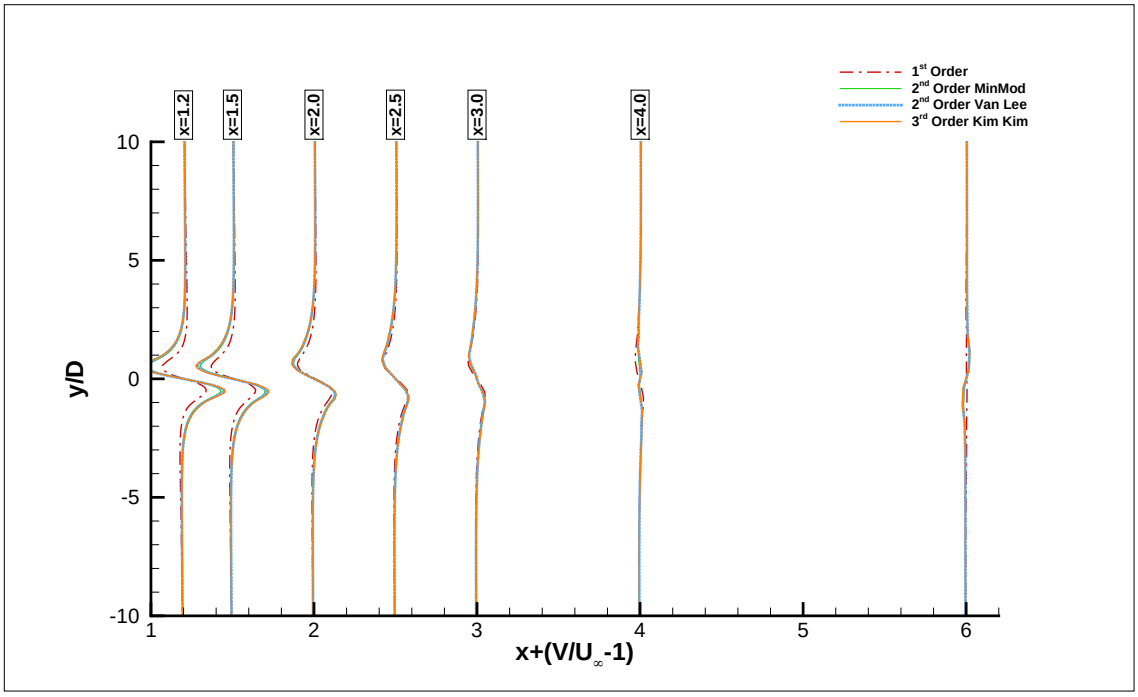

(a) Crossflow momentum along vertical lines in the wake

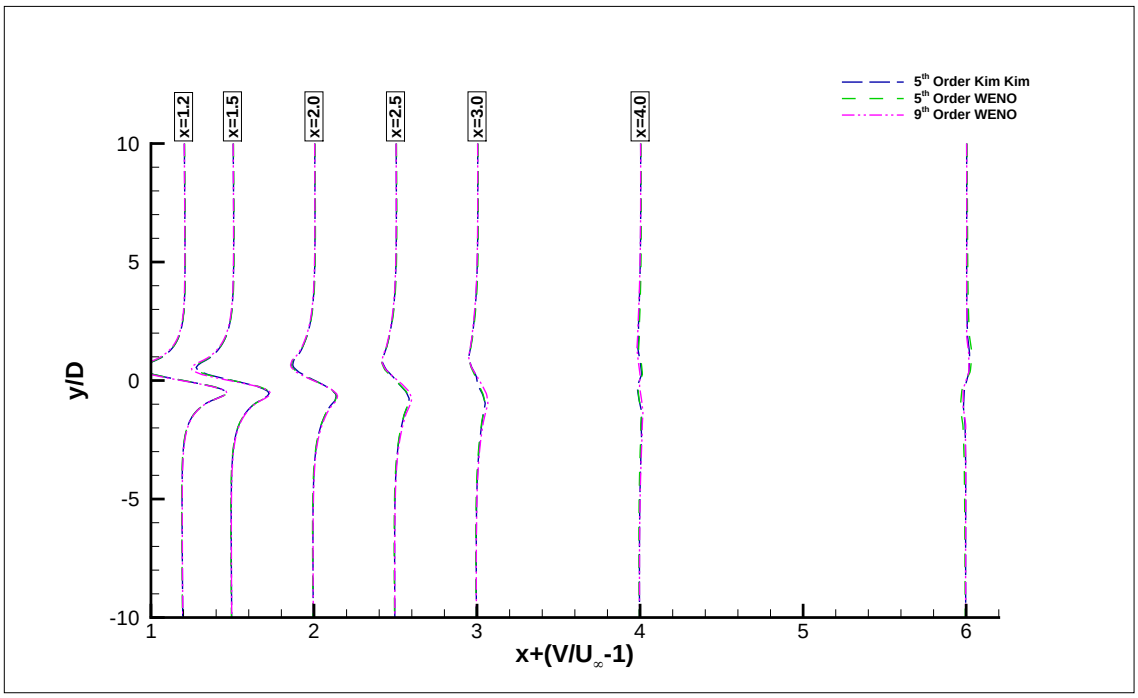

(b) Crossflow momentum along vertical lines in the wake

FIGURE 5.21: Reynolds Number 300, 2*D* flows (a) showing lower-order Cross-flow momentum, and (b) showing the higher order Cross-flow momentum.

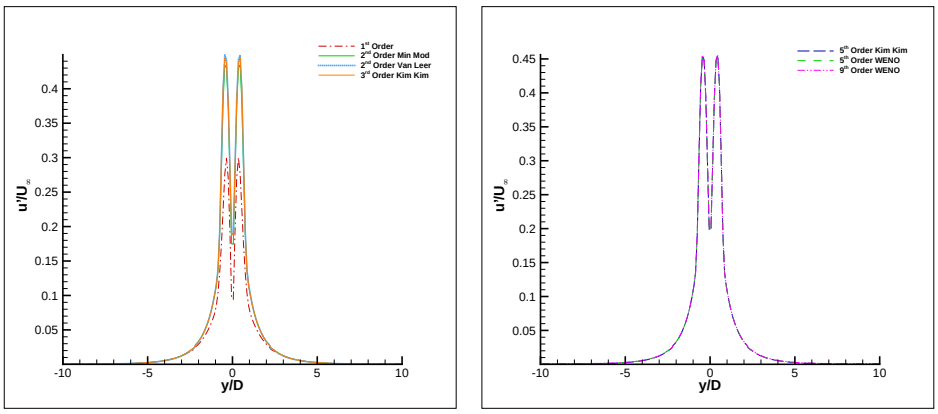

(a) Streamwise fluctuations at $x/D = 1.00$

(b) Streamwise fluctuations at $x/D = 1.00$

(c) Crossflow fluctuations at $x/D = 1.00$

(d) Crossflow fluctuations at $x/D = 1.00$

FIGURE 5.22: Reynolds Number 300, $2D$ flow. Fluctuations in the near wake, at $x/D = 1.00$.

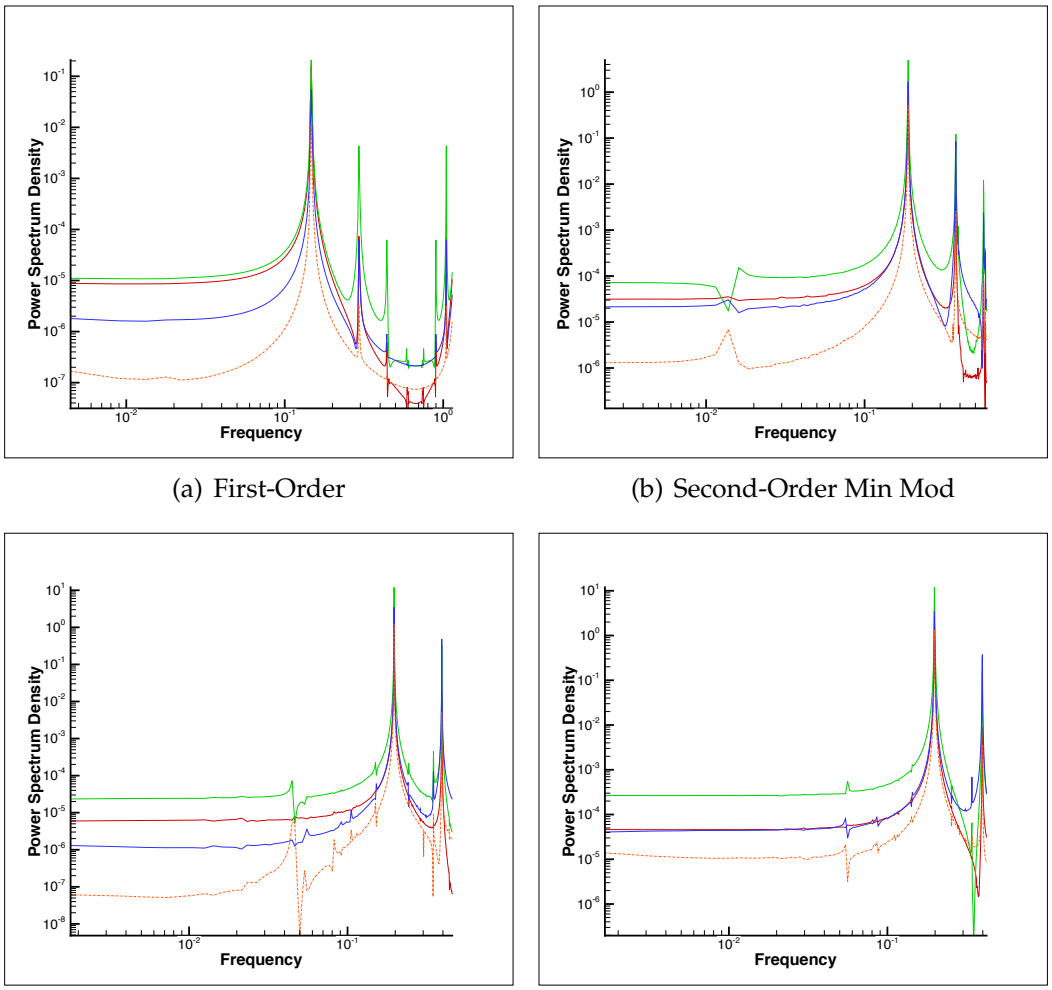

(a) First-Order (b) Second-Order Min Mod

(c) Second-Order Van Leer (d) Third-Order Kim Kim

FIGURE 5.23: Reynolds Number 300, 2D flows. Plots showing spectral plots for points at $y/D = 0$, with Red Line: $x/D = 0.58$, Green Line: $x/D = 1.50$, Blue Line: $x/D = 4.00$ and Orange Line: $x/D = 7.00$. Plots shown for each numerical scheme.

Figures 5.23 and 5.24 show the spectral plots of frequency of fluctuations. There is a clear harmonic frequency for most of the simulations in the wake of the cylinder, though it is interesting to note that the strength of the harmonic and sub-harmonic frequencies alter downstream such that certain frequencies are stronger further downstream in the wake of the cylinder. An example of this is visible in the second-order Van Leer plot (figure 5.31(c)) where the main sub-harmonic frequency (the second-highest peak in the data) occurs strongest at $x/D = 4.00$. These spectral plots show the differing Strouhal numbers present in the wake of the cylinder, and how the frequency of the fluctuations in the wake change as the flow is examined further downstream of the cylinder.

The first-order simulation previously showed some discrepancies in the values obtained around

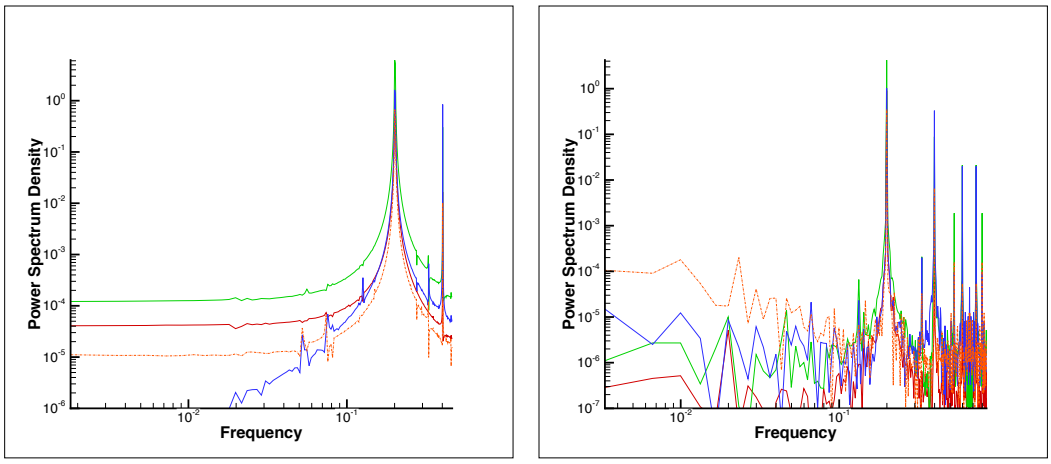

(a) Fifth-Order Kim Kim (b) Fifth-Order WENO

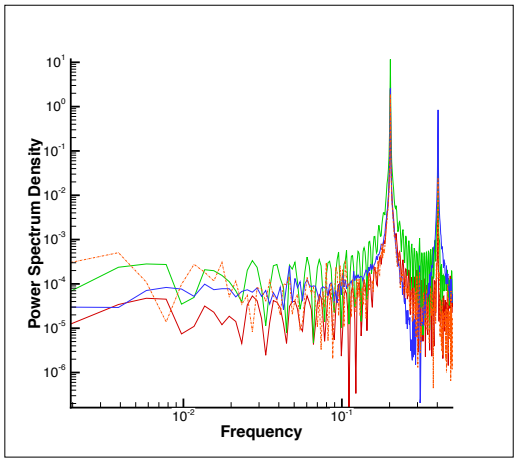

(c) Ninth-Order WENO

FIGURE 5.24: Reynolds Number 300, 2D flows. Plots showing spectral plots for points at $y/D = 0$, with Red Line: $x/D = 0.58$, Green Line: $x/D = 1.50$, Blue Line: $x/D = 4.00$ and Orange Line: $x/D = 7.00$. Plots shown for each numerical scheme.

the cylinder surface. This is again reflected in the wake of the cylinder, where the spectral plots show that the density of fluctuations is at least an order of magnitude lower than the remaining simulations.

Dataset Info		C_d	C_l	C_{p_b}	U_{min}	θ_{sep}[1]	St
Analytic (from eqn. 4.5)		-	-	-	-	-	0.2030
Exp.	Norberg [38]	-	0.435	-	-	-	0.203
	Williamson [35]	-	-	-0.96	-	-	0.203
	Wieselsberger [113]	1.22	-	-	-	-	-
Num.	Rajani [109]	1.37	0.604	-1.48	-	110.923°	0.215
	Mittal[2] [112]	1.38	0.65	-1.22	-	-	0.203
	Kravchenko [93]	1.28	0.40	-	-	-	0.203
This Work	First-Order	1.17	0.44	-1.22	-0.328	107.2°	0.147
	Second Order MinMod	1.33	0.57	-1.45	-0.196	109.2°	0.188
	Second Order Van Leer	1.35	0.59	-1.38	-0.171	109.4°	0.197
	Third Order Kim-Kim	1.36	0.58	-1.37	-0.171	109.2°	0.198
	Fifth Order Kim-Kim	1.37	0.58	-1.46	-0.163	109.3°	0.201
	Fifth Order WENO	1.38	0.60	-1.46	-0.149	109.4°	0.200
	Ninth Order WENO	1.37	0.59	-1.48	-0.154	108.9°	0.203

TABLE 5.3: $Re = 300$ 2-dimensional Results

Table 5.3 shows numerical data extracted from the simulations, compared to literature values. The first-order scheme shows the resulting quantities of the differing flow around the cylinder surface, with lower coefficient of lift, higher drag, and a lower base pressure. Interestingly, the first-order simulation provides good agreement in some areas with the experimental values obtained, however with a Strouhal number that is quite different from all literature values, as well as the effects seen earlier around the cylinder circumference, it is clear that the results from the first-order simulation are not satisfactory.

The higher-order simulations show some over-prediction of a number of the values compared to experiment, though show good agreement with other two-dimensional based numerical values. This is a finding that has been reported elsewhere [112]. The two dimensional simulations lose some of the flow features present in an experimental set up - namely the three-dimensional perturbations that occur. As a result, the two-dimensional Reynolds stresses are reduced, leading to a reduction in base suction pressure.

[1]For simulations carried out for this work, θ_{sep} has potential errors of $\pm 1.08°$, due to the resolution of cells (and their subsequent arc sizes) around the circumference of the cylinder

[2]$2D$ Simulations

5.5 Reynolds Number = 3900

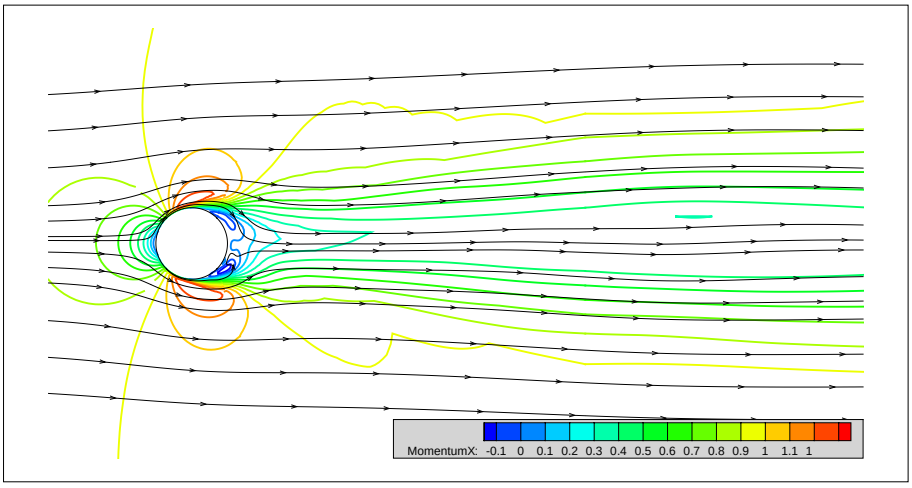

(a) Time averaged plot of Reynolds number 3900 2D flow

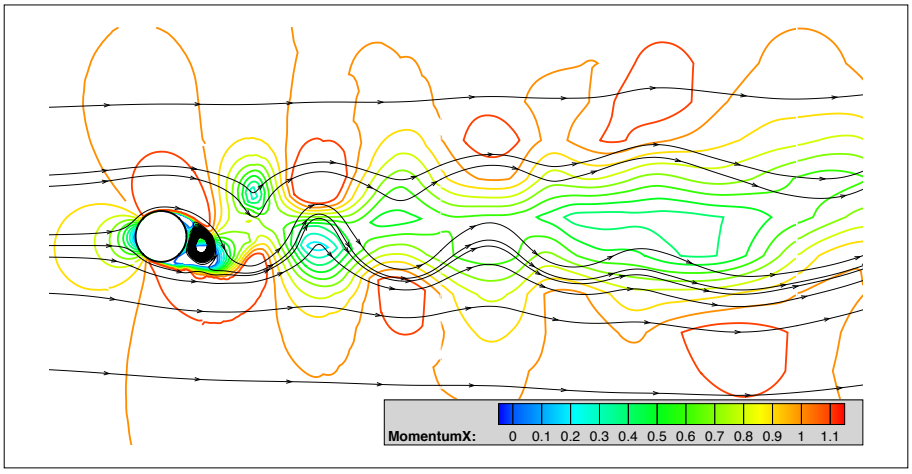

(b) Instantaneous plot of Reynolds number 3900 2D flow

FIGURE 5.25: Time averaged (subfigure 5.25(a)) and instantaneous (subfigure 5.25(b)) plots of Reynolds number 300 2D flow, 5^{th} Order WENO scheme.

As the Reynolds number increases beyond 1,000, flow velocity increases such that vortices are expected to appear in free shear layers [106], resulting in fully turbulent flow in the wake of the cylinder in a 3D or experimental case. Spanwise effects aren't computed in the two-dimensional flow and so we do not get all the turbulent effects of the flow. However, there are some additional instabilities evident in the flow due to the flow speed over the cylinder; this is clearly visible in figure 5.25(b), with a strong vortical flow to the rear of the cylinder that oscillates in position in an up/down direction. The vortices are shed from the wake and flow downstream within the wake, eventually dissipating into the surrounding flow.

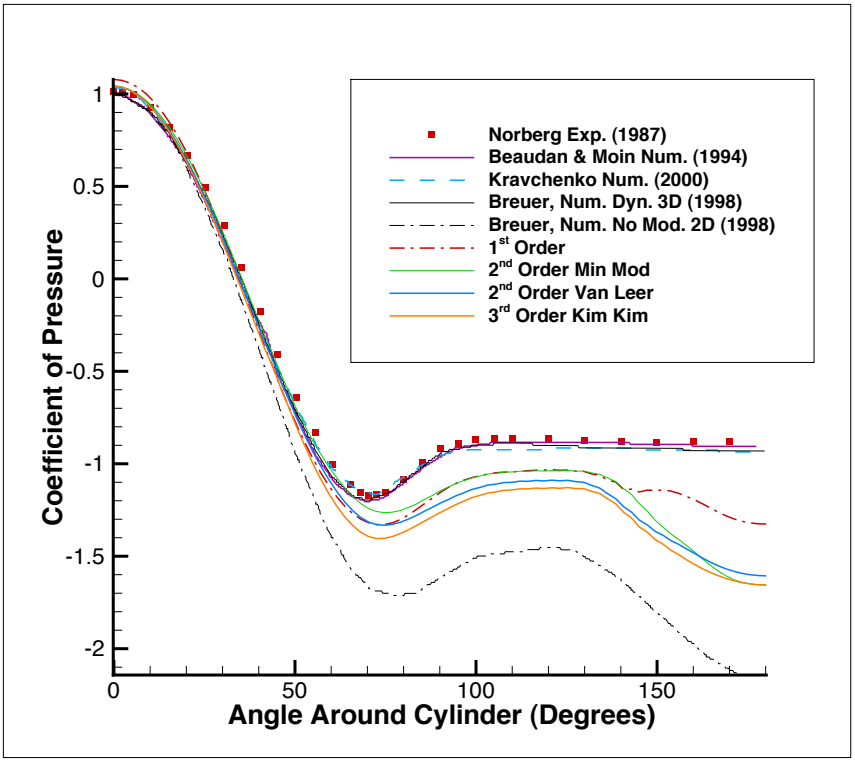

(a)

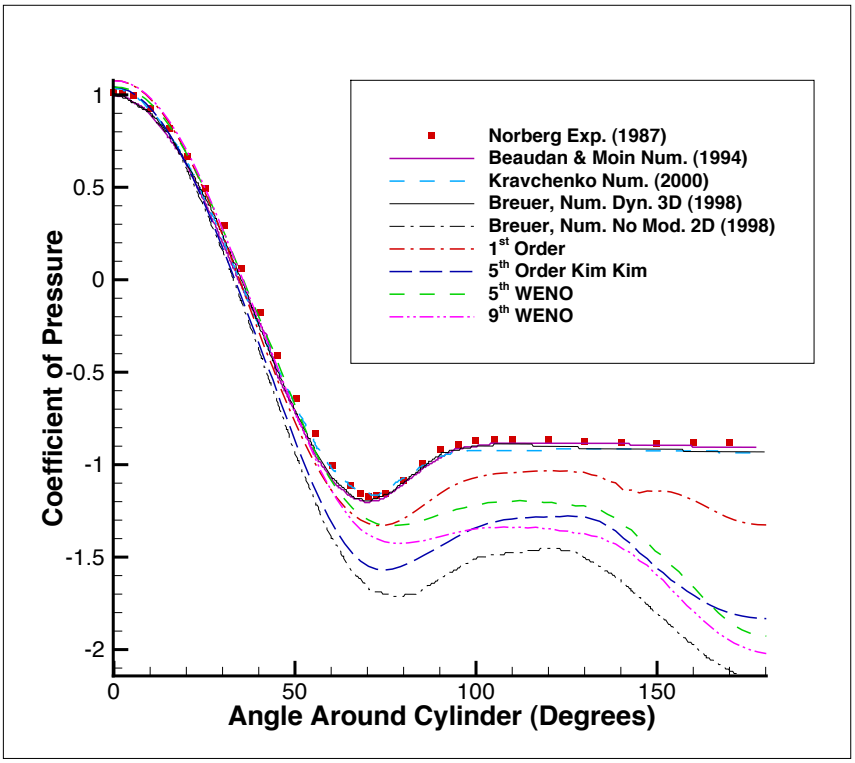

(b)

FIGURE 5.26: Reynolds Number 3900, 2*D* flows giving coefficient of pressure around the cylinder for differing orders of run.

Figure 5.26 shows the plots of Coefficient of pressure around the cylinder at Reynolds number 3900, for the different numerical schemes. Rather interestingly, it is clear that the lower-order schemes show better agreement to the experimental and three-dimensional numerical literature data available. On the other hand, the higher-order simulations show a tendency to steer towards the two-dimensional numerical data. As these simulations have been run in two-dimensions, the

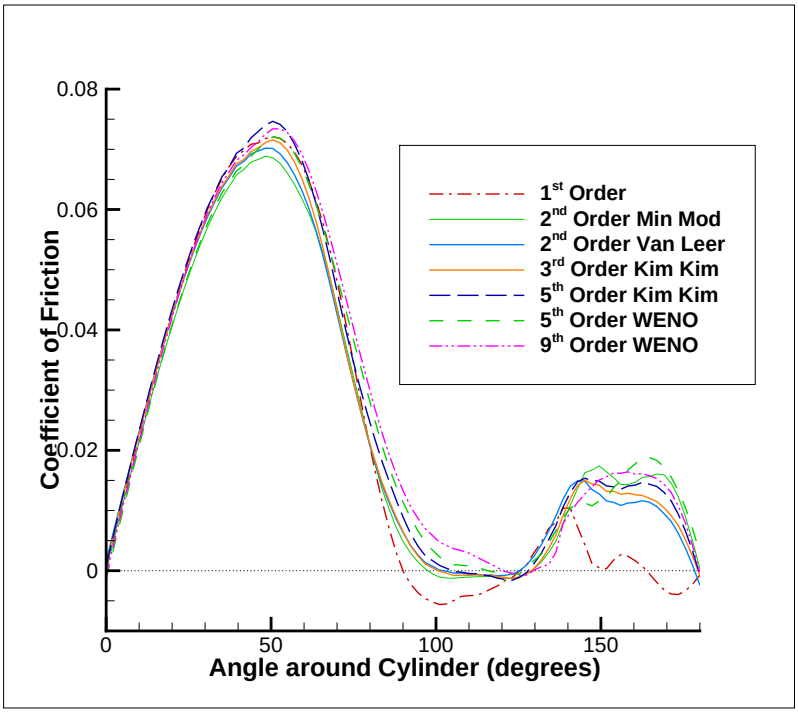

(a)

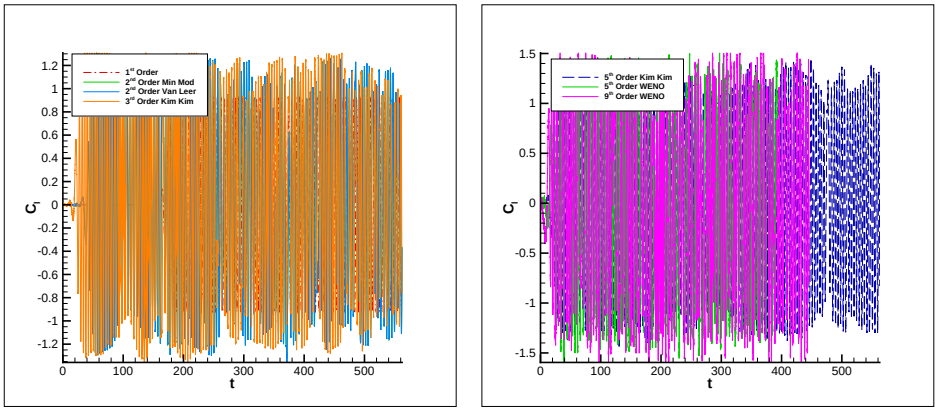

(b) (c)

FIGURE 5.27: Reynolds Number 3900, 2*D* flows giving coefficients of friction (subfigure 5.27(a)) and lift (subfigures 5.27(b) and 5.27(c)) around the cylinder for differing orders of run.

expectation was that the simulations would tend towards the two-dimensional literature data as opposed to the three-dimensional literature data. For the higher-order schemes, this does appear to be the case.

The coefficient of friction (figure 5.27(a)) shows some agreement between the different simulations, with the first-order simulation once again under-predicting the friction coefficient to the rear of the separation point. However, these plots of coefficient of friction are slightly different from that expected, with a rapid drop of friction at the rear of the cylinder. While this corresponds with vortical flow to the rear of the cylinder, this indicates that the vortices present are extremely close to the rear of the cylinder.

The plots of coefficient of lift (subfigures 5.27(b) and 5.27(c)) for the simulations show the simulations reached a state of highly fluctuating flow fairly rapidly. The mean coefficients of lift and drag for the simulations were determined, and are listed at the end of this section, in table 5.4.

Figures 5.28 and 5.29 show the time-averaged flow values for the different simulations, in the wake of the cylinder. Figure 5.28 shows the flow in the stream-wise direction, while figure 5.29 shows the cross-stream flow - that is, momentum in X and momentum in Y respectively. Each of these figures is split into two, to differentiate between the different numerical schemes. At this higher Reynolds number (where the flow is actually expected to be fully three-dimensional in nature), it would appear that both the first-order and 9^{th} order WENO schemes show similar characteristics to each other - underpredicting the flow momentum in both momentum directions compared to the remaining simulations. The flow clearly dissipates downstream of the cylinder most rapidly for both the first-order and ninth-order based schemes, while the fifth-order schemes also show dissipation more rapidly than the second- and third-order based schemes.

Figure 5.30 shows the fluctuations in the near-wake of the cylinder. Unlike the time-averaged velocity plots, the fluctuations show that in most cases the fluctuations are more consistent between the numerical schemes. However, unlike the lower Reynolds numbers where fluctuations were found to increase marginally before dropping off, at this Reynolds number the fluctuations dissipate continuously downstream of the cylinder. The plots containing the fluctuations further downstream in the wake are included in Appendix B.

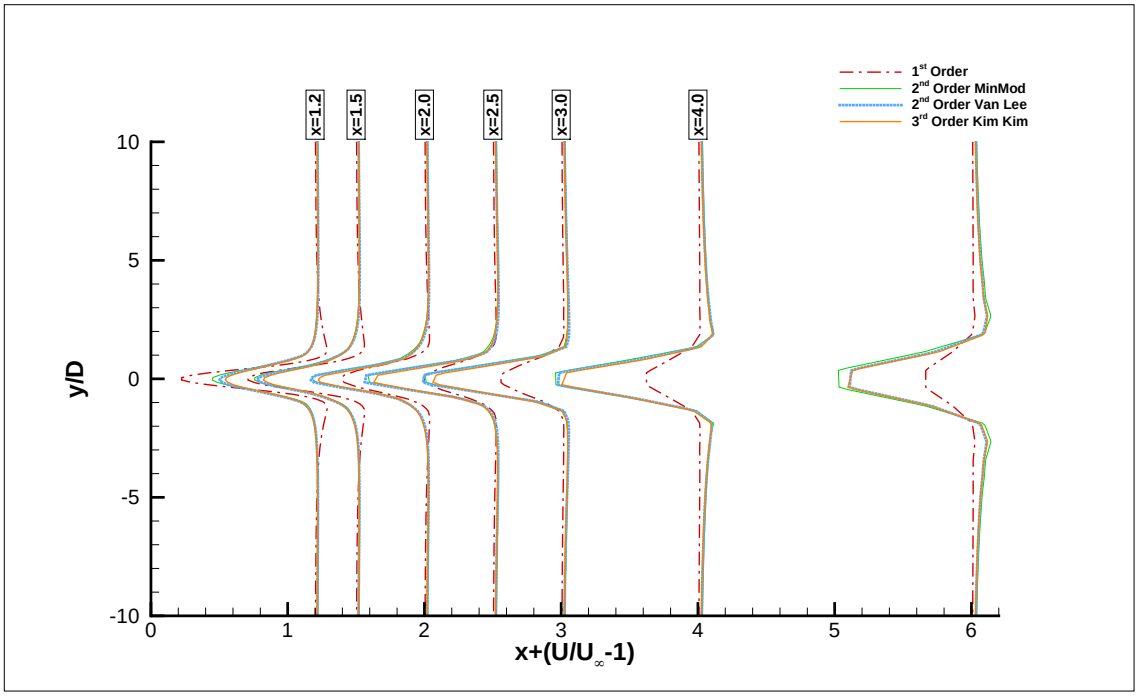

(a) Streamwise momentum along vertical lines in the wake

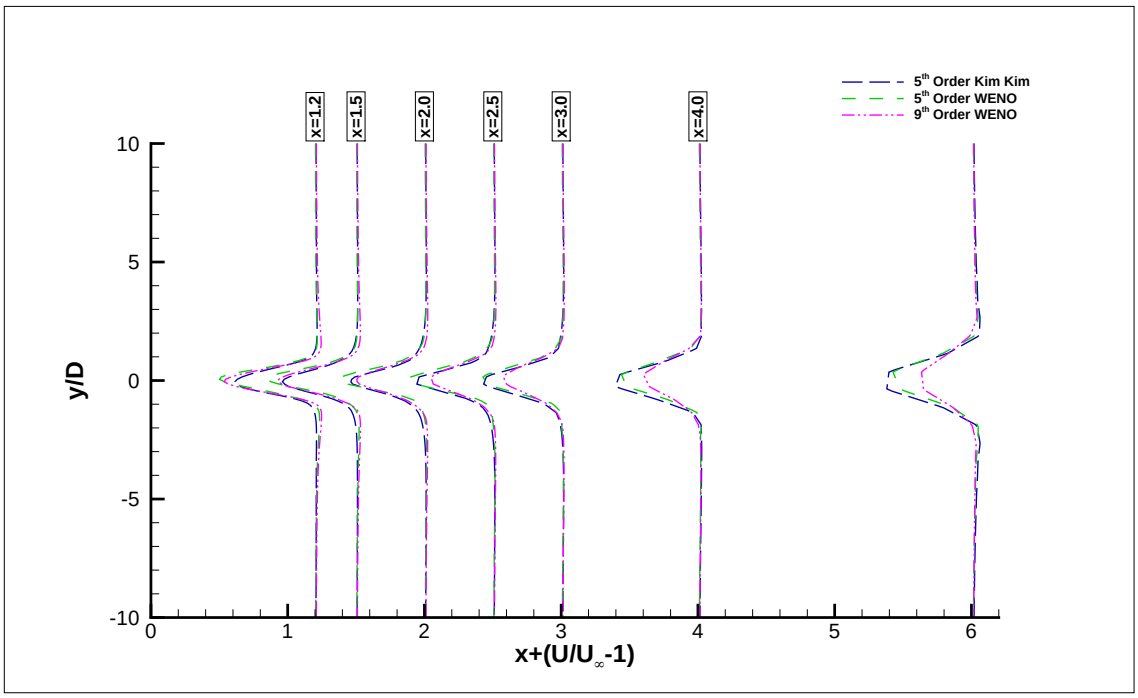

(b) Streamwise momentum along vertical lines in the wake

FIGURE 5.28: Reynolds Number 3900, 2*D* flows (a) showing lower-order stream-wise flow momentum, and (b) showing the higher order stream-wise flow momentum.

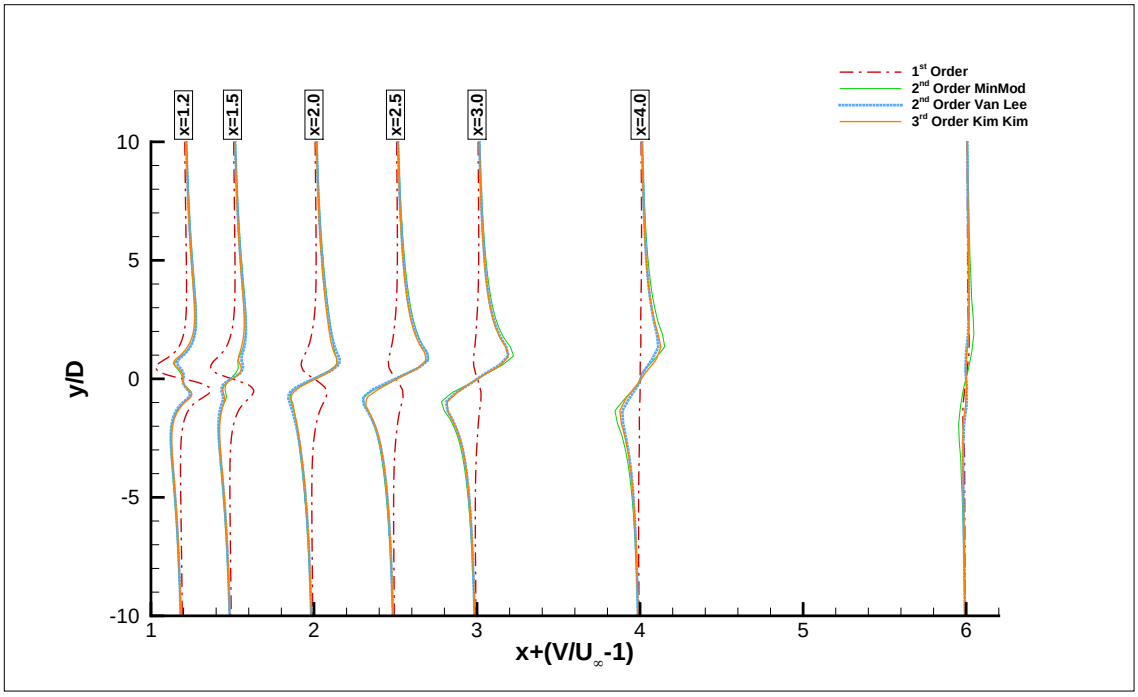

(a) Crossflow momentum along vertical lines in the wake

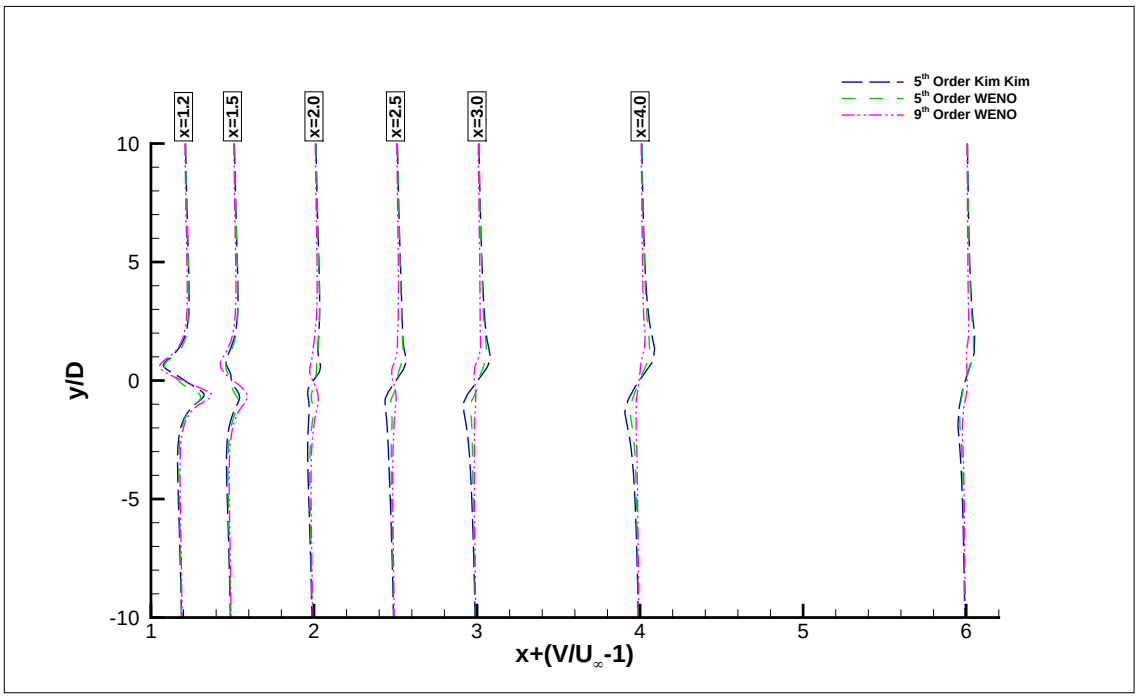

(b) Crossflow momentum along vertical lines in the wake

FIGURE 5.29: Reynolds Number 3900, 2*D* flows (a) showing lower-order Cross-flow momentum, and (b) showing the higher order Cross-flow momentum.

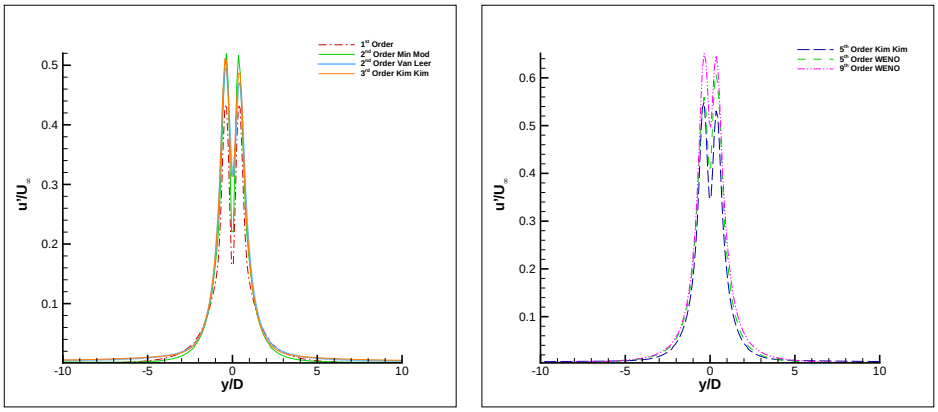

(a) Streamwise fluctuations at $x/D = 1.00$

(b) Streamwise fluctuations at $x/D = 1.00$

(c) Crossflow fluctuations at $x/D = 1.00$

(d) Crossflow fluctuations at $x/D = 1.00$

FIGURE 5.30: Reynolds Number 3900, $2D$ flow. Fluctuations in the near wake, at $x/D = 1.00$.

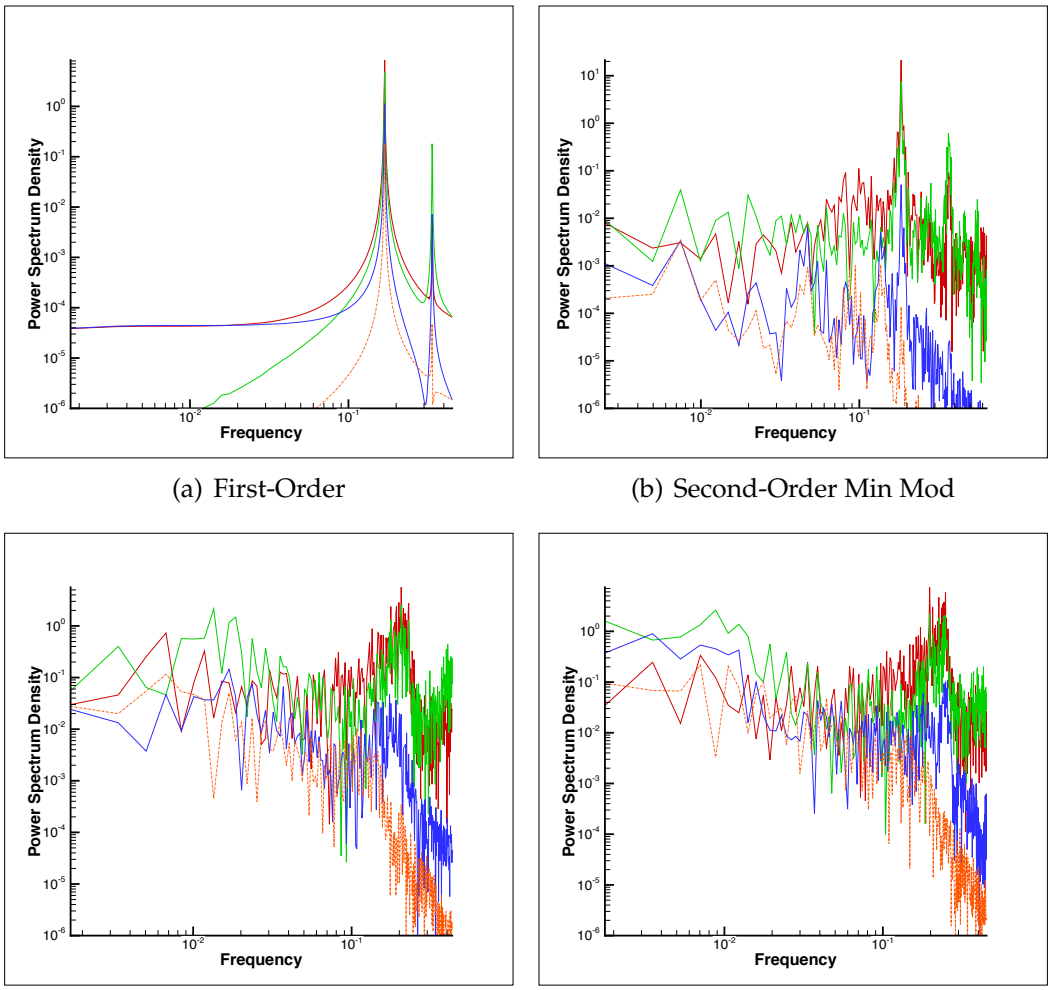

(a) First-Order

(b) Second-Order Min Mod

(c) Second-Order Van Leer

(d) Third-Order Kim Kim

FIGURE 5.31: Reynolds Number 3900, 2D flows. Plots showing spectral plots for points at $y/D = 0$, with Red Line: $x/D = 0.58$, Green Line: $x/D = 1.50$, Blue Line: $x/D = 4.00$ and Orange Line: $x/D = 7.00$. Plots shown for each numerical scheme.

Figures 5.31 and 5.32 show the spectral plots of frequency of fluctuations in the cylinder wake. There is a clear harmonic frequency in the wake of the cylinder for the first order simulation, but it is also clear that this simulation isn't correctly displaying the flow characteristics fully. The first-order simulation previously showed some discrepancies in the values obtained around the cylinder surface, and this is again reflected in the wake of the cylinder.

Previously, at Reynolds number 300, some clear signs of peakedness representing the harmonic and sub-harmonic frequencies were evident. This has now changed, with only the first-order simulation showing distinct peak values. The remaining higher-order runs instead show quite noisy frequency data, proving the existence of features resembling turbulence (although as this is a 2D run, they are instead violent fluctuations) in the wake.

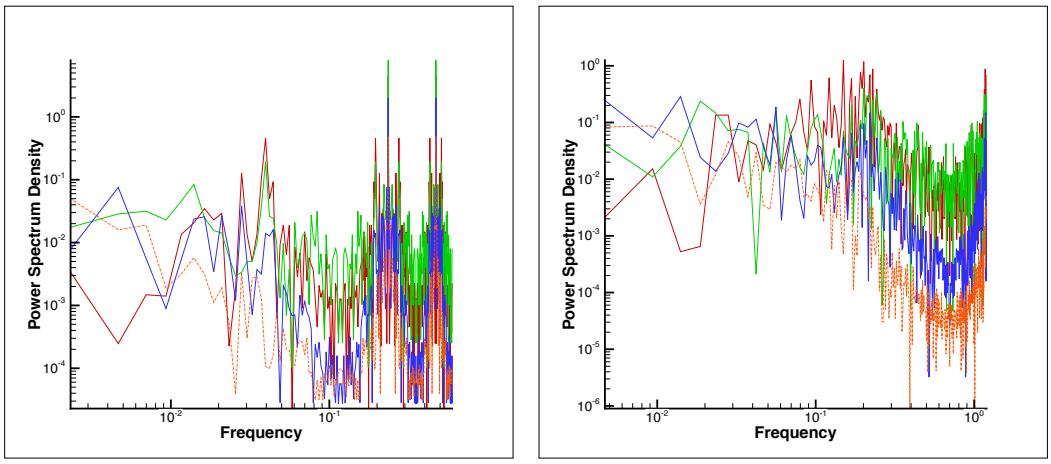

(a) Fifth-Order Kim Kim

(b) Fifth-Order WENO

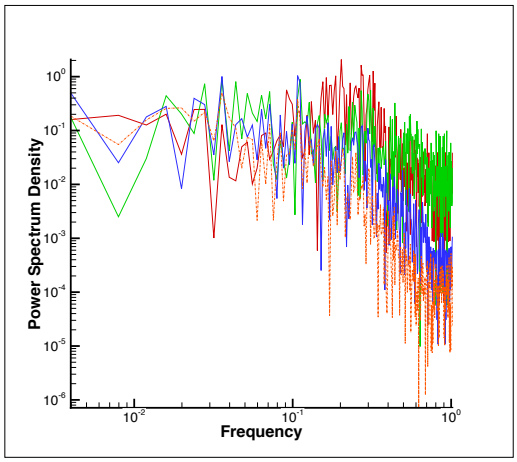

(c) Ninth-Order WENO

FIGURE 5.32: Reynolds Number 3900, $2D$ flows. Plots showing spectral plots for points at $y/D = 0$, with Red Line: $x/D = 0.58$, Green Line: $x/D = 1.50$, Blue Line: $x/D = 4.00$ and Orange Line: $x/D = 7.00$. Plots shown for each numerical scheme.

Dataset Info		C_d	C_l	U_{min}	θ_{sep}[1]	St
Predicted from model given in Norberg [38]		-	0.0830	-	-	0.2089
Experimental	Reported in [45, 114, 115]	0.98	0.03-0.08	-0.24	86.0°	0.215
	From [38, 116, 117]	$\pm$0.05	-	$\pm$0.1	$\pm$2	$\pm$0.005
	Son [98]	-	-	-	85/86°	-
	Norberg [117]	0.98	-	-	-	-
	Cardell [116]	-	-	-	-	0.215
	Lourenco [118]	0.99	-	-0.24	86°	0.215
	Ong [119]	-	-	-	-	0.21
Numerical	Mittal [120]	1.0	-	-0.35	86.9°	0.207
	Breuer[2] [85]	1.625	-	-	100.7°	-
	Fröhlich [121]	1.08	-	-0.24	88.1°	0.216
	Kravchenko [45]	1.04	-	-0.37	88.0°	0.210
	Ma[3] [122]	0.96	-	-	89.1°	0.203
	Franke [123]	0.98	-	-	88.2°	0.209
	Mahesh [124]	1.00	-	-0.31	87.6°	0.218
	Park [125]	1.02	-	-0.33	-	0.209
	Young[4] [115]	1.59	1.17	-	-	0.235
	Young[5] [115]	1.55	1.08	-	-	0.217
This Work	First-Order	1.13	0.94	-0.285	90.0°	0.169
	Second Order MinMod	1.31	1.13	-0.260	97.7°	0.183
	Second Order Van Leer	1.29	1.09	-0.252	102.4°	0.206
	Third Order Kim-Kim	1.34	1.05	-0.239	100.3°	0.198
	Fifth Order Kim-Kim	1.43	1.25	-0.119	104.6°	0.236
	Fifth Order WENO	1.52	1.30	-0.165	115.9°	0.200
	Ninth Order WENO	1.56	1.31	-0.193	120.5°	0.202

TABLE 5.4: $Re = 3900$ 2-dimensional Results

As was previously observed at the lower Reynolds number of 300, the two-dimensional results at $Re = 3900$ over-predict the values of the coefficients for the cylinder. However, they do correspond with literature two-dimensional results (such as those given by Breuer [85] and Young [115]). The angle of separation, however, generally is too high for this case. The flow clearly stays attached to the cylinder for too long around the cylinder, leading to the higher coefficient values. The closest angle of separation value is given by the first-order simulation, however it has already been seen that the first-order simulation does not satisfactorily predict the flow at this

[1]For simulations carried out for this work, θ_{sep} has potential errors of $\pm 1.08°$, due to the resolution of cells (and their subsequent arc sizes) around the circumference of the cylinder

[2]2D Case

[3]DNS Run as opposed to other numerical data from LES simulations

[4]2D URANS method

[5]3D LES, using 4 cells in z direction to give closest LES simulation to a 2-dimensional run

Reynolds number. The Strouhal number values, however, show better agreement with literature values. Thus it seems that in spite of the increased coefficient values, the frequency of fluctuations of flow over the cylinder is generally fairly consistent with literature values, once again with the exception of the first-order simulation.

5.6 Discussion of two-dimensional results

Examining the two-dimensional flows detailed over this chapter, some clear patterns become noticeable. Perhaps the most clear is the results from the first-order simulations; these simulations did not provide adequate results overall. Even in the laminar flow simulation at $Re = 40$, the first-order simulation noticeably under-predicted the coefficients of pressure and friction at the rear of the cylinder. It was expected that, were the first-order simulation to provide comparatively good results, it would be the laminar flow of Reynolds number 40 that would show the best outcome. Instead, even at the lowest Reynolds number, an artificial drop in coefficient of friction at the rear of the cylinder is clear. This artificial drop of C_f continues with the first-order simulation through all the Reynolds number runs, to worsening extents. This shows the first order simulations struggle with resolving the separated flow and the near-wake of the cylinder. The first-order coefficient of pressure values show an increase in C_p to the rear of the cylinder, corresponding to the drop in C_f. Interestingly, at $Re = 300$, the first-order simulation gave a plot of C_p closer to the experimental values than any of the higher-order runs. However, the higher-order runs agreed much stronger with the numerical literature data available, and thus the quality of the experimental data (which was obtained as far back as 1933) may not be ideal. Furthermore, at $Re = 200$, when the flow is transitioning to have periodicity in the wake, the first-order flow remains laminar whilst the remainder of the simulations showed the oscillations expected.

The results for $Re = 40$ and $Re = 200$ with the two-dimensional simulations show good agreement with the literature data available. In literature, (such as [85, 108, 112]) it was found that three-dimensionality effects produce higher coefficient values compared to experimental data, and thus as the Reynolds number increases three-dimensional simulations are preferable to two-dimensional simulations. This can be seen with the results from these simulations such that deviation from literature values increases once Reynolds number 300 is reached, and so it can be said that as that Reynolds number is reached and exceeded, two-dimensional simulations are no longer suitable. Even the use of the higher-order methods does not help resolve the flow adequately, due to the lack of presence of three-dimensional flow perturbations that affect the wake flow and the flow values over the cylinder itself. However, the examination of the two-dimensional higher-order simulations at Reynolds number 3900 shows improvement over other two-dimensional simulation methods such as the LES computations carried out by Breuer [85], when compared with three-dimensional simulation values and experimental values.

Comparing the higher-order methods to each other, it would appear firstly that with regards to reaching developed flow from a cold start, the higher-order the method, the earlier the arrival of the expected fluctuating flow. The subsequent effects to the rear of the cylinder (such as the Von Karman vortex street) also appearing in the flow in a shorter simulation run time than the lower-order methods such as the second-order simulations. However, the difference in time for flow to develop isn't always extreme. An interesting exception is the Kim Kim based schemes at the Reynolds number flows below 3900 that generally takes longest to develop.

With the highly fluctuating flow at Reynolds number 3900, the flow in the wake has resemblance with turbulent features, and regions of vortices are strongly detached from the recirculating flow. This is as expected, and is likely due to the lack of three-dimensional perturbations as previously discussed. The wake of the WENO schemes at Reynolds number 300 was shown to have stronger non-repeating fluctuations than the remaining flow simulations at that Reynolds number; again, this is likely due to a lack of three-dimensionality. At the lower Reynolds number of 200, the spectral plots show the simulations have presented sub-harmonic fluctuations in the wake. Most of the higher-order simulations show these with good agreement, with an exception being the ninth-order WENO scheme which shows a greater number of sub-harmonic frequencies than the remainder of the simulations. It would seem that at both Reynolds numbers 200 and 300, the WENO scheme is attempting to resolve highly unstable flow effects in the wake, in spite of the lack of the third-dimension.

Overall, the second-order schemes show good agreement with literature values (taking into account discrepancies due to a lack of three-dimensionality of the simulations), though of the two the Van Leer MUSCL scheme shows best agreement, particularly with regards to the frequency of oscillations over the cylinder (the Strouhal number). Thus, for the three-dimensional simulations, the second-order Van Leer is chosen as being a candidate for testing. Equally, the fifth-order numerical schemes are also chosen for three-dimensional testing as not only does this test both the Kim Kim and WENO schemes, but tests both at the same numerical order.

6

3D Simulation Results

The most exciting phrase to hear in science, the one that heralds new discoveries, is not 'Eureka!' (I found it!) but 'That's funny...'
Isaac Asimov (1920 - 1992)

* * * * *

6.1 Chapter description

As in chapter 5, this chapter contains the results of the 3D simulations that were carried out, split into appropriate sections for each Reynolds number run. As listed in table 4.3, the Reynolds numbers at which 3D simulations were run were 200, 300 and 3900. These flow speeds are those at which 3-dimensional effects are expected to play a part in the overall resulting flow, thus differences between the 2-dimensional and 3-dimensional results are expected. Furthermore, fully turbulent flow is expected at both Reynolds numbers of 300 and 3900. Therefore, the range of chosen Reynolds numbers spans flow from transitional to turbulent flow.

The three-dimensional simulations were carried out by restarting from developed flow points in the relevant two-dimensional simulations (that is, second-order Van Leer simulations were started from the developed flow in the two-dimensional second-order Van Leer simulation at the same Reynolds number). This was in order to speed up the processing of the three-dimensional simulations, as even with this restart method a great number of CPU hours were required for

the flow to be sufficiently resolved. In order to promote turbulent effects in the flow, a test was carried out adding a random perturbation to the flow at the inlet. However, following this, the flow was allowed to develop on its own accord with steady inlet conditions.

The Reynolds numbers whose results are presented in this section are as follows (with section numbers given in brackets):

- Reynolds Number = 200 (6.2)
- Reynolds Number = 300 (6.3)
- Reynolds Number = 3900 (6.4)

6.2 Reynolds Number = 200

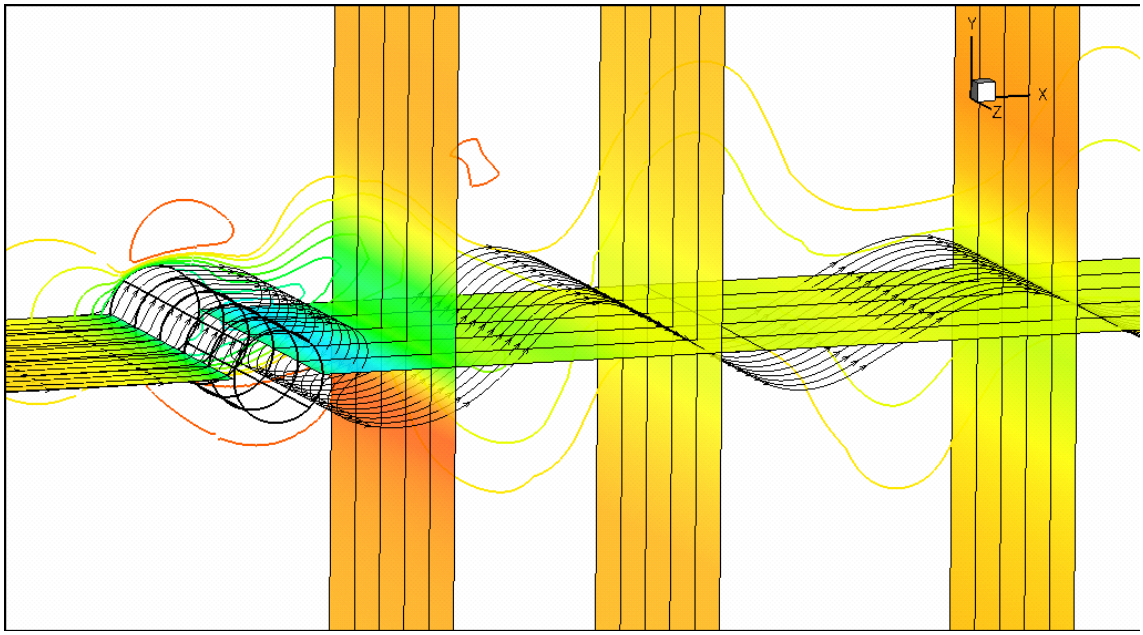

FIGURE 6.1: Instantaneous plot at one time-step of the 3D flow at Reynolds Number 200 for 2^{nd} Order Van Leer

With the flow at Reynolds number 200, the von Karman instability and vortex streets are generated within the flow, and correspondingly in the simulations. To the rear of the cylinder, vortex shedding is observed, whereby the vortices generated just above and below the near wake of the cylinder 'break away' from the surrounding flow. However, the oscillations in the wake are periodic, as is the shedding of the vortices. The flow separates at a point around the cylinder, that changes according to the Reynolds number of the flow, (and is defined in the table of numerical values, table 6.1) but is generally on the rear half of the cylinder. There is a stagnation point at the fore of the cylinder.

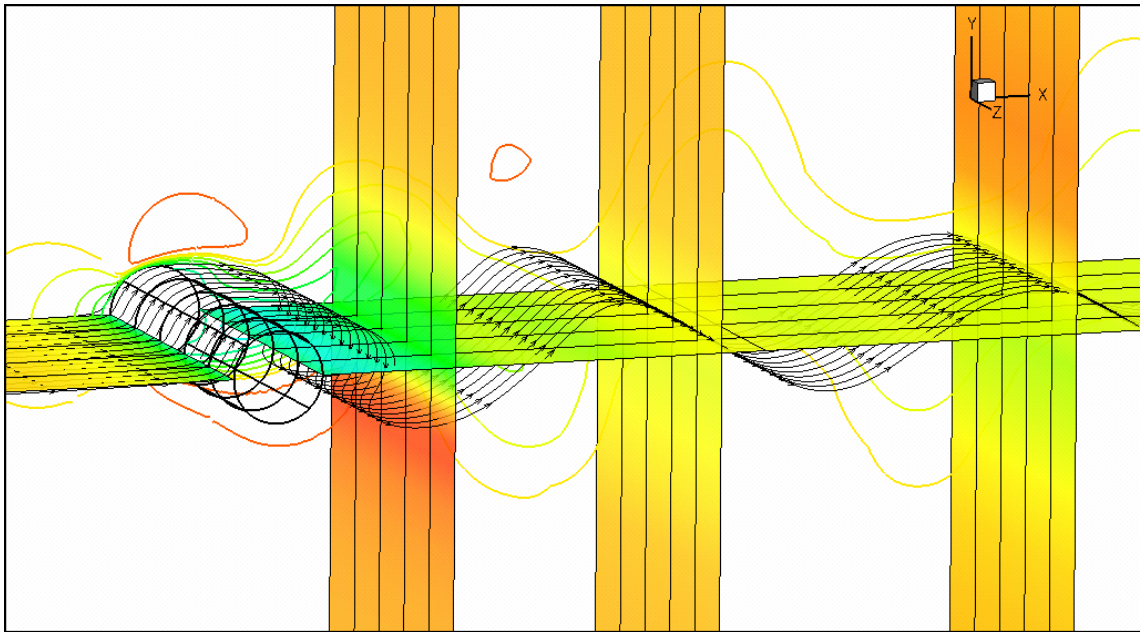

(a) 5^{th} Order Kim Kim

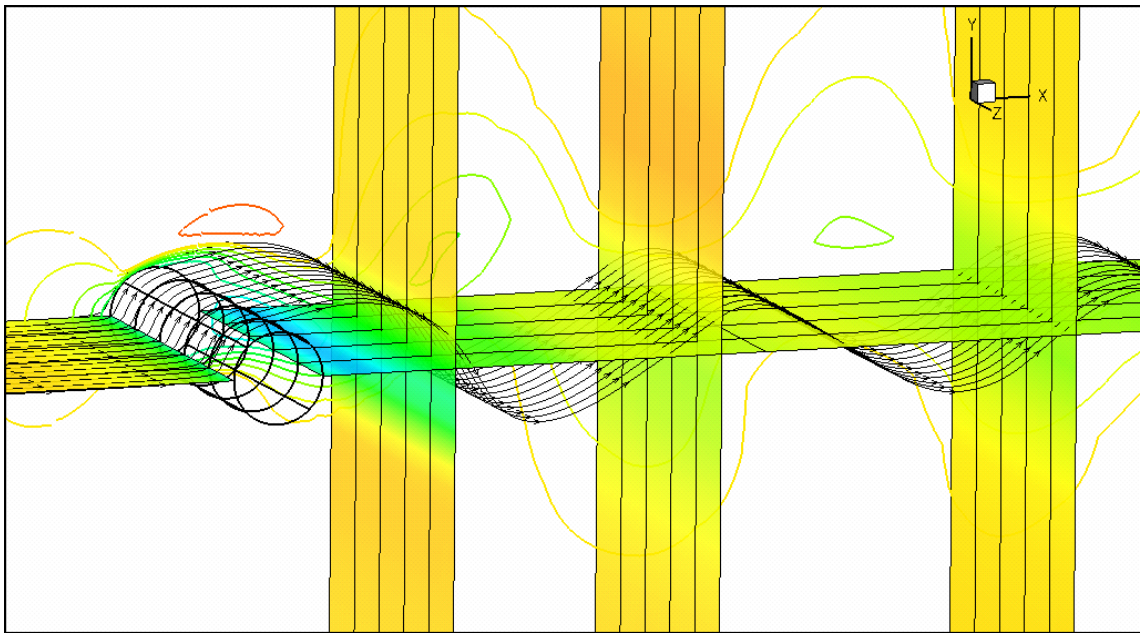

(b) 5^{th} Order WENO

FIGURE 6.2: Instantaneous plots at one time-step of the $3D$ flow at Reynolds Number 200

At this Reynolds number, the flow regime changes due to the presence of three-dimensional shear stresses. The flow has now entered a phase of transition in the wake for the formation of Karman Vortex Streets that separate from the cylinder in the wake [106]. In a three-dimensional flow, such as in experimental flows and the three-dimensional simulations here, where the third direction of momentum is present three-dimensional instabilities lead to the formation of stream-wise vortices. In [107], it was reported that above a value of $Re = 170$, the periodic solution becomes unstable, with any two-dimensional perturbations more rapidly damped than three-dimensional perturbations, as previously discussed in the two-dimensional results section for this reynolds number (chapter 5.3). At this Reynolds number, fluctuations of finite-amplitude play a decisive role in the determination of the 'branch' that the system will follow, influencing the state of the wake significantly [108]. The change in these simulations to a three-dimensional simulation set up clearly allows the effects of the three-dimensional perturbations to become more significant, such that the stream-wise vortices clearly appear in all simulations and are stronger than those observed in the two-dimensional simulations. It was also previously observed in the two-dimensional simulations that there were discrepancies between two-dimensional simulations and three-dimensional flow values. Here, the differences between the same simulations, run in two-dimensions and three-dimensions are made clear, with improvement in all the schemes.

Figure 6.3 shows the plots of Coefficient of pressure and coefficient of lift around the cylinder at Reynolds number 200, for the different numerical schemes. Subfigure 6.3(b) showing the change in coefficient of lift shows that once flow has developed at this Reynolds number, the coefficient oscillates continuously. The plot for 5^{th} order WENO is not included to aid in clarity of the figure. The coefficient of drag plot over time showed a similar pattern to the coefficient of lift.

Subfigure 6.3(a) shows good agreement of the coefficient of pressure from the higher-order simulations with literature data available, however, the Van Leer and Kim Kim simulations do appear to under-predict the values slightly compared to the experimental literature results as the flow reaches and passes the separation point. It is interesting to note that the fifth-order WENO scheme predicts the coefficient of pressure closer to the experimental values than the other. However, the non-WENO schemes show very good agreement with each other, and both appear to predict the coefficient of pressure all around the cylinder slightly better than the numerical data from Rajani [109]. Comparing these values of C_p with those from the two dimensional plots, the 5^{th} order Kim Kim scheme doesn't show a great difference, while the WENO scheme shows good improvement and the 2^{nd} order Van Leer scheme actually deviates further from the experimental data at the rear of the cylinder than had been observed in the corresponding two-dimensional simulations. The greatest improvement, however, would appear to be from the WENO scheme run in three-dimensional form as opposed to the previous two-dimensional form.

Examining the coefficient of friction plot, figure 6.4, shows that with regards to this coefficient, the fifth-order Kim Kim numerical simulation agrees best with both the numerical literature data, as well as the experimental data at $Re = 287$. It was discussed in the two-dimensional section that there is a critical point of transition at around $Re = 170$, and so it would seem that the experimental data from $Re = 151$ is for a flow prior to the transition of flow. The experimental data at $Re = 287$ however, is clearly in a suitable regime of flow, given that the numerical results

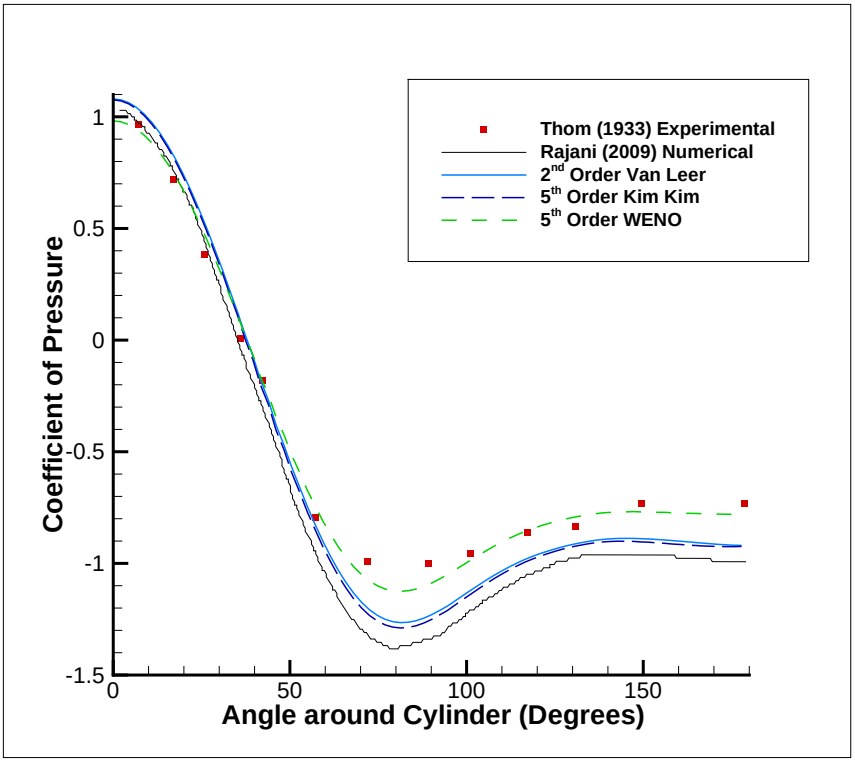

(a) C_p around the cylinder. Note: Experimental data from [105] ($Re = 229$), numerical data from [109]

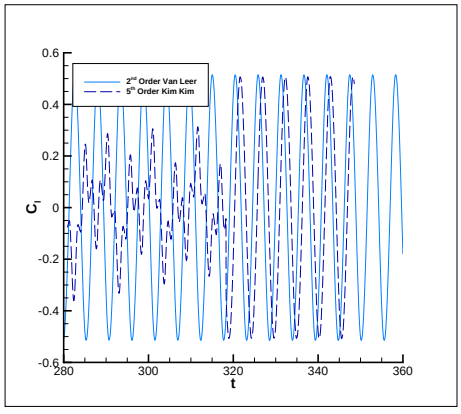

(b) An example of development of coefficient of lift over time, 2^{nd} Order Van Leer and 5^{th} Order Kim Kim schemes

FIGURE 6.3: Reynolds Number 200, $3D$ flows giving coefficient of pressure (a) and coefficient of lift over time, around the cylinder for differing orders of run.

all match very well with this data. There is a difference in results between the coefficient of pressure plot and this coefficient of friction plot. Whereas, in the coefficient of pressure plot, the fifth-order WENO scheme showed very good agreement, the coefficient of friction for this scheme

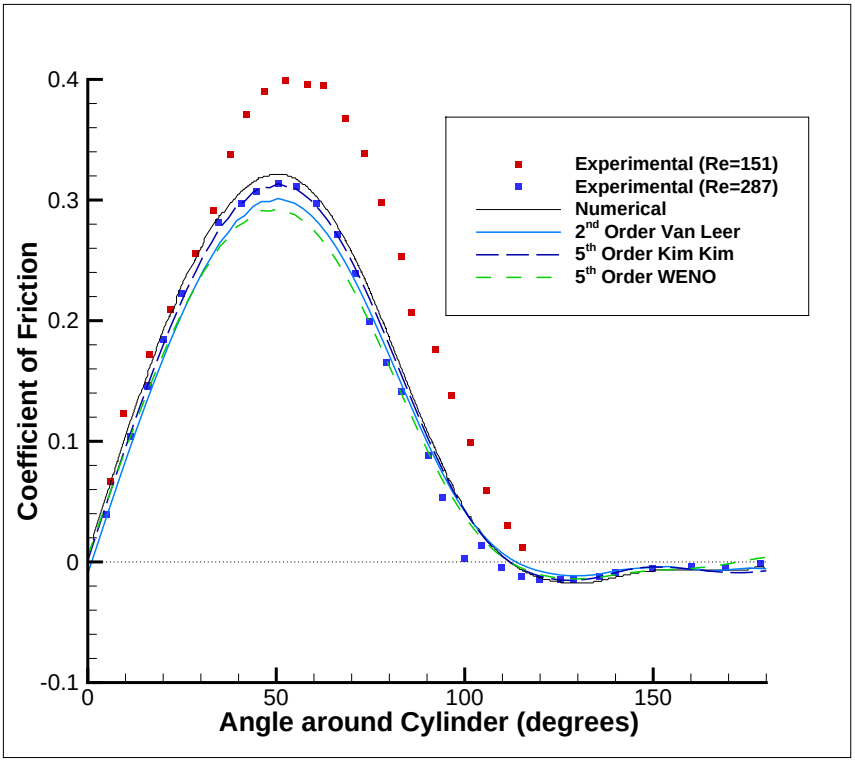

FIGURE 6.4: Reynolds Number 200, $3D$ flows showing coefficient of friction. Note: Experimental data from [110], numerical data from [109]

does not show the same agreement between the two, with the WENO scheme under-predicting the peak of coefficient of friction. In addition, the second order Van Leer and fifth-order Kim Kim schemes both under-predicted the coefficients of pressure, while those schemes showed good agreement with the literature data available for the coefficient of friction values, particularly the fifth-order Kim Kim scheme. However, the angle of separation (where $C_f = 0.0$) shows very good agreement between all the numerical schemes and the numerical literature data available.

The figures in 6.6 shows the time-averaged flow values for the different simulations, in the wake of the cylinder in both stream-wise and cross-flow directions - that is, momentum in X and momentum in Y respectively. The simulations show very good agreement with one another of the time-averaged momentum along the wake, with almost identical values downstream. The dissipation rates into the surrounding flow shows agreement across all the simulations, with only marginal differences between the different numerical schemes. As with the previous two-dimensional simulations, the momentum in Y reduces towards freestream momentum more rapidly than the momentum in X flow - that is the flow in the Y direction has less 'strength' downstream than the flow in the x direction to maintain its momentum. This is likely due to the lower momentum values of the flow in the Y direction.

Figure 6.7 shows the fluctuations in the momentum, in time-averaged form, in the near wake of the cylinder. The fluctuations of the momentum increase slightly downstream as the flow

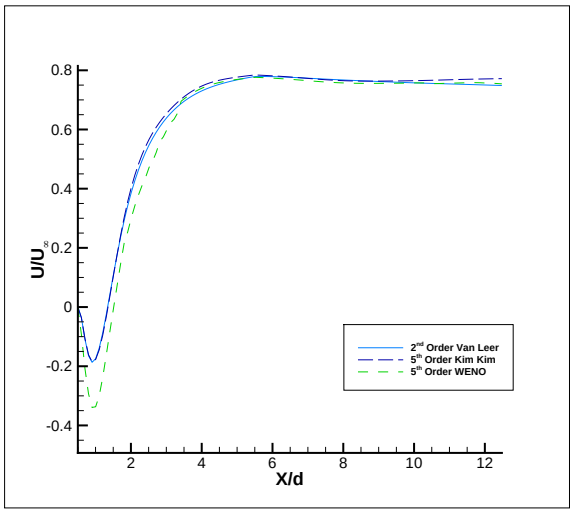

FIGURE 6.5: Reynolds Number 200, 3D flow. Time-averaged streamwise momentum in the wake of the cylinder, along the line $y/D = 0$.

dissipates into the surrounding flowfield, before steadily dropping again. The fifth-order WENO scheme interestingly shows quite different fluctuations with the other simulations (though the lack of symmetry present in the fifth-order WENO scheme these figures is due to a need for reprocessing of the data in post-processing phase) with greater magnitude of fluctuations. In spite of this, the averaged flow momentum values agree well with the other numerical schemes.

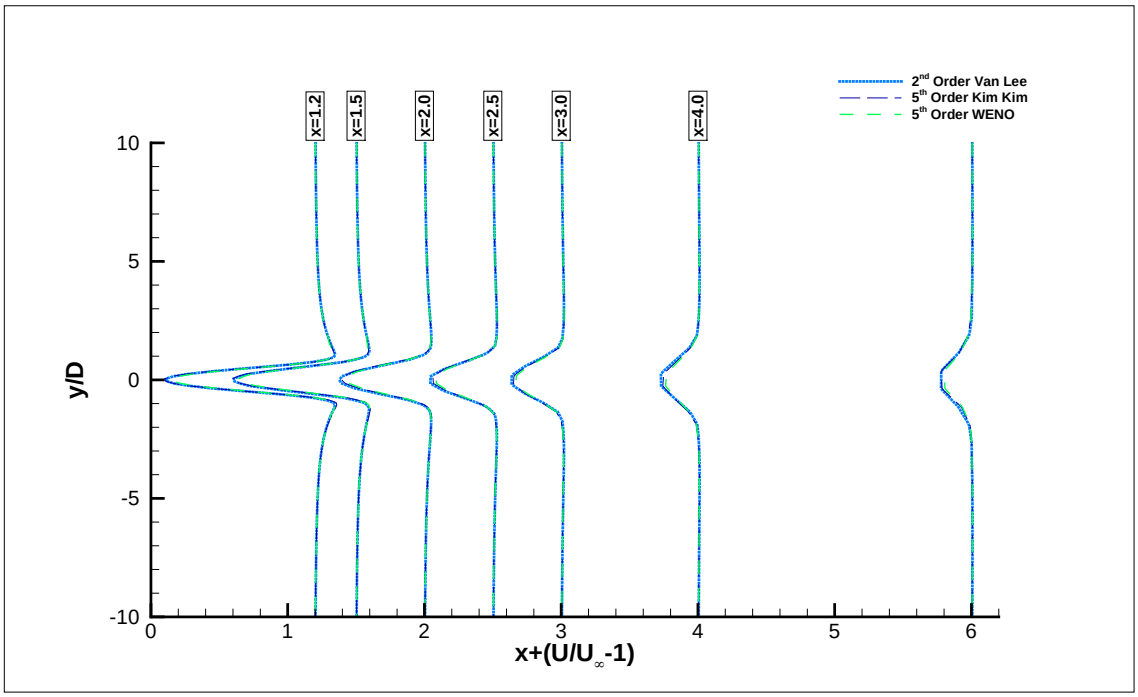

(a) Streamwise momentum along vertical lines in the wake

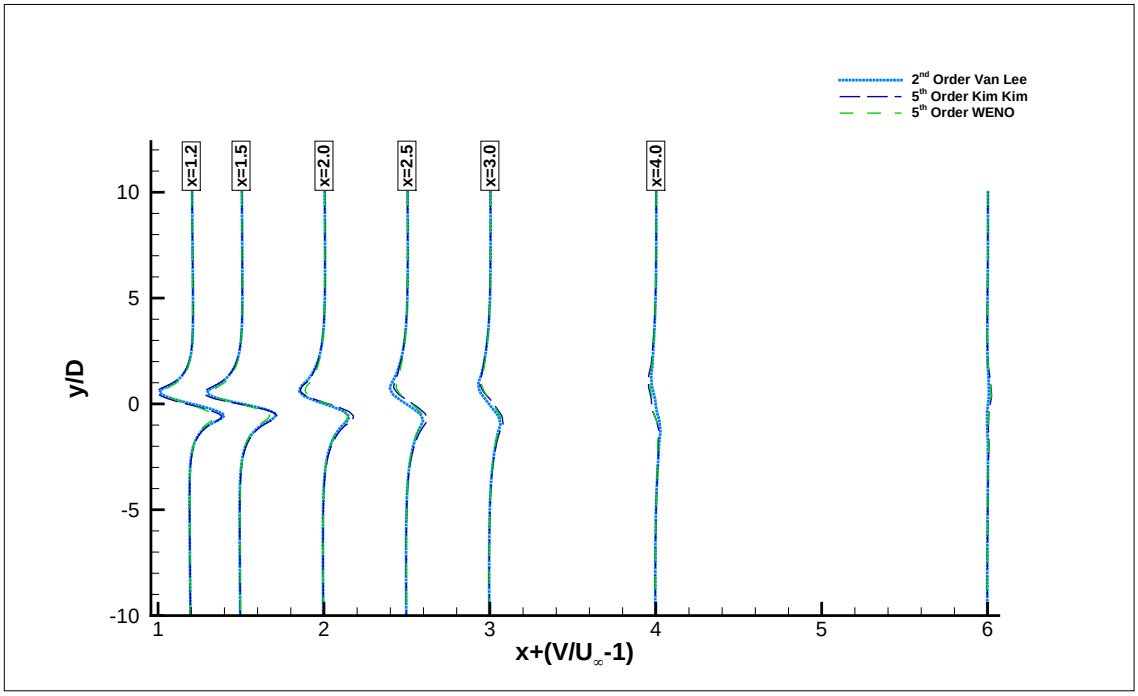

(b) Cross-flow momentum along vertical lines in the wake

FIGURE 6.6: Reynolds Number 200, 3*D* flows (a) showing stream-wise flow momentum (a) and cross-flow momentum (b).

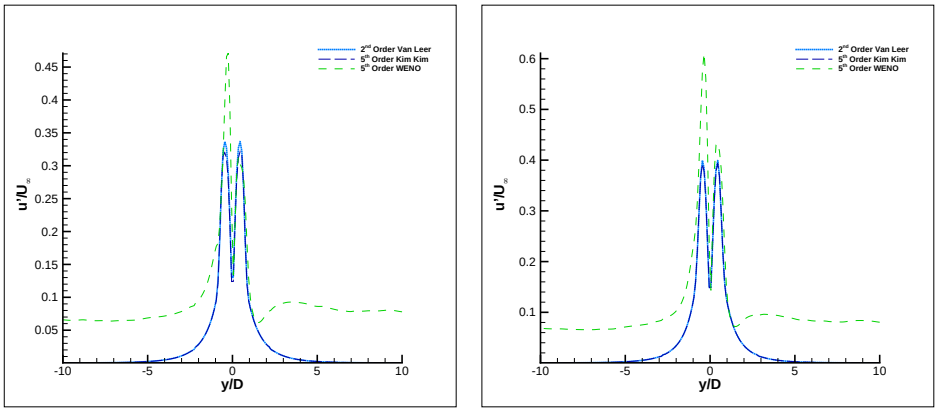

(a) Streamwise fluctuations at $x/D = 1.00$

(b) Streamwise fluctuations at $x/D = 1.20$

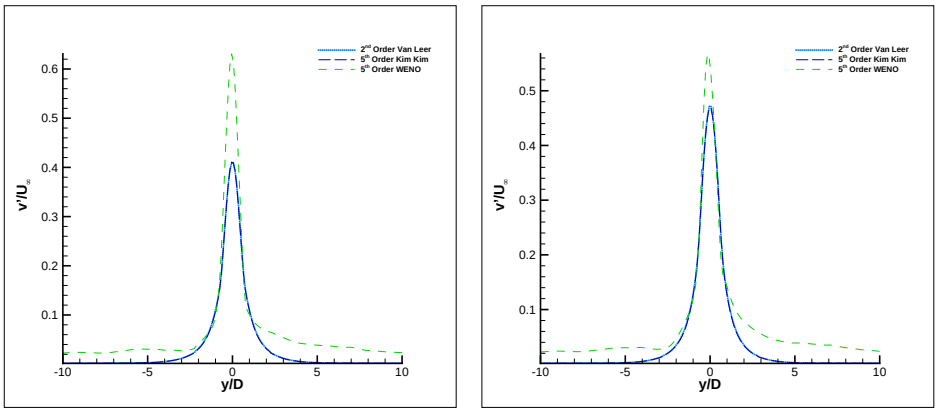

(c) Crossflow fluctuations at $x/D = 1.00$

(d) Crossflow fluctuations at $x/D = 1.20$

FIGURE 6.7: Reynolds Number 200, $3D$ flow. Fluctuations in the near wake, at $x/D = 1.00$ and $x/D = 1.20$.

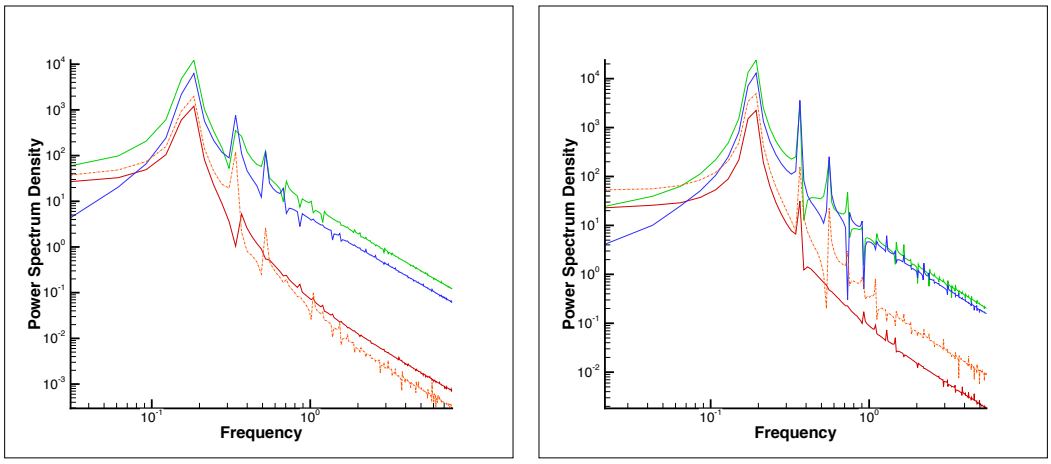

(a) Second-Order Van Leer (b) Fifth-Order Kim Kim

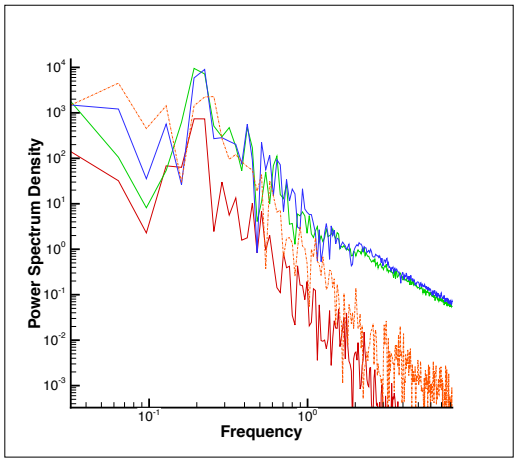

(c) Fifth-Order WENO

FIGURE 6.8: Reynolds Number 200, $3D$ flows. Plots showing spectral plots for points at $y/D = 0$, with Red Line: $x/D = 0.58$, Green Line: $x/D = 1.50$, Blue Line: $x/D = 4.00$ and Orange Line: $x/D = 7.00$. Plots shown for each numerical scheme.

Figure 6.8 show the spectral plots of frequency of fluctuations. These have been carried out with a greater number of time-points in the flow time, and thus compared to the two-dimensional simulations, higher frequencies are visible. The spectral data is taken from the mid-point in the z direction of the flow and $y = 0$, essentially placing along the most central point of the flow in the wake at varying x/D points. There are clear peaks in fluctuation frequencies in the wake for both the second-order Van Leer scheme as the fifth-order Kim Kim scheme, as well as clearly defined sub-harmonic frequencies. The fifth-order WENO scheme, however, shows different effects in the wake, with more subdued harmonic and sub-harmonic frequencies, and more 'noisy' wake, with highly fluctuating effects present.

All three schemes display the effects seen in the two-dimensional simulations of wake increasing in strength initially (note the higher density of fluctuations at $x/D = 1.50$, $x/D = 4.00$ and $x/D = 7.00$ than at $x/D = 0.58$), with the strongest wake at $x/D = 1.50$ before dissipating.

Dataset Info		C_d	C_l	U_{min}	θ_{sep}[1]	St
Exp.	Wieselsberger [111] (from [46])	1.28	-	-	-	-
	Williamson [35]	-	-	-	-	0.184
Num.	Franke [102]	1.31	0.65	-	111.5°	0.194
	Zhang [46]	1.42	0.531	-	-	0.202
	Persillon [108]	1.306	-	-	107.9	0.181
	Rajani [109]	1.337	-	-	111.904°	0.196
	Cao [60]	1.300	-	-	-	0.186
2D	Second Order Van Leer	1.36	0.54	-0.199	111.8°	0.185
	Fifth Order Kim-Kim	1.36	0.53	-0.193	111.8°	0.188
	Fifth Order WENO	1.36	0.53	-0.186	111.8°	0.187
3D	Second Order Van Leer	1.30	0.51	-0.202	112.6°	0.185
	Fifth Order Kim-Kim	1.30	0.51	-0.193	111.9°	0.192
	Fifth Order WENO	1.30	0.50	-0.186	111.9°	0.193

TABLE 6.1: $Re = 200$ 3-dimensional Results

Table 6.1 shows numerical data extracted from the simulations, compared to literature values and previous two-dimensional run data. The agreement with literature values is now very good, and the differences between two-dimensional and three-dimensional simulations are clearly visible. It is interesting to note that the previously run two-dimensional cases predicted separation angle and Strouhal number well, in that there is minimal difference in these values between the two-dimensional and three-dimensional runs under the same numerical schemes.

[1]For simulations carried out for this work, θ_{sep} has potential errors of $\pm 1.08°$, due to the resolution of cells (and their subsequent arc sizes) around the circumference of the cylinder

6.3 Reynolds Number = 300

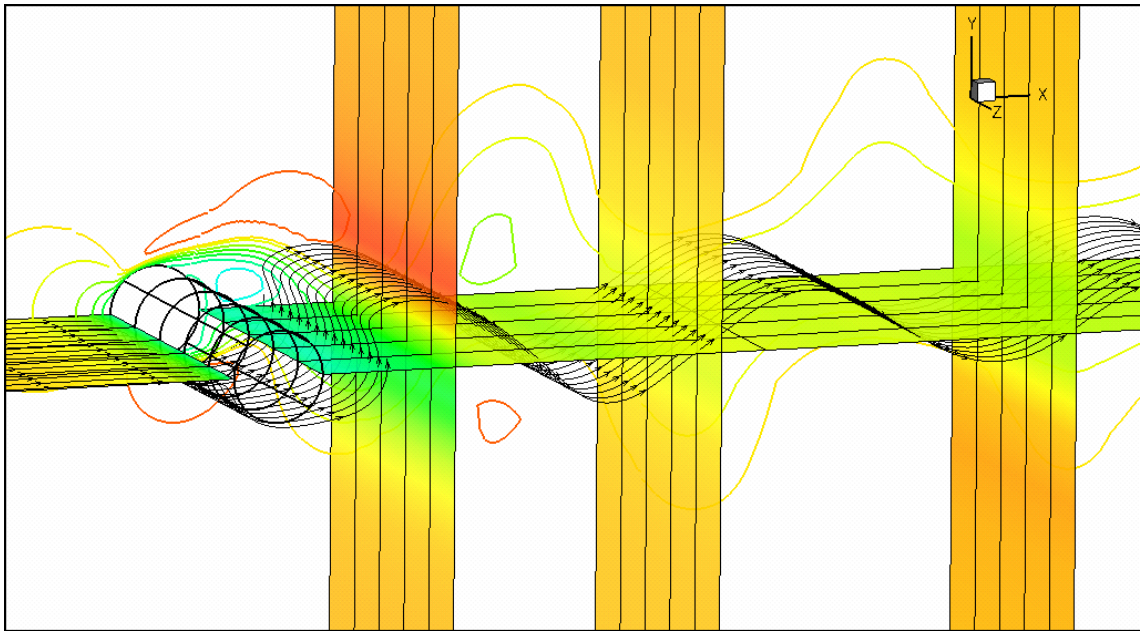

FIGURE 6.9: Instantaneous plots at one time-step of the 3*D* flow at Reynolds Number 300 for 2^{nd} Order Van Leer

At the Reynolds number of 300, the flow now exhibits vortex formation and shedding to the rear of the cylinder [106], particularly in three-dimensional forms of flow where the three-dimensional shear effects can be appropriately simulated. In this regime, the flow around the cylinder oscillates in the upwards and downwards directions resulting in an oscillating wake directly to the rear of the cylinder, which is clear in both the two-dimensional as well as the three-dimensional flows. The frequency with which this happens, combined with the viscosity of the fluid (which together define the Reynolds number) is such that the vortical formations to the rear of the cylinder are broken away from the wake as the wake direction oscillates. It is these broken-away formations that make up the vortex street flow in the wake. This was clearly evident in the instantaneous time plot given in the two-dimensional flow in figure 5.16(b) (section 5.4). This is further evidenced in the instantaneous plots shown for the three-dimensional flow, given in figures 6.9 and 6.10. Averaged over a long period of time, these oscillations appear as a steady flow, due to the symmetry of the oscillations along the line $y = 0$ to the rear of the cylinder.

With the flow now simulated in three-dimensions, the three-dimensional perturbations are now computed. This results in an unstable flow downstream of the cylinder, with some periodicity still evident in the coefficients of the flow. However, the flow around the cylinder exhibits a change in behaviour from the lower Reynolds number run, such that, whereas previously merely a point of separation of flow around the cylinder was observed, there is now a point where the flow reattaches to the cylinder around the circumference of the cylinder, generally remaining attached afterwards.

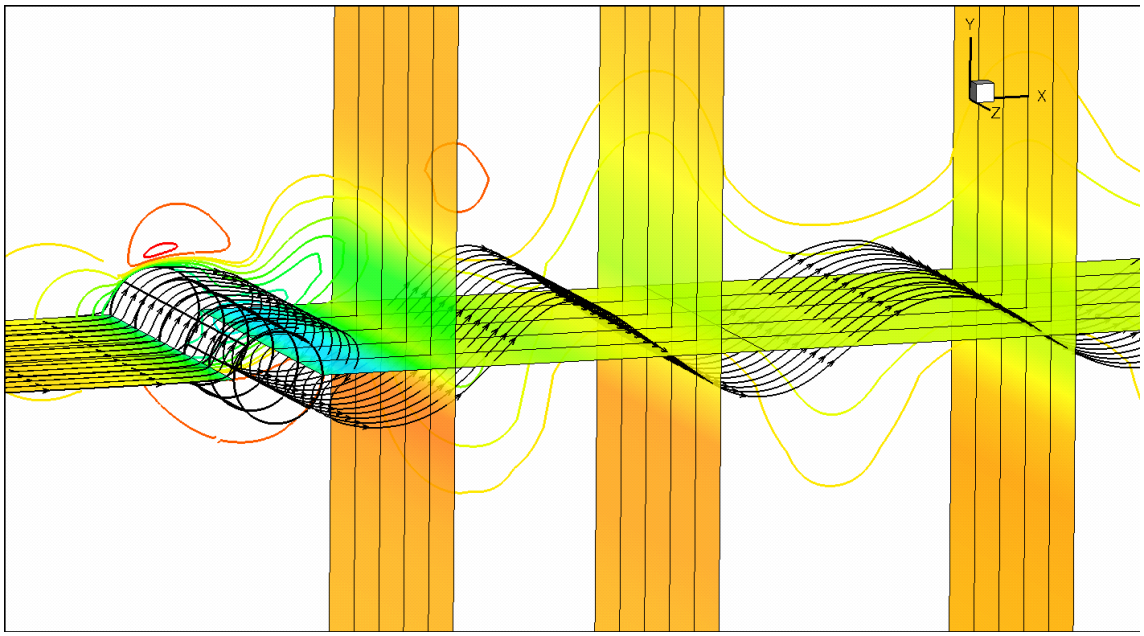

(a) 5^{th} Order Kim Kim

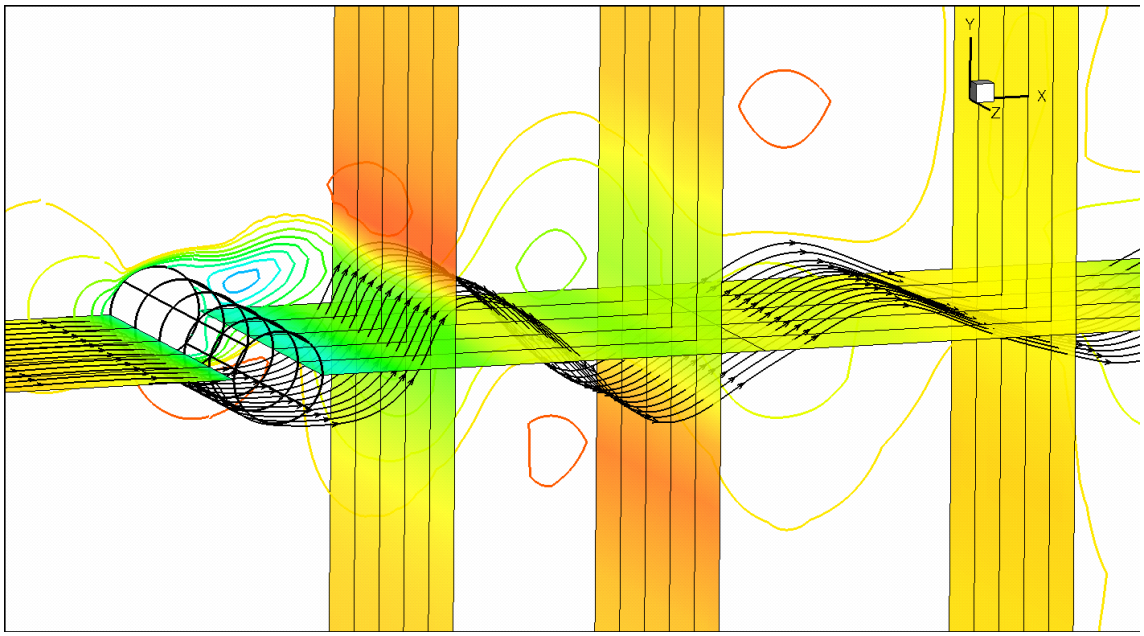

(b) 5^{th} Order WENO

FIGURE 6.10: Instantaneous plot at one time-step of the $3D$ flow at Reynolds Number 300

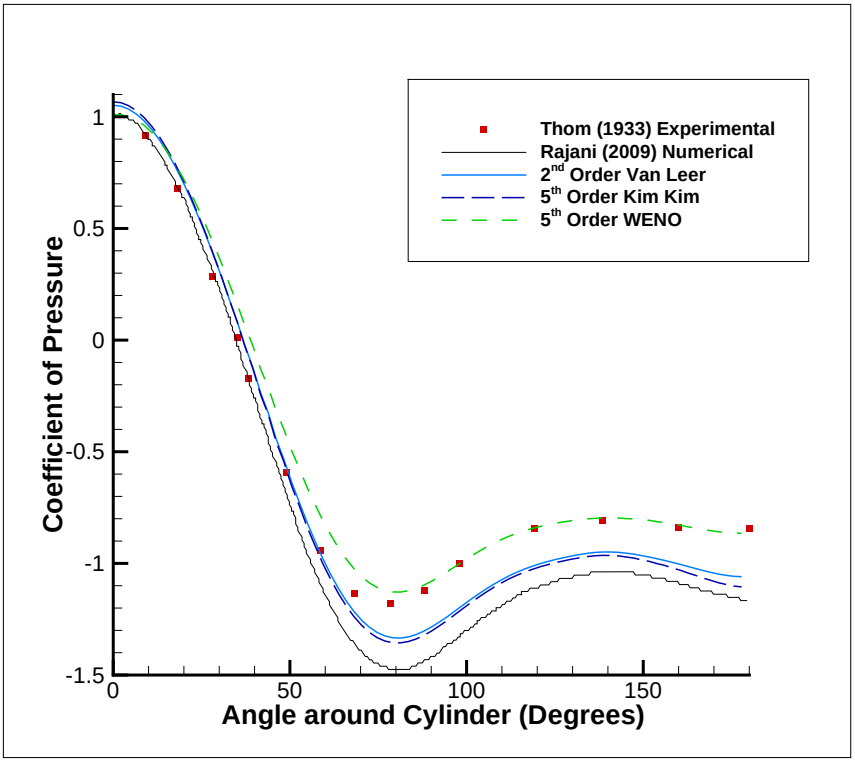

FIGURE 6.11: Reynolds Number 300, 3D flows for coefficient of pressure with differing orders of run. Note: Experimental data from [105] ($Re = 229$), numerical data from [109]

Figure 6.11 shows the plot of Coefficient of pressure around the cylinder at Reynolds number 300, for the different numerical schemes. As was noted for the three-dimensional flow at Reynolds number 200, the fifth-order WENO scheme agrees very strongly with the experimental data to the rear of the cylinder. Again, the other two schemes don't agree with the experimental data as closely as the WENO scheme, yet they both provide better predictions of the coefficient of pressure than the numerical literature data from Rajani [109]. However, the coefficient of pressure at the front of the cylinder, where the stagnation point lies, is higher than the expected $C_p = 1$ for the second-order and fifth-order Kim Kim schemes, while the fifth-order WENO scheme gives a good value for C_p at the fore of the cylinder.

Examining the coefficient of friction plot, figure 6.12, shows that with regards to this coefficient, the fifth-order WENO numerical simulation agrees best with the numerical literature data. As was evidenced in the Reynolds number 200 results, the second order Van Leer simulation outputs the lowest values of coefficient of friction and clearly under-predicts this slightly at the fore of the cylinder. After the point of separation, the simulations all show good agreement with literature data. However, while the values for the angle of separation were in very good agreement at the lower Reynolds number, there is now a wider range of angles of separation, though the differences in this value across the different numerical schemes are not large.

Figure 6.13 shows the time-averaged flow values for the different simulations in the wake of

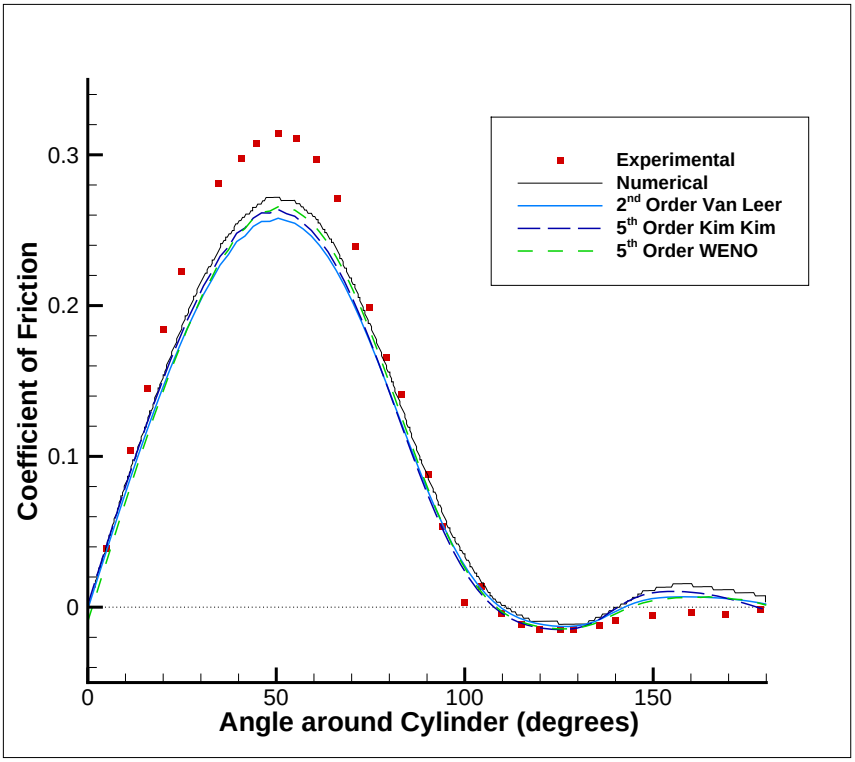

FIGURE 6.12: Reynolds Number 300, 3D flows showing coefficient of friction. Note: Experimental data from [110] at $Re = 287$, numerical data from [109]

the cylinder. The numerical schemes agree very well with one another on the values of momentum in the wake of the cylinder, with slight differences between the schemes. The WENO scheme shows greatest differences from the other two schemes that agree very well with one another, showing greater dissipation of flow in the stream-wise flow direction but stronger flow momentum in the cross-flow direction. However, once again the flow in the y-direction dissipates more rapidly than the flow in the x-direction.

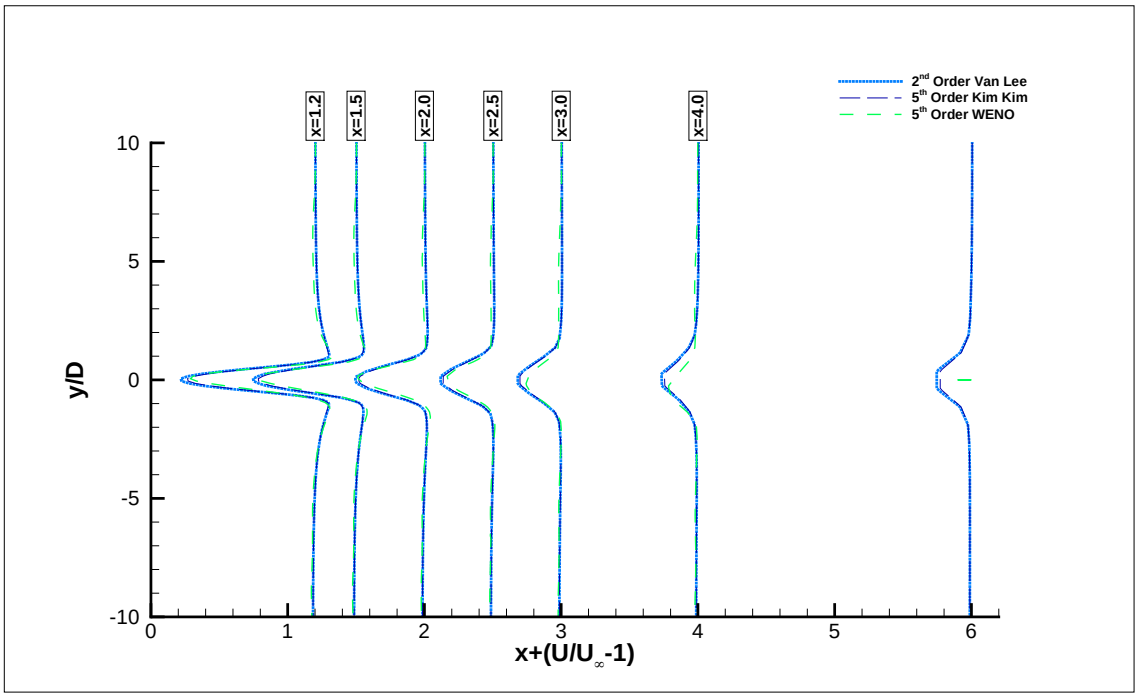

(a) Streamwise momentum along vertical lines in the wake

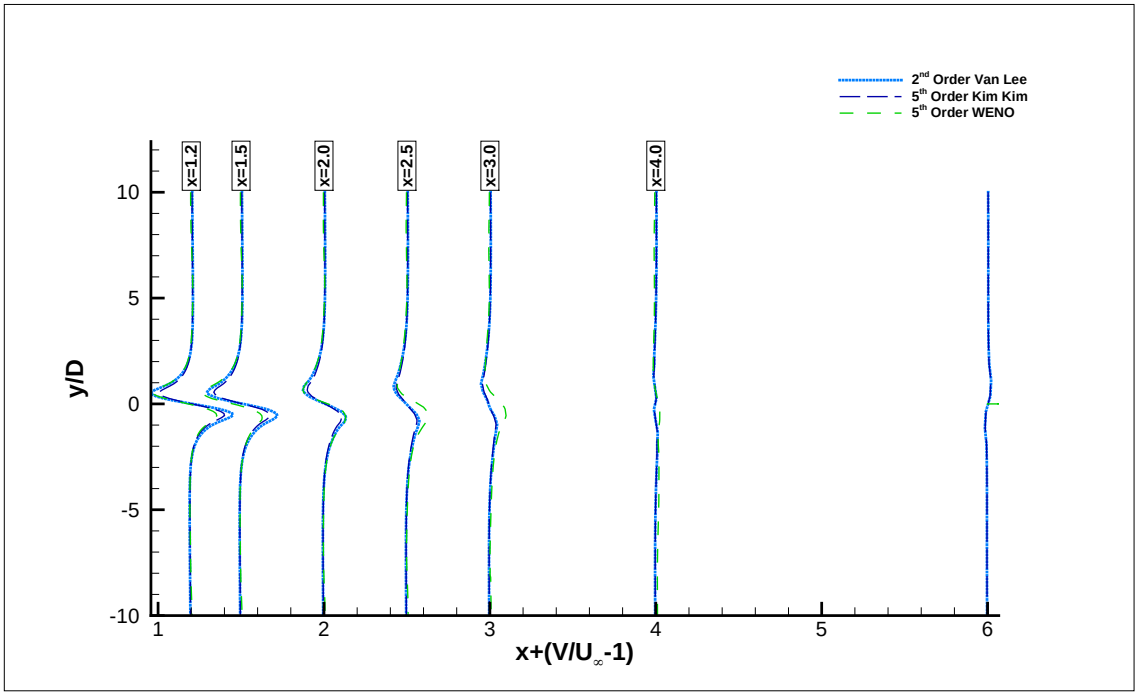

(b) Cross-flow momentum along vertical lines in the wake

FIGURE 6.13: Reynolds Number 300, 3*D* flows (a) showing stream-wise flow momentum (a) and cross-flow momentum (b).

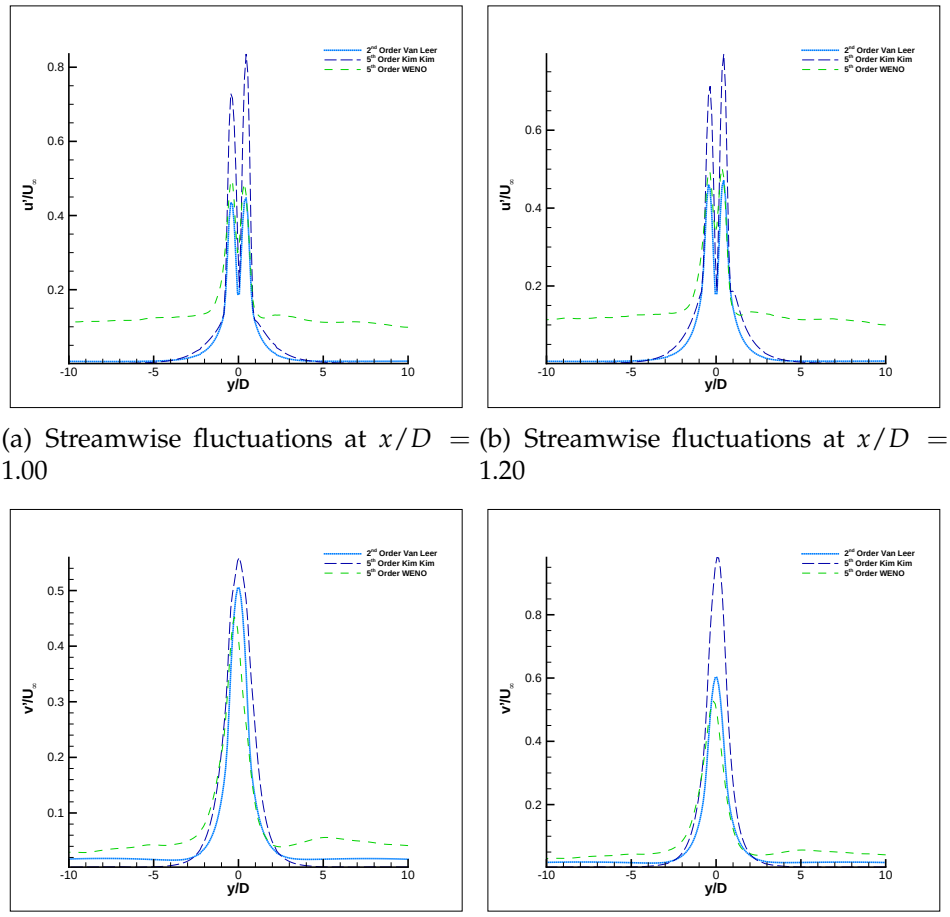

(a) Streamwise fluctuations at $x/D = 1.00$

(b) Streamwise fluctuations at $x/D = 1.20$

(c) Crossflow fluctuations at $x/D = 1.00$

(d) Crossflow fluctuations at $x/D = 1.20$

FIGURE 6.14: Reynolds Number 300, $3D$ flow. Fluctuations in the near wake, at $x/D = 1.00$ and $x/D = 1.20$.

Figure 6.14 shows the fluctuations in the momentum, in time-averaged form, in the near wake of the cylinder. The fluctuations of the momentum increase slightly downstream as the flow dissipates into the surrounding flowfield, before steadily dropping again. The fifth-order WENO scheme once again (as previously observed at Reynolds number 200) interestingly shows quite different fluctuations with the other simulations with greater magnitude of fluctuations. In spite of this, the averaged flow momentum values agree well with the other numerical schemes.

Figure 6.15 show the spectral plots of frequency of fluctuations. These have been carried out with a greater number of time-points in the flow time, and thus compared to the two-dimensional simulations, higher frequencies are visible. The spectral data is taken from the mid-point in the z direction of the flow. There are clear peaks in fluctuation frequencies in the wake for the fifth-order Kim Kim scheme as well as clearly defined sub-harmonic frequencies. The other two schemes, however, shows different effects in the wake, with more subdued harmonic and sub-harmonic frequencies, and in the case of the fifth-order WENO scheme more 'noisy' wake with

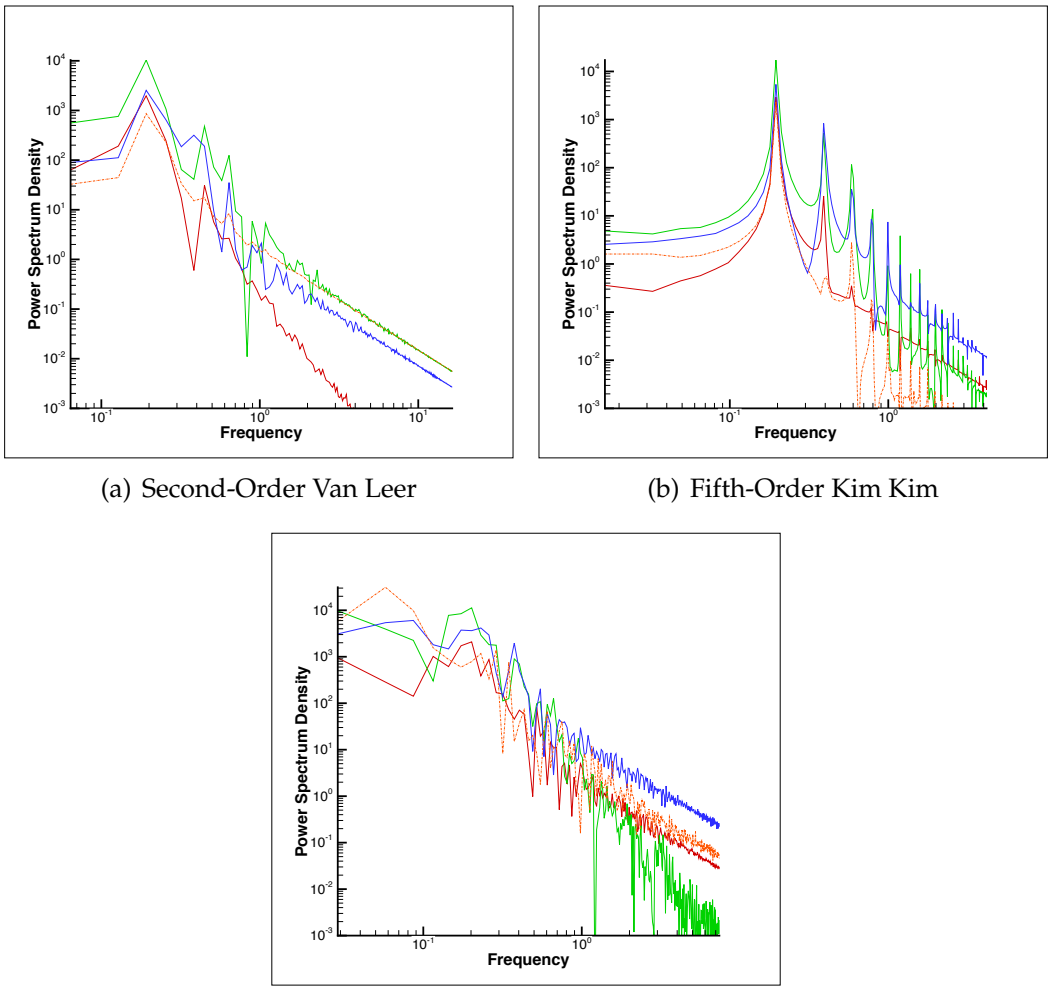

(a) Second-Order Van Leer

(b) Fifth-Order Kim Kim

(c) Fifth-Order WENO

FIGURE 6.15: Reynolds Number 300, 3D flows. Plots showing spectral plots for points at $y/D = 0$, with Red Line: $x/D = 0.58$, Green Line: $x/D = 1.50$, Blue Line: $x/D = 4.00$ and Orange Line: $x/D = 7.00$. Plots shown for each numerical scheme.

more turbulent effects present. The second-order scheme, on the other hand, displays less clearly defined fluctuation values in the wake of the cylinder.

All three schemes once again display the effects seen in the two-dimensional simulations of wake increasing in strength initially (note the higher density of fluctuations at $x/D = 1.50$, $x/D = 4.00$ and $x/D = 7.00$ than at $x/D = 0.58$), with the strongest wake fluctuations at $x/D = 1.50$ before dissipating.

Table 6.1 shows numerical data extracted from the simulations, compared to literature values

[1]For simulations carried out for this work, θ_{sep} has potential errors of $\pm 1.08^{\circ}$, due to the resolution of cells (and their subsequent arc sizes) around the circumference of the cylinder

Dataset Info		C_d	C_l	U_{min}	θ_{sep}[1]	St
Analytic (from eqn. 4.5)		-	-	-	-	0.2030
Exp.	Norberg [38]	-	0.435	-	-	0.203
	Williamson [35]	-	-	-	-	0.203
	Wieselsberger [111]	1.22	-	-	-	-
Num.	Rajani [109]	1.37	0.602	-	-	0.215
	Persillon [108]	1.366	0.477	-	106.5°	0.206
	Mittal 2007	1.26	0.380	-	-	0.203
	Kravchenko [93]	1.28	0.40	-	-	0.203
2D	Second Order Van Leer	1.35	0.59	-0.171	109.39°	0.197
	Fifth Order Kim-Kim	1.37	0.58	-0.163	109.29°	0.201
	Fifth Order WENO	1.38	0.60	-0.149	109.42°	0.200
3D	Second Order Van Leer	1.29	0.47	-0.199	109.5°	0.193
	Fifth Order Kim-Kim	1.29	0.49	-0.193	107.8°	0.196
	Fifth Order WENO	1.27	0.46	-0.186	108.4°	0.200

TABLE 6.2: $Re = 300$ 3-dimensional Results

and previous two-dimensional run data. The agreement with literature values for the coefficients is good, and the differences between two-dimensional and three-dimensional simulations are clearly visible. While at Reynolds number 200 it was found that there was good agreement between the two-dimensional simulations and the three-dimensional simulations, there is a clearer difference between the dimensionality of the simulations visible at this Reynolds number. The second-order Van Leer simulation gives similar values for separation angles and Strouhal number. The fifth-order WENO scheme shows very good agreement with the Strouhal number, essentially being unchanged, yet the remaining values show differences, with the values for coefficient agreeing better with the literature values.

6.4 Reynolds Number = 3900

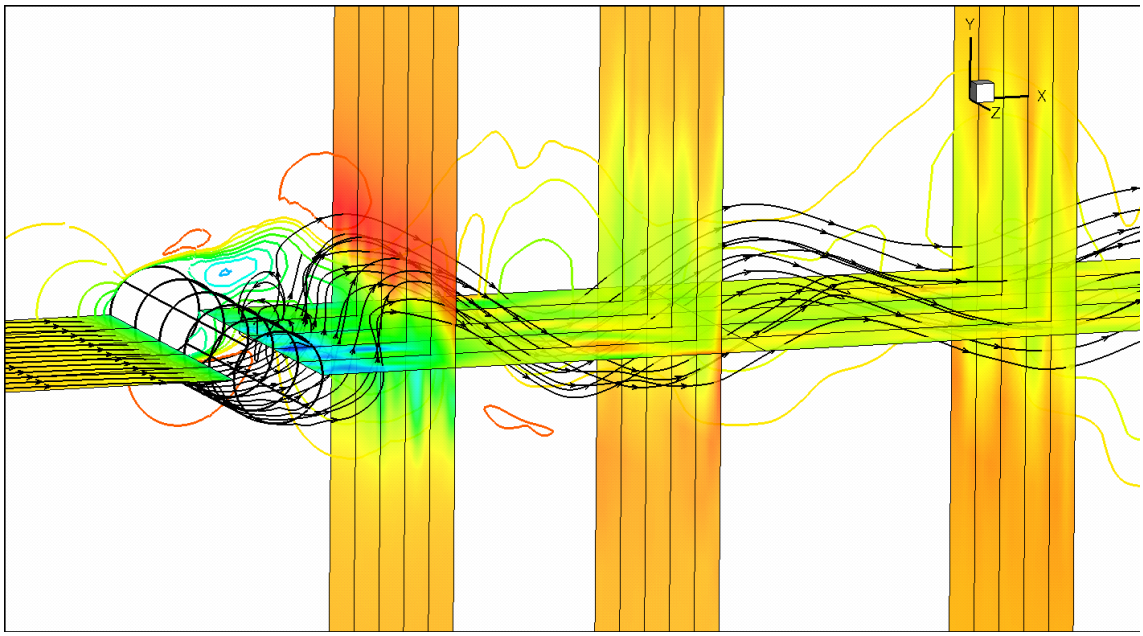

FIGURE 6.16: Instantaneous plots at one time-step of the 3*D* flow at Reynolds Number 3900 for 2^{nd} Order Van Leer

At the Reynolds number of 3,900, the flow to the rear of the cylinder is expected to show vortical flow, with vortices expected to appear in free shear layers [106], resulting in fully turbulent flow in the wake of the cylinder. This turbulent flow is visible in figures 6.16 and 6.17, particularly the fifth-order Kim Kim scheme where the flow to the rear of the cylinder is clearly three-dimensional and a strong vortical flow to the rear of the cylinder is visible. This vortical flow is subsequently shed from the wake at the rear of the cylinder, flowing downstream of the cylinder and eventually dissipating into the surrounding flow. This is a clearly visible von Kàrmàn vortex street shown by the streamlines in the flow. The three-dimensionality of the flow strongly influences the near-wake of the flow, where there exist a pair of counter-rotating streamwise vortices. The structure and length of these rotating vortices has been previously shown to be strongly influenced by the numerical scheme used [85] yet the recirculation region is visible in all the numerical schemes.

A further difference at this higher Reynolds number occurs, specifically to do with separation of flow around the cylinder. Whereas at lower speed flows only a single separation angle is evident, with the flow remaining separated from the cylinder from that point onwards, at this speed of flow there exists a reattachment point of the flow around the cylinder as well. Beyond this is a second separation angle. Thus in some literature (e.g. [85]) there are three angles given for separation, representing each of these flow phenomena around the cylinder circumference. This behaviour is visible in the coefficient of friction plot within this chapter.

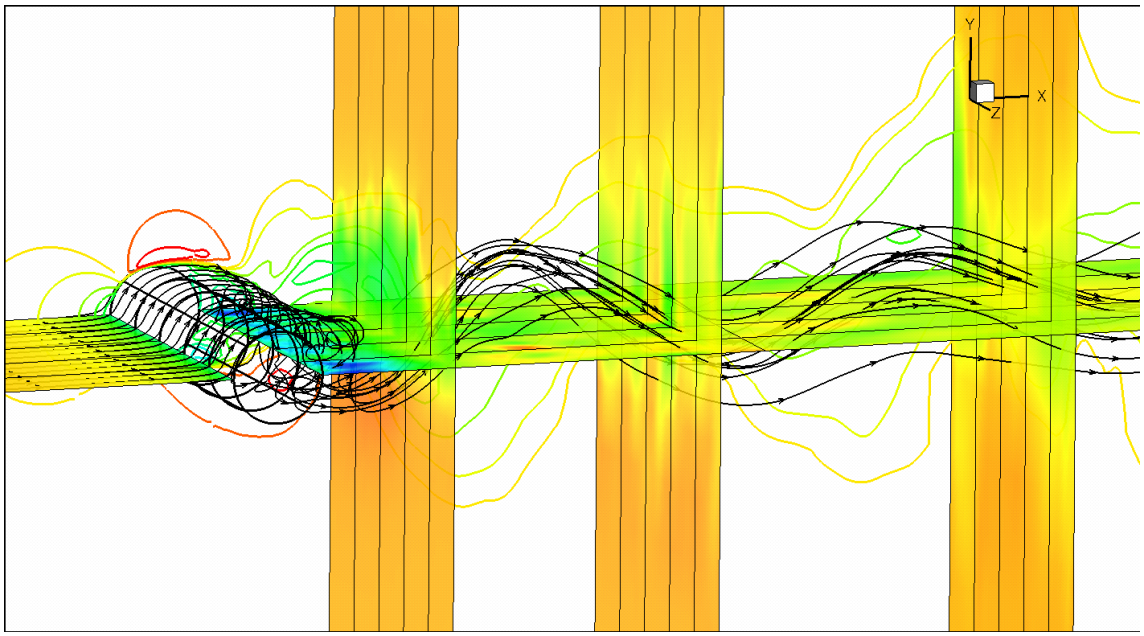

(a) 5^{th} Order Kim Kim

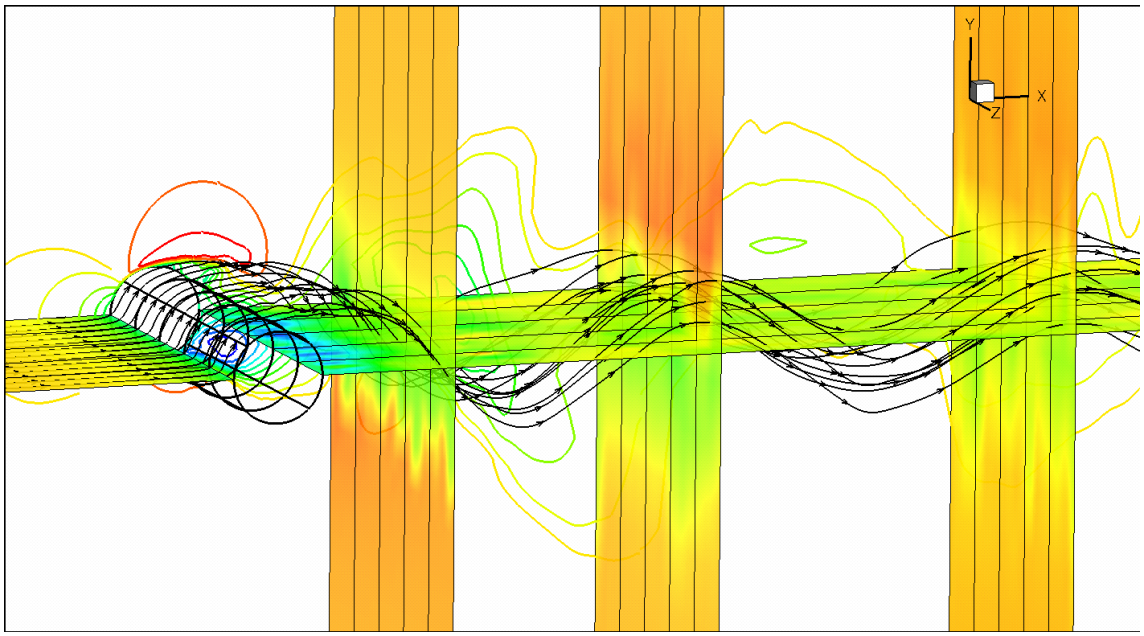

(b) 5^{th} Order WENO

FIGURE 6.17: Instantaneous plots at one time-step of the $3D$ flow at Reynolds Number 3900

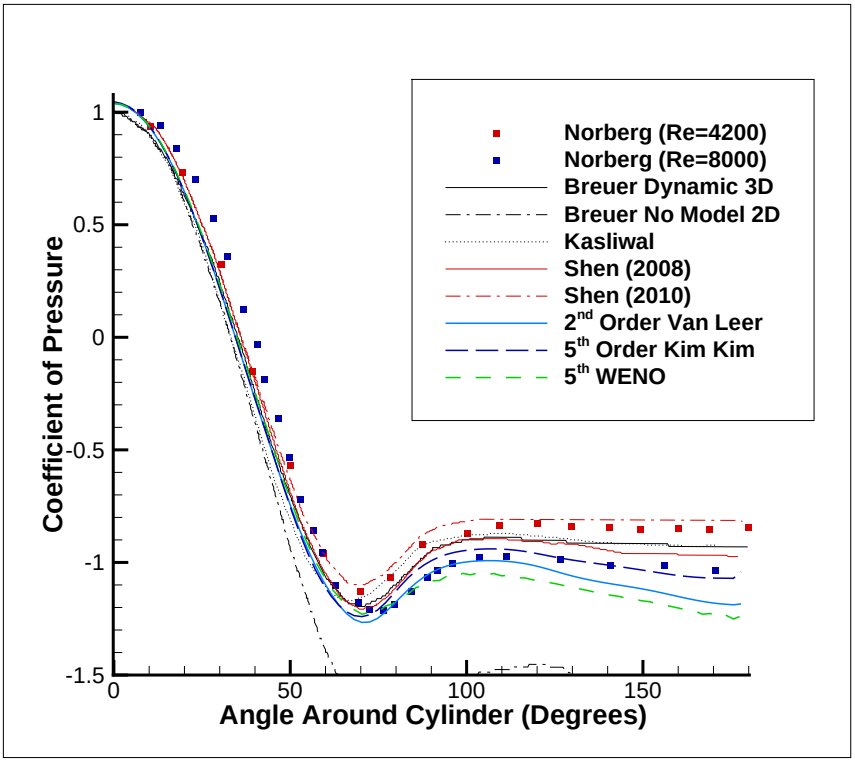

FIGURE 6.18: Reynolds Number 3900, 3*D* flows for coefficient of pressure with differing orders of run. Note: Experimental data from [117] at $Re = 4200$ and $Re = 8000$, numerical data from [85, 126, 127]

Figure 6.18 shows the plots of Coefficient of pressure around the cylinder at Reynolds number 3900, for the different numerical schemes. The values for the coefficient of pressure are not quite as expected; while they were improved significantly when compared to the differences between the earlier two-dimensional values and the literature data, the values to the rear of the cylinder are still lower than expected. The C_p values to the fore of the separation point are in very good agreement with literature and each other; at this region the flow is laminar and thus the differing choices in numerical reconstruction method does not have a great impact on the C_p.

In the two-dimensional flows, the coefficient of pressure dropped rapidly after the separation point. The values in the three-dimensional simulations do not exhibit such a severe drop of coefficient of pressure after the separation point, giving a line closer in shape of the literature data than the two-dimensional simulations. However, the drop-off of the coefficient of pressure to the rear of the cylinder was unexpected. The values of coefficient of pressure remain within the two-dimensional and literature values, with a closer 'leaning' towards the literature (experimental and three-dimensional numerical) values, though the drop-off is difficult to explain, particularly as later plots reveal flow values and coefficient of friction to have better agreement with literature. Furthermore, at the lower Reynolds number runs, the fifth-order WENO scheme showed best agreement with literature for coefficient of pressure, while at this Reynolds number it is the

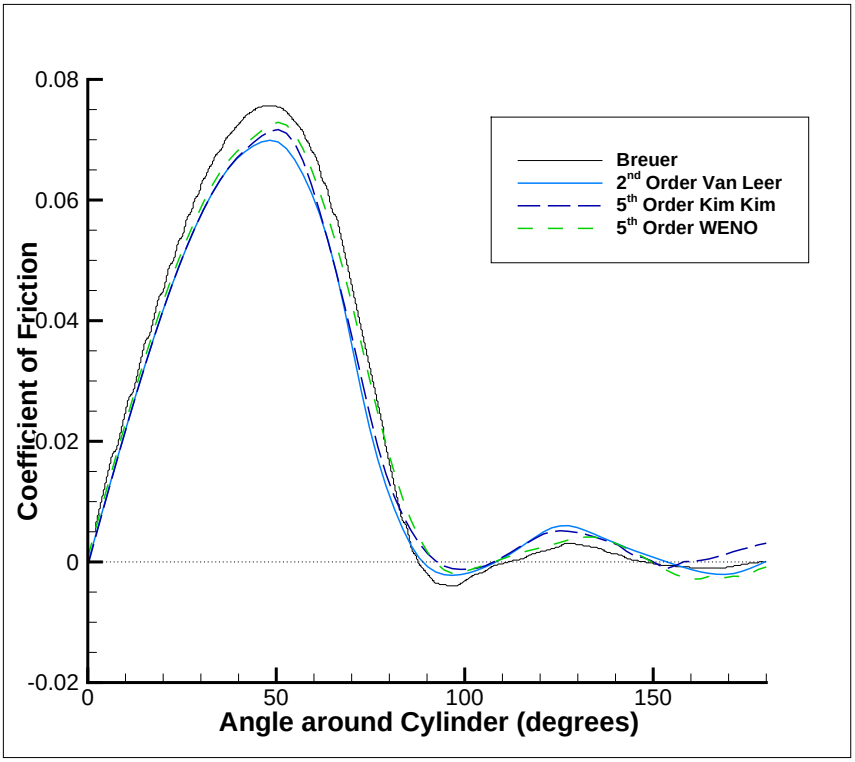

FIGURE 6.19: Reynolds Number 3900, 3D flows showing coefficient of friction. Note: numerical values from [85].

fifth-order Kim Kim scheme that shows the best agreement with literature. Examining the literature (i.e. [85, 114]), it was found that other numerical schemes exhibited similar behaviour for the C_p at the rear of the cylinder. In the paper by Breuer [85], a number of the three-dimensional numerical schemes showed this behaviour, with really only one numerical method producing an output for C_p in accordance with the experimental data - this was case $D1$ and is the case plotted in figure 6.18. In spite of this discrepancy of C_p, other results from the simulations still showed reasonable agreement with experiment.

In the two-dimensional simulations, the vortical flow to the rear of the cylinder was closer than expected, and closer than in the three-dimensional simulations (these were measured individually using a visual measurement within Tecplot of the flow). This corresponded in the two-dimensional simulations with an under-prediction of the coefficient of friction at the rear of the separation point. However, as shown by figure 6.19, the coefficient of friction at Reynolds number $3,900$ shows generally better agreement with literature than the two-dimensional simulations. In spite of this, there are still some clear differences, particularly with a higher coefficient of friction to the rear of the cylinder than the literature data. As mentioned, the vortices were closer to the rear of the cylinder than previously observed in the two-dimensional flow; the results from the coefficient of pressure and friction plots are no doubt linked to this, with the outcome being that in fact the vortices are now located closer to the rear of the cylinder than in experimental flows.

Furthermore, as was mentioned earlier, at this Reynolds number we expect a reattachment and second separation point of the flow around the cylinder. This is visible in the coefficient of pressure plot; that is, the angle where C_f first drops with a negative gradient past 0.0 is the first separation point. The reattachment point is defined as the angle at which C_f once again passes 0.0, this time with a positive gradient. The final separation point is defined as the second point at which C_f passes 0.0 with a negative gradient for the line of C_f. These distinct points are visible in the coefficient of friction plot (figure 6.19), however clear differences between the numerical schemes start to become more obvious. Perhaps the biggest, and most important, disparity is in this point of flow re-separation; that is, the second separation point. This point is quite clear for the fifth-order WENO and second-order Van Leer schemes, while the fifth-order Kim Kim scheme only just touches $C_f = 0.0$ at 150° (the value was only very briefly negative) before having positive values for C_f once again.

Figure 6.20 shows the time-averaged flow values for the different simulations, in the wake of the cylinder. At this Reynolds number the effects of the cylinder on the downstream wake are clear with greater loss in flow momentum in the near wake region of the cylinder than at the lower Reynolds numbers, in particular with negative flow momentum in the stream-wise direction at the point closest to the cylinder, $x/D = 1.2$. This is a characteristic shared by all the simulations, as well as in the literature [45, 126]. Overall, however, the flow momentum in the wake are in good agreement with each other across the different numerical order of simulation. In the cross-flow direction, there is a slight discrepancy between the second-order Van Leer simulation and the fifth-order simulations. This is likely due to the run time that was required for the fifth-order simulations, not allowing as large a temporal averaging region as the second-order simulation.

Figure 6.21 shows the fluctuations in the near-wake of the cylinder. The patterns observed at the lower Reynolds number flows with regards to the greater fluctuation magnitudes within the fifth-order WENO scheme are evident once again at this Reynolds number. A noteworthy point is that there is asymmetry present in the second-order simulation fluctuations. Similar behaviour was noted by authors such as Breuer [85, 114] for their two-dimensional simulations, where even an increase in the averaging time did not remove this inconsistency. Further examination of the instantaneous flow field showed asymmetric vortex shedding, with vortices shed from the cylinder having a reference plane above the line of symmetry to the rear of the cylinder. At irregular time intervals the axis of the vortex street was observed in the literature to change from positive to negative angles, and vice versa. It is likely that similar behaviour in the change of the axis of the vortex street would have been observed in this second-order Van Leer simulation had the simulation been run for a longer time-period, but due to time constraints this was not possible.

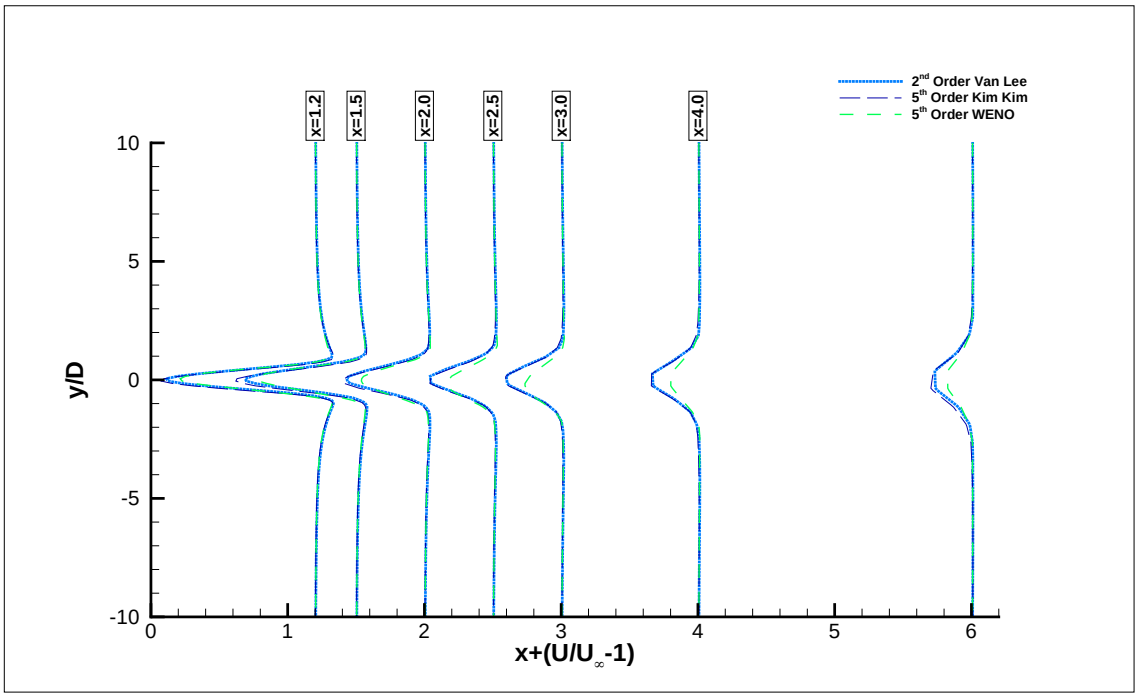

(a) Streamwise momentum along vertical lines in the wake

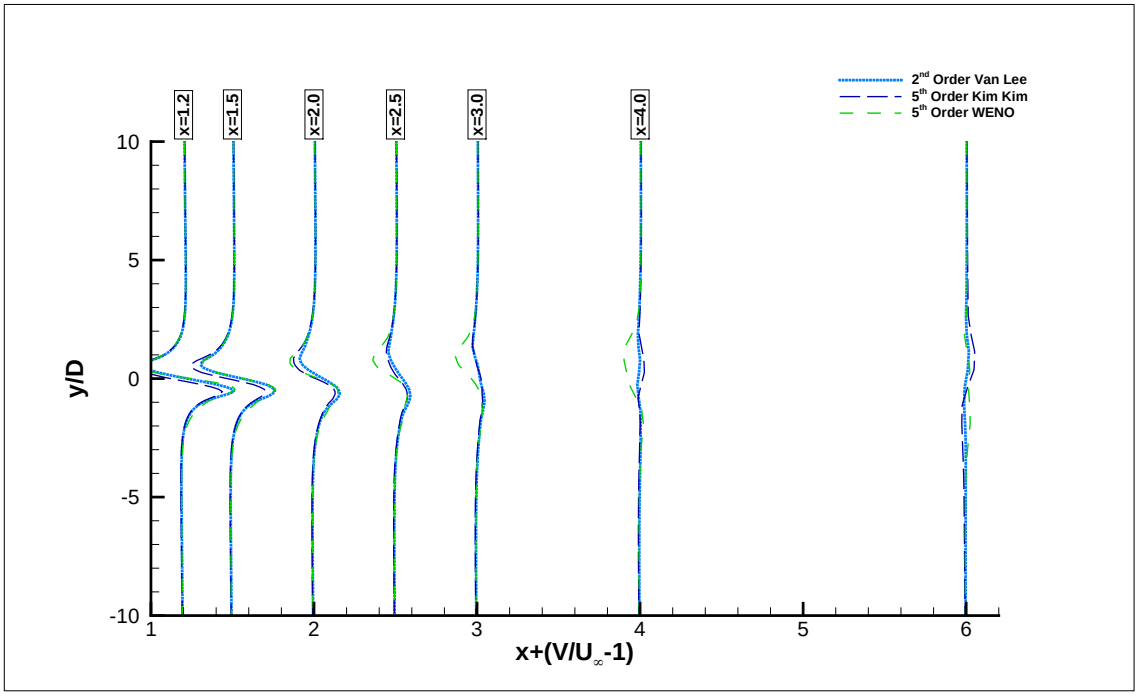

(b) Cross-flow momentum along vertical lines in the wake

FIGURE 6.20: Reynolds Number 3900, 3*D* flows showing stream-wise momentum (a) and cross-flow momentum (b).

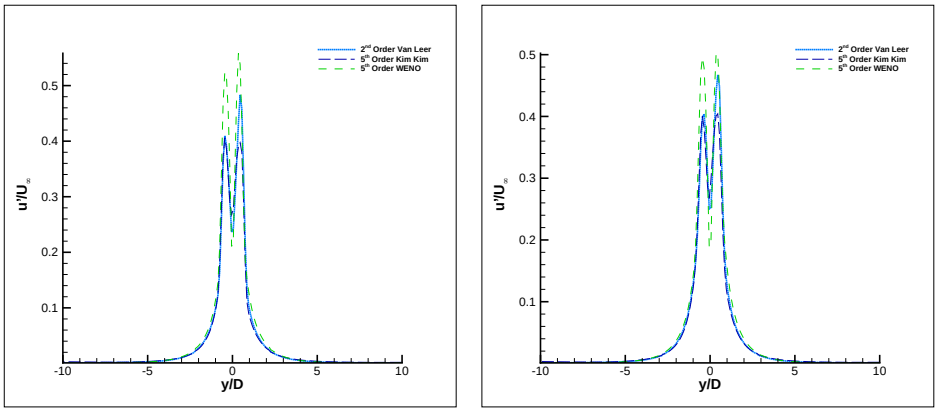

(a) Streamwise fluctuations at $x/D = 1.00$

(b) Streamwise fluctuations at $x/D = 1.00$

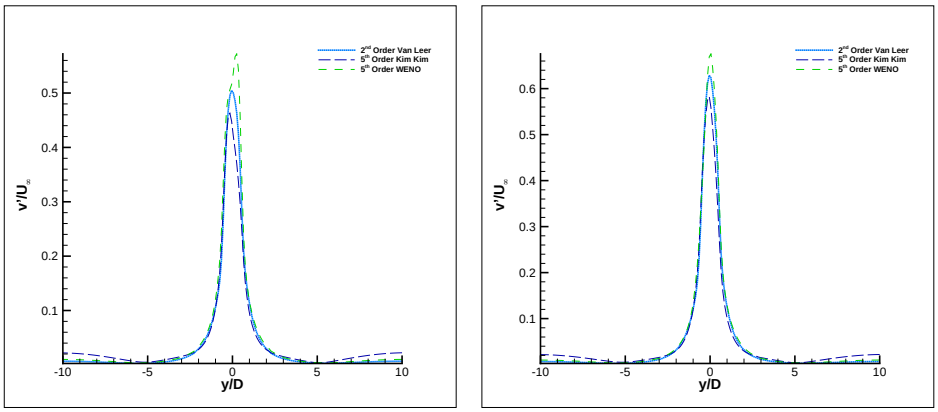

(c) Crossflow fluctuations at $x/D = 1.20$

(d) Crossflow fluctuations at $x/D = 1.20$

FIGURE 6.21: Reynolds Number 3900, $3D$ flow. Fluctuations in the near wake, at $x/D = 1.00$ and $x/D = 1.20$.

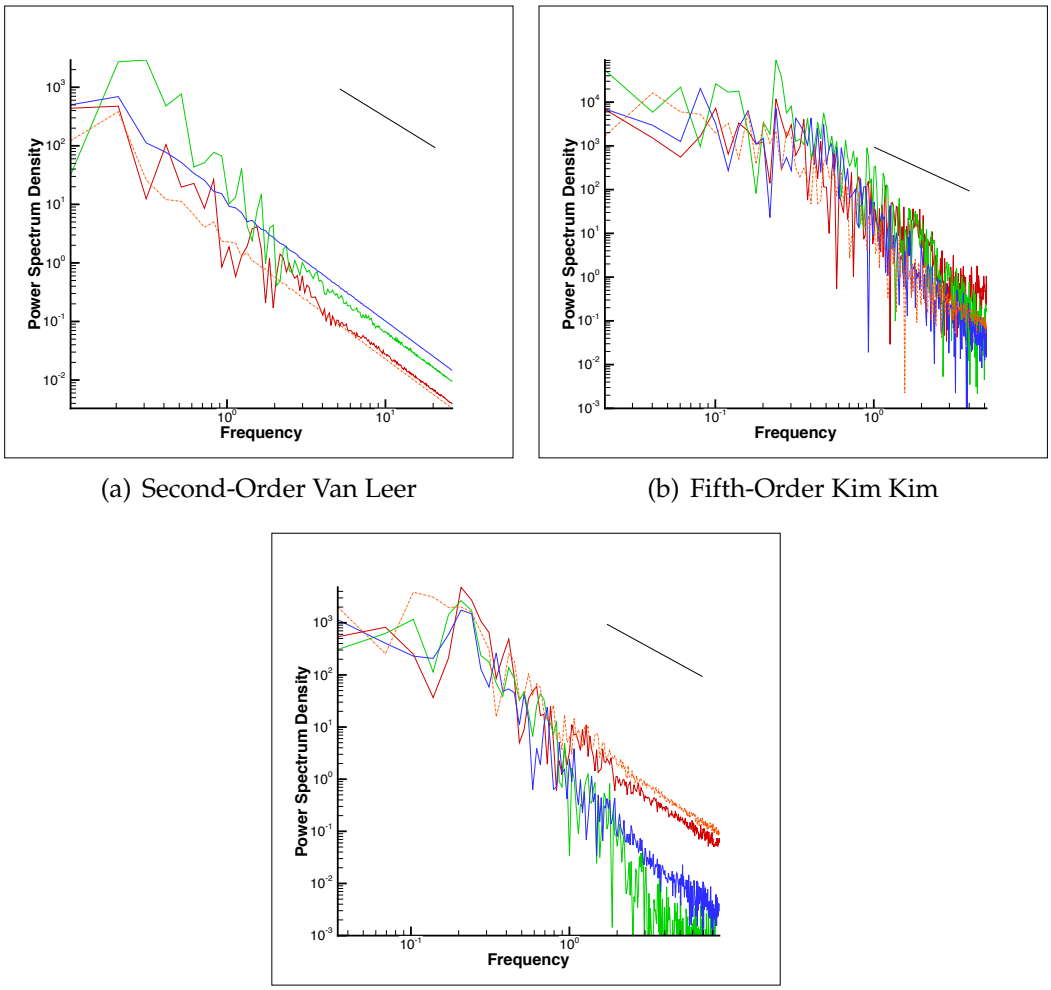

(a) Second-Order Van Leer

(b) Fifth-Order Kim Kim

(c) Fifth-Order WENO

FIGURE 6.22: Reynolds Number 3900, $3D$ flows. Plots showing spectral plots for points at $y/D = 0$, with Red Line: $x/D = 0.58$, Green Line: $x/D = 1.50$, Blue Line: $x/D = 4.00$ and Orange Line: $x/D = 7.00$. Black line shows Kolmogorov spectrum scale, $\kappa^{-5/3}$. Plots shown for each numerical scheme.

Figure 6.22 shows the spectral plots of frequency of fluctuations in the cylinder wake. Whereas previously at the lower Reynolds number runs, some clear signs of peakedness representing the harmonic and sub-harmonic frequencies were evident, the flow in the wake now exhibits generally more turbulent flow with quite noisy frequency data. The Kolmogorov length scale line for $\kappa^{-5/3}$ is included in the plots, as well as a corresponding κ^{-3} line. There is overall good agreement with the $\kappa^{-5/3}$ scales, with the exception being the fifth-order Kim Kim that shows more similarity with the κ^{-3} scale.

Dataset Info		C_d	C_l	U_{min}	θ_{sep}[1]	St
Predicted from model given in Norberg [38]		-	0.0830	-	-	0.2089
Experimental	Reported in [45, 114, 115]	0.98 $\pm$0.05	0.03-0.08	-0.24 $\pm$0.1	86.0° $\pm$2	0.215 $\pm$0.005
	From [38, 116, 117]		-			
	Son [98]	-	-	-	85/86°	-
	Norberg [117]	0.98	-	-	-	-
	Cardell [116]	-	-	-	-	0.215
	Lourenco [118]	0.99	-	-0.24	86°	0.215
	Ong [119]	-	-	-	-	0.21
Numerical	Beaudan[2] [114]	0.96	0.07	-0.33	$\pm$85.3°	0.216
	Beaudan[3] [114]	1.00	-	-0.32	85.8°	0.203
	Mittal [120]	1.0	-	-0.35	86.9°	0.207
	Breuer[4] [85]	1.016	-	-	87.4°	0.215
	Fröhlich [121]	1.08	-	-0.24	88.1°	0.216
	Kravchenko [45]	1.04	-	-0.37	88.0°	0.210
	Ma[5] [122]	0.96	-	-	89.1°	0.203
	Franke [123]	0.98	-	-	88.2°	0.209
	Mahesh [124]	1.00	-	-0.31	87.6°	0.218
	Park [125]	1.02	-	-0.33	-	0.209
	Young[6] [115]	1.03	0.177	-	-	0.212
2D	Second Order Van Leer	1.29	1.09	-0.252	102.4°	0.206
	Fifth Order Kim-Kim	1.43	1.25	-0.119	104.6°	0.236
	Fifth Order WENO	1.52	1.30	-0.165	115.9°	0.200
3D	Second Order Van Leer	1.10	0.25	-0.373	88.4°	0.208
	Fifth Order Kim-Kim	1.08	0.19	-0.325	93.0°	0.242
	Fifth Order WENO	1.02	0.18	-0.336	92.0°	0.208

TABLE 6.3: $Re = 3900$ 3-dimensional Results

Previously, in the two-dimensional simulations at Reynolds number $3,900$ the values for the coefficients of the cylinder were generally over-predicted. The best set of results for the two-dimensional simulations were in the Strouhal number values; these are once again well predicted in the three-dimensional simulations. However, it was noted in the literature [128] that the Strouhal number is not necessarily an indication of a quality simulation. Furthermore, the value

[1]For simulations carried out for this work, θ_{sep} has potential errors of $\pm 1.08°$, due to the resolution of cells (and their subsequent arc sizes) around the circumference of the cylinder

[2]Results from $3D$ run with No Model

[3]Results used from $3D, 5^{th}$ Order Upwind method

[4]3D Case, $D1$

[5]DNS Run as opposed to other numerical data from LES simulations

[6]3D LES, using 48 cells in z direction

for the Stouhal number is not very sensitive to the differing parameters of the simulations [85]. Therefore, examination of the remaining numerical results in the table is necessary, and shows the fifth-order schemes have good agreement with literature values. The second-order simulation, on the other hand, has elevated values for the coefficients. It was noted in examination of the fluctuating momentum to the rear of the cylinder that the second order simulation exhibited asymmetrical effects with the shedding of vortices having a tendancy towards an axis above the line of symmetry. This behaviour is clearly influenced by the coefficients around the cylinder also being over-predicted.

6.5 Discussion of Three-dimensional simulations

The three-dimensional simulations had to be run in addition to the two-dimensional simulations as it was shown previously in the two-dimensional simulation section that the results from the flows at higher Reynolds numbers were not wholly satisfactory. One of the chief reasons for this was the three-dimensional nature of the flow at Reynolds numbers above the transitional Reynolds number of approximately $Re = 170$. One of the main disadvantages of two-dimensional simulations was that coefficients were generally over-predicted, as discussed in the $2D$ results chapter. Assessment of the same simulations run in a three-dimensional set up shows that this is indeed also the case with the ILES simulations with the higher-order reconstruction methods, as the results generally predict the coefficients with greater accuracy when compared to literature data available. Thus it has been shown once again in this work that three-dimensional simulations provide better results than the two-dimensional simulations at these Reynolds numbers.

Perhaps the largest disadvantage of running simulations in three-dimensions, as opposed to two-dimensions, is the additional computational demands of the simulations. They require a significantly greater number of CPU hours to compute, as well as much more storage space of output data. In the case of this thesis, this necessitated a careful choice of specific higher-order methods to be run, and as such the second-order Van Leer, fifth-order Kim Kim and fifth-order WENO schemes were chosen. It was felt these would show a spectrum of results showing a difference both between increasing the numerical order, as well as the use of different numerical reconstruction methods. Any differences in the run-times of the numerical schemes become more pronounced as the simulations are run in three-dimensions, with a stark difference in run time for the WENO scheme clearly obvious, as shown in table 6.4. Over a run of $10,000$ iterations, the fifth-order WENO scheme requires around an hour longer to compute than the equivalent order WENO scheme. With at least two million iterations required for the three-dimensional flow to develop, the time difference required between numerical schemes is clearly important when choosing which of the schemes to use for flows such as those in this thesis. The second-order Van Leer scheme is clearly the fastest computing scheme, at the times available. Unfortunately, there was a computational error with the timing of the $Re = 200$ 2^{nd} Order Van Leer simulation. As a result, the timing for that simulation has not been included.

Reynolds number	2^{nd} Order VL	5^{th} Order KK	5^{th} Order WENO
200	–	1:51	3:00
300	1:43	1:52	2:59
3,900	1:42	1:50	3:02

TABLE 6.4: Averaged run times for $10,000$ iterations of $3D$ simulations, given in hours, for the 2^{nd} Order Van Leer, 5^{th} Order Kim Kim and 5^{th} Order WENO schemes

Examining the results output from the simulations, at the lower Reynolds numbers of 200 and 300, the fifth-order WENO generally predicted the coefficients of flow around the cylinder best, with the coefficient of pressure around the cylinder matching experimental values, while the coefficients of lift and drag were also very well predicted. The coefficient of friction results,

however, show some discrepancies with results for this at $Re = 200$ being furthest from literature data, while being the closest to literature data at $Re = 300$. In the earlier two-dimensional results, it was found that at both Reynolds numbers 200 and 300, the WENO schemes were attempting to resolve highly unstable (and greatly fluctuating) flow effects in the wake with effects resembling turbulence shown in the spectral plots of the wake. This behaviour was repeated in these three-dimensional simulations, (where turbulence is physical and can be properly solved for) with the fifth-order WENO scheme showing both greater fluctuation values in the wake, as well as more 'noisy' spectral data in the wake. In spite of this, the prediction of the flow values in the wake agreed very well with the other two simulations, with only a slight amount of additional dissipation of the flow to freestream values over the other two three-dimensional simulations.

The results for both the second-order Van Leer scheme and the fifth-order Kim Kim scheme at both Reynolds numbers 200 and 300 show many similarities. Neither generally performed as well as the fifth-order WENO at these lower Reynolds numbers, yet both performed relatively well compared to the literature numerical data they were compared with. This has been clearly demonstrated with the coefficient of pressure plots for these Reynolds numbers, where both schemes predicted the C_p around the cylinder better than the RANS technique employed by Rajani [109]. Both schemes also showed good agreement with regards to the C_f plots, as well as lift and drag coefficients. Both schemes predicted the angles of separation around the cylinder well at $Re = 200$, though the fifth-order Kim Kim couldn't predict this well at the higher Reynolds number of 300. Furthermore, both schemes provided repeatable oscillations in the wake and flows around the cylinder, making it relatively straightforward to measure flow-field values such as momentum and fluctuations. This is clearly visible through examination of the spectral plots which, for the second-order Van Leer and fifth-order Kim Kim schemes, are relatively 'clean' when compared with the WENO scheme, with clear harmonic and sub-harmonic frequencies in the wake. Overall, however, at the Reynolds numbers of 200 and 300, there is no great improvement in results by moving from a second-order Van Leer scheme to a fifth-order Kim Kim scheme. However, these schemes do give better results downstream of the cylinder, in the wake.

Moving on to the faster flow speed at $Re = 3900$, it is clear that the flow is now more turbulent, and this was well illustrated in the instantaneous flow plots. This change in flow regime clearly affects the simulations of the flow at this speed, with the Van Leer and Kim Kim schemes not simulating the reattachment and second separation points of flow around the cylinder correctly. This would clearly affect other parameters of the flow, and yet the coefficient of pressure plots for these schemes produces results closer to literature values than the WENO scheme managed. The coefficient of pressure results were not quite as expected, with lower pressures to the rear of the cylinder than expected, and values deviating further from literature values around the circumference of the cylinder. Similar effects had been shown in some literature data, though the results included in the C_p plot in figure 6.18 were the results that improved upon these C_p plots. Generally, the two-dimensional simulations under-predicted the C_p to the rear of the cylinder (as was shown in the two-dimensional results section) though these three-dimensional simulations had great improvement over those. The flow regime at $Re = 8000$, results from Norberg for which are included, is similar in characteristics to the $Re = 3900$ flow, yet with a lower C_p to the

rear of the cylinder. It is interesting to note that both the second-order Van Leer scheme and the fifth-order Kim Kim schemes predict C_p similar to that higher flow speed, (though further around the cylinder, the second-order Van Leer flow deviates from the higher-Reynolds number flow as well) suggesting the flow over the cylinder in these simulations increases in velocity too greatly. An initial thought was that this was due to the lack of the second separation angle angle, yet the WENO scheme predicts this separation angle but has lower values of C_p. It is worth noting that Shen et al [126] ran three-dimensional simulations of flow over a cylinder at $Re = 3900$ using a fifth-order WENO scheme with LES and an implicit sub-grid scale model. Their initial results showed similar C_p characteristics, but by subsequently doubling their grid resolution, they could improve on these results for C_p. Furthermore, two years later [127] they managed to improve on these results further still using a seventh-order WENO equivalent scheme and a mesh that was finer in resolution still. This, combined with the results from the simulations carried out here, would suggest that the value of C_p is very sensitive to changes in mesh resolution.

Moving on to the coefficient of friction plots, a similar pattern to the results of $Re = 300$ was observed for $Re = 3900$ for the WENO scheme; where the WENO scheme was able to replicate the literature values of coefficient of friction, while also being the scheme that was best able to reproduce the flow reattachment and second separation around the cylinder. As has already been alluded to, it was clear from the C_f plot that the Kim Kim scheme was not able to correctly predict the reattachment of flow to the cylinder. The second-order scheme was best at predicting the first angle of separation of the cylinder. All of the flows showed turbulent effects in the wake of the cylinder, yet the second-order Van Leer scheme showed different wake flows to the two other schemes, such that many of the turbulent features were not seen. At this higher Reynolds number, the WENO scheme showed fastest loss of momentum of flow towards freestream values in the wake of the cylinder, while both the fifth-order schemes showed the most consistent wake fluctuations. Finally, measurement of the Strouhal number once again showed its lack of sensitivity to simulation parameters, given all the simulations were able to give a good agreement of Strouhal number around the cylinder compared with literature values.

Evaluation of Cylinder Wake Spectral Properties

The spectral plots for the $3D$ flows have been presented throughout this chapter. It was observed in all cases that, in the wake of the cylinder, there was a redistribution of energy to higher frequency oscillations. Furthermore, there was an increase in power of the frequencies until a region of around $x/D = 4.00$, at which point dissipation took place. The peak frequency for each of these spectral plots can be extracted (by picking the maxima value point of each spectral plot for each x/D location) and plot against each other along the length of the wake. This shows the maximum power density along the line $y = 0$ and z at the mid-point span-wise (i.e. along the line of symmetry). The spectrum power density (note: not actual power as this would instead be the integral under each curve) at each point is plot in figures 6.23 to 6.25.

The plot for spectral data at $Re = 200$ in figure 6.23 shows a relatively low density of fluctuations. The fluctuations initially rise to the rear of the cylinder before peaking at $x/D = 2.00$

and steadily dropping again. A steady drop of the density of fluctuations was expected, though the fifth-order WENO scheme showed some unsteadiness in these fluctuations in the wake. The second-order Van Leer and fifth-order Kim Kim schemes both show stable oscillations in the wake. This would be expected for a steady wake at this Reynolds number. The fifth-order WENO scheme shows further instabilities, with the frequency of the oscillations in the wake increasing.

At the higher Reynolds number of 300, a similar pattern to that seen at Reynolds number 200 is visible. This reiterates the results seen earlier with regards to the noisy, highly fluctuating wake in the WENO simulation. Once again, a relatively smooth drop after the initial (now higher density) rise in fluctuation density is expected. However the WENO scheme has fluctuation densities increasing in the wake. Comparing the Reynolds number 300 plots to the $Re = 200$ plots, it can also be seen that the peak of the fluctuation densities has now moved closer to the rear of the cylinder, showing vortical flow is closer to the rear of the cylinder.

Interestingly, the Reynolds number 3900 spectral data plots show the WENO scheme performing closer to that expected. With the flow now fully turbulent, the fluctuation density is now more as expected. The Van Leer scheme, on the other hand, has relatively much lower density of fluctuations to the two other schemes. This plot once again also shows the vortices moving closer still to the rear of the cylinder than observed at the lower Reynolds numbers.

Overall, an examination of the spectral properties in the wake of the cylinder appears to give a good overview of what is taking place in the centreline of the wake, particularly at the lower speed steady flow. These plots once again agree with the earlier conclusion that, in the wake of the cylinder, the WENO scheme produces results that are essentially too noisy at the lower Reynolds numbers to be satisfactory. However, at the turbulent flow, the second-order scheme is instead shown to be the numerical scheme that is lacking in turbulent flow features to the rear of the cylinder.

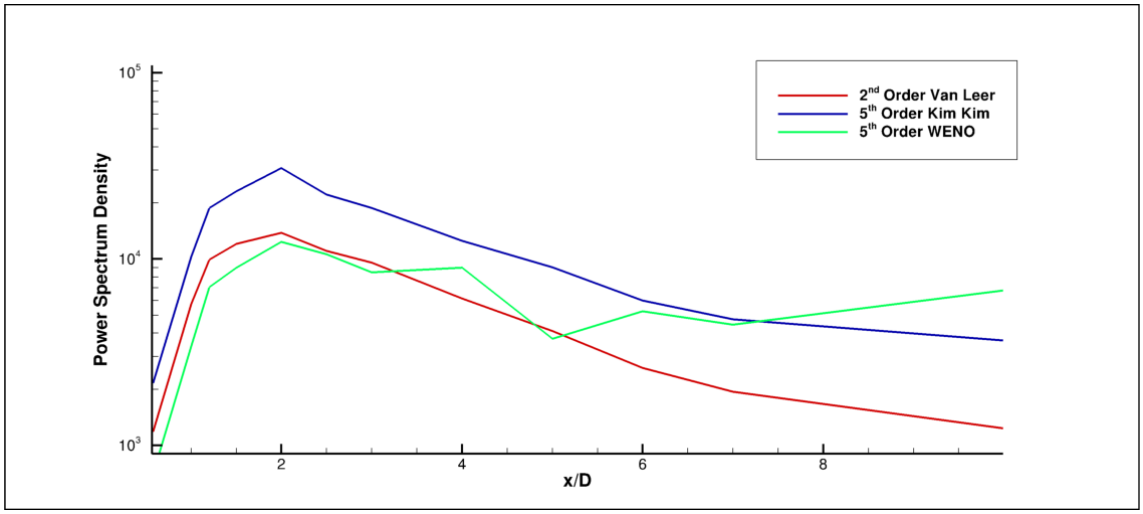

FIGURE 6.23: Spectral data for harmonic frequencies in the wake for Reynolds Number 200, $3D$ simulations.

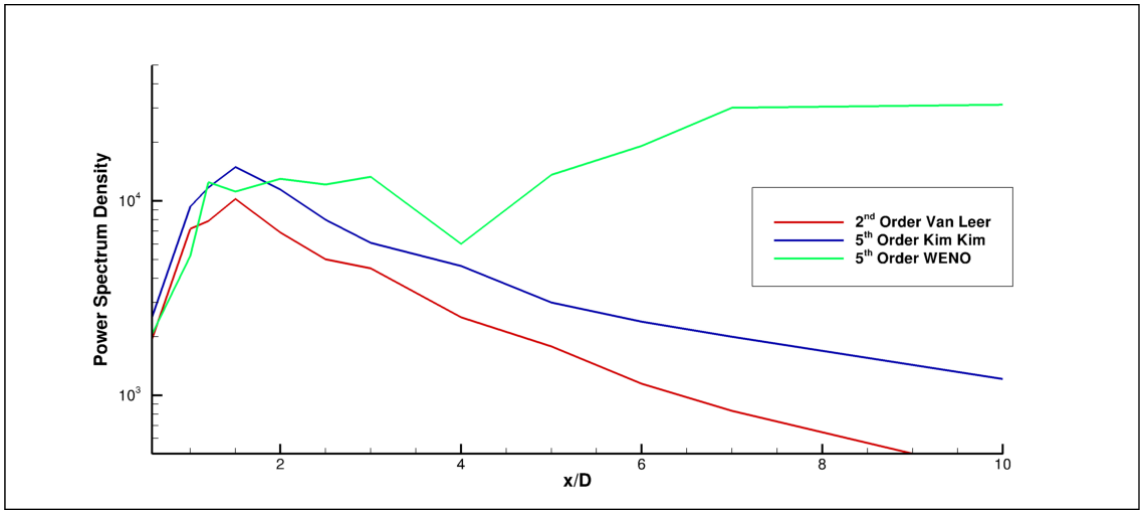

FIGURE 6.24: Spectral data for harmonic frequencies in the wake for Reynolds Number 300, 3D simulations. Power spectrum densities on the y axis are 10^3 to 10^5.

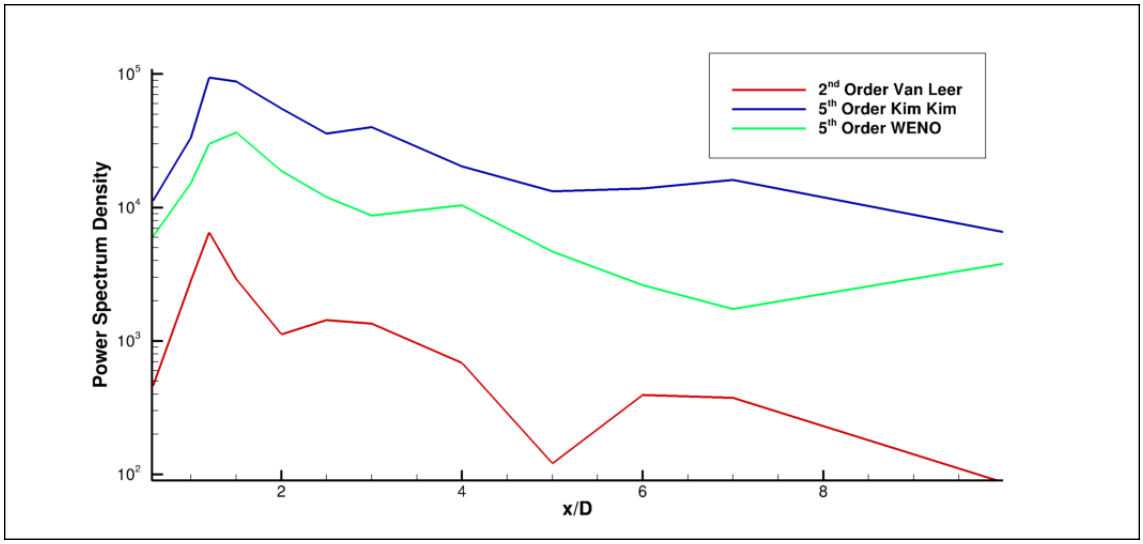

FIGURE 6.25: Spectral data for harmonic frequencies in the wake for Reynolds Number 3900, 3D simulations. Power spectrum densities on the y axis are 10^2 to 10^4.

7 Conclusion

Statistics: The only science that enables different experts using the same figures to draw different conclusions.
Evan Esar (1899 - 1995)

* * * * *

The aim of this thesis was chiefly to simulate a cylinder test case over a range of Reynolds numbers that spanned laminar to turbulent flow regimes, carrying out a comparative analysis of the accuracy of a range of reconstruction methods for the convective flux. An evaluation of the spectral properties of the flow in the cylinder wake was included, to examine the changes from steady flow to turbulent flow. The overall findings and conclusions drawn from the results is discussed in this chapter, followed by a section regarding future possible work that could help to obtain a greater examination of the high-resolution reconstruction methods.

7.1 Conclusions of Work

The thesis aimed at choosing a singular test case that would allow a sufficient examination of the range of reconstruction methods for the convective flux that were available within Cranfield's in

house CFD code. The code is based on the Implicit Large Eddy Simulation (ILES) method, central to which is the use of Riemann-solvers and high-order methods. This code had already been designed with a range of reconstruction methods present, but no direct comparative analysis of these reconstruction methods was found for flow over a cylinder for a range of Reynolds numbers. The aim was to choose an incompressible flow that could present difficulties for the code to resolve. The cylinder test case was chosen as it is a classic validation case that is computationally challenging, yet allows direct comparative analysis without having to make changes to other factors than the Reynolds number.

In previous studies, supersonic boundary conditions have been used with a Low Mach Number Treatment [82, 83] successfully. Investigations revealed that the use of supersonic boundary conditions was not sufficient for this case with flow at Mach number 0.2. It was found that the supersonic inflow and outflow boundary conditions introduced instabilities upstream of the cylinder, when the higher-order reconstruction schemes were implemented. This ultimately affected the flow over the cylinder - in particular the coefficients of flow over the cylinder. In order to remove these upstream instabilities, a sub-sonic boundary condition for inflow and outflow was implemented and used.

The grid chosen was an H-type mesh, created using commercial software. The grid was kept identical in all simulations except for those run at the fully laminar flow of Reynolds number 40. A lower-resolution grid was used for this Reynolds number as it was expected (and shown) to have a larger boundary layer that could more easily be resolved. With the increased speed of simulation offered by the coarser grid, the post-processing tools were developed and tested using this $Re = 40$ grid.

Reynolds number 200 flow is generally considered to be a transient regime of flow. While investigating grid independence, it was felt this would make its use as a test case inappropriate. Thus the higher Reynolds number case of 300 was used for further grid study, as this flow is non-transitional. Reynolds number 3900, with the smallest boundary layer, would then be a further test of the grid. This would ensure the grid was fine enough to resolve the boundary layer for all these speeds of flow.

In order to analyse the flow field, a range of marker points were placed in the flow. These points were chosen to be around the cylinder surface and in the wake (covering near, medium and far wake ranges). A post-processing code was then written to extract required data from these points.

With regards to three-dimensionality of the simulations, it was already shown that previous literature showed [85, 108, 112] increasing differences with increasing Reynolds numbers. At Reynolds numbers of around $Re = 170$[1] and above, there exists an onset of three-dimensional perturbations. Therefore, it is generally regarded that at these higher Reynolds numbers, a three-dimensional simulation is required. In the investigation for this thesis, it was confirmed that a three-dimensional simulation improves the results at higher Reynolds number. With the use

[1] As has been mentioned earlier in the thesis, there is no definite known critical Reynolds number, with a variety of Reynolds numbers presented as being the critical value for onset of three-dimensional perturbations. However, $Re = 170$ is generally considered as the critical value.

of higher-order methods, a satisfactory set of results may be obtained through two-dimensional simulations up to and including Reynolds number 300. Three-dimensional simulations (run from cold start) could take a matter of months to process. Contrary to this computational requirement, two-dimensional simulations only require a matter of weeks. Depending on the required accuracy, a two-dimensional simulation may be suitable for these lower speed flows. However, a marked difference was found at Reynolds number $3,900$ flow. This regime of flow onwards clearly require three-dimensional simulations. It was shown that using developed two-dimensional flows as a starting point for a three-dimensional simulation is possible, and can significantly aid in reducing simulation time.

Examining the points of the aims of the thesis individually, the first one involved the two-dimensional simulations:

- Simulation of two-dimensional cylinder flow from steady state laminar regime to fully turbulent regime and comparative analysis of the accuracy of various reconstruction methods for the convective flux.

The key difference between all the simulations was the order of reconstruction used. The observed stark differences were pointed out in the discussion. This is most clearly visible with the first-order reconstruction scheme, which showed itself to be wholly unreliable in producing satisfactory results. While this is common knowledge amongst those who use Riemann solvers and their corresponding reconstruction techniques, it was interesting to note just how much of a difference the first-order reconstruction scheme made compared with just the second-order reconstruction schemes. The first-order simulations did not require as much time to reach a developed regime of flow, but the development that was reached was not always correct. This was very much evident with the two-dimensional flow at $Re = 200$, where flow of an oscillatory nature with vortex streets to the rear of the cylinder is expected. The use of the first-order resulted in undeveloped flow; the flow retained a laminar nature and did not resolve the coefficients around the cylinder correctly at all.

In the two-dimensional simulations, the higher-order reconstruction methods improved the simulation results significantly, but all to varying degrees. At the fully laminar flow of $Re = 40$, the predictions of the higher-order simulations were consistent and of good quality, in spite of a low resolution grid. It was clear that in this laminar regime of flow, the second-order Van Leer simulation already provided good results, with the higher-order simulations only marginally improving upon it. The second-order Min Mod simulation, however, did not perform as well as the Van Leer method, over-predicting a number of the results. This trend continued at $Re = 200$, though the higher-order methods did not add any additional benefits to the second-order schemes. The ninth-order WENO scheme actually significantly (relative to the other schemes) over-predicted a range of the values and output noisy data in the wake compared with the other simulations. Already, at this Reynolds number, the effects of three-dimensionality of the flow were becoming visible, with over-prediction of coefficients occurring across the board. In spite of this, the two-dimensional simulations generally satisfactorily predicted the flow.

As the flow speed increased to $Re = 300$, there were greater deviations from experimental

values than previously observed. Clearly the lack of the third-dimension in the simulation was beginning to have an effect on the results of the simulation at this point. Yet, in spite of this missing dimension, the higher-order simulations generally were in good agreement with regards to predicting the flow. Once again, the ninth-order WENO scheme was the outlier, giving an early prediction of flow separation angle, as well as differing values for coefficients of pressure and friction around the cylinder. The fifth-order schemes performed well at this Reynolds number, reproducing the values determined in the numerical literature performed by Rajani [109] (using a RANS solver in $2D$, and a similar mesh resolution using an O-mesh as opposed to H-mesh).

Increasing the flow speed once again to the turbulent flow of $Re = 3900$, it was expected that in the two-dimensional form of simulations there would be the greatest discrepancies between numerical schemes. This was indeed the case, with two-dimensional simulations clearly having difficulties with correctly predicting the flow and coefficients around the cylinder. To the rear of the cylinder, the vortices were observed to be further from the rear of the cylinder than expected. With this turbulent flow, the two-dimensional simulations were considered to be unsatisfactory at predicting the flow correctly.

Overall, from the two dimensional simulations, it was felt that for laminar flows the higher-order methods suffered very early from the law of diminishing returns. That is, the second-order simulations (in particular the Van Leer scheme) provided results that were satisfactory, making higher-order simulations redundant. A similar conclusion was drawn from the flow at $Re = 200$. Although the higher-order schemes reached flow development rapidly in terms of number of iterations required, they did not add a significant degree of accuracy to the simulations to warrant their use all the time. Of these simulations, the fifth-order Kim Kim scheme was felt to perform best, when time needed to run was balanced against final results. As the flow speed increased to $Re = 300$, the effects of lack of three-dimensionality were becoming more noticeable. If these simulations were to be run in two-dimensions, the fifth-order schemes once again showed they could produce satisfactory results, performing better than some comparable numerical literature simulations.

With the fully turbulent flow at $Re = 3900$, the simulations were really pushed in two-dimensional form. Once again, they were shown to perform better than a range of two-dimensional numerical results in the literature. Yet overall the picture was that the simulations could not satisfactorily resolve the flow at this Reynolds number in two-dimensions even with the use of the higher-order methods.

The next aim of the thesis involved flow in three-dimensional simulations:

- Simulation of three-dimensional cylinder flow at Reynolds numbers corresponding to three-dimensional transitional and turbulent regimes and comparative analysis of the accuracy of various reconstruction methods for the convective flux.

With the three-dimensional simulations, runs were carried out for the higher Reynolds number flows of 200, 300 and 3900. The second-order Van Leer, and fifth-order schemes were felt to give the best performance in two-dimensional simulations with regards to runtime against quality of results. Thus these were the schemes chosen to be run in the three-dimensional simulations. At

the lower Reynolds number of 200, the fifth-order schemes were found to perform well oversall, with the WENO scheme predicting coefficients well, except for the coefficient of friction which was much better predicted by the Kim Kim scheme. The second-order Van Leer scheme also gave a fairly good prediction of flow characteristics around the cylinder, particularly given it was the fastest of the computational methods. However, it was found to suffer a little with regards to flow computations in the wake of the cylinder.

This trend was repeated with the Reynolds number 300 flow, whereby the fifth-order WENO scheme performed best of the three run schemes. Yet it showed greatest instabilities (with regards to fluctuations in flow momentum) in the wake of the cylinder, that was neither expected nor repeated by the other two numerical schemes. It was at the highest Reynolds number of 3900 where the WENO scheme showed a particular improvement over the other two schemes, however. While all three schemes correctly predicted the characteristics of the flow, such as the second separation point, it was the WENO scheme that best represented the effects of flow around the cylinder. It was the second-order Van Leer that best predicted the actual separation angle, and the fifth-order Kim Kim scheme that best predicted the coefficients around the cylinder and fluctuating velocities in the wake. In spite of the three-dimensionality of the flow, however, the coefficient of pressure values at the rear of the cylinder deviated from the expected values.

Ultimately, it proved to be difficult to decide on a best approach numerical scheme; each scheme seemed to perform better in one area of the flow over the others. A choice of best approach is made more difficult still when the time penalty in running the fifth-order WENO scheme is taken into account. Taking at least 150% of the run time of the other two schemes, it would have to offer good benefits to justify its use. While there were aspects of the flow that were well predicted by the WENO scheme at all three flows (particularly at the lower two speeds), it also output more noisy, turbulent wake at each of the flow speeds. While not an ideal numerical reconstruction scheme, it was felt the fifth-order Kim Kim scheme provided best overall results of the flow, without suffering the time penalty of the WENO scheme.

Finally, it was found in the literature (i.e. [127]) that the WENO scheme is very sensitive to an increase in grid resolution. Mesh refinement would help improve many of the results further (though it should be added that some of the resulting quantities were found to be insensitive to numerical scheme or grid changes such as the Strouhal number). However, it was felt that this would add to an already restrictive time penalty requirement on the simulations. In fact, it could be said that all the three-dimensional simulations added a time penalty over the two-dimensional simulations. However, the $3D$ simulations at the higher Reynolds number flows outperformed the $2D$ simulations, so the time penalty for $3D$ simulations could be considered worthwhile.

Returning to the aims of this thesis given in the introduction, the final aim of the thesis was stated as:

- Evaluation of spectral properties of the cylinder wake from steady flow to turbulence.

As discussed in the discussion at the end of the $3D$ results chapter, the values for the power spectrum densities can be extracted in the wake of the cylinder, along the line of symmetry. This

was undertaken as it was observed in all cases that, in the wake of the cylinder, there was a re-distribution of energy to higher frequency oscillations. These plots were presented in the results chapter (chapter 6), with the final conclusion being drawn that the spectral properties in the wake of the cylinder appears to give a good overview of what is taking place in the centreline of the wake – particularly at the lower speed steady flow. These plots once again agreed with the earlier conclusion that, in the wake of the cylinder, the WENO scheme produces results that are essentially too noisy at the lower Reynolds numbers to be satisfactory. However, at the turbulent flow, the second-order scheme is instead shown to be the numerical scheme that is lacking in turbulent flow features to the rear of the cylinder. At Reynolds number 3900, the spectral data plots showed the WENO scheme performing closer to that expected. With the flow now fully turbulent, the fluctuation density is now more as expected.

7.2 Future Work

A single grid resolution was used for a majority of the simulations. One of the key advantages the use of higher-order methods is supposed to offer is the ability to use coarser meshes for simulations while still obtaining good results. It would have been a good addition to this work to have supplemented the completed simulations with several matching simulations using finer grids to determine the differences in results this would make. Indeed it was shown in the literature, with comparable high-order schemes, that good results have been obtained by increasing grid resolution. A number of the parameters measured for the cylinder flow (particularly the coefficients directly around the cylinder itself) are sensitive to changes in the grid resolution used, as well as the numerical scheme. It would have been interesting to have investigated this further for the three-dimensional cases to determine whether it was easy to tell where a point of diminishing returns lies. On the other hand, other parameters were well predicted; these parameters have equally been shown to be less sensitive to choice of grid resolution and numerical method used.

Furthermore, the three-dimensional simulations were the simulations expected to give the best results. Unfortunately there was a time-constraint on the amount of time for which these could be run, which proved to be rather limiting given the amount of time these simulations needed. It is likely that even letting these simulations run for longer would present results closer to experimentation, and perhaps also allow examination of additional flow effects over time. For example, it was noted in the literature that when the flow cannot fully develop, (such as in a two-dimensional simulation) the oscillations in the wake occur with a centreline plane either above or below the line of symmetry to the rear of the cylinder, with this plane changing height over time. Movement of this centreline of oscillations may contribute to results not being as expected, but the only way to determine this would be to run the simulations for a longer period of time.

Finally, the effects of the higher-order methods can be tested at a much higher set of Reynolds numbers than those presented here; there is a great range of experimental and numerical data for significantly faster flow speeds such as $Re = 140,000$ while literature examining the capabilities of higher-order ILES codes at these flow speeds was not found. For these flows, a three-dimensional

simulation would be absolutely necessary, subsequently requiring more run time for the simulations.

References

[1] J. Maitin-Shepard, M. Cusumano-Towner, J. Lei, and P. Abbeel. *Cloth grasp point detection based on multiple-view geometric cues with application to robotic towel folding*. Department of Electrical Engineering and Computer Science, University of California, Berkeley (2010).

[2] C. S. Peskin. *Flow patterns around heart valves: A digital computer method for solving the equations of motion*. Tech. rep., Albert Einstein College of Medicine, Yeshiva University (1972).

[3] A. Persson. *Early operational numerical weather prediction outside the usa: an historical introduction part iii: Endurance and mathematics - british nwp, 1948-1965*. Meteorological Applications, Cambridge Journals Online **12**(4), 381 (2005).

[4] *Moore's law, wikipedia*. http://en.wikipedia.org/wiki/Moores_law .

[5] *Moore's law is dead, says gordon moore*. http://news.techworld.com/operating-systems/3477/moores-law-is-dead-says-gordon-moore/.

[6] M. S. B. Starr, M. D. Powe, and J. I. R. Owen. *A long-term statistical analysis of the accuracy of GPS and GLONASS broadcast orbit and clock models*. Proceedings of the 17th International Technical Meeting of the Satellite Division of The Institute of Navigation (ION GNSS 2004) **0**, 2095 (2004).

[7] M. Hondzo and A. Wüest. *Do microscopic organisms feel turbulent flows?* Environmental Science and Technology **43**, 764 (2009).

[8] T. crew of STS 51-I. *Shuttle views the Earth: Clouds from Space*. http://www.lpi.usra.edu/publications/slidesets/clouds/ (1985).

[9] H. Tennekes and J. L. Lumley. *A First Course in Turbulence* (The MIT Press, 1972).

[10] S. B. Pope. *Turbulent Flows* (Cambridge University Press, 2001).

[11] D. C. Wilcox. *Turbulence modeling for CFD* (D C W Industries, 2006).

[12] U. Frisch. *Turbulence, the legacy of A.N. Kolmogorov* (Cambridge University Press, 1996).

[13] *Centenial of flight: Evolution of technology*. http://www.centennialofflight.gov/essay/Evolution_of_Technology/first_wind_tunnels/Tech34.htm (2003).

[14] J. D. Anderson. *A History of Aerodynamics* (Cambridge University Press, 1997).

[15] M. V. Dyke. *An Album of Fluid Motion* (The Parabolic Press, 1982).

[16] J. Katz. *Race Car Aerodynamics* (Bentley Publishers, 1995).

[17] P. Moin and J. Kim. *Tackling turbulence with supercomputers*. Scientific American **276**(1), 62 (January 1997).

[18] *Top 500 supercomputers*. http://top500.org/list/2010/06/100 (2010).

[19] H. Versteeg and W. Malalasekera. *An Introduction to Computational Fluid Dynamics: The Finite Volume Method* (Pearson Education Limited, ISBN: 0131274988, 2007).

[20] F. F. Grinstein, L. G. Margolin, and W. J. Rider. *Implicit Large Eddy Simulation: Computing Turbulent Fluid Dynamics* (Cambridge University Press, 2007).

[21] S. Ghosal and P. Moin. *The basic equations for the large eddy simulation of turbulent flows in complex geometry*. Journal of Computational Physics **118**, 24 (1995).

[22] J. Smagorinsky. *General circulation experiments with the primitive equations: 1. the basic experiment*. Monthly Weather Review **91**, 99 (1963).

[23] F. F. Grinstein and C. Fureby. *Recent progress on MILES for high Reynolds number flows*. Journal of Fluids Engineering **124**, 848 (2002).

[24] F. F. Grinstein and C. Fureby. *Large Eddy Simulation of High-Reynolds number free and Wall-Bounded flows*. Journal of Computational Physics **181**, 68 (2002).

[25] E. F. Toro. *Riemann Solvers and Numerical Methods for Fluid Dynamics* (Springer-Verlag, 1997).

[26] D. Drikakis and W. Rider. *High-Resolution Methods for Incompressible and Low-Speed Flows* (Springer, New York, 2005).

[27] D. Drikakis. *Advances in turbulent flow computations using high-resolution methods*. Progress in Aerospace Sciences **39**, 405 (2003).

[28] A. Bagabir and D. Drikakis. *Numerical experiments using high-resolution schemes for unsteady, inviscid, compressible flows*. Computer Methods in Applied Mechanics and Engineering **193**, 4675 (2004).

[29] B. Thornber, A. Mosedale, and D. Drikakis. *On the implicit large eddy simulations of homogeneous decaying turbulence*. Journal of Computational Physics **226**, 1902 (2007).

[30] B. Thornber, M. Starr, and D. Drikakis. *Implicit large eddy simulation of ship airwakes*. The Aeronautical Journal **114**(1162), 715 (2010).

[31] A. Roshko. *Experiments on the flow past a circular cylinder at very high Reynolds number*. Journal of Fluid Mechanics **10**, 345 (1961).

[32] E. Berger and R. Willie. *Periodic flow phenomena*. Annual Review of Fluid Mechanics **4**, 313 (1972).

[33] A. Roshko. *Perspectives on bluff body aerodynamics*. The Journal of Wind Engineering and Industrial Aerodynamics **49**, 79 (1993).

[34] C. Norberg. *An experimental investigation of the flow around a circular cylinder: influence of aspect ratio*. Journal of Fluid Mechanics **258**, 287 (1994).

[35] C. H. K. Williamson. *Vortex dynamics in the cylinder wake*. Annual Review of Fluid Mechanics **28**, 477 (1996).

[36] T. Sarpkaya. *A critical review of the intrinsic nature of vortex-induced vibrations*. Journal of Fluids and Structures **19**, 389 (2004).

[37] M. C. Potter and D. C. Wiggert. *Schaum's Outline of Fluid Mechanics* (McGraw-Hill, 2008).

[38] C. Norberg. *Fluctuating lift on a circular cylinder: review and new measurements*. Journal of Fluids and Structures **17**, 57 (2003).

[39] C. H. K. Williamson. *Oblique and parallel modes of vortex shedding in the wake of a circular cylinder at low Reynolds numbers*. Journal of Fluid Mechanics **106**, 579 (1989).

[40] T. Lee and R. Budwig. *A study of the effect of aspect ratio on vortex shedding behind circular cylinders*. Physics of Fluids **A3**, 309 (1991).

[41] J. Park, K. Kwon, and H. Choi. *Numerical solutions of flow past a circular cylinder at Reynolds numbers up to 160*. KSME International Journal **12**, 1200 (1998).

[42] D. Barkley and R. D. Henderson. *Three-dimensional Floquet stability analysis of the wake of a circular cylinder*. Journal of Fluid Mechanics **322**, 215 (1996).

[43] C. H. K. Williamson. *The natural and forced formation of spot-like "vortex dislocations" in the transition of a wake*. Journal of Fluid Mechanics **243**, 393 (1993).

[44] R. Mittal and S. Balachandar. *Effect of three-dimensionality on the lift and drag of nominally two-dimensional cylinders*. Physics of Fluids **8**, 1841 (1995).

[45] A. G. Kravchenko and P. Moin. *Numerical studies of flow over a circular cylinder at* $Re_D = 3900$. Physics of Fluids **12**(2), 403 (2000).

[46] H. Q. Zhang, U. Fey, B. R. Noack, M. König, and H. Eckelmann. *On the transition of the cylinder wake*. Physics of Fluids **7**, 779 (1995).

[47] A. Prasad and C. H. K. Williamson. *Three-Dimensional Effects in Turbulent Bluff Body Wakes*. Experimental Thermal and Fluid Science **14**, 9 (1997).

[48] M. M. Zdravkovich. *Flow Around Circular Cylinders, Volume 1: Fundamentals* (Oxford University Press, 1997).

[49] P. W. Bearman and M. M. Zdravkovich. *Flow around a circular cylinder near a plane boundary*. Journal of Fluid Mechanics **89**, 33 (1978).

[50] A. J. Grass, P. W. J. Raven, R. J. Stuart, and J. A. Bray. *The influence of boundary layer velocity gradients and bed proximity on vortex shedding from free spanning pipelines*. ASME Journal of Energy Resources Technology **106**, 70 (1984).

[51] S. Taniguchi and K. Miyakoshi. *Fluctuating fluid forces acting on a circular cylinder and interference with a plan wall*. Experiments in Fluids **9**, 197 (1990).

[52] G. Bosch, M. Kappler, and W. Rodi. *Experiments on the flow past a square cylinder placed near a wall*. Experimental Thermal and Fluid Science **13**, 292 (1996).

[53] C. Lei, L. Cheng, and K. Kavanagh. *Re-examination of the effect of a plane boundary on force and vortex shedding of a circular cylinder*. Journal of Wind Engineering and Industrial Aerodynamics **80**, 263 (1999).

[54] S. Sarkar and S. Sarkar. *Vortex dynamics of a cylinder wake in proximity to a wall*. Journal of Fluids and Structures **26**, 19 (2010).

[55] M. C. Ong, T. Utnes, L. E. Holmedal, D. Myrhaug, and B. Pettersen. *Numerical simulation of flow around a circular cylinder close to a flat seabed at high Reynolds numbers using a $\kappa - \epsilon$ model*. Coastal Engineering (2010).

[56] M. Coutanceau and R. Bouard. *Experimental determination of the main features of the viscous flow in the wake of a circular cylinder in uniform translation. part 1, Steady flow*. Journal of Fluid Mechanics **79**, 231 (1977).

[57] M. M. Zdravkovich. *Flow Around Circular Cylinders, Volume 2: Applications* (Oxford University Press, 2003).

[58] T. Tamura, I. Ohta, and K. Kuwahara. *On the reliability of two-dimensional simulation for unsteady flows around a cylinder type structure*. The Journal of Wind Engineering and Industrial Aerodynamics **35**, 275 (1990).

[59] D. Labbé and P. Wilson. *A numerical investigation of the effects of the spanwise length on the 3-D wake of a circular cylinder*. Journal of Fluids and Structures **23**, 1168 (2007).

[60] S. Cao, S. Ozono, Y. Tamura, Y. Ge, and H. Kikugawa. *Numerical simulation of reynolds number effects on velocity shear flow around a circular cylinder*. Journal of Fluids and Structures (2010).

[61] J. L. D. Ribeiro. *Effects of surface roughness on the two-dimensional flow past circular cylinders I: mean forces and pressures*. Journal of Wind Engineering and Industrial Aerodynamics **37**, 299 (1990).

[62] B. Cantwell and D. Coles. *An experimental study on entrainment and transport in the turbulent near wake of a circular cylinder*. Journal of Fluid Mechanics **136**, 321 (1983).

[63] E. Achenbach. *Distribution of local pressure and skin friction around a circular cylinder in cross-flow up to Re* 5×10^6. Journal of Fluid Mechanics **34**(4), 625 (1968).

[64] E. Achenbach. *Influence of surface roughness on the cross-flow around a circular cylinder*. Journal of Fluid Mechanics **46**, 321 (1971).

[65] E. Achenbach and E. Heinecke. *On vortex shedding from smooth and rough cylinders in range of Reynolds numbers* 6×10^3 *to* 5×10^6. Journal of Fluid Mechanics **109**, 239 (1981).

[66] J. D. Anderson. *Computational Fluid Dynamics: The Basics with Applications* (McGraw-Hill, 1995).

[67] C. B. Laney. *Computational Gasdynamics* (Cambridge University Press, 1998).

[68] H. Schlichting. *Boundary Layer Theory* (McGraw-Hill, New York, 1979), 7 ed.

[69] G. F. C. Rogers and Y. R. Mayhew. *Thermodynamic and Transport Properties of Fluids: SI Units* (Blackwell Publishers, Oxford, 1995).

[70] C. Hirsch. *Numerical Computation of Internal and External Flows (*2^{nd} *Edition)* (Butterworth-Heinemann, 2007).

[71] J. Blazek. *Computational Fluid Dynamics: Principles and Applications* (Elsevier, 2001).

[72] B. van Leer. *Towards the ultimate conservative difference scheme. part ii: Monotonicity and conservation combined in a second order scheme*. Journal of Computational Physics **14**, 361 (1974).

[73] B. van Leer. *Towards the ultimate conservative difference scheme. part v*. Journal of Computational Physics **32**, 101 (1979).

[74] A. Mosedale. *Modelling Shock Induced Instabilities, Transition and Turbulent Mixing using High Order Methods*. Ph.D. thesis, Cranfield University (2008).

[75] J. Zoltak and D. Drikakis. *Hybrid upwind methods for the simulation of unsteady shock-wave diffraction over a cylinder*. Comput. Method Appl. Mech. Eng **162**, 165 (1998).

[76] K. H. Kim and C. Kim. *Accurate, effcient and monotonic numerical methods for multi-dimensional compressible flows. part ii: Multi-dimensional limiting process*. Journal of Computational Physics **208**, 570 (2005).

[77] G.-S. Jiang and C.-W. Shu. *Efficient implementation of weighted eno schemes*. Journal of Computational Physics **126**, 202 (1996).

[78] D. Balsara and C.-W. Shu. *Monotonicity preserving weighted essentially non-oscillatory schemes with increasingly high order of accuracy*. Journal of Computational Physics **160**, 405 (2000).

[79] V. Titarev and E. Toro. *Finite volume weno schemes for three dimensional conservation laws*. Journal of Computational Physics **201**, 238 (2004).

[80] A. Henrick, T. Aslam, and J. Powers. *Mapped weighted essentially non-oscillatory schemes: Achieving optimal order near critical points*. Journal of Computational Physics **207**, 542 (2005).

[81] C.-W. Shu. *High-order finite difference and finite volume WENO schemes and discontinuous galerkin methods for CFD*. International Journal of Computational Fluid Dynamics **17(2)**, 107 (2003).

[82] B. Thornber. *PhD Thesis* (Cranfield University, 2007).

[83] B. Thornber, A. Mosedale, D. Drikakis, D. Youngs, and R. Williams. *An improved reconstruction method for compressible flows with low Mach number features*. Journal of Computational Physics **227**, 4873 (2008).

[84] T. J. Chung. *Computational Fluid Dynamics* (Cambridge University Press, 2002).

[85] M. Breuer. *Numerical and modeling influences on large eddy simulations for the flow past a circular cylinder*. International Journal of Heat and Fluid Flow **19**, 512 (1998).

[86] B. Thornber. private communication (2009).

[87] F. I. Barada. private communication (2009).

[88] N. MacDonald. *Writing Message Passing Parallel Programs with MPI*. University of Edinburgh. Course Notes.

[89] M. Breuer. *A challenging test case for large eddy simulation: high Reynolds number circular cylinder flow*. International Journal of Heat and Fluid Flow **21**, 648 (2000).

[90] *Gridgen version 15 user manual, volume 1*. Tech. rep., Pointwise, Inc (2010).

[91] M. Vinokur. *On one-dimensional stretching functions for finite-difference calculations*. Tech. rep., NASA Contractor Report 3313 (1980).

[92] *cfd general notation system (cgns) standard*. URL http://cgns.sourceforge.net/.

[93] A. G. Kravchenko, P. Moin, and K. Shariff. *B-Spline Method and Zonal Grids for Simulations of Complex Turbulent Flows*. Journal of Computational Physics **151**, 757 (1999).

[94] M. Breuer. *Large eddy simulation of the sub-critical flow past a circular cylinder: numerical and modelling aspects*. International Journal for Numerical Methods in fluids **28**, 1281 (1998).

[95] D. J. Tritton. *Physical fluid dynamics* (Clarendon Press, 1988).

[96] D. J. Tritton. *Experiments on the flow past a circular cylinder at low Reynolds numbers*. Journal of Fluid Mechanics **6**, 547 (1959).

[97] A. S. Grove, F. H. Shair, E. E. Petersen, and A. Acrivos. *An experimental investigation of the steady separated flow past a circular cylinder*. Journal of Fluid Mechanics **19**, 60 (1964).

[98] J. S. Son and T. J. Hanratty. *Numerical solution for the flow around a cylinder at Reynolds numbers of 40, 200 and 500*. Journal of Fluid Mechanics **35**, 369 (1969).

[99] S. Dennis and G. Chang. *Numerical solutions for steady flow past a circular cylinder at Reynolds numbers up to 100*. Journal of Fluid Mechanics **42**, 471 (1970).

[100] B. Fornberg. *A numerical study of steady viscous flow past a circular cylinder*. Journal of Fluid Mechanics **98**, 819 (1980).

[101] A. Borthwick. *Comparison between two finite-difference schemes for computing the flow around a cylinder*. Journal of Numerical Methods of Fluids **6**, 275 (1986).

[102] R. Franke, W. Rodi, and B. Schönung. *Numerical calculation of laminar vortex-shedding flow past cylinders*. Journal of Wind Engineering and Industrial Aerodynamics **35**, 237 (1990).

[103] R. D. Henderson. *Details of the drag curve near the onset of vortex shedding*. Physics of Fluids **7**, 2102 (1995).

[104] M. P. Kirkpatrick, S. W. Armfield, and J. H. Kent. *A representation of curved boundaries for the solution of the Navier-Stokes equations on a staggered three-dimensional Cartesian grid*. Journal of Computational Physics **184**, 1 (2003).

[105] A. Thom. *The flow past circular cylinders at low speeds*. Proceedings of the Royal Society of London: Series A **141**, 651 (1933).

[106] M. M. Zdravkovich. *Conceptual overview of laminar and turbulent flows past smooth and rough circular cylinders*. Journal of Wind Engineering and Industrial Aerodynamics **33**, 53 (1990).

[107] B. R. Noack and H. Eckelmann. *A global stability analysis of the steady and periodic cylinder wake*. Journal of Fluid Mechanics **270**, 297 (1994).

[108] H. Persillon and M. Braza. *Physical analysis of the transition to turbulence in the wake of a circular cylinder by three-dimensional Navier-Stokes simulation*. Journal of Fluid Mechanics **365**, 23 (1998).

[109] B. N. Rajani, A. Kandasamy, and S. Majumdar. *Numerical simulation of laminar flow past a circular cylinder*. Applied Mathematical Modelling **33**, 1228 (2009).

[110] H. G. Dimopoulos and T. J. Hanratty. *Velocity gradients at the wall for flow around a cylinder for Reynolds numbers between 60 and 360*. Journal of Fluid Mechanics **33**, 303 (1968).

[111] C. Wieselsberger. *über den flüssigkeits und luftwiderstand*. Zeitschrift f′ur Physik **22**, 321 (1921).

[112] R. Mittal and S. Balachandar. *On the inclusion of three-dimensional effects in simulations of two-dimensional bluff-body wake flows*. The 1997 ASME Fluids Engineering Division Summer Meeting (1997).

[113] C. Wieselsberger. *New data on the laws of fluid resistance*. NACA Technical Notes **84** (1922).

[114] P. Beaudan and P. Moin. *Numerical Experiments on the flow past a circular cylinder at sub-critical Reynolds number, Report No. TF-62* (Department of Mechanical Engineering, Stanford university, 1994).

[115] M. E. Young and A. Ooi. *Comparitive Assessment of LES and URANS for Flow Over a Cylinder at a Reynolds Number of 3900*. 16th Australasian Fluid Mechanics Conference pp. 1063–1070 (2007).

[116] G. S. Cardell. *Flow past a circular cylinder with a permeable splitter plate, PhD Thesis (reported in [94])* (California Institute of Technology, 1993).

[117] C. Norberg. *Effects of Reynolds number and low-intensity free stream turbulence on the flow around a circular cylinder* (Chalmers University of Technology, Gothenburg, Sweden, 1987).

[118] L. M. Lourenco and C. Shih. *Characteristics of the plane turbulent near wake of a circular cylinder. A particle image velocimetry study.* from [93, 120, 124] (1993).

[119] L. Ong and J. Wallace. *The velocity field of the turbulent very near wake of a circular cylinder*. Journal of Experimental Fluids **20**, 441 (1996).

[120] R. Mittal. *Progress on LES of flow past a circular cylinder*. Annual Research Briefs, Center for Turbulence Research, Stanford University pp. 233–241 (1996).

[121] J. Frölich, W. Rodi, P. Kessler, S. Parpais, J. P. Bertoglio, and D. Laurence. *Large eddy simulation of flow around circular cylinders on structured and unstructured grids*. CNRS DFG Collaborative Research Programme **66**, 319 (1998).

[122] X. Ma, G.-S. Karamanos, and G. E. Karniadakis. *Dynamics and low-dimensionality of a turbulent near wake*. Journal of Fluid Mechanics **410**, 29 (2000).

[123] J. Franke and W. Frank. *Large eddy simulation of the flow past a circular cylinder at* $Re_D = 3900$. Journal of Wind Engineering and Industrial Aerodynamics **90**, 1191 (2002).

[124] K. Mahesh, G. Constantinescu, and P. Moin. *A numerical method for large-eddy simulation in complex geometries*. Journal of Computational Physics **197**, 215 (2004).

[125] N. Park, J. Y. Yoo, and H. Choi. *Discretization errors in large eddy simulation: on the suitability of centered and upwind-biased compact difference schemes*. Journal of Computational Physics **198**, 580 (2004).

[126] Y. Shen, G. Zha, and B. Wang. *Large eddy simulation of circular cylinder flow by using high order weno scheme*. 38th Fluid Dynamics Conference and Exhibit (2008).

[127] Y. Shen and G. Zha. *Large eddy simulation using a new set of sixth order schemes for compressible viscous terms*. Journal of Computational Physics **229**, 8296 (2010).

[128] W. Rodi, J. H. Ferziger, M. Breuer, and M. Pourquié. *Status of large eddy simulation: Results of a workshop, workshop on les of flows past bluff bodies*. Journal of Fluids Engineering **119**, 248 (1997).

A

Appendix A: Non-Dimensionalisation of Equations and Input Values

A.1 Introduction

The computational scheme requires non-dimensionalisation of the equations used, as well as input values. If everything were to be left dimensional, the numerical solution of the Navier-Stokes equations would involve operations between values varying by several orders of magnitude. This would seriously affect the end result, giving a failed numerical solution or, in best case, an unstable solution as calculations are carried out beyond the computational floating point limit. Thus, the initialisation values and equations are non-dimensional. Furthermore, the Navier-Stokes equations are calculated in non-dimensional form. This also ensures that characteristic (non-dimensional) parameters such as the Mach and Reynolds numbers can be regulated independently of other variables.

This chapter briefly introduces the non-dimensionalised Navier-Stokes equations as well as the related non-dimensional variables. The input equations for the code used are then checked for non-dimensionality.

A.2 Non-dimensional Navier-Stokes Equations

In order to properly describe the non-dimensional form of the Navier-Stokes equations, we have to begin with the non-dimensional variables. These are generally presented in a standard form, with variables with an asterisk denoting non-dimensional variables. Variables with subscript ∞ represent the freestream condition values. Many of the variables have to be modified according to the reference (or characteristic) length used for the simulation, defined as L.

$$(x^*, y^*, z^*) = \frac{(x, y, z)}{L}, \quad t^* = \frac{t}{\frac{L}{u_\infty}}, \quad (u^*, v^*, w^*) = \frac{(u, v, w)}{u_\infty}$$

$$\rho^* = \frac{\rho}{\rho_\infty}, \quad p^* = \frac{p}{\rho_\infty v_\infty^2}, \quad T^* = \frac{T}{T_\infty}, \quad \mu^* = \frac{\mu}{\mu_\infty}, \quad F_i^* = \frac{F_i}{\frac{v_\infty^2}{L}}$$

The reference length is used in the determination of the Reynolds number of the simulation (or to determine other values within the Reynolds number equation at a fixed Reynolds number). The equation for the Reynolds number is non-dimensional as shown.

$$Re = \frac{\rho_\infty v_\infty L}{\mu_\infty} = \frac{kg \cdot m^{-3} \times m \cdot s^{-1} \times m}{kg \cdot m^{-1} \cdot s^{-1}} = \frac{m \cdot s^{-1} \times m}{m^2 \cdot s^{-1}} = \text{non-dimensional} \tag{A.1}$$

Following from the form of Navier-Stokes equations given in chapter 3, the dimensionless form of the Navier-Stokes equations can now be written as:

A.3 Initial Parameters

For the purposes of initialisation of simulations, we start from an initial set of parameters. In order to check that equations in the code are non-dimensionalised, example cases using air at standard pressure and room temperature are used. Thus we use the following values:

Mach number, $M_\infty = 0.2$

Temperature, $T_{free} = 293K$

Density, $\mu_{ref} = 1.716 \times 10^{-5} kgm^{-1}s^{-1}$

Ratio of specific heats, $\gamma = 1.4$

Reference Length Scale, $L_{ref} = 1$

Sutherland's Constant, $D_{SUTH} = 110K$

Sutherland's Temperature, $T_{SUTH} = 273.15K$

A.4 Non-dimensionalised equations

We begin by ensuring that equations used are non-dimensional, where needed, by analysing the resultant units from each equation. The calculations begin with determining a reference flow velocity value based on Mach number and freestream air characteristics:

$$V_{ref} = M_\infty \times \sqrt{\frac{\gamma_{ref} \times P_{free}}{\rho_{free}}} \tag{A.2}$$

The units of the variables with dimensions are as follows:

$$\begin{aligned} V_{ref} &= m \cdot s^{-1} \\ P_{free} &= Pa = N \cdot m^{-2} = kg \cdot m^{-1} \cdot s^{-2} \\ \rho_{free} &= kg \cdot m^{-3} \end{aligned} \tag{A.3}$$

Giving:
$V_{ref} = (kg \cdot m^{-1} \cdot s^{-2} \cdot kg^{-1} \cdot m^3)^{\frac{1}{2}} = (m^2 \cdot s^{-2})^{\frac{1}{2}} = m \cdot s^{-1}$ As expected. Next the gas constant is determined for the specific gas used, through calculation of the freestream values. The equation for this is:

$$R_{gas} = \frac{P_{free}}{(\rho_{free} \times T_{free})} \tag{A.4}$$

Once again, the units of the variables with dimensions are:

$$P_{free} = Pa = N \cdot m^{-2} = kg \cdot m^{-1} \cdot s^{-2} \tag{A.5}$$
$$\rho_{free} = kg \cdot m^{-3} \tag{A.6}$$
$$T_{free} = K \tag{A.7}$$
$$\tag{A.8}$$

Giving:

$$R_{gas} = kg \cdot m^{-1} \cdot s^{-2} \times kg^{-1} \cdot m^3 \times K^{-1} = m^2 \cdot s^{-2} \cdot K^{-1} \tag{A.9}$$

See equation 2.28, page 47 pdf, page 34 thesis.

A.5 Test of Reynolds numbers

In the code, the reference velocity, V_{ref} is computed from the Mach number and reference ratio of specific heats, as given in equation A.2.

$$V_{ref} = M_\infty \times \sqrt{\frac{\gamma_{ref} \times P_{free}}{\rho_{free}}} = 0.2 \times \sqrt{\frac{1.4 \times 100,000}{1.204}} = 68.199 ms^{-1} \tag{A.10}$$

The equation of state for a gas gives the relationship between temperature, pressure, and volume with a gas constant, R. The gas constant has a unique value for every gas. The equation of state giving the gas constant is given in equation A.4 .

$$R_{gas} = \frac{P_{free}}{(\rho_{free} \times T_{free})} = \frac{100,000}{1.204 \times 293} = 283.47 \tag{A.11}$$

From the gas constant, R, we compute the c_v of the gas:

$$c_v = \frac{R_{gas}}{\gamma_{ref} - 1} = \frac{283.47}{0.4} = 708.68 \tag{A.12}$$

A reference temperature is then computed:

$$T_{ref} = \frac{V_{ref}^2}{c_v} = 6.56K \tag{A.13}$$

The viscosity is then non-dimensionalised in a similar method to the velocity, density and the length scales. This viscosity is then scaled using Sutherlands Law, whereby a scaling viscosity (μ_{suth}) is determined and used to scale the flow viscosity appropriately. The Sutherlands Viscosity is given by:

$$\mu_{suth} = \frac{C_1 \times T_{free}^{\frac{3}{2}}}{T_{free} + D_{suth}} \tag{A.14}$$

Where C_1 is computed by:

$$C_1 = \mu_{ref} \times \frac{T_{suth} + D_{suth}}{T_{suth}^{\frac{3}{2}}} = 1.716 \times 10^{-5} \times \frac{273.15 + 110}{273.15^{\frac{3}{2}}} = 1.456 \times 10^{-6} \tag{A.15}$$

This gives a μ_{suth} of:

$$\mu_{suth} = \frac{1.456 \times 10^{-6} \times 293^{\frac{3}{2}}}{293 + 110} = 1.813 \times 10^{-5} \tag{A.16}$$

The units for C_1 are:

$$C_1 = kg \cdot m^{-1} \cdot s^{-1} \times K \cdot K^{-\frac{3}{2}} = kg \cdot m^{-1} \cdot s^{-1} \cdot K^{-\frac{1}{2}} \tag{A.17}$$

This gives units for μ_{suth} as being:

$$\mu_{suth} = \frac{kg \cdot m^{-1} \cdot s^{-1} \cdot K^{-\frac{1}{2}} \times K^{\frac{3}{2}}}{K} = kg \cdot m^{-1} \cdot s^{-1} \tag{A.18}$$

Viscosity is computed specifically for this case; with use made of the Reynolds number set for the case.

$$\mu = \frac{\rho_{free} \times V_{ref} \times L_{ref}}{Re} \tag{A.19}$$

The scaling of the viscosity is then carried out:

$$\mu_{scale} = \frac{\mu}{\mu_{suth}} \tag{A.20}$$

$$\mu_{ref} = \mu_{scale} \times \mu_{ref} \tag{A.21}$$

The equation for Reynolds number is:

$$Re = \frac{\rho VL}{\mu} = \frac{VL}{\nu} = \frac{kg \cdot m^{-3} \times m \cdot s^{-1} \times m}{kg \cdot m^{-1} \cdot s^{-1}} = \frac{m \cdot s^{-1} \times m}{m^2 \cdot s^{-1}} \tag{A.22}$$

B

Appendix B: Additional two-dimensional result plots

The two-dimensional results given in chapter 5 give the main relevant results of the $2D$ simulations. While that chapter gives a range of the key results obtained, this appendix chapter extends the results given with further result plots from the two-dimensional simulations. A range of additional plots are given here to allow for further details of the flow to be examined. It was felt that, due to the number of simulations (and corresponding output plots) run, these plots were unnecessary amongst the main body of results.

Time-averaged versus instantaneous flow field plots are initially presented for each numerical scheme run within each Reynolds number section, with the simulations at Reynolds number greater than 40 including Reynolds stress ($u'v'$) and fluctuation plots. These plots were essentially zero at $Re = 40$.

B.1 Reynolds Number $= 40$

Figures B.1 to B.7 show time-averaged and instantaneous plots of the flow field showing details of flow around the cylinder. The small vortices to the rear of the cylinder are clearly visible. At this laminar flow speed, there is little discernible difference between the different numerical schemes

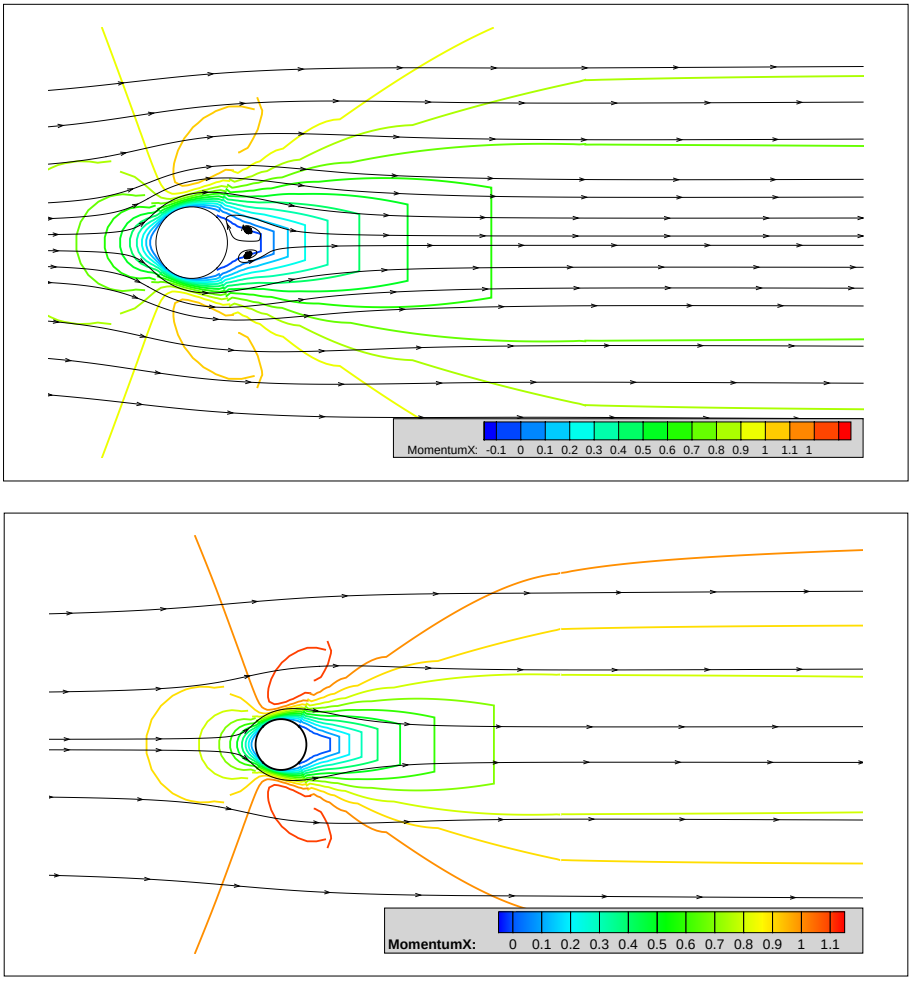

FIGURE B.1: Time averaged (top) and instantaneous (bottom) plots of Reynolds number 40 2D flow, 1^{st} order scheme

when looking at the flow field. In addition, there is little difference between the time-averaged plots and the instantaneous plots. Due to the laminar flow field, plots such as the Reynolds stresses and fluctuation plots have values very close to zero, and thus are omitted.

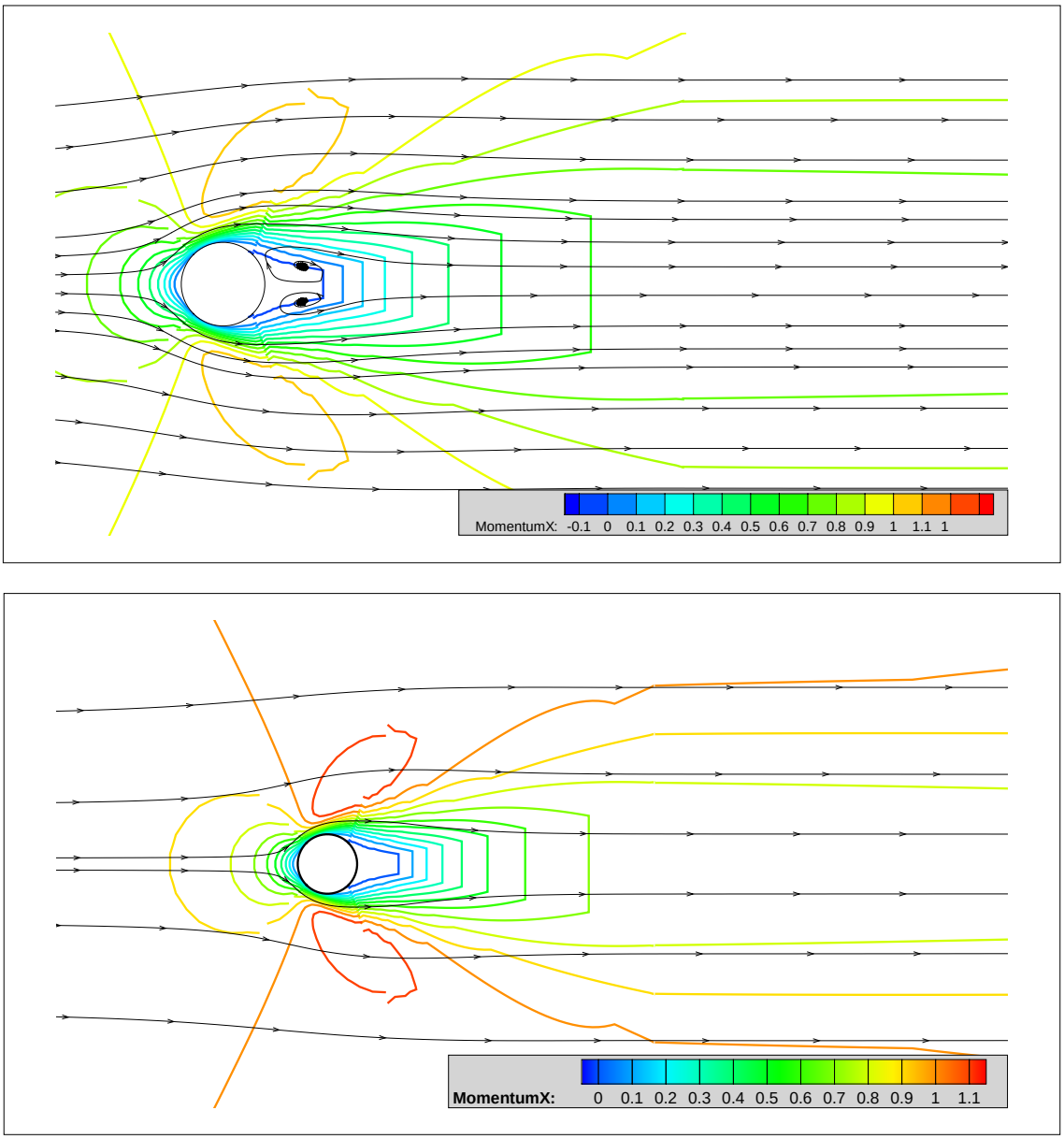

FIGURE B.2: Time averaged (top) and instantaneous (bottom) plots of Reynolds number 40 2D flow, 2nd order Min Mod scheme

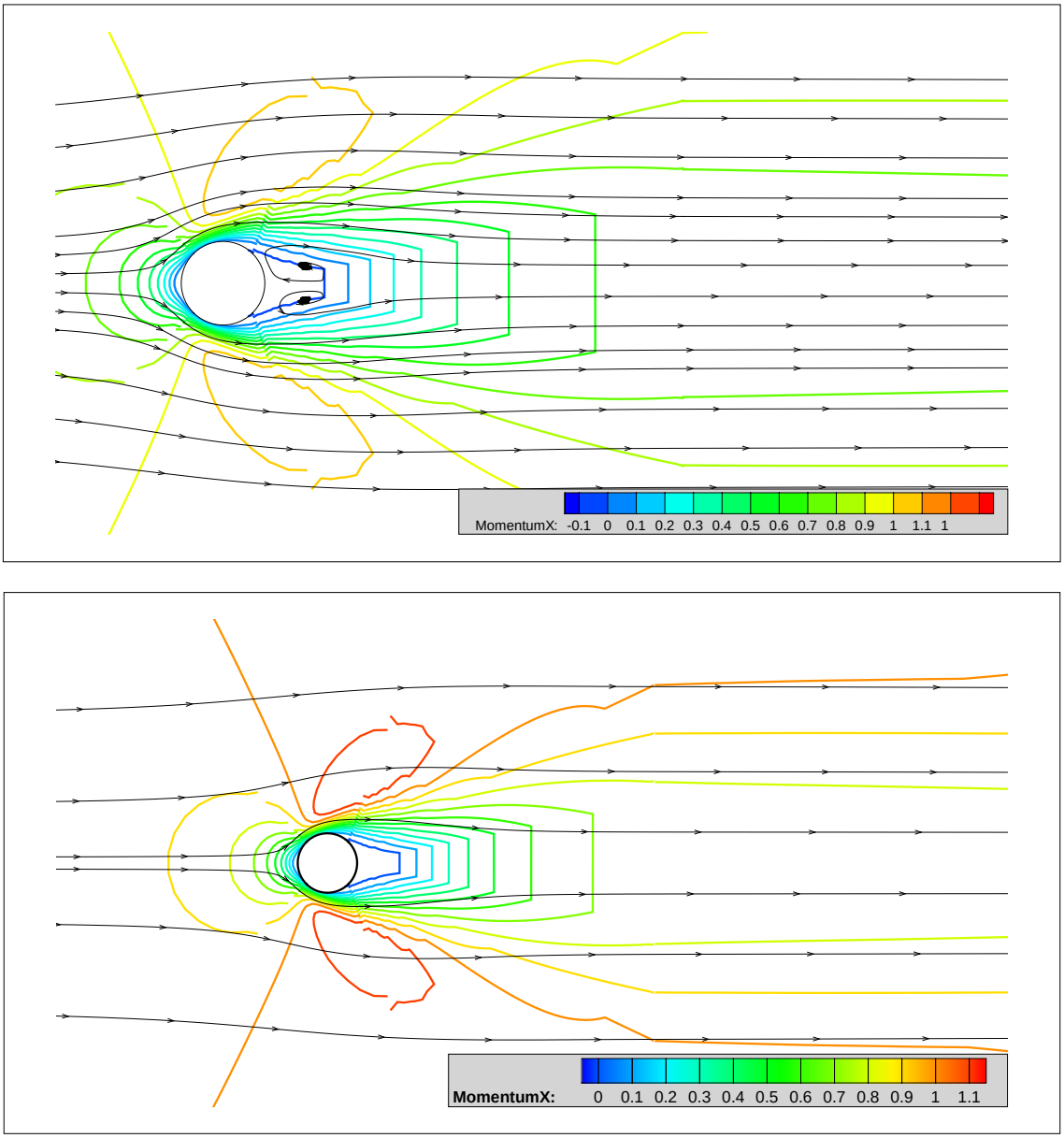

FIGURE B.3: Time averaged (top) and instantaneous (bottom) plots of Reynolds number 40 2D flow, 2^{nd} order Van Leer scheme

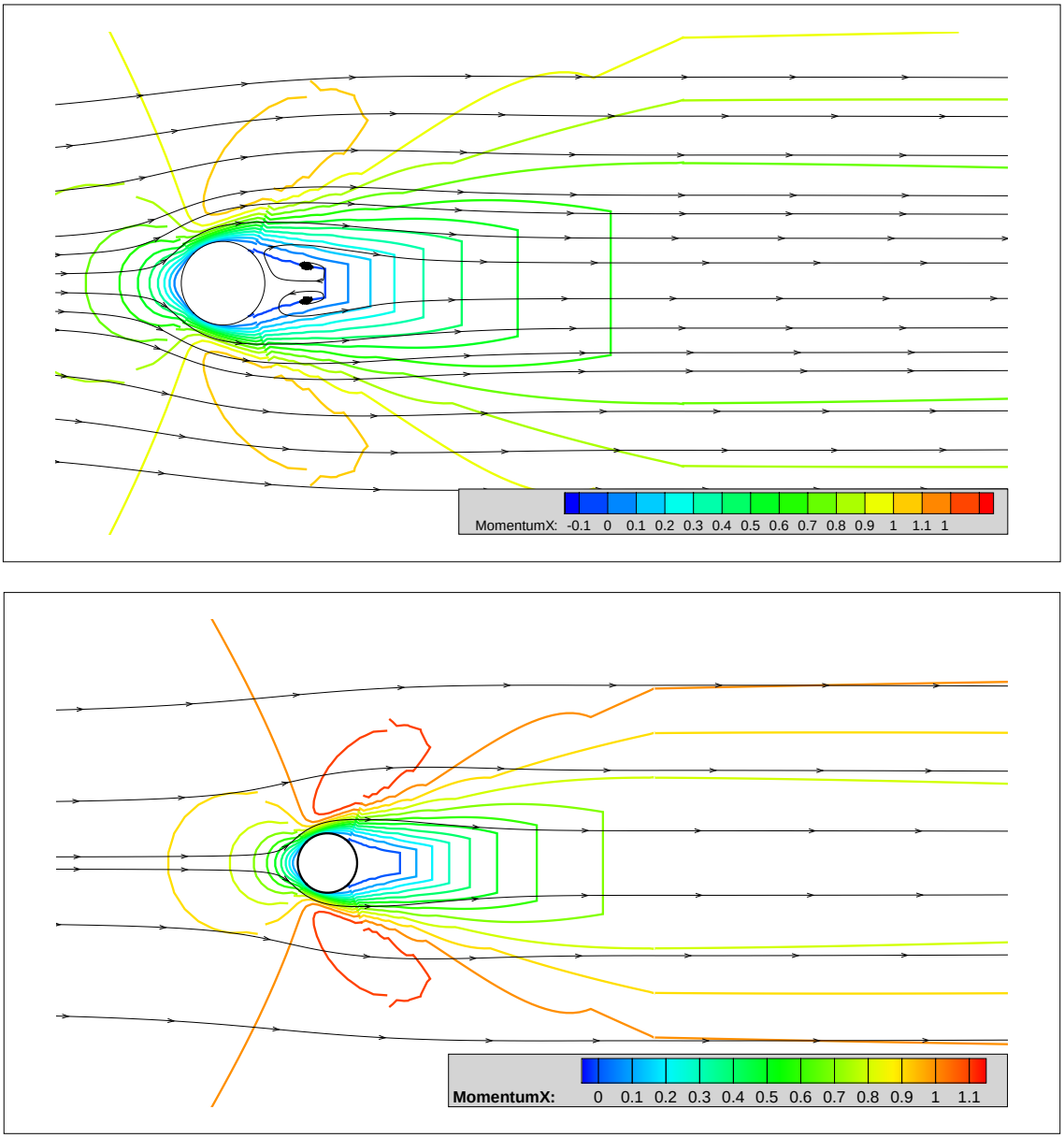

FIGURE B.4: Time averaged (top) and instantaneous (bottom) plots of Reynolds number 40 2D flow, 3^{rd} order Kim Kim scheme

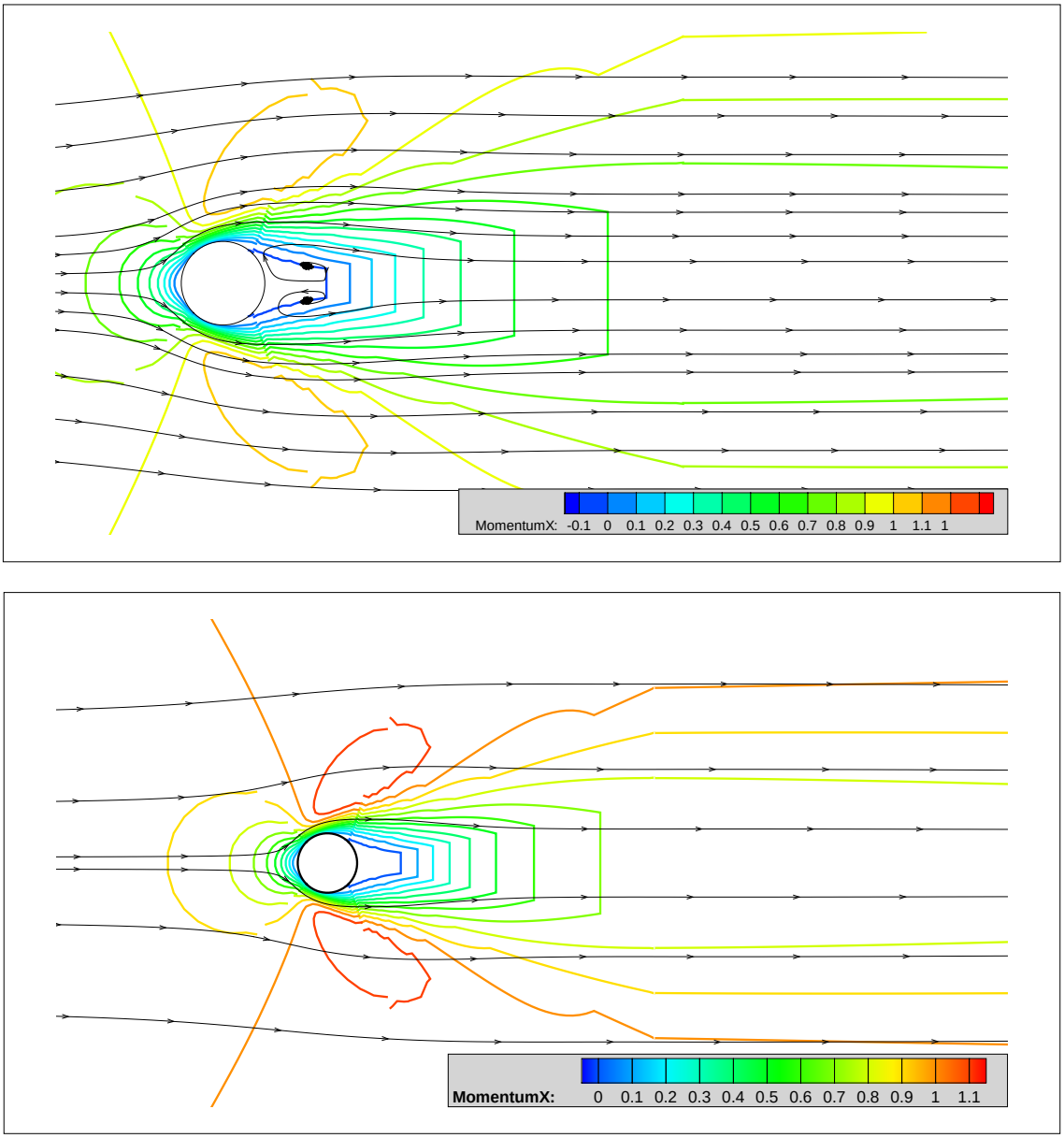

FIGURE B.5: Time averaged (top) and instantaneous (bottom) plots of Reynolds number 40 2D flow, 5^{th} order Kim Kim scheme

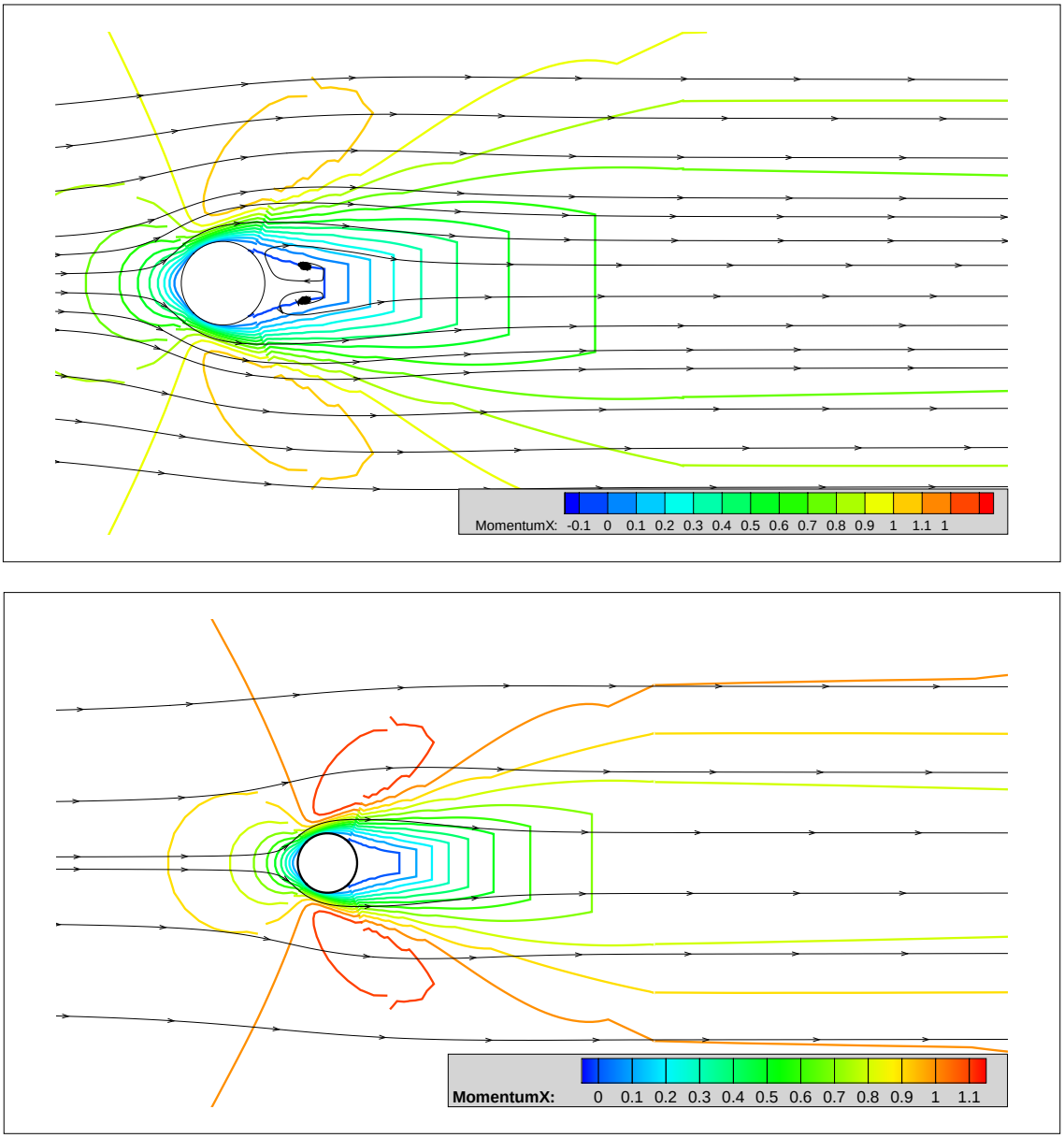

FIGURE B.6: Time averaged (top) and instantaneous (bottom) plots of Reynolds number 40 2D flow, 5^{th} order WENO scheme

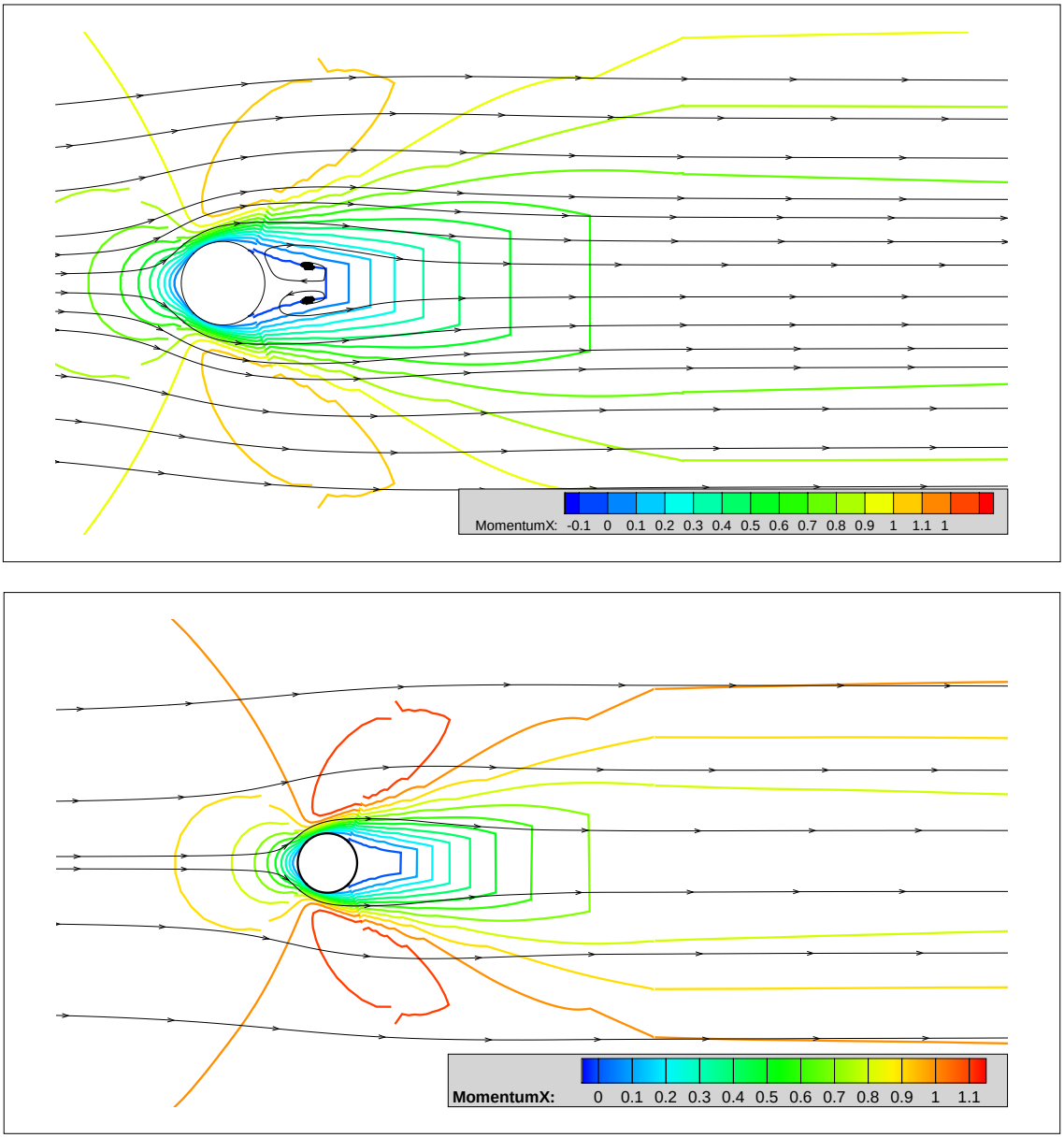

FIGURE B.7: Time averaged (top) and instantaneous (bottom) plots of Reynolds number 40 2D flow, 9^{th} order WENO scheme

B.2 Reynolds Number = 200

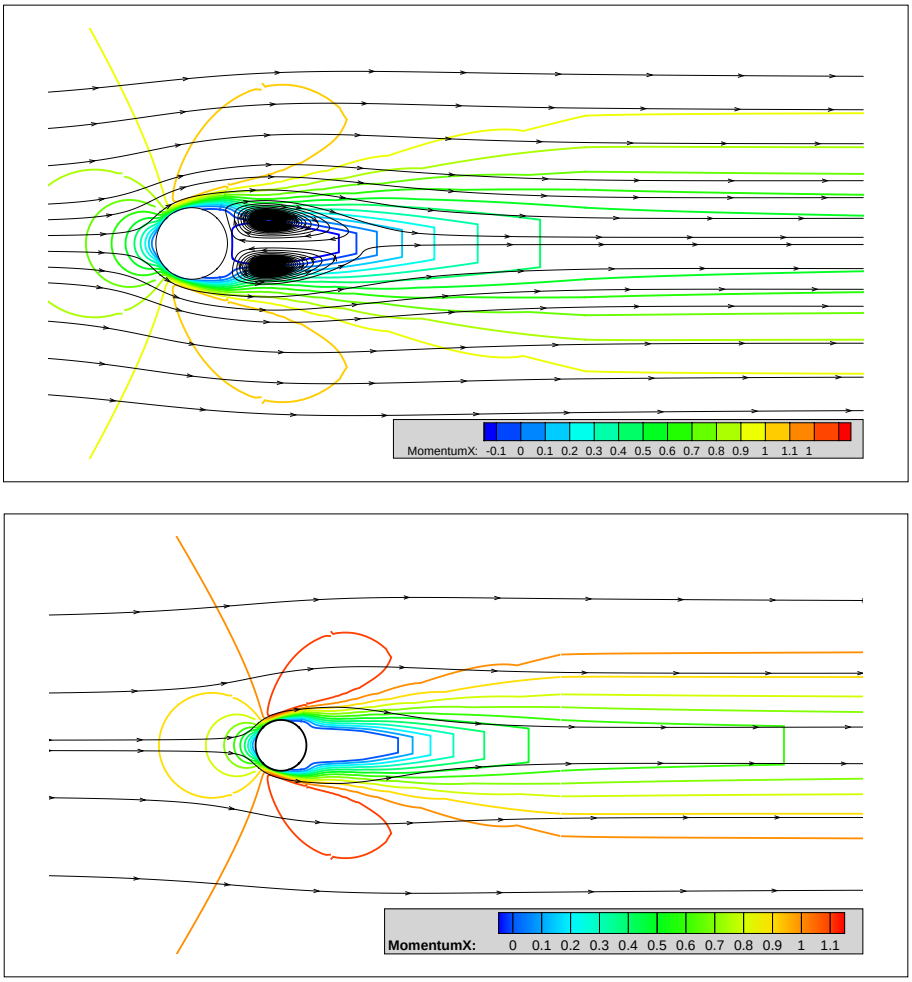

FIGURE B.8: Time averaged (top) and instantaneous (bottom) plots of Reynolds number 200 2D flow, 1^{st} order scheme

Figures B.8 to B.14 show time-averaged and instantaneous plots of the flow field showing details of flow around the cylinder. The small vortices to the rear of the cylinder are clearly visible. At this flow speed, there is little discernible difference between the different numerical schemes when looking at the flow field, with the exception of the first-order scheme which continues to display laminar flow as previously discussed in the main results chapter (section 5.3). In addition, there is now a clear difference between the time-averaged plots and the instantaneous plots.

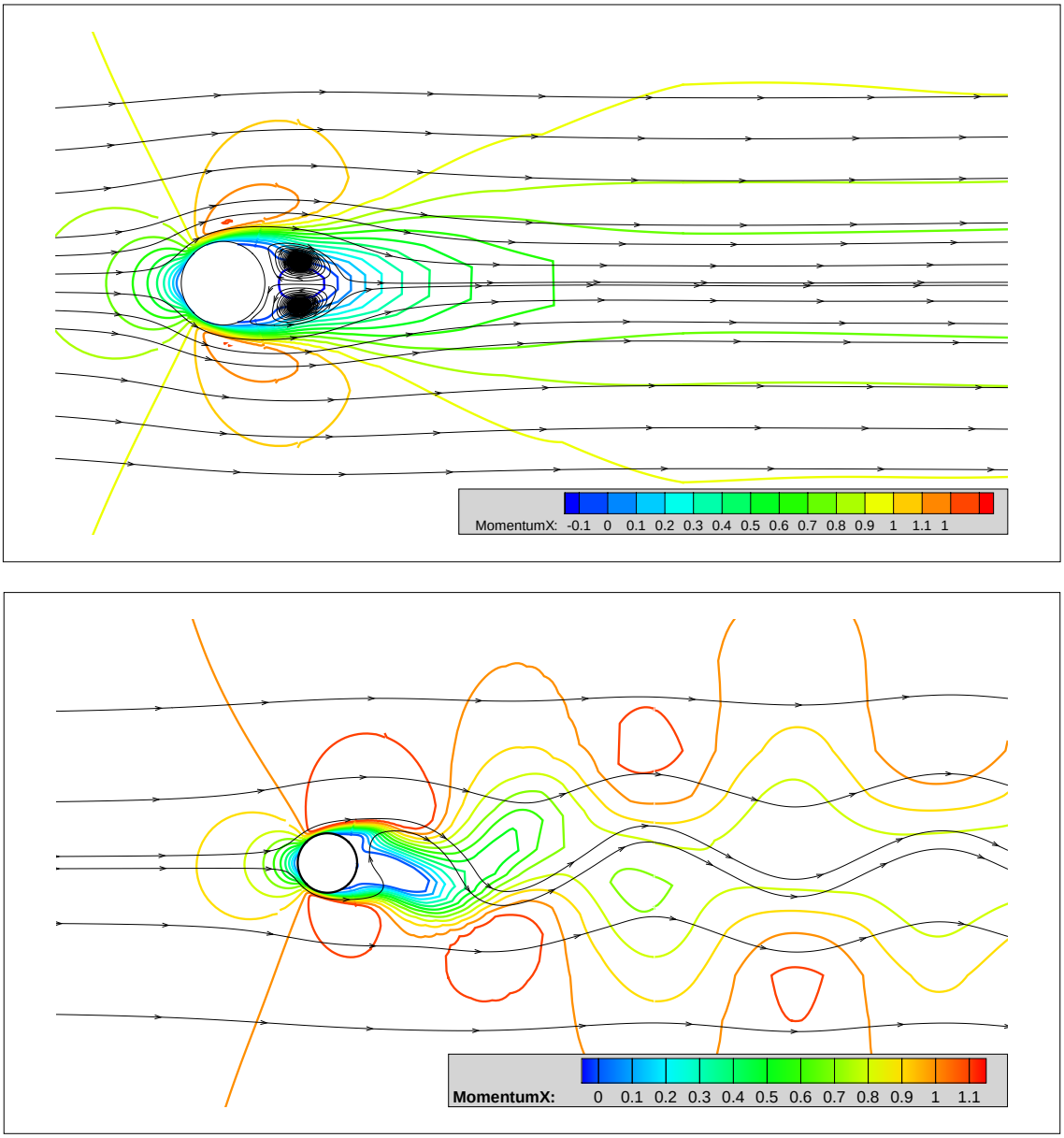

FIGURE B.9: Time averaged (top) and instantaneous (bottom) plots of Reynolds number 200 2D flow, 2nd order Min Mod scheme

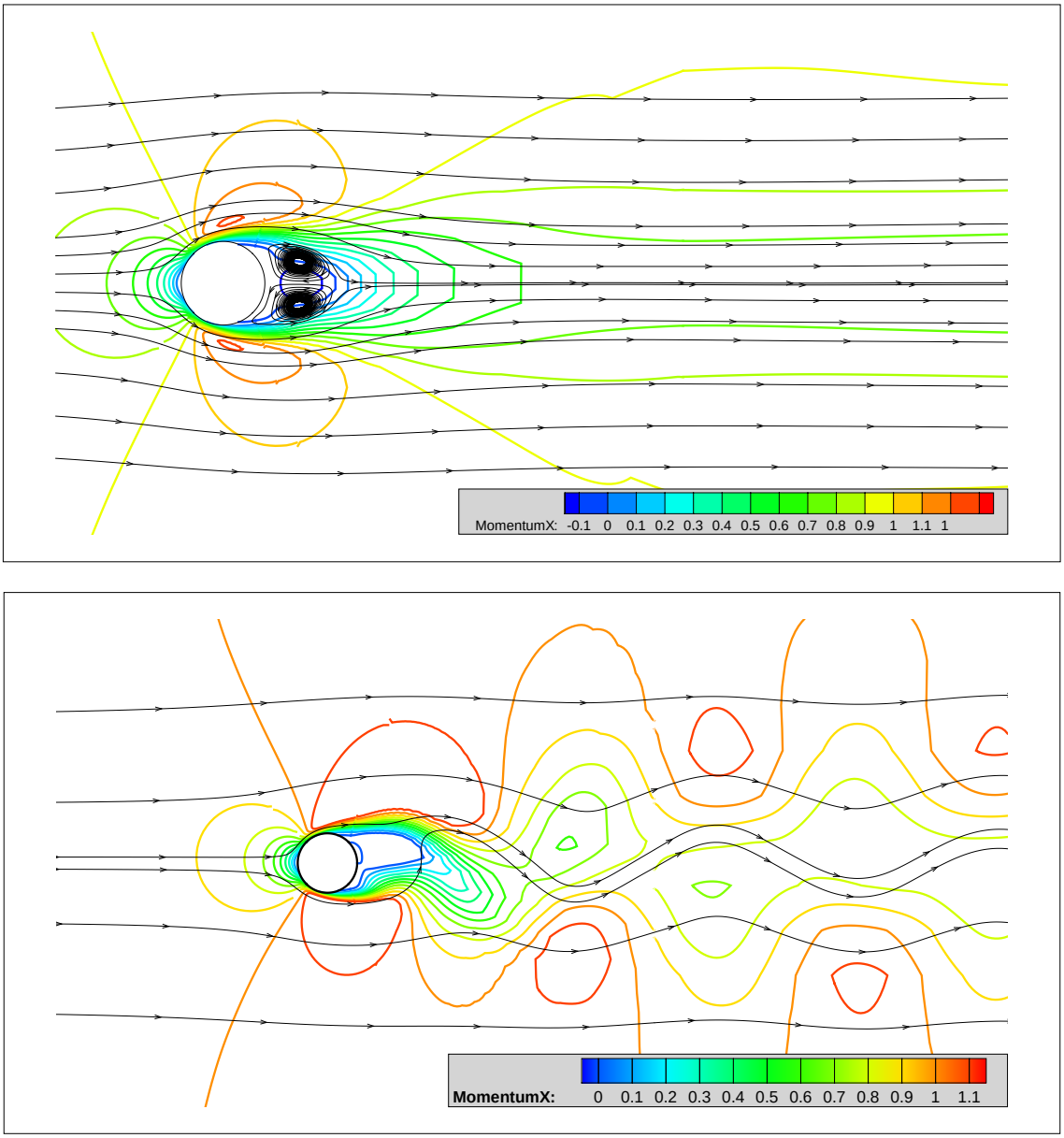

FIGURE B.10: Time averaged (top) and instantaneous (bottom) plots of Reynolds number 200 $2D$ flow, 2^{nd} order Van Leer scheme

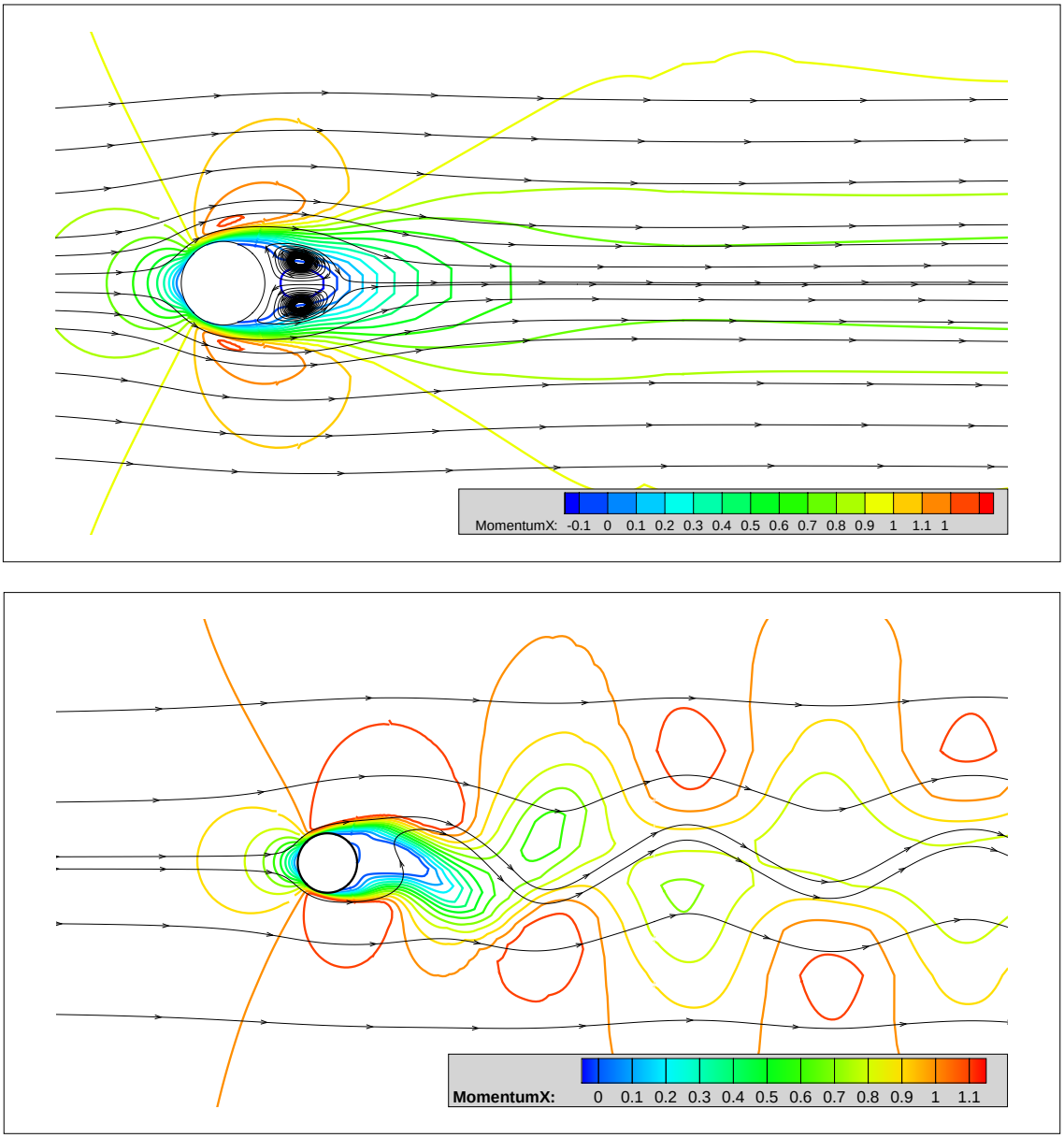

FIGURE B.11: Time averaged (top) and instantaneous (bottom) plots of Reynolds number 200 2D flow, 3^{rd} order Kim Kim scheme

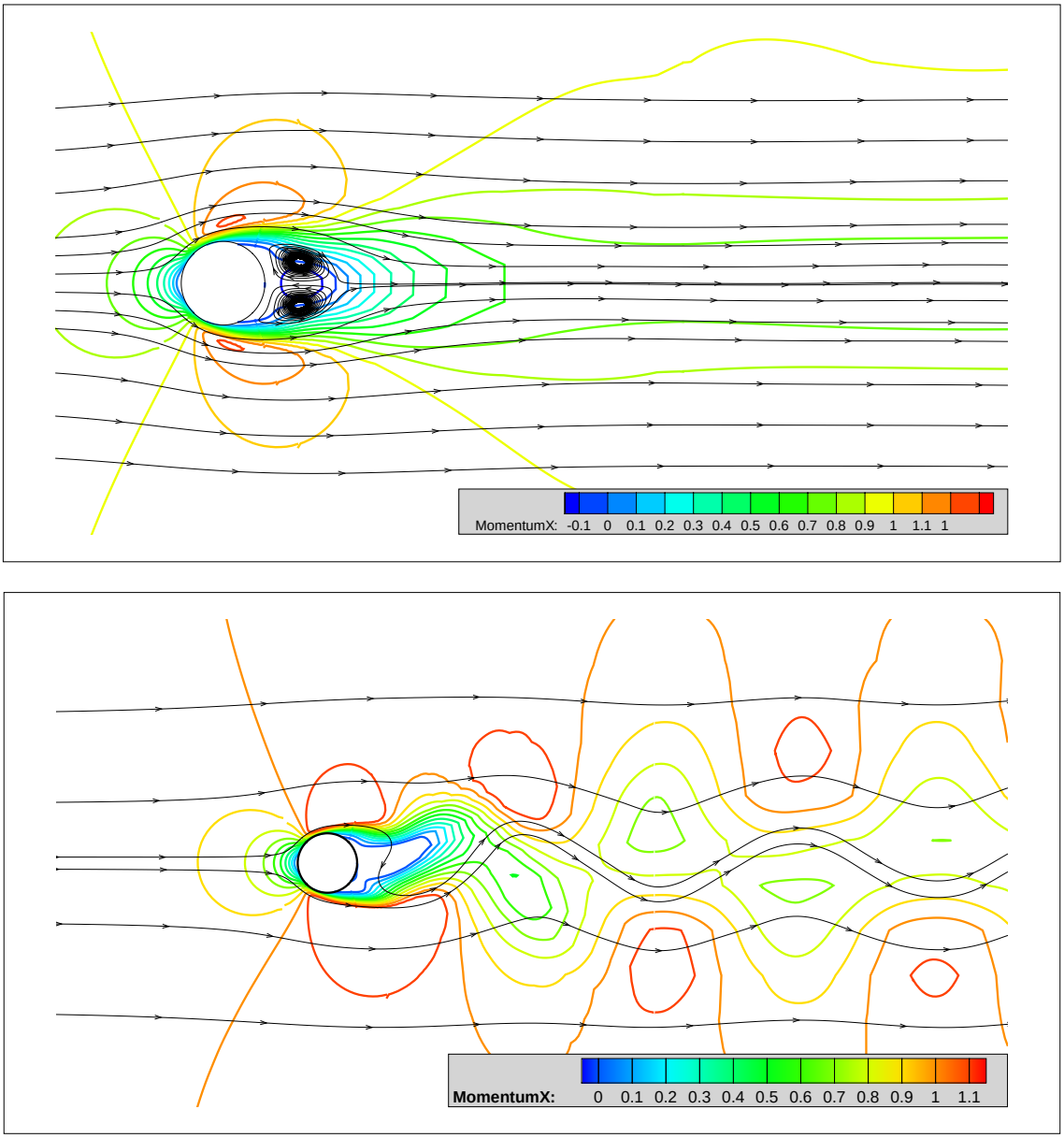

FIGURE B.12: Time averaged (top) and instantaneous (bottom) plots of Reynolds number 200 $2D$ flow, 5^{th} order Kim Kim scheme

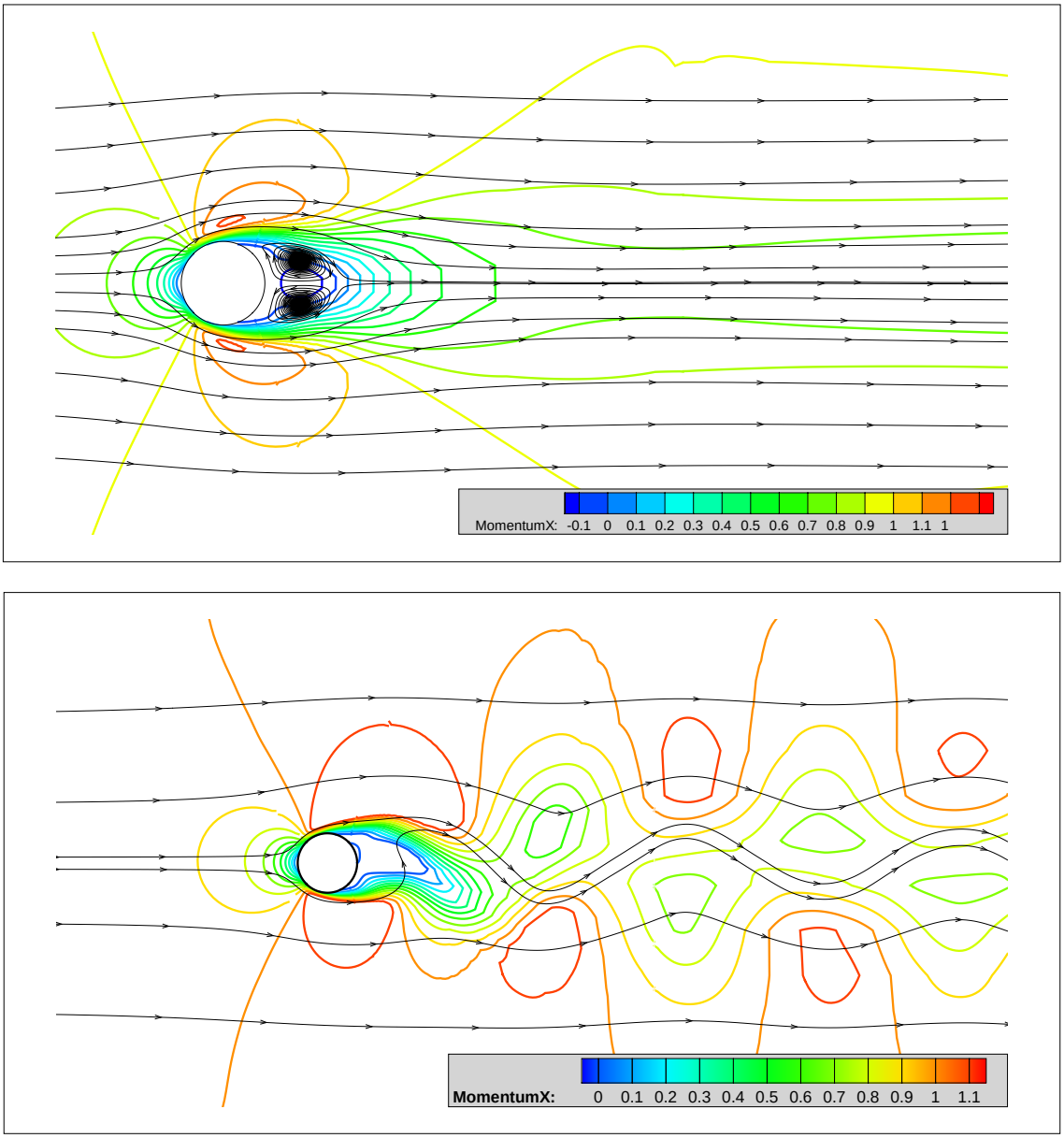

FIGURE B.13: Time averaged (top) and instantaneous (bottom) plots of Reynolds number 200 $2D$ flow, 5^{th} order WENO scheme

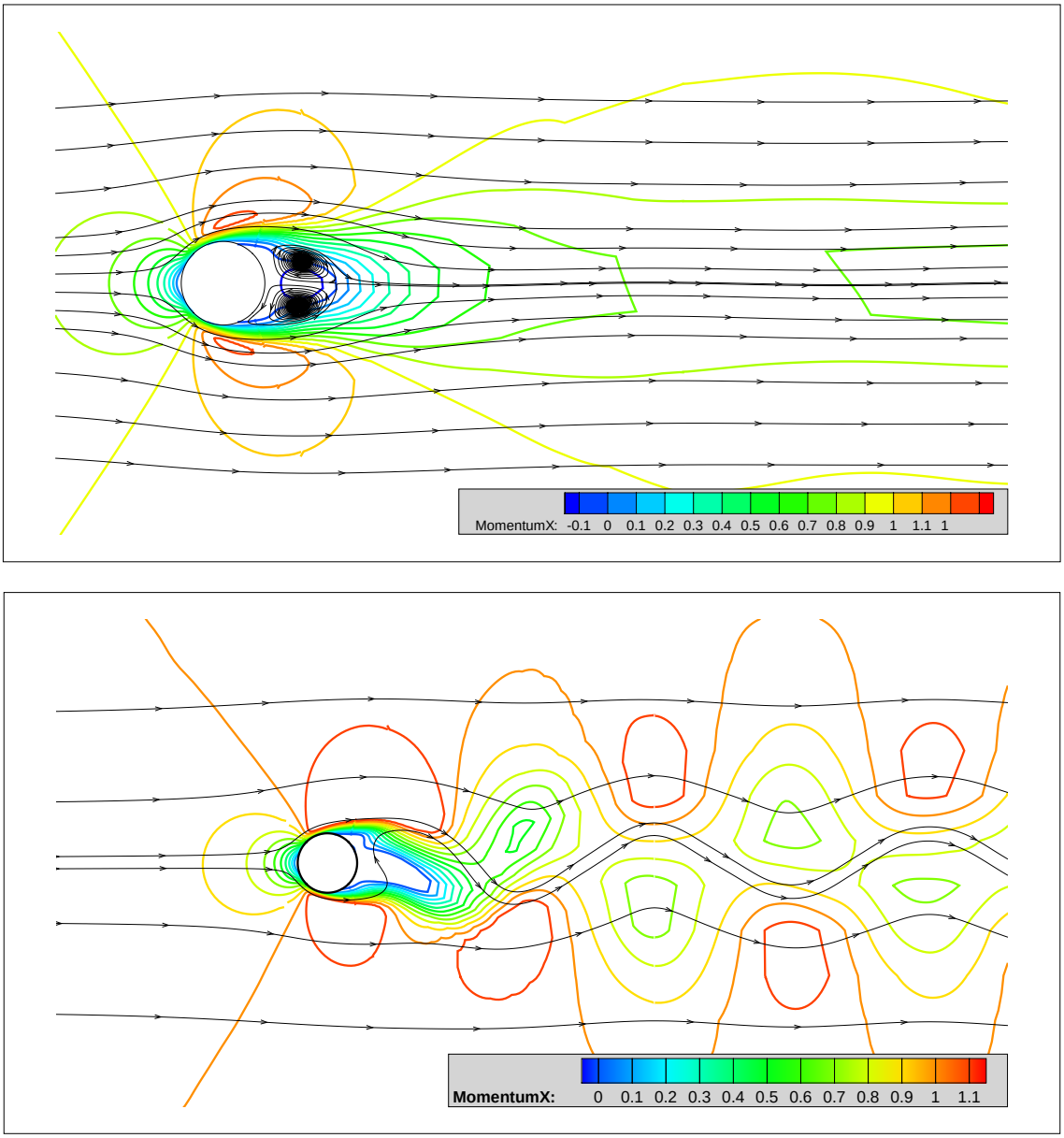

FIGURE B.14: Time averaged (top) and instantaneous (bottom) plots of Reynolds number 200 $2D$ flow, 9^{th} order WENO scheme

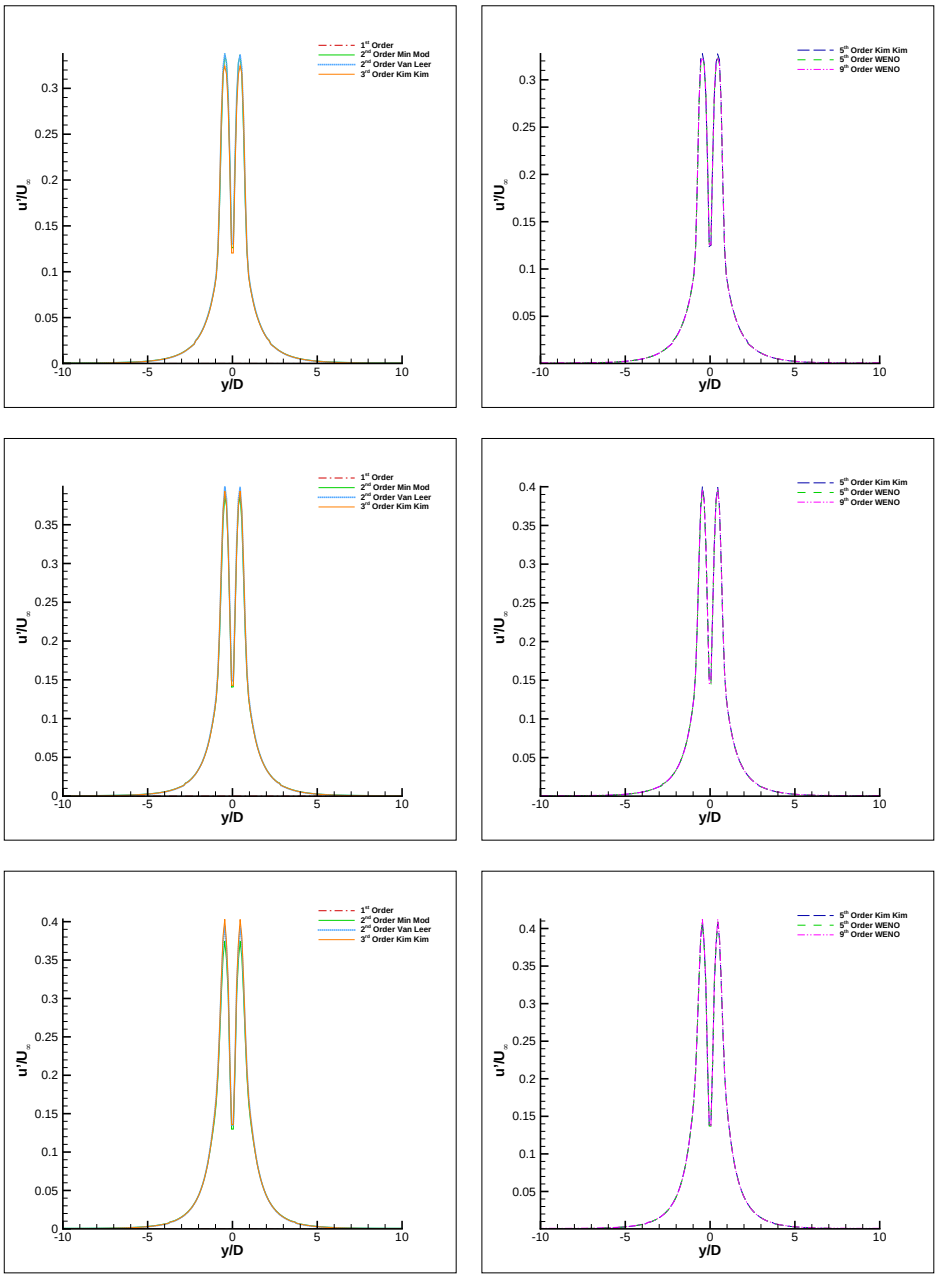

FIGURE B.15: Reynolds Number 200, 2D flow. Fluctuations in the streamwise flow near wake, at $x/D = 1.00$ (top), $x/D = 1.20$ (middle) and $x/D = 1.50$ (bottom).

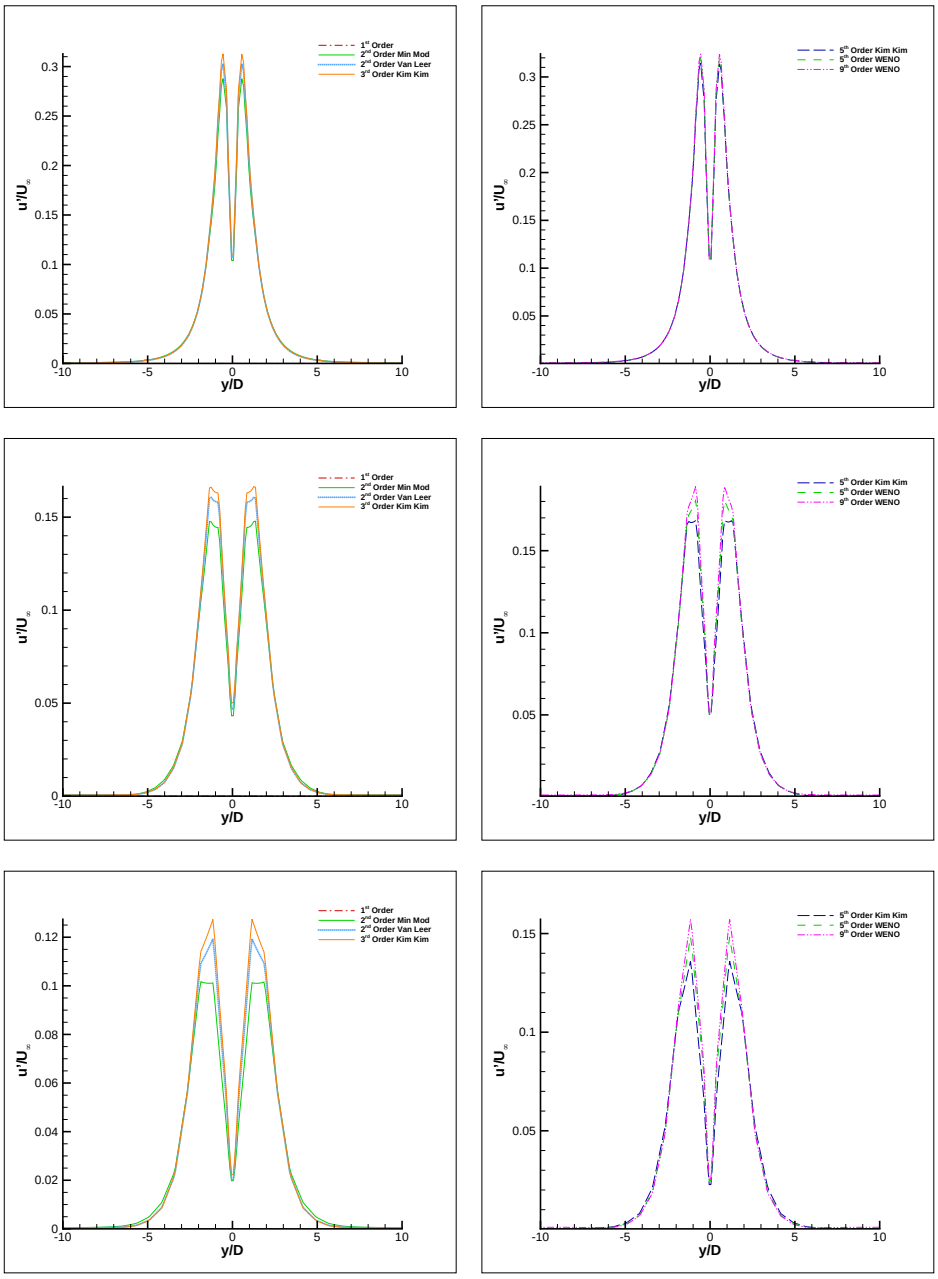

FIGURE B.16: Reynolds Number 200, $2D$ flow. Fluctuations in the streamwise flow medium wake, at $x/D = 2.00$ (top), $x/D = 4.00$ (middle) and $x/D = 6.00$ (bottom).

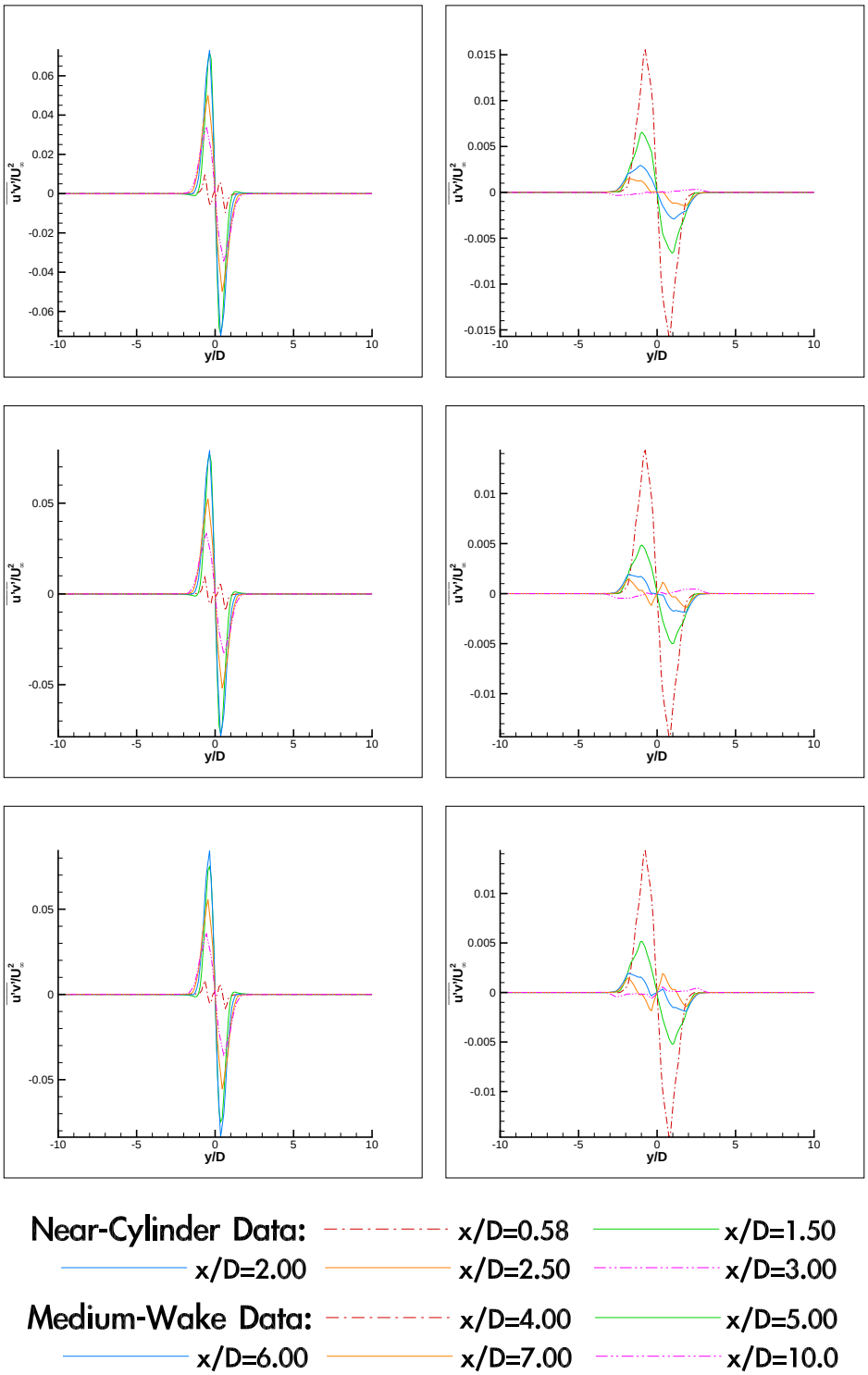

FIGURE B.17: Reynolds Number 200, 2D flow. Reynolds stresses in the $u'v'$ direction in the cylinder wake. 2^{nd} order Min Mod (top), 2^{nd} order Van Leer (middle) and 3^{rd} order Kim Kim (bottom). Left images are near-cylinder points, right images are medium-wake points, with lines labelled appropriately.

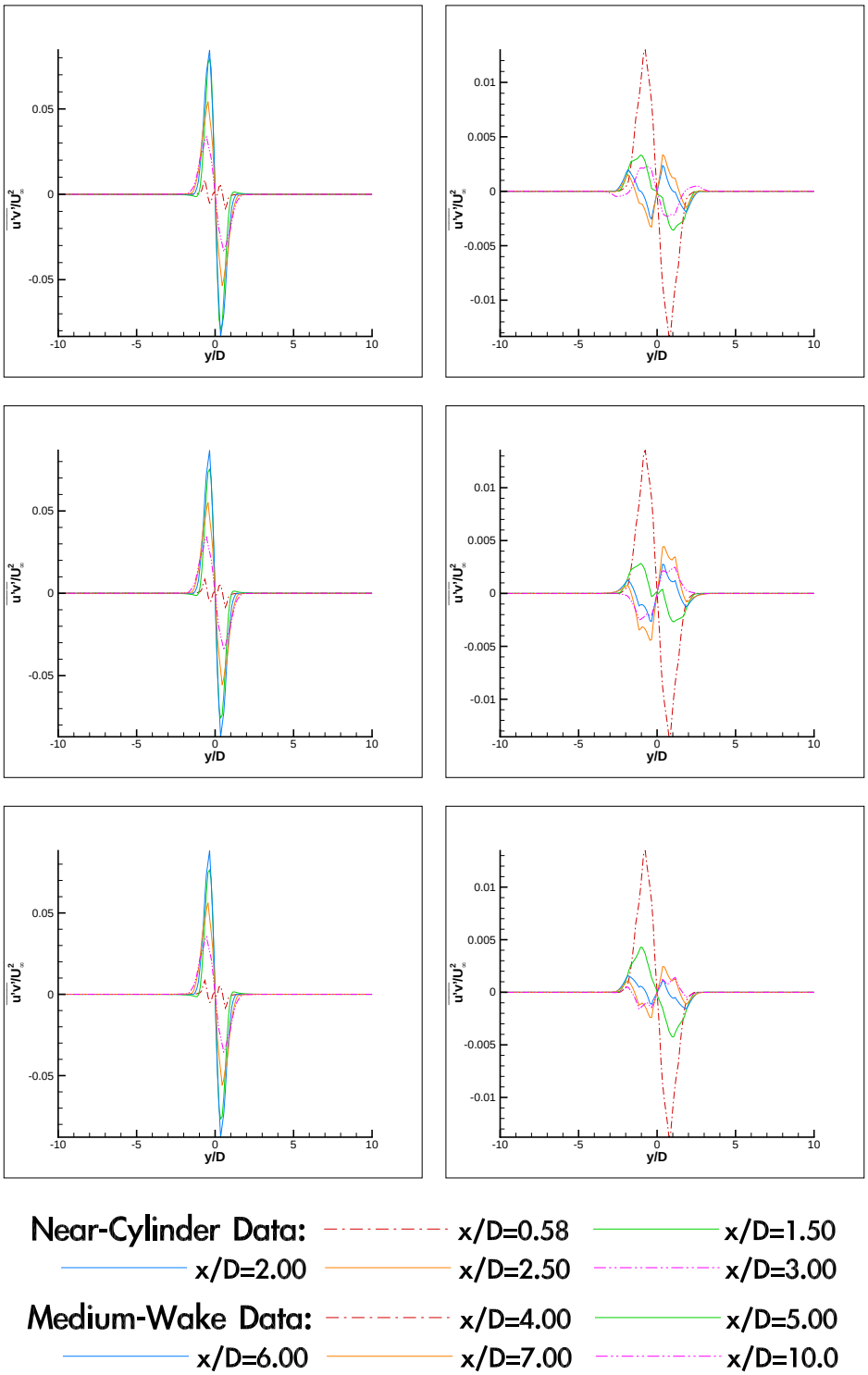

FIGURE B.18: Reynolds Number 200, 2D flow. Reynolds stresses in the $u'v'$ direction in the cylinder wake. 5^{th} order Kim Kim (top), 5^{th} order WENO (middle) and 9^{th} order WENO (bottom). Left images are near-cylinder points, right images are medium-wake points, with lines labelled appropriately.

B.3 Reynolds Number = 300

Figures B.19 to B.25 show time-averaged and instantaneous plots of the flow field showing details of flow around the cylinder. The vortices to the rear of the cylinder are clearly visible and have now grown in strength over $Re = 200$ flow. At this flow speed, there is now greater difference between the different numerical schemes when looking at the flow field. In addition, there is a clear difference between the time-averaged plots and the instantaneous plots.

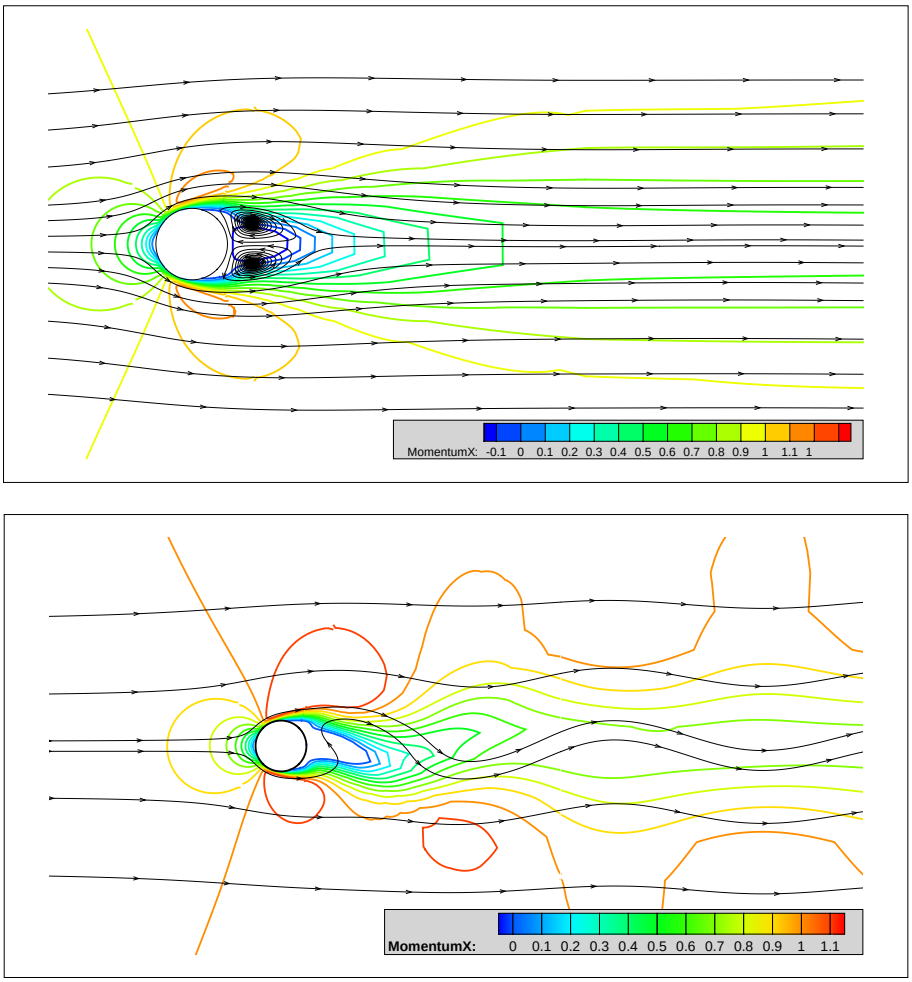

FIGURE B.19: Time averaged (top) and instantaneous (bottom) plots of Reynolds number 300 2D flow, 1^{st} order scheme

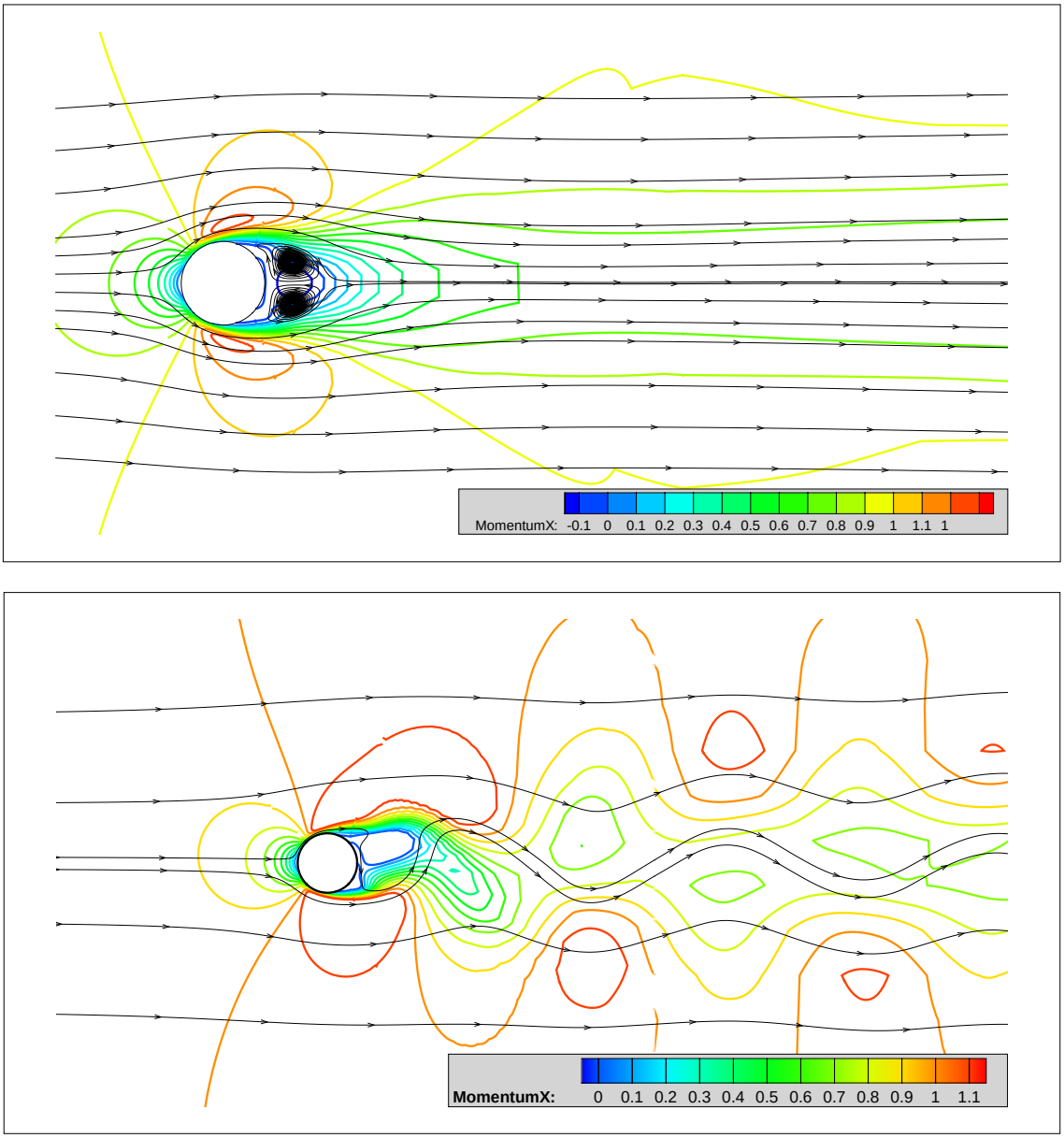

FIGURE B.20: Time averaged (top) and instantaneous (bottom) plots of Reynolds number 300 2D flow, 2nd order Min Mod scheme

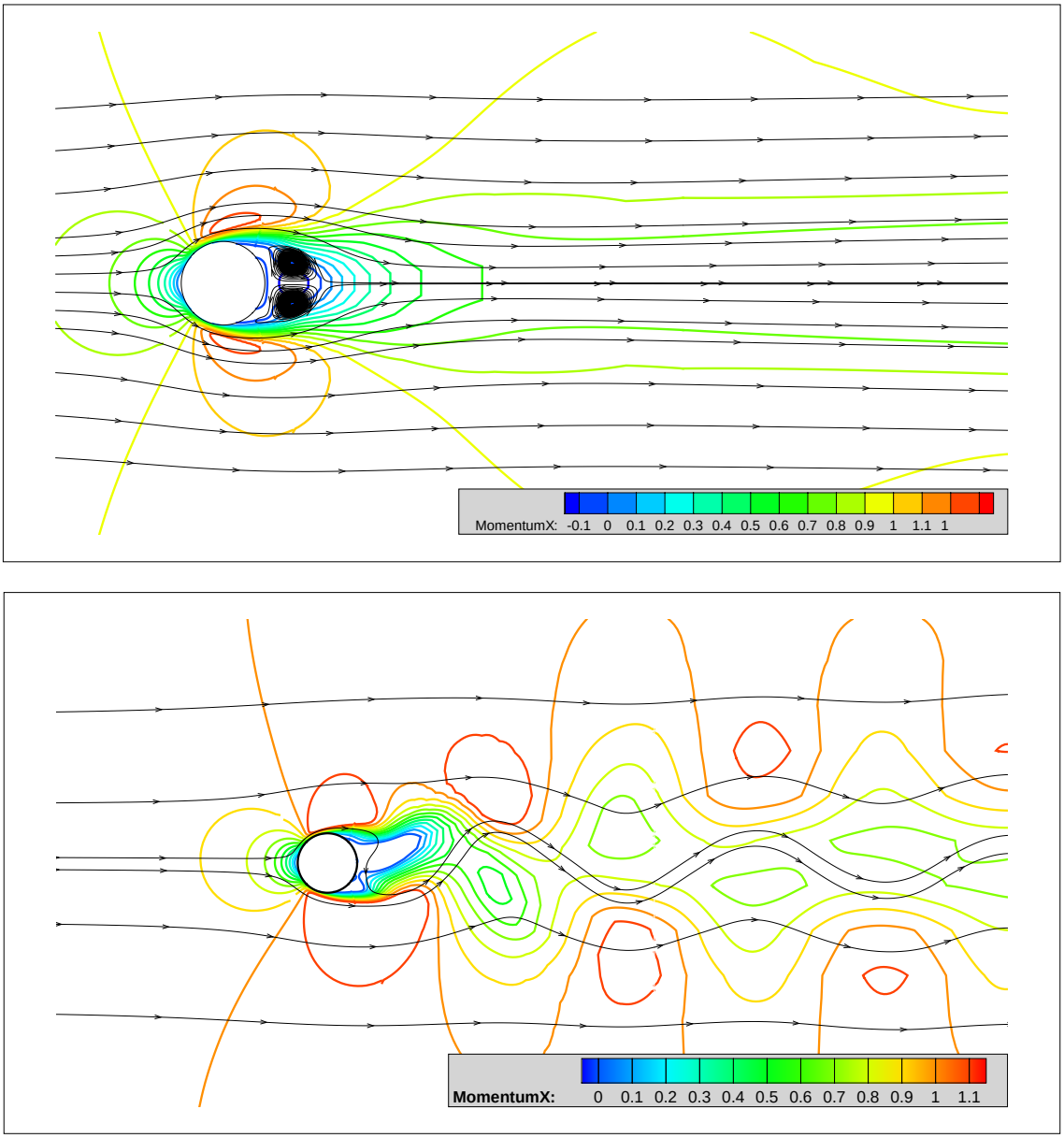

FIGURE B.21: Time averaged (top) and instantaneous (bottom) plots of Reynolds number 300 2D flow, 2nd order Van Leer scheme

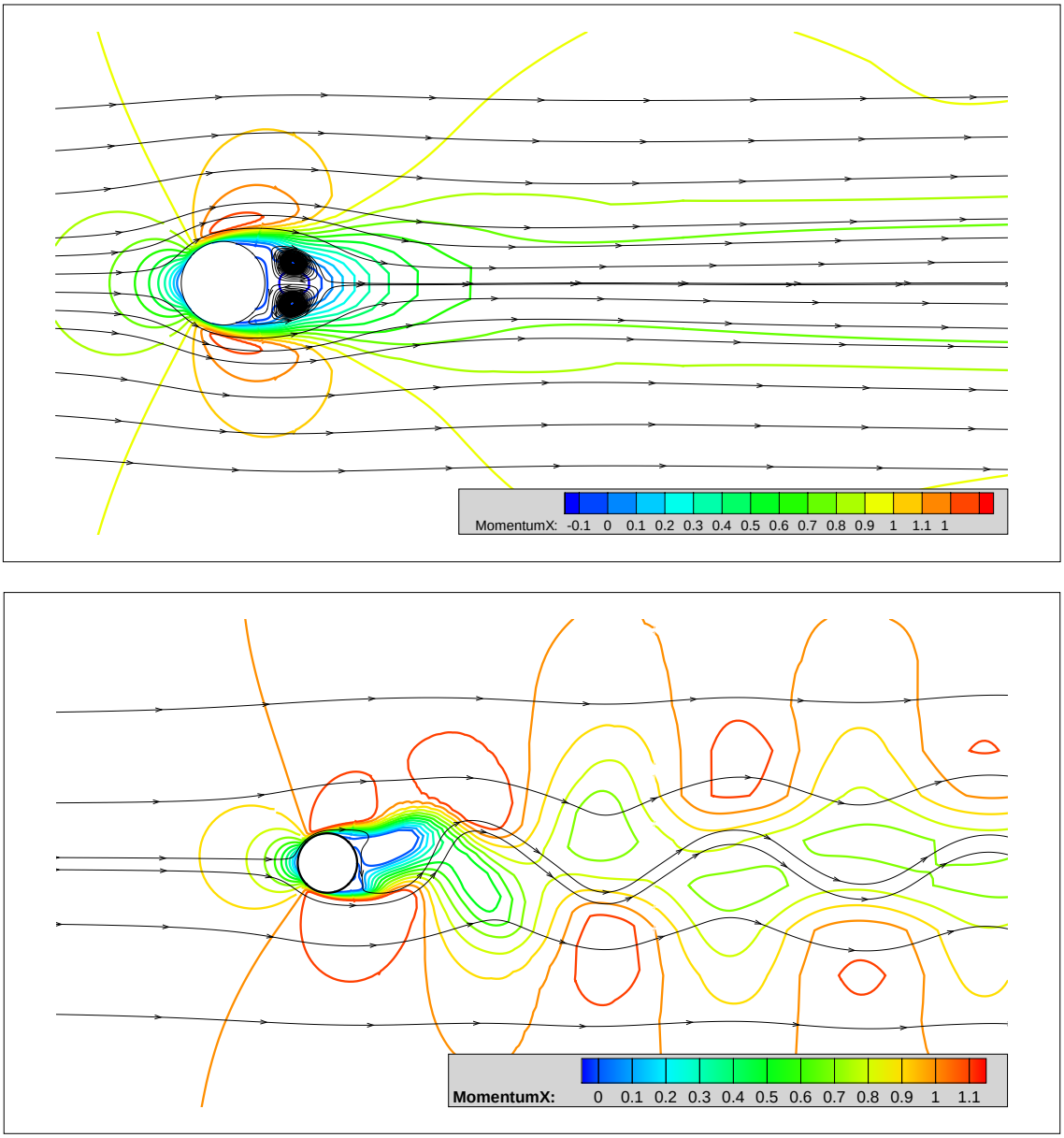

FIGURE B.22: Time averaged (top) and instantaneous (bottom) plots of Reynolds number 300 2D flow, 3^{rd} order Kim Kim scheme

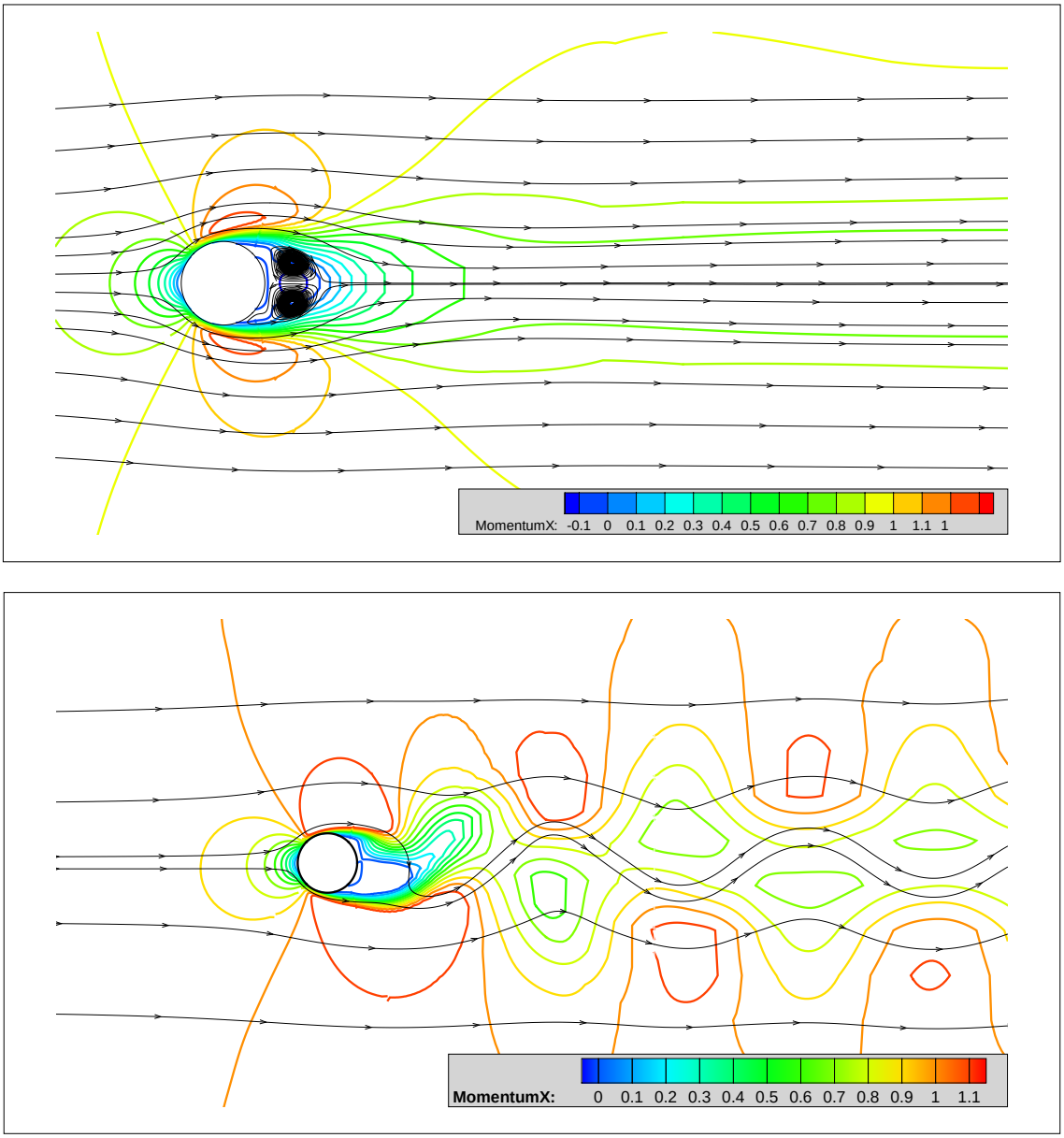

FIGURE B.23: Time averaged (top) and instantaneous (bottom) plots of Reynolds number 300 2D flow, 5^{th} order Kim Kim scheme

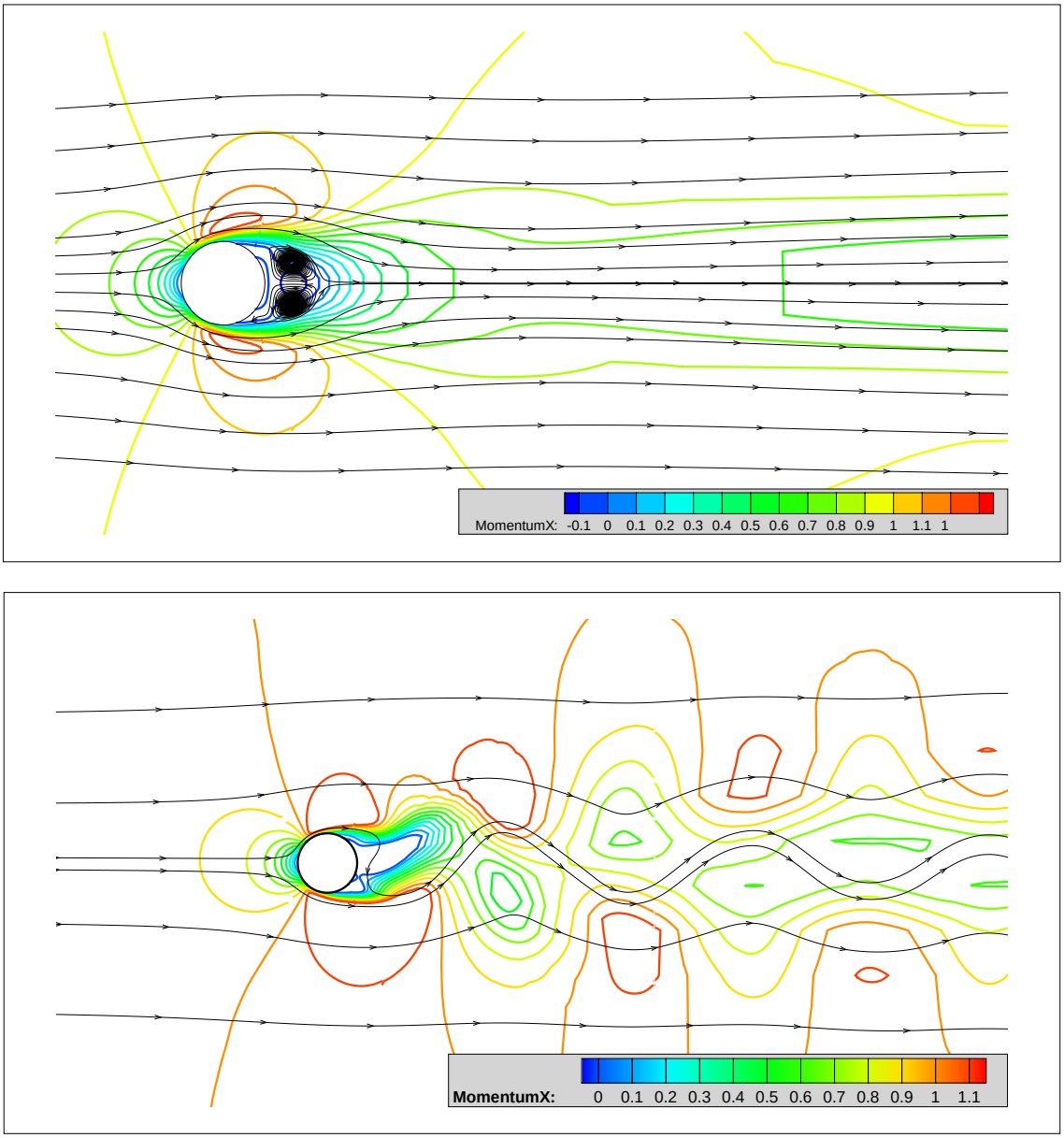

FIGURE B.24: Time averaged (top) and instantaneous (bottom) plots of Reynolds number 300 2D flow, 5^{th} order WENO scheme

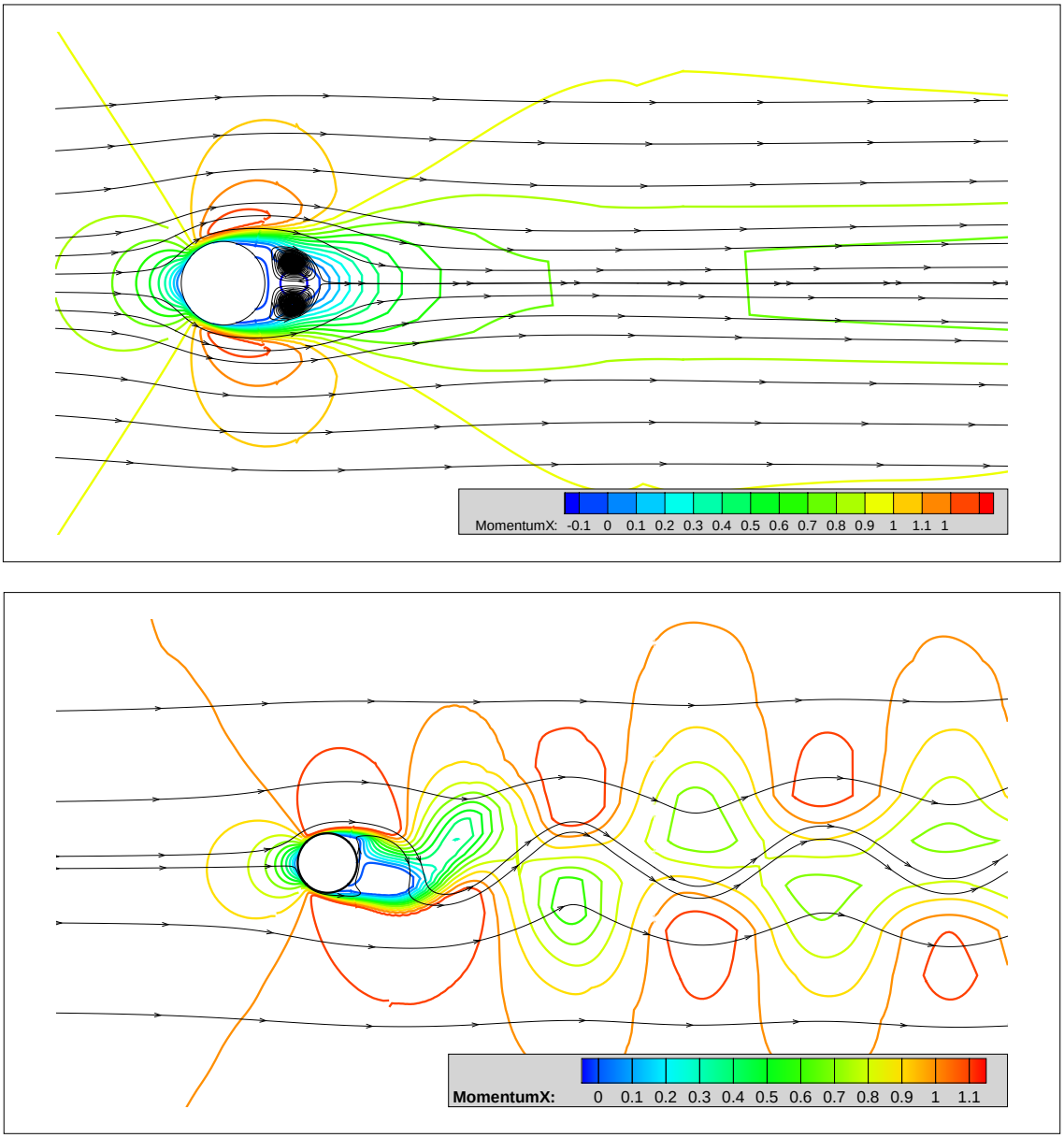

FIGURE B.25: Time averaged (top) and instantaneous (bottom) plots of Reynolds number 300 2D flow, 9^{th} order WENO scheme

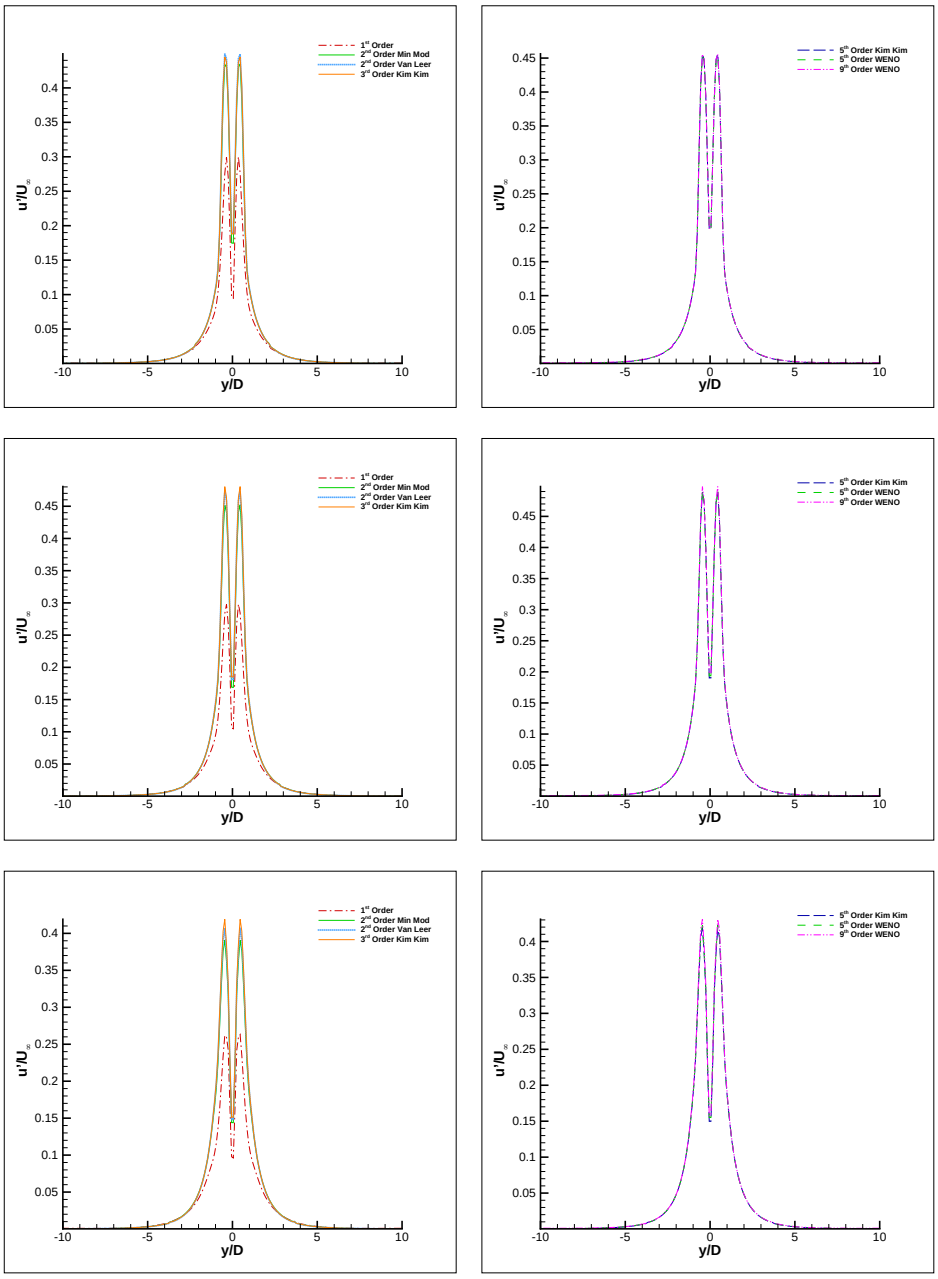

FIGURE B.26: Reynolds Number 300, 2D flow. Fluctuations in the streamwise flow near wake, at $x/D = 1.00$ (top), $x/D = 1.20$ (middle) and $x/D = 1.50$ (bottom).

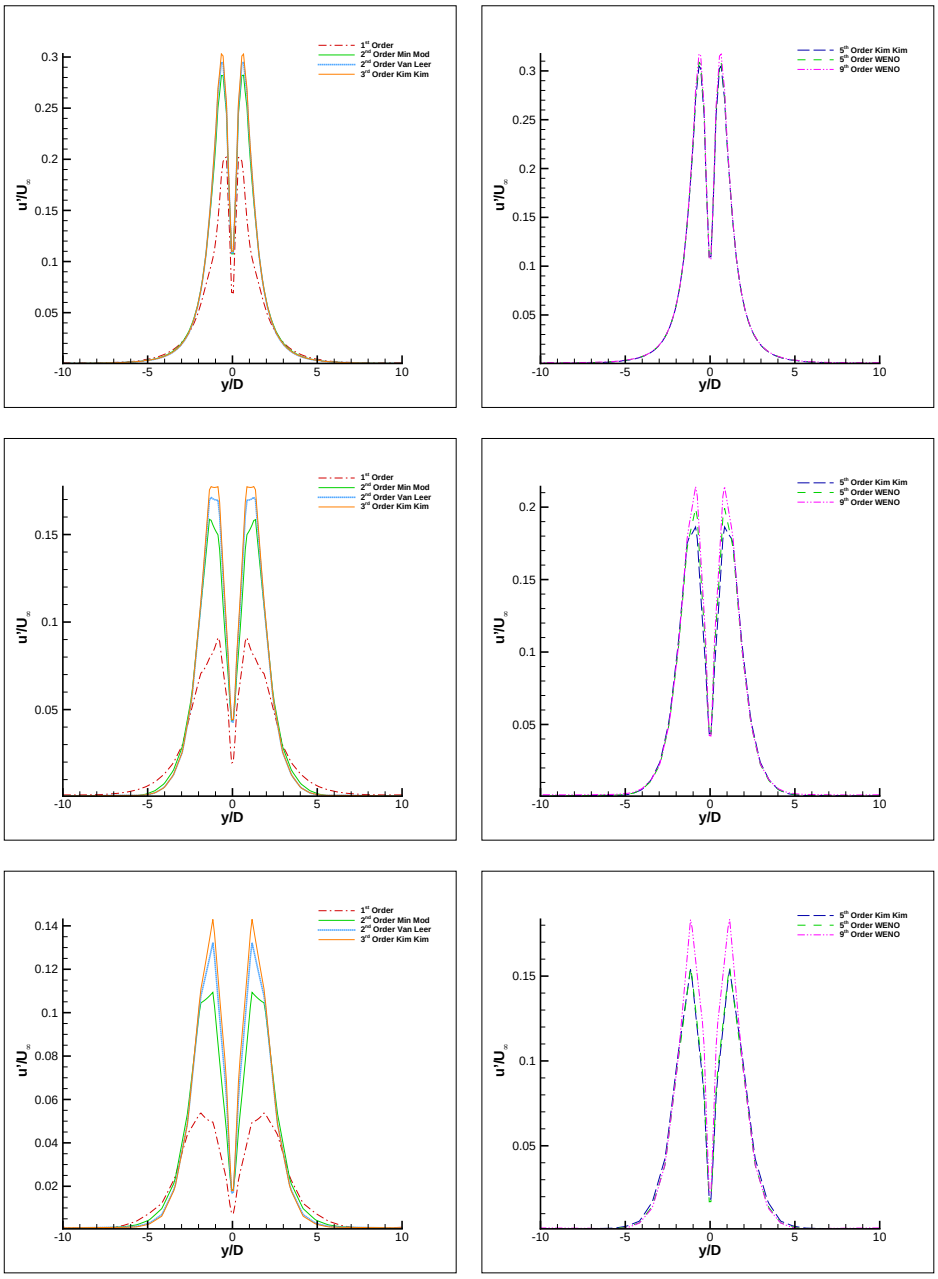

FIGURE B.27: Reynolds Number 300, $2D$ flow. Fluctuations in the streamwise flow medium wake, at $x/D = 2.00$ (top), $x/D = 4.00$ (middle) and $x/D = 6.00$ (bottom).

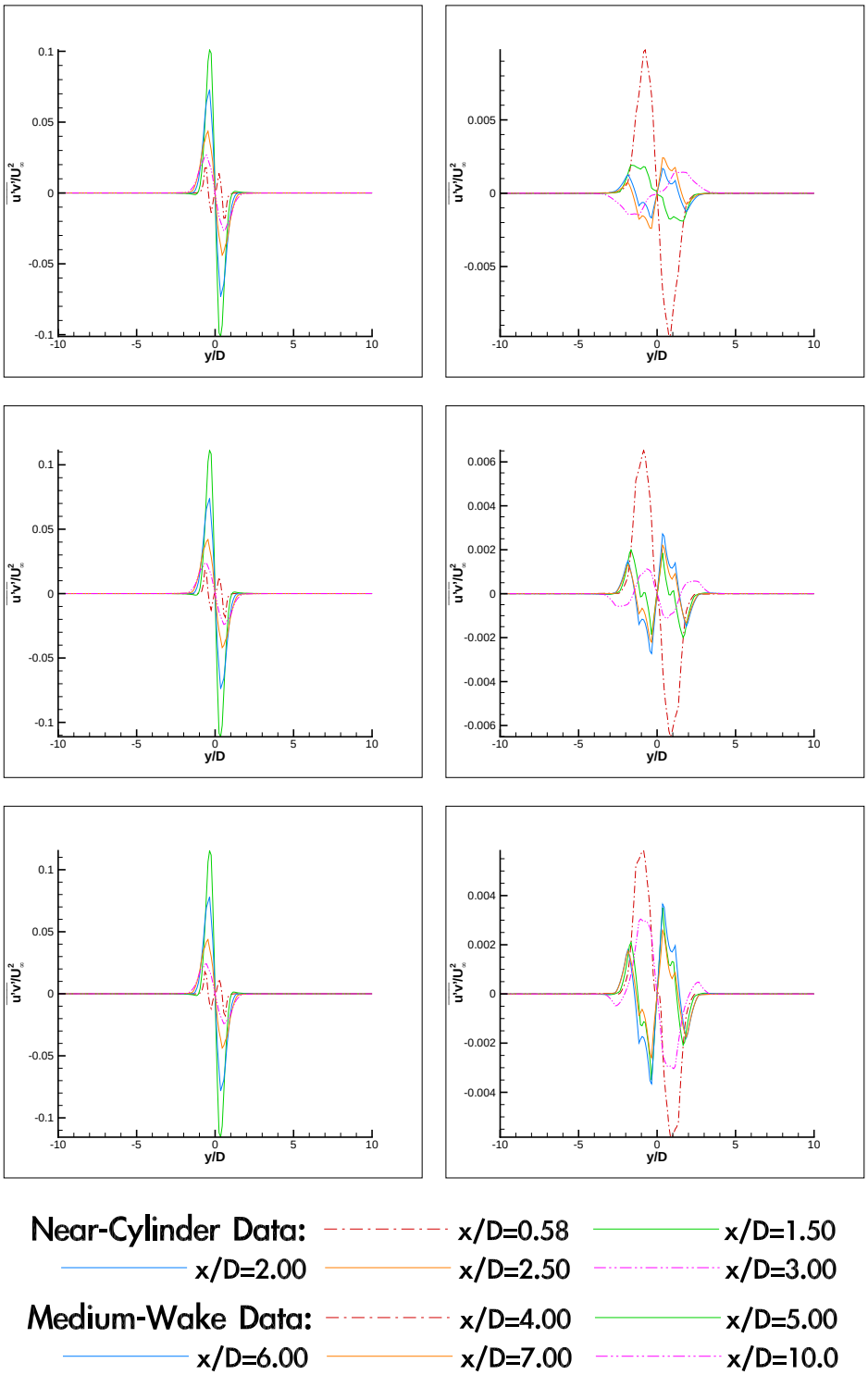

FIGURE B.28: Reynolds Number 300, 2D flow. Reynolds stresses in the $u'v'$ direction in the cylinder wake. 2^{nd} order Min Mod (top), 2^{nd} order Van Leer (middle) and 3^{rd} order Kim Kim (bottom). Left images are near-cylinder points, right images are medium-wake points, with lines labelled appropriately.

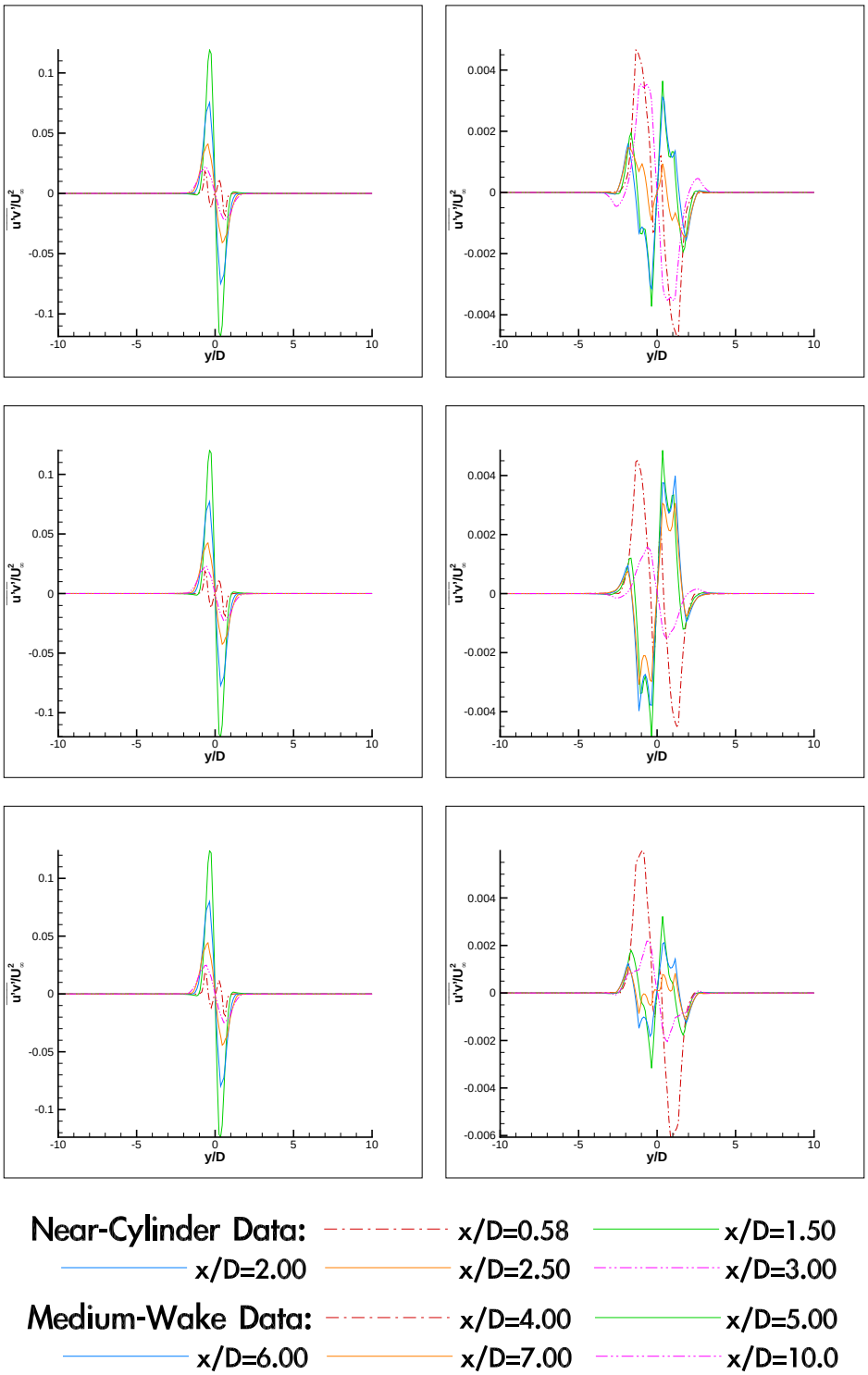

FIGURE B.29: Reynolds Number 300, 2D flow. Reynolds stresses in the $u'v'$ direction in the cylinder wake. 5^{th} order Kim Kim (top), 5^{th} order WENO (middle) and 9^{th} order WENO (bottom). Left images are near-cylinder points, right images are medium-wake points, with lines labelled appropriately.

B.4 Reynolds Number = 3900

At this flow speed, we now expect fully turbulent flow, and this is shown by the instantaneous flow field plots given in figures B.30 to B.36. The time-averaged flow field plots are also included, showing the effects of time-averaging that essentially cancel out the oscillations in the flow. The separated flow is now also clearly visible in the time-averaged flow plots.

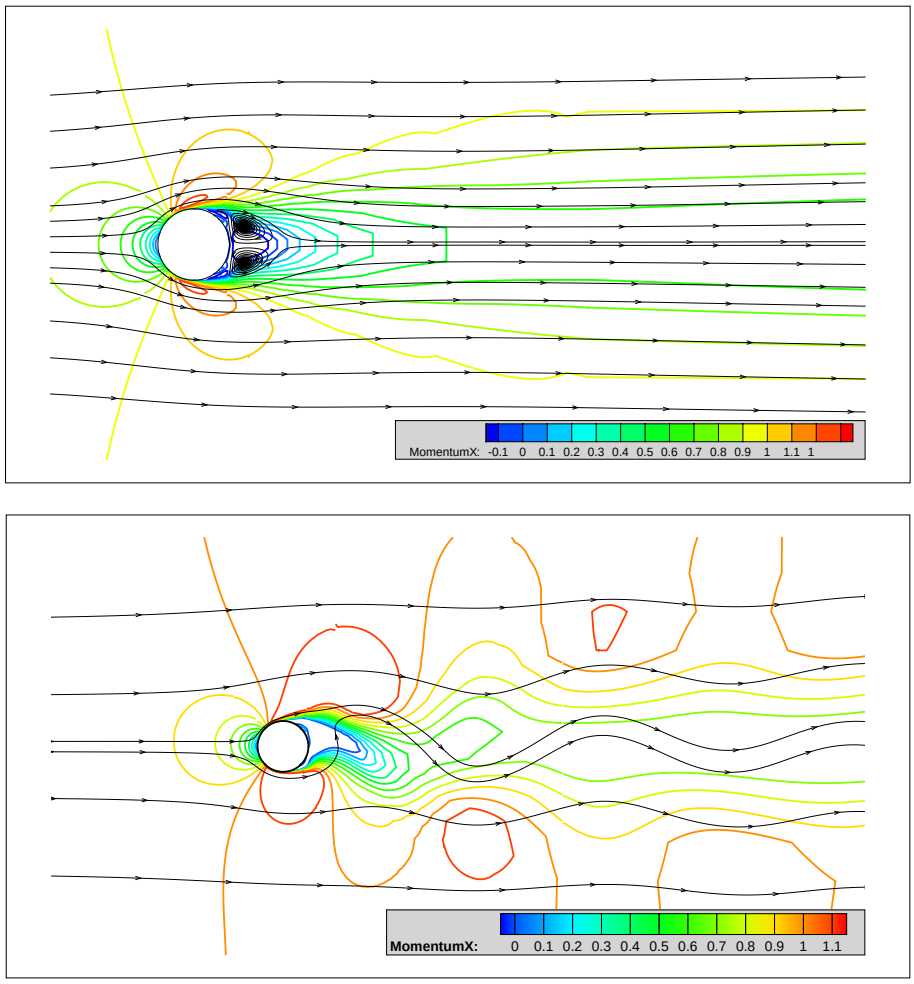

FIGURE B.30: Time averaged (top) and instantaneous (bottom) plots of Reynolds number 3900 $2D$ flow, 1^{st} order scheme

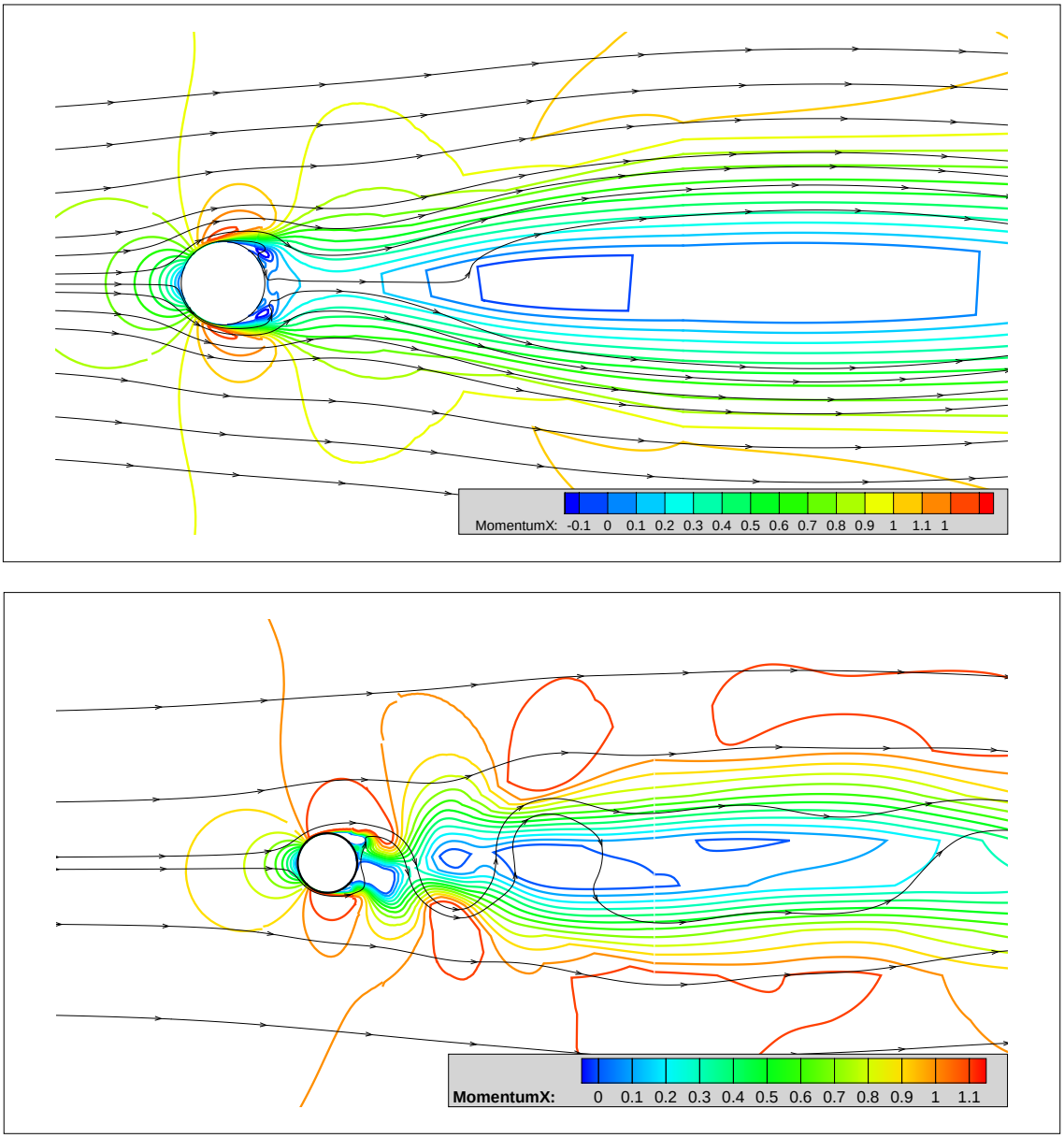

FIGURE B.31: Time averaged (top) and instantaneous (bottom) plots of Reynolds number 3900 2D flow, 2nd order Min Mod scheme

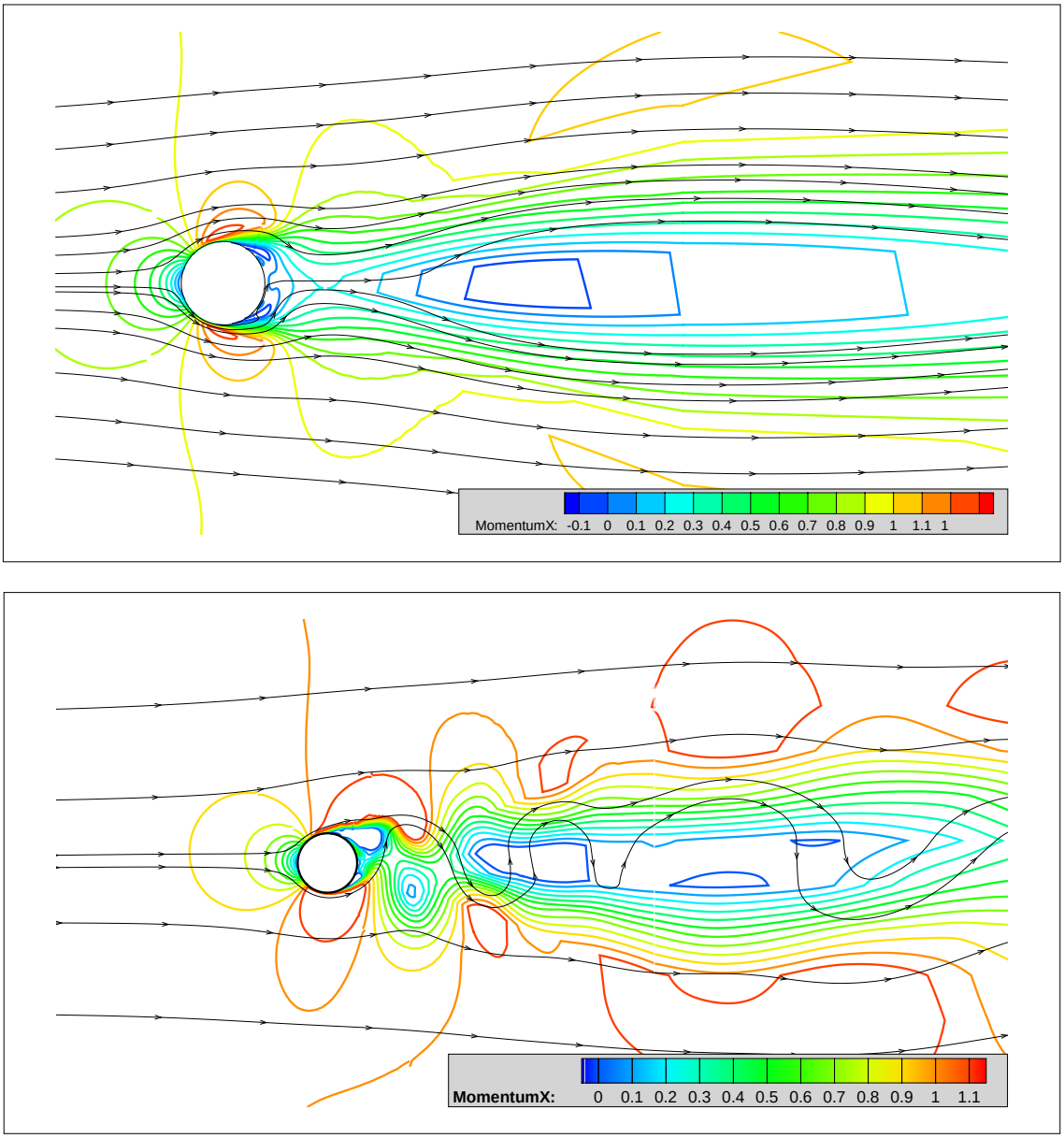

FIGURE B.32: Time averaged (top) and instantaneous (bottom) plots of Reynolds number 3900 $2D$ flow, 2^{nd} order Van Leer scheme

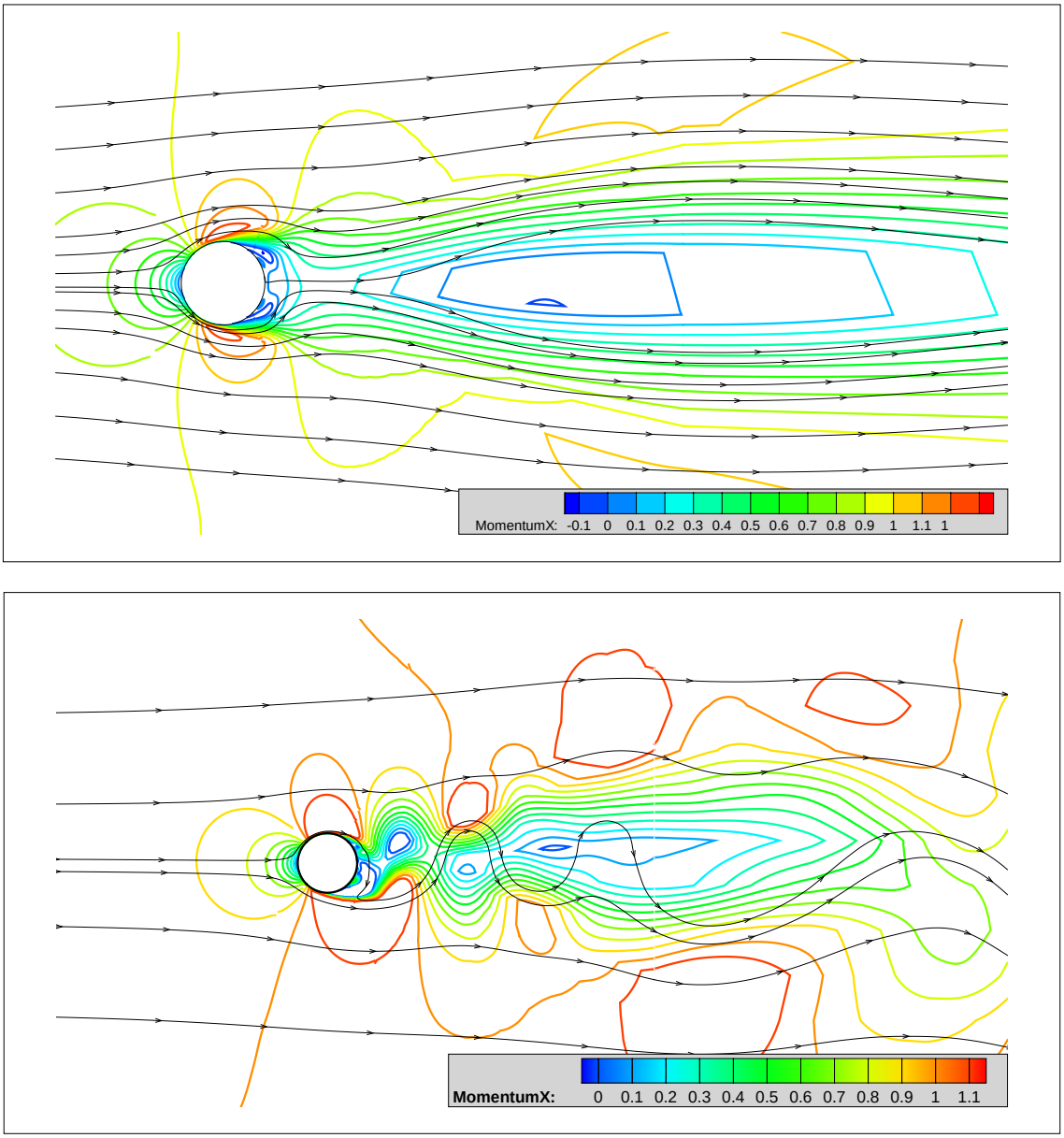

FIGURE B.33: Time averaged (top) and instantaneous (bottom) plots of Reynolds number 3900 2D flow, 3^{rd} order Kim Kim scheme

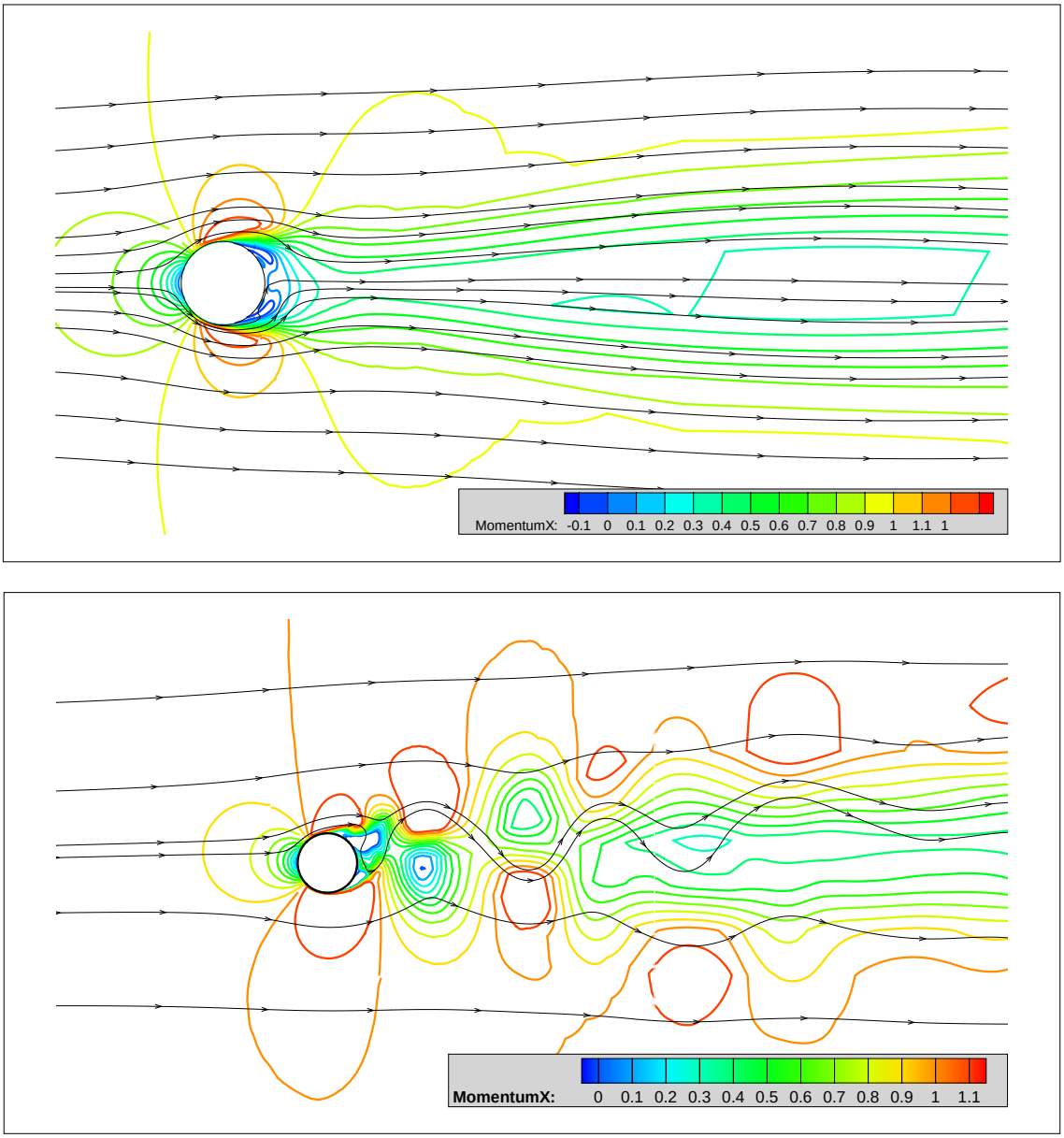

FIGURE B.34: Time averaged (top) and instantaneous (bottom) plots of Reynolds number 3900 2D flow, 5^{th} order Kim Kim scheme

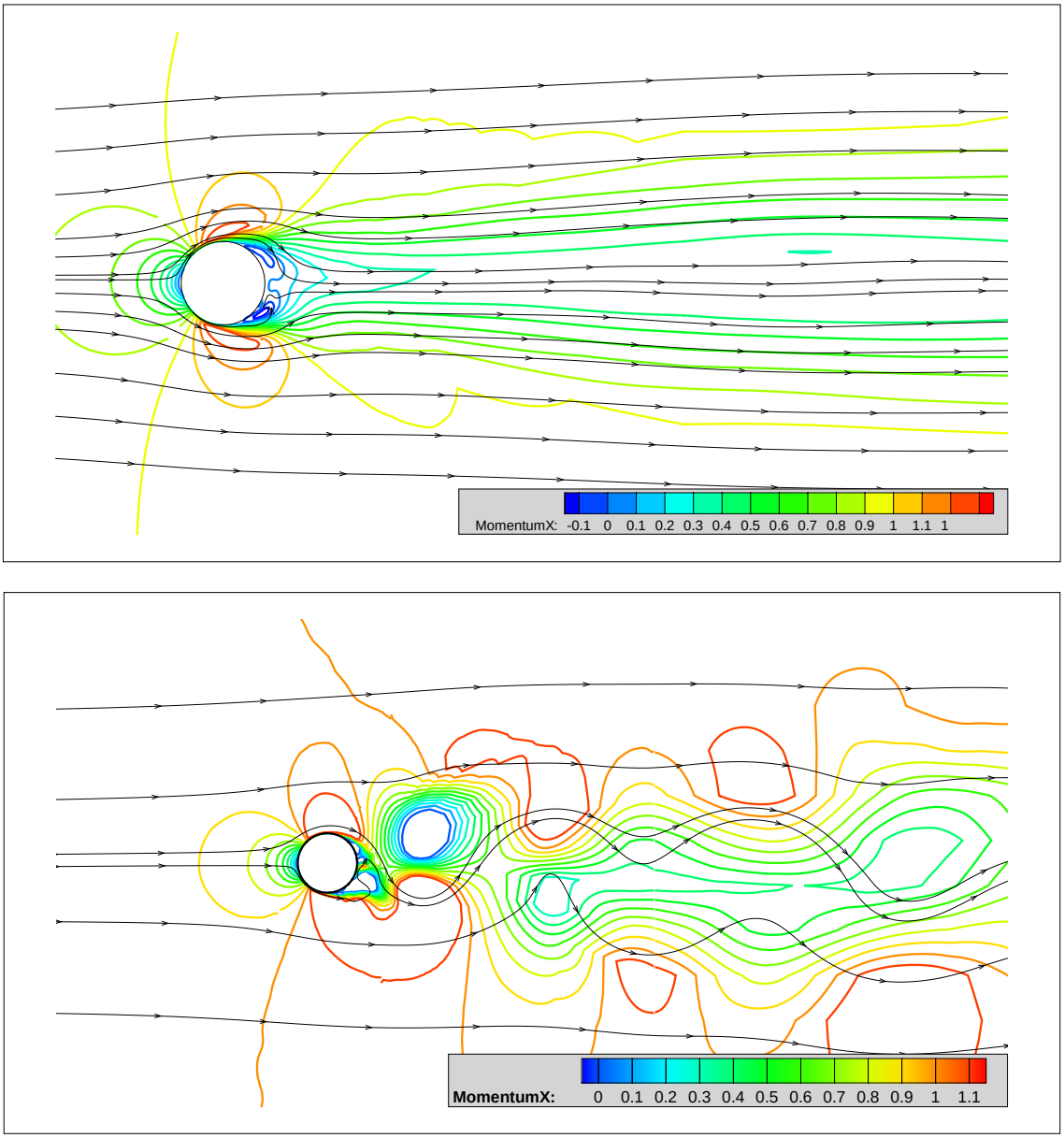

FIGURE B.35: Time averaged (top) and instantaneous (bottom) plots of Reynolds number 3900 2D flow, 5^{th} order WENO scheme

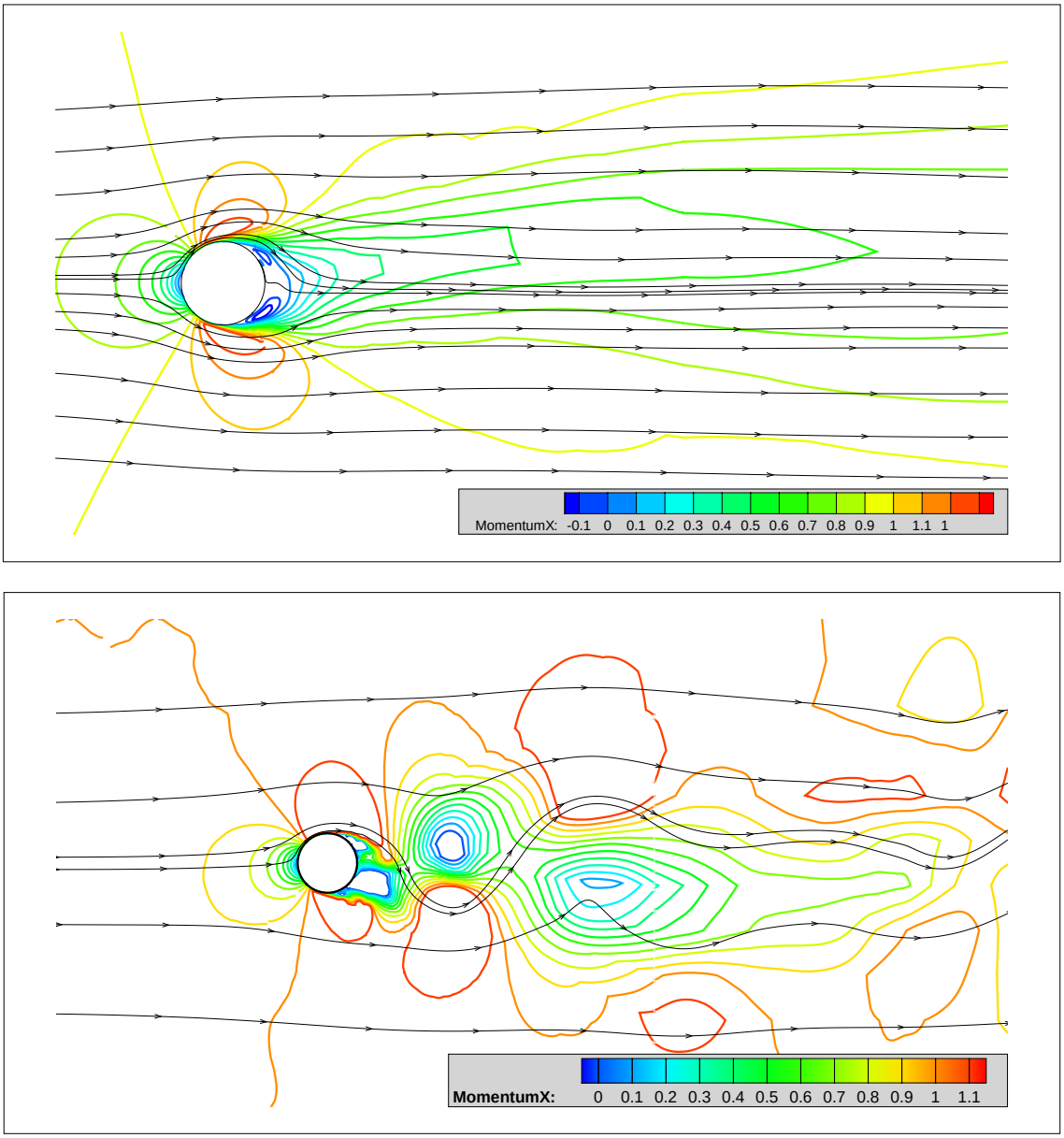

FIGURE B.36: Time averaged (top) and instantaneous (bottom) plots of Reynolds number 3900 2D flow, 9^{th} order WENO scheme

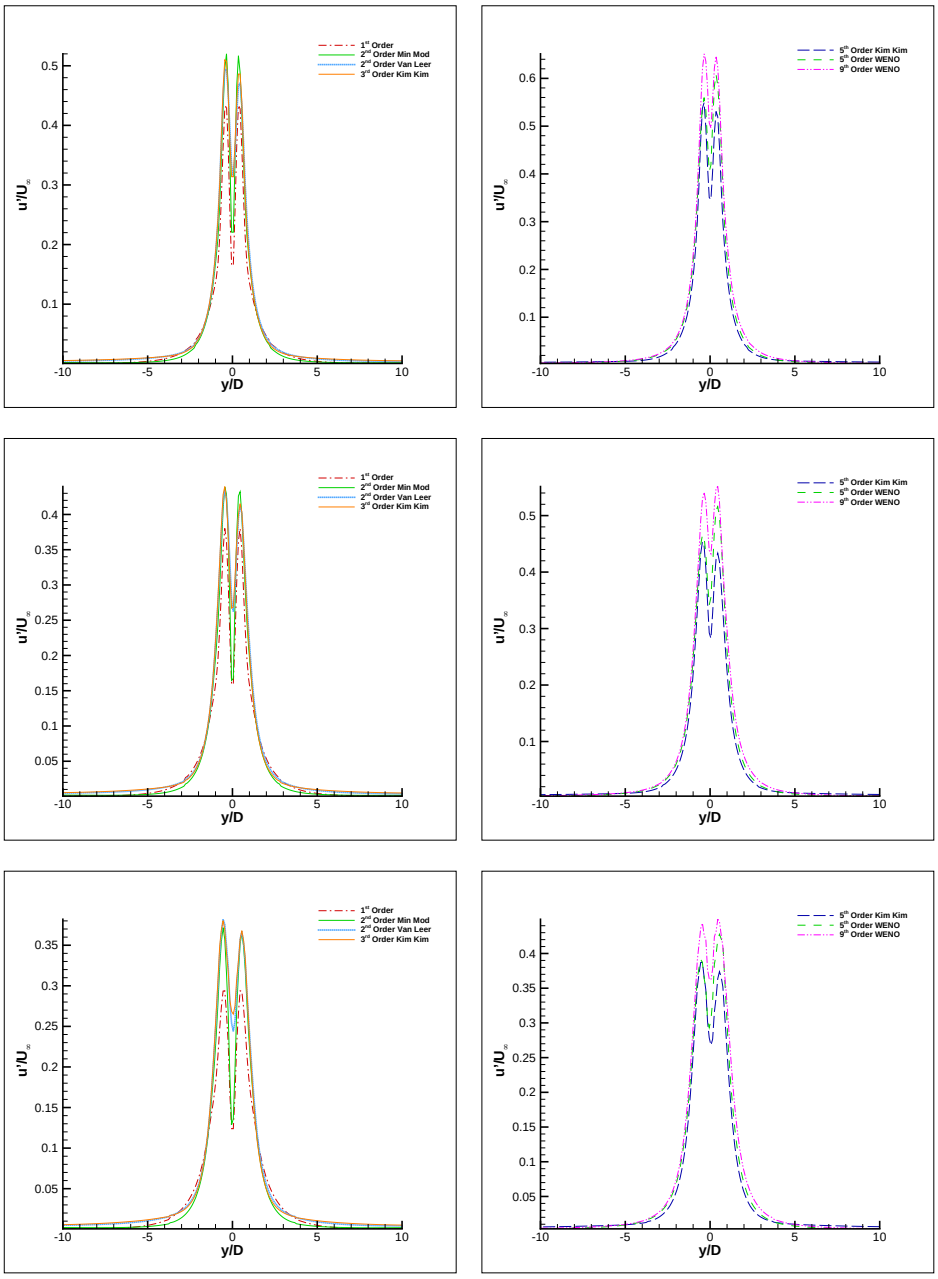

FIGURE B.37: Reynolds Number 3900, 2D flow. Fluctuations in the streamwise flow near wake, at $x/D = 1.00$ (top), $x/D = 1.20$ (middle) and $x/D = 1.50$ (bottom).

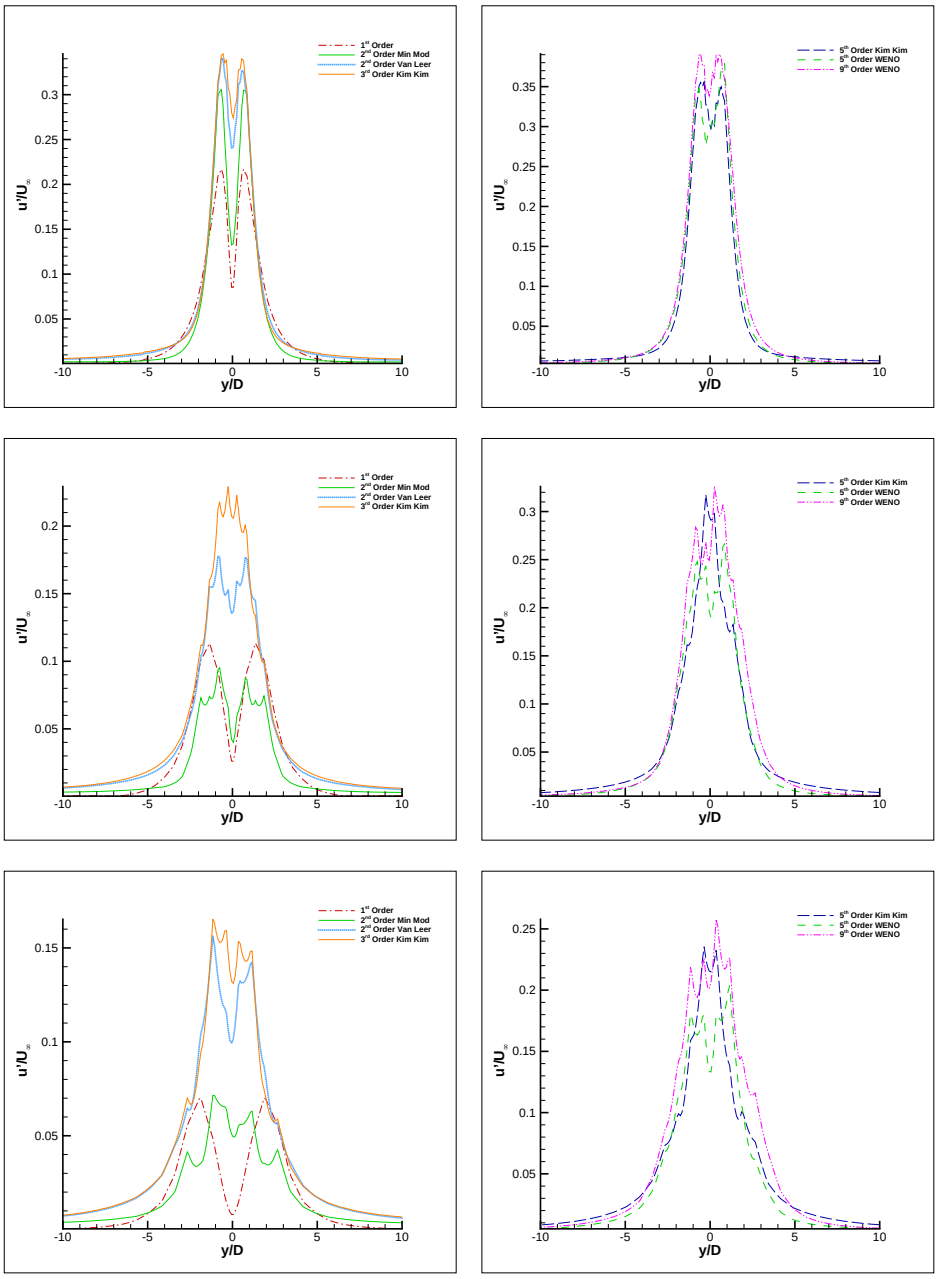

FIGURE B.38: Reynolds Number 3900, 2D flow. Fluctuations in the streamwise flow medium wake, at $x/D = 2.00$ (top), $x/D = 4.00$ (middle) and $x/D = 6.00$ (bottom).

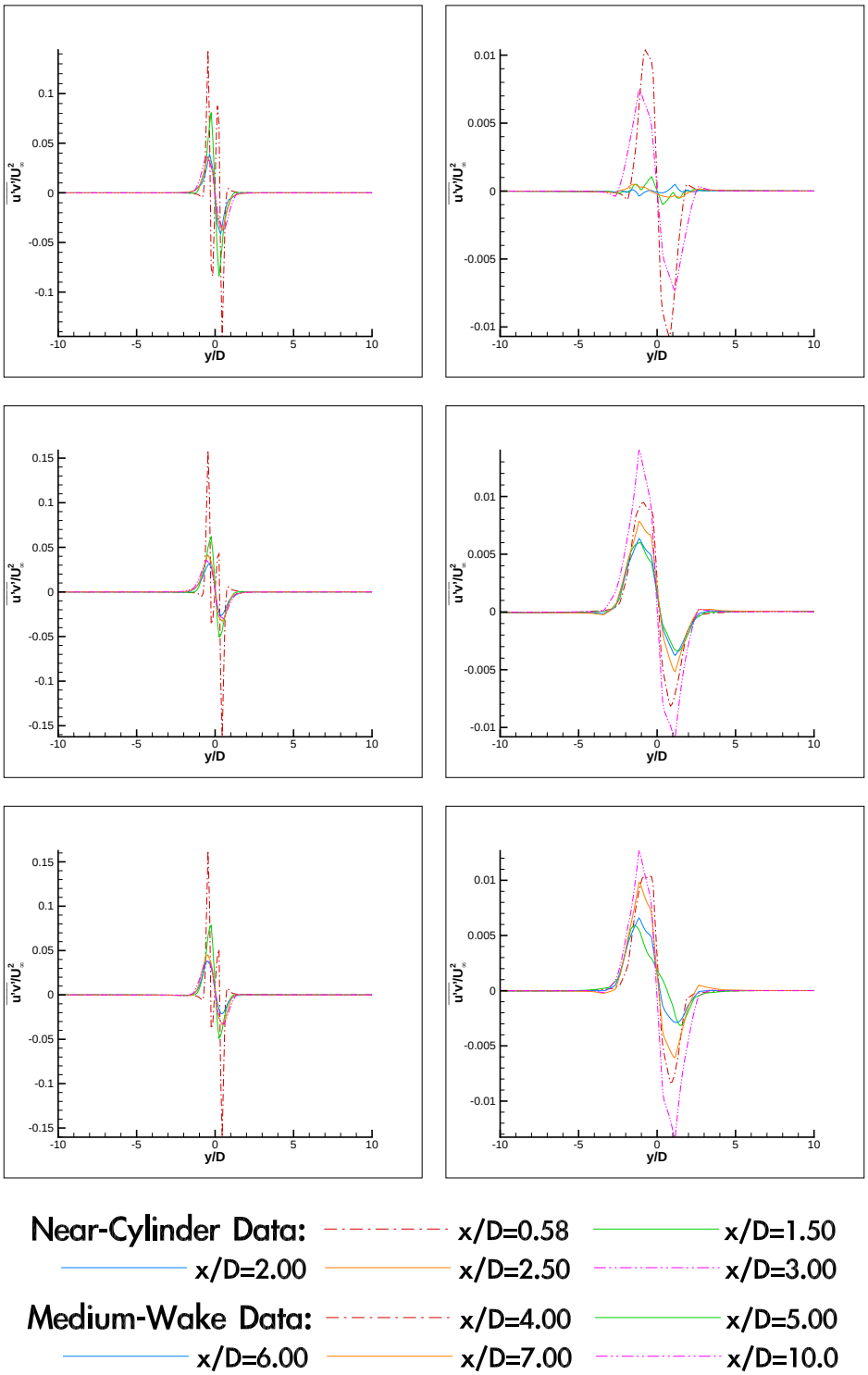

FIGURE B.39: Reynolds Number 3900, 2D flow. Reynolds stresses in the $u'v'$ direction in the cylinder wake. 2^{nd} order Min Mod (top), 2^{nd} order Van Leer (middle) and 3^{rd} order Kim Kim (bottom). Left images are near-cylinder points, right images are medium-wake points, with lines labelled appropriately.

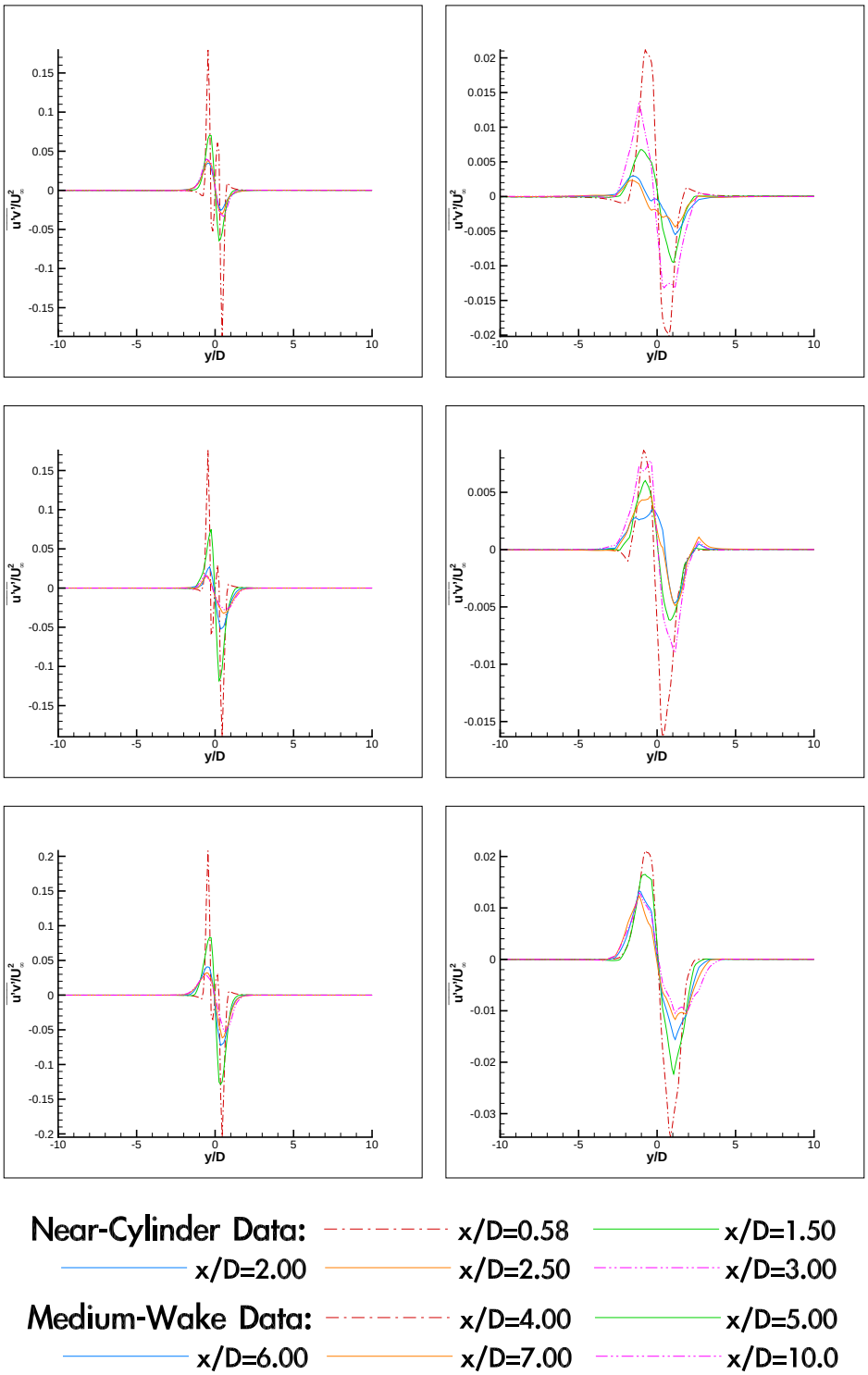

FIGURE B.40: Reynolds Number 3900, 2D flow. Reynolds stresses in the $u'v'$ direction in the cylinder wake. 5^{th} order Kim Kim (top), 5^{th} order WENO (middle) and 9^{th} order WENO (bottom). Left images are near-cylinder points, right images are medium-wake points, with lines labelled appropriately.

C

Appendix C: Simulation of flow over a large frigate

An additional portion of work carried out between the end of November 2007 and March 2008 was part of a project undertaken by the group to carry out CFD analysis of the Wave Class Auxiliary Oiler Tanker vessel. The Wave Class (shown in figure C.1) is a supply vessel tasked with replenishing warships with fuel, water and other stores whilst at sea. At the aft (rear) of the ship is a flight deck and hanger to support the Merlin class helicopter. The project was to carry out CFD simulations at a range of wind-speeds and directions, in order to determine the airflow characteristics that will be encountered by helicopters approaching the flight deck.

The work required for this project was to model the vessel in CAD software from detailed technical drawings, so that a grid file could be generated using Gridgen. This was then converted to be used with the group CFD software.

The main vessel superstructure is positioned at the aft of the ship slightly forward of the flight deck, with the front and mid section of the vessel taken up by the replenishment rigs and machinery. The CAD model for the vessel was created with thought being given to the grid resolution and which of the above-deck features had to be modelled (and in what level of detail) for the CFD simulation in order to determine how the air-flow over the ship (and in particular over the flight deck) was affected. For example, additional care was taken to maintain the sharp edges at the border of the ship as these would be the source of large-scale separation in CFD simulations. Discussion was carried out over whether to maintain spherical geometries, or whether these should

be modelled as rectangular blocks. These were ultimately kept spherical, as this went some way to correctly capturing flow shedding behaviour around these features.

The mesh was generated in a complex, high resolution, grid form, with smaller cell dimensions closer to significant features. The flow over the vessel was then computed using the group code and the designed mesh, with flow directions set at varying angles of attack around the vessel. The sea surface was assigned a separately derived boundary condition for these runs. The output was then carefully examined, with particular attention paid to the flow over the rear deck of the vessel, and the results published in a paper [30]. A collage of the animated air flow from the initial results is shown in figure C.2.

FIGURE C.1: A Photo of RFA Wave Knight - a vessel of the Wave Class type. Photo source: Royal Navy Internet Photo Gallery

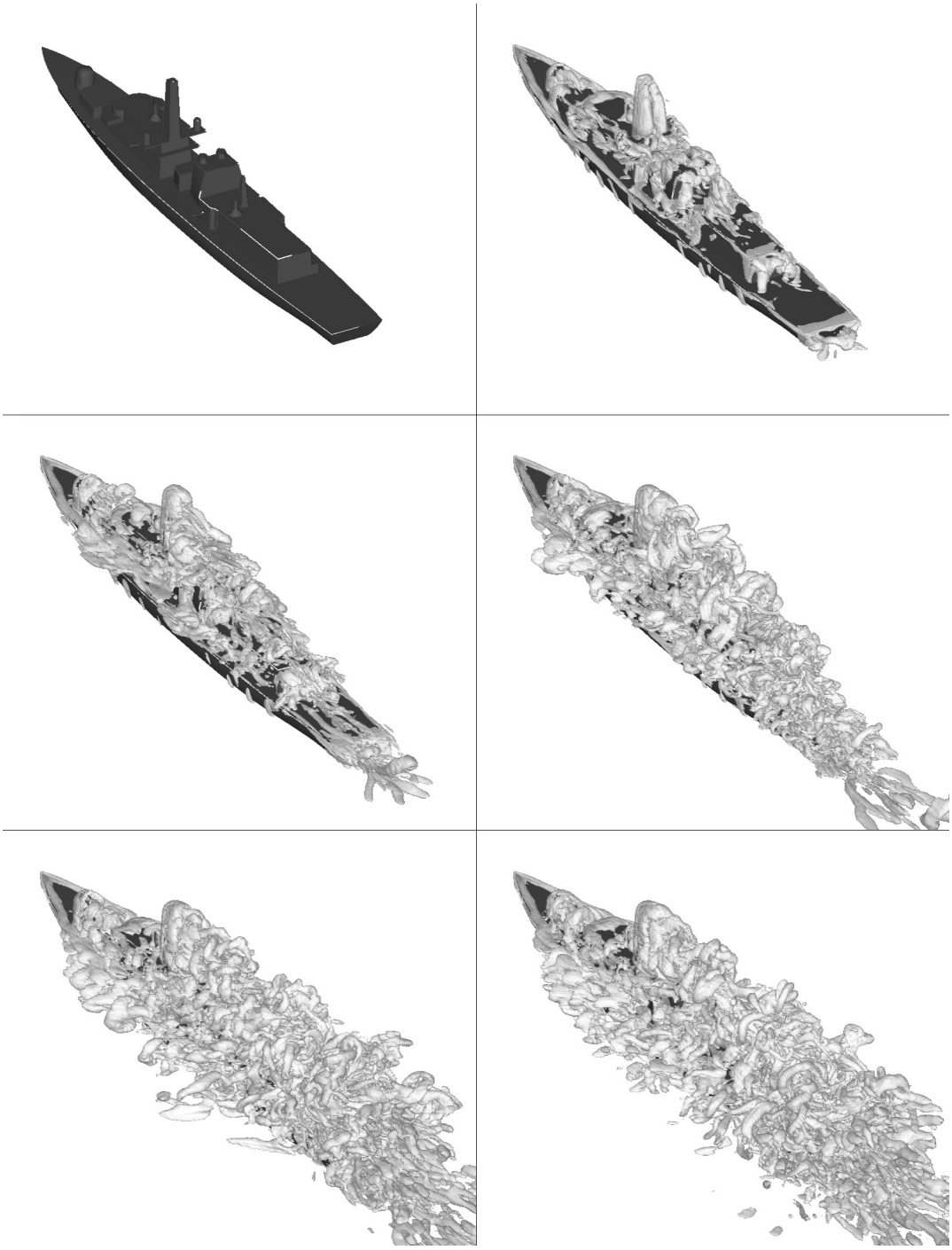

FIGURE C.2: A collage of the initial results for 0°flow